Electron correlation and electro-nuclear couplings in the dissociative-ionization dynamics of molecules in intense laser fields

Jean-Nicolas Vigneau

Electron correlation and electro-nuclear couplings in the dissociative-ionization dynamics of molecules in intense laser fields

Corrélation électronique et couplages électro-nucléaires dans la dynamique d'ionisation dissociative de molécules en champs laser intenses

Thèse de doctorat de l'Université Paris-Saclay et de l'Université Laval

École doctorale n°572 : Ondes et Matière (EDOM)
Spécialité de doctorat : Physique
Graduate School : Physique
Référent : Faculté des sciences d'Orsay

Thèse préparée à l'**Institut des Sciences Moléculaires d'Orsay** (Université Paris-Saclay, CNRS), et au **Département de chimie** (Université Laval), sous la direction d'**Éric CHARRON**, Professeur, sous la co-direction de **Thanh-Tung NGUYEN-DANG**, Professeur, et le co-encadrement d'**Osman ATABEK**, Directeur de recherche

Thèse soutenue à Paris-Saclay, le 21 Mai 2024, par

Jean-Nicolas VIGNEAU

Composition du jury
Membres du jury avec voix délibératives

Christian CORNAGGIA Directeur de recherche, CEA Saclay, France	Président
Anh-Thu LE Professeur, University of Connecticut, USA	Rapporteur & Examinateur
Richard TAIEB DR CNRS, Sorbonne Université, France	Rapporteur & Examinateur
Paul JOHNSON Professeur, Université Laval, Québec, Canada	Examinateur

THESE DE DOCTORAT
NNT : 2024UPASP028

Electron correlation and electro-nuclear couplings in the dissociative-ionization dynamics of molecules in intense laser fields

Thèse en cotutelle
Doctorat en chimie

Jean-Nicolas Vigneau

Université Laval
Québec, Canada
Philosophiæ doctor (Ph. D.)

et

Université Paris-Saclay
Orsay, France
Philosophiædoctor (Ph. D.)

université PARIS-SACLAY | ÉCOLE DOCTORALE Ondes et matière (EDOM)

Titre: Corrélation électronique et couplages électro-nucléaires dans la dynamique d'ionisation dissociative de molécules en champs laser intenses

Mots clés: corrélations électroniques, dynamique électro-nucléaire, champ intense

Résumé: Cette thèse, en deux parties distinctes, se concentre sur l'étude de la dynamique moléculaire de H_2 soumis à un champ laser intense.

Dans la première partie (chapitres 2 et 3), j'explore le rôle crucial de la corrélation électronique dans le processus d'ionisation simple de la molécule H_2, en utilisant une méthode ab-initio pour résoudre l'équation de Schrödinger dépendant du temps dans l'approximation de Born-Oppenheimer. J'examine différentes configurations géométriques de la molécule, correspondant à différentes distances internucléaires : à l'état d'équilibre, dans une configuration allongée et dans une configuration quasi-dissociée. Cette analyse permet de mieux apréhender les mécanismes fondamentaux impliqués dans l'ionisation de la molécule H_2 en champs laser intenses.

Dans la seconde partie (chapitres 4, 5 et 6), je me suis tourné vers le développement d'un modèle semi-classique permettant d'étudier l'ionisation simple et double de la molécule H_2. Ce modèle permet de calculer de manière quasi-analytique les taux d'ionisation, y compris jusqu'à l'explosion coulombienne, tout en intégrant la propagation des paquets d'onde vibrationnels de la molécule dans sa forme neutre et ionisée. J'ai ainsi été en mesure de prendre en compte les effets résultant de la dynamique de vibration des noyaux, ce qui constitue une avancée significative dans la modélisation de la dynamique moléculaire sous l'impact de champs laser suffisamment intenses pour engendrer une ionisation multiple des molécules.

Dans le cadre de ma première étude axée sur les interactions électroniques, j'ai modifié le programme « Many Electron Dynamics System », ou MEDYS, afin de pouvoir désactiver adiabatiquement la corrélation électronique. Ce programme, qui est basé sur un algorithme multi-configurationnel dépendant du temps, est issu de plusieurs décennies de travail au sein du groupe du Prof. Nguyen-Dang de l'Université Laval au Canada. En comparant les dynamiques obtenues avec et sans corrélation électronique, j'ai pu sonder les limites et les conséquences de l'approximation SAE, pour « Single Active Electron ». Cette analyse m'a permis de mieux comprendre l'importance de la corrélation électronique dans le processus d'ionisation simple de la molécule H_2.

Dans ma seconde étude, j'ai développé un programme entièrement nouveau pour représenter le processus d'ionisation de manière semi-classique tout en tenant compte de la dynamique vibrationnelle. J'ai commencé par étudier l'influence de différentes approximations dans le calcul des vitesses d'ionisation de la molécule, telles que les approximations ADK ou PPT moléculaires, sur les probabilités de première et seconde ionisation, pour différentes longueurs d'onde d'un champ laser pulsé. J'ai également étudié l'impact sur la distribution vibrationnelle non-Franck-Condon formée dans l'ion moléculaire H_2^+, des différents paramètres de l'impulsion laser, y compris la polarisation linéaire ou circulaire du champ. J'ai intégré la dynamique vibrationnelle dans ce modèle en utilisant une approche de type opérateur fractionné, pour propager les paquets d'onde de H_2 et H_2^+. En comparant ces résultats avec ceux obtenus en figeant la dynamique nucléaire, j'ai pu confirmer l'importance d'inclure le mouvement des noyaux dans la modélisation de la dynamique d'ionisation moléculaire, en particulier pour des noyaux très légers comme c'est le cas dans la molécule H_2. Enfin, j'ai pu générer et analyser les spectres de distribution d'énergie cinétique des protons, dans le processus de dissociation de la forme ionisée de la molécule et lors de l'explosion Coulombienne. Ces résultats pourraient être précieux pour de futures collaborations avec des chercheurs en physique des plasmas, leur fournissant un outil permettant d'estimer les probabilités d'ionisation simple et double, et les spectres d'énergie cinétique des protons, contribuant ainsi à une meilleure compréhension des phénomènes physiques se produisant dans certains plasmas.

université PARIS-SACLAY

ÉCOLE DOCTORALE
Ondes et matière
(EDOM)

Title: Electron correlation and electro-nuclear couplings in the dissociative-ionization dynamics of molecules in intense laser fields

Keywords: electronic correlation, electro-nuclear dynamics, intense field

Abstract: This thesis, in two distinct parts, focuses on the study of the molecular dynamics of H_2 subjected to an intense laser field.

In the first part (Chapters 2 and 3), I explore the crucial role of electronic correlation in the single ionization process of the H_2 molecule, using an ab-initio method to solve the time-dependent Schrödinger equation in the Born-Oppenheimer approximation. I study different geometric configurations of the molecule corresponding to different internuclear distances: at equilibrium, in an extended configuration, and in a quasi-dissociated configuration. This analysis provides a better understanding of the fundamental mechanisms involved in the ionization of the H_2 molecule in intense laser fields.

In the second part (Chapters 4, 5 and 6), I turned to the development of a semiclassical model for the study of single and double ionization of the H_2 molecule. This model allows the quasi-analytical calculation of ionization rates, including up to the Coulomb explosion, while integrating the propagation of vibrational wave packets of the molecule in its neutral and ionized form. This allowed me to take into account the effects resulting from the vibrational dynamics of the nuclei, which represents a significant advance in the modeling of molecular dynamics under the influence of laser fields intense enough to produce multiple ionization of molecules.

In my first study of electronic interactions, I modified the program "Many Electron Dynamics System", or MEDYS, to adiabatically deactivate the electronic correlation. This program, based on a time-dependent multi-configuration algorithm, is the result of decades of work in the group of Prof. Nguyen-Dang at Laval University in Canada. By comparing the dynamics obtained with and without electronic correlation, I was able to explore the limits and consequences of the SAE approximation, for "Single Active Electron". This analysis allowed me to better understand the importance of electronic correlation in the single ionization process of the H_2 molecule.

In my second study, I developed a new model to represent the ionization process in a semi-classical way, taking into account vibrational dynamics. I started by investigating the influence of different approximations in calculating the ionization rates of the molecule, such as the ADK or PPT molecular approximations, on the first and second ionization probabilities, for different wavelengths of a pulsed laser field. I also studied the influence of different laser pulse parameters, including the linear or circular polarization of the field, on the non-Franck-Condon vibrational distributions formed in the H_2^+ molecular ion. I have integrated vibrational dynamics into this model, using a split-operator approach to propagate the H_2 and H_2^+ wave packets. By comparing these results with those obtained by freezing the nuclear dynamics, I was able to confirm the importance of including nuclear motion in the modeling of molecular ionization dynamics, especially for very light nuclei such as in the H_2 molecule. Finally, I was able to generate and analyze proton kinetic energy release spectra during the process of dissociation of the ionized form of the molecule and during the Coulomb explosion. These results could prove useful in future collaborations with plasma physics researchers, providing them with a tool for estimating single and double ionization probabilities and proton kinetic energy spectra, thus contributing to a better understanding of the physical phenomena occurring in certain plasmas.

Contents

List of Tables

List of Figures

Glossary

ADK: Ammosov-Delone-Kraïnov
AO: Atomic Orbital
ATD: Above-Threshold Dissociation
ATI: Above-Threshold Ionization
a.u.: Atomic Units
BO: Born-Oppenheimer
BS: Bond Softening
COLTRIMS: Cold Target Recoil Ion Momentum Spectroscopy
CI: Configuration Interaction
CPA: Chirped Pulse Amplification
CSF: Configuration State Function
DDQ: Dynamical Dissociation Quenching
KS-DFT: Kohn-Sham Density-Functional Theory
FC: Franck-Condon
FWHM: Full Width at Half Maximum
HF: Hartree-Fock
HHG: High-Order Harmonic Generation
JES: Joint Energy Spectrum
KED: Kinetic Energy Distribution
LCAO: Linear Combination of Atomic Orbitals
LIED: Laser-Induced Electron Diffraction
MCTDH(F): Multiconfigurational Time-Dependent Hartree(-Fock)
MEDYS: Many-Electrons-Dynamics System Program
MO: Molecular Orbital
MO-ADK: Molecular Ammosov-Delone-Kraïnov
MO-PPT: Molecular Popov-Perelomov-Terent'ev
MPI: Multiphoton Ionization
PPT: Popov-Perelomov-Terent'ev
QRS: Quantitative Rescattering
SAE: Single Active Electron
SC: Semi-Classical
SFA: Strong Field Approximation
SO: Split-Operator
TDCI: Time-Dependent Configuration Interaction
TD-MCSCF: Time-Dependent Multiconfiguration Self-Consistent Field
TDSE: Time-Dependent Schrödinger Equation
TI: Tunnel Ionization
VT: Vibrational Trapping

*To my daughter **Éliane***
*and my partner **Sabrina**,*
for their support in my academic and professional endeavours;

*In the memory of Dr. **Osman Atabek**,*
a renown scientist in the domain of strong field molecular dynamics, and a caring supervisor to his foreign students in this important stage of their life.

[...] electrons are not particles in the classical sense—they are more of a wave—and attosecond physics is about describing and characterizing, these waves.

Anne L'Huillier
Lund University News,
October 4^{th} 2023,
« Anne L'Huillier awarded Nobel Prize in Physics. »

Acknowledgements

I would like to thank everyone that have supported me during my academic endeavours, and helped me grow to become the scientist that I am today and aim to become tomorrow.

I am thankful to my supervisors for their guidance during the research project;

To my canadian thesis co-director, the Professor **Thanh-Tung Nguyen-Dang**, whom I have had the pleasure to collaborate with since I started in his theoretical laboratory as an intern, back in 2017. It is working by his side that my passion for attosecond physics and, more broadly, computational sciences, grew and flourished, enough so to reorient myself from an organic chemist background to a quantum physicist one. It is under his supervision and with his trust in my capacities that I reached my goals and obtained my degrees at the Université Laval, and I hope one day to make him proud with significant contributions to the rich and promising domain of strong field molecular dynamics.

To my french thesis co-director, the Professor **Eric Charron**, with whom I have had the privilege to work for the duration of the thesis and, hopefully, for other collaboration projects in the future. Since my arrival in France, which has been a first international experience for me, Eric has been not only a professional and caring supervisor, but also a reassuring presence in a temporary new life far from old friends and family. Even if he has a lot of responsibilities as the director of the EDOM, he always found the time for (bi-)weekly meetings to discuss the progress of the research, and give crucial recommendations to solve computational and conceptual problems, as well as insights for the next logical steps to the project. I wish my future involvements in the science community to be as fruitful as his, and to similarly be able to gain the trust of my peers as a respected administrative figure.

To my french thesis co-supervisor, the Researcher Emeritus Dr. **Osman Atabek**, for the rich scientific knowledge he always so gladly like to share with the new generation of researcher, and his broad interest in everything that involves the understanding of our universe. He was well known in our research group and among his colleagues for his love of celebrations—any occasion that warranted

the tasting of french delicacies, and especially chocolate—and his rigour in his scientific methodology. He was also personally invested in the well being of his students, having himself travelled from Turkey to study in France at the age of 18, and eventually find love and establish his home. A resourceful supervisor, Mr. Atabek was also very helpful to accustom to the french administrative procedures and culture. Dr. Atabek regrettably quit us for a more peaceful place on June 27^{th} 2022, but in a sense, still remains through our collective remembrance of his person, and forever in the grounds he has laid for future generations with his research.

Warm thanks are due to the members of the jury—Director of Research Dr. **Christian Cornaggia** from the French Alternative Energies and Atomic Energy Commission (CEA) Paris-Saclay, Professor **Paul Johnson** from the Université Laval, Professor **Anh-Thu Le** from the University of Connecticut and Director of Research Dr. **Richard Taïeb** from the Sorbonne Université—who have accepted to be part of the finalization of this wonderful project, to challenge me as a future scientist so that I can develop my curiosity in different facets of the strong field molecular dynamics domain and to push my knowledge to ensure better collaborations with theoricians and experimentalists of related research fields.

I also thank the thesis follow-up committee for their time and energy in making sure that the PhD goes smoothly in administrative and scientific regards: Professor **Jean-François Morin**, Professor **Anna Ritcey** and again, Professor **Paul Johnson** from the Université Laval, as well as Director of Research Dr. **Thomas Pino** and Director of Research Dr. **Jacques Robert** from the Université Paris-Saclay.

The thesis project could not have happened without the funding from the Doctoral Scholarship of the French Minister of Higher Education, Research and Innovation (MESRI), attributed by the the École Doctorale Ondes et Matière (EDOM). Travels between Canada and France were rendered possible by the Citizens of the World Scholarship of the Choquette Family Foundation, and the Paul-Antoine-Giguère Scholarship.

I would also like to thank my colleagues and friends of the Université Laval: Dr. **François Dion**, who thought me how to code along with Prof. Dang, and never hesitated to give a hand computer-wise; Dr. **Salima Hennani**, for her guidance through the enriching discussions that we have had about our domain of research; Dr. **Peyman Fahimi**, a great friend of mine that I met during his stay in the laboratory of Prof. Dang, and who has unconsciously been a source of reassurance when I travelled abroad, for he has lived a similar scenario with lesser cultural similarities; Prof. **Chérif F. Matta**, for the wonderful opportunities he

has presented me to advance my scientific career, and his trust in my skills as a researcher and presenter, which has tremendously helped with my confidence in my beginnings.

To my colleagues and friends of the Institut des Sciences Moléculaires d'Orsay (ISMO), thanks to them for accepting me arms open into the research group, and for our cultural exchanges and outings in Paris: Dr. **Laïla Dakroub**, **Timothé Estrampes**, Dr. **Jennifer Joseph**, Dr. **Samrit Mainali**, Dr. **Annie Pichery**, Dr. **Lei Shi** and all the permanent members of the research team Dynamiques et Interactions: Rayonnement, Atomes, Molécules (DIRAM).

I am also thankful to my family and friends, who have been by my side during this project among others and have given me the necessary moral support to follow my dreams.

My daughter, **Éliane**, who have brought me motivation and joy during the final months of my PhD. I hope this document to be, along with the unconditional love of her parents, a source of ambition to follow her dreams, wherever they might lead her. My partner, **Sabrina**, who has braved this long distance experience with the strength and love one can only hope of a wonderful woman, and best friend. Your moral support had no price and no bound, and I certainly couldn't have done it without your support. My parents, **Roger** and **Liette**, who fueled my ambitions from the cradle and always helped me however they could, and my brother, **William**, of whom I have always been proud. My extended family, that has also encouraged me to pursue my interest in science.

My dear friends, **Mathieu** and **Nathaniel**, that I have known since more than 20 years, as well as **Morgan**, **Émilie**, **Frédéric**, **Marc** and **Éva**, with whom I have shared countless life experiences.

Thanks to everyone involved in the administrative process of the PhD in both institutions, and to the others working in the shadow that have indirectly contributed to this thesis.

Foreword

Some of the chapters (Chaps. 3, 5 and 6) found in this thesis are inserted published articles from the research conducted during the PhD, enhanced by annexes that deepen the analysis upon results that have been overlooked for the sake of editorial conciseness. Each co-author's contribution to those articles is described in the following paragraphs.

Chapter 3 covers the article "***Strong-Field Molecular Ionization Beyond the Single Active Electron Approximation***" (DOI: 10.1063/5.0111636), which has been submitted on July 19^{th} 2022 and accepted on September 14^{th} 2022 in *the Journal of Chemical Physics*. The article has been inserted as is, without any modification besides layout adjustments. The author of this thesis, Jean-Nicolas Vigneau, is also the first author of the presented article. Other co-authors are, in order, Thanh-Tung Nguyen-Dang, Eric Charron and Osman Atabek. All authors contributed to the study conception and design. The numerical simulations were performed by Jean-Nicolas Vigneau. The first draft of the manuscript was written by Thanh-Tung Nguyen-Dang and all authors commented on previous versions of the manuscript. All authors read and approved the final manuscript.

Chapter 5 covers the article "***Strong Field Non-Franck-Condon Ionization of H_2: A Semi-Classical Analysis***" (DOI: 10.1140/epjs/s11734-022-00750-z), which has been submitted on June 22^{nd} 2022, accepted on December 3^{rd} 2022 and published on January 4^{th} 2023 in *the European Physical Journal Special Topics*. The article has been inserted as is, without any modification besides layout adjustments. The author of this thesis, Jean-Nicolas Vigneau, is also the first author of the presented article. Other co-authors are, in order, Osman Atabek, Thanh-Tung Nguyen-Dang and Eric Charron. All authors contributed to the study conception and design. The numerical simulations were performed by Jean-Nicolas Vigneau. The first draft of the manuscript was written by Eric Charron and all authors commented on previous versions of the manuscript. All authors read and approved the final manuscript.

Chapter 6 covers the article "***Electro-nuclear Dynamics of single and double ionization of H_2 in ultrafast intense laser pulses***" (DOI: 10.1021/acs.jpca.3c06525), which has been submitted on September 29^{th} 2023, accepted on January 4^{th}

2024, revised on January 26^{th} 2024, published online on February 13^{th} 2024 and published in issue on February 22^{nd} 2024 in *the Journal of Physical Chemistry A*. The article has been inserted as is, without any modification besides layout adjustments. The author of this thesis, Jean-Nicolas Vigneau, is also the first author of the presented article. Other co-authors are, in order, Thanh-Tung Nguyen-Dang and Eric Charron. All authors contributed to the study conception and design. The numerical simulations were performed by Jean-Nicolas Vigneau. The first draft of the manuscript was written by Eric Charron and all authors commented on previous versions of the manuscript. All authors read and approved the final manuscript.

Chapter 1

Introduction

Contents

1.1 . Context

Recent developments in laser generation technologies have rendered possible experiments studying non-linear quantum phenomena. Since the beginning of the 21st century, experimentalists are able to produce laser pulses with durations of the order of sub-femtoseconds [1], thus achieving irradiation of molecules within time scales comparable to that of the electronic and vibrational motions of molecules. In terms of intensity, it is possible to generate pulses of over 10^{14} W/cm^2 since the mid 1960s, and with the development of the Chirped Pulsed Amplification (CPA) method in the mid 1980s [2], pulses with an intensity of more than 10^{16} W/cm^2 are commonly used for the generation of plasma channels [3]. With pulses of such parameters within reach, theoretical physicists now have the tools to study and control molecular dynamics in a strong laser field [4–6].

When operating in the near-IR, these ultrafast electromagnetic pulses, which combine both long wavelengths and high intensities, expose the system to a high concentration of low-energy photons. This situation gives rise to a non-negligible range of control over the molecular dynamics under consideration, through the parameters of the field that govern the selective ionization and dissociation pathways of the molecule.

The simulation of complete molecular dynamics in strong laser fields should be a powerful tool to predict the behaviour of complex chemical and biological systems under such conditions. Alas, with our current technological means, it constitutes a significant challenge at two levels: First, on a time resolution standpoint, it requires attosecond (10^{-18} s) time steps to ensure the adiabatic evolution of the perturbed system on the very short time-scale of the pulse. Then, as more complex molecules are studied, one faces challenge from the standpoint of size (number of degrees of freedom).

Adding more nuclei and electrons to the system amplifies the challenges of the so-called many-body problem [7]. Not only does it imply the consideration of new degrees of freedom associated with the particles, but it also requires the consideration of new interactions between existing particles. The electro-nuclear couplings increase the complexity considerably, as do the non-negligible electron correlations. For this reason, many research groups focus on the molecular dynamics of the benchmark dihydrogen H_2 molecule, which contains electro-nuclear couplings with a single vibrational degree of freedom, and is thus simple enough to simulate with relative ease. The even simpler one-electron dihydrogen molecular ion H_2^+ is also often used since the absence of electronic correlations greatly simplifies the interpretation of its excitation, ionization and dissociation dynamics.

From the wave packet initially created when H_2 is ionized to H_2^+, some dissociation pathways are found to be the result of Above-Threshold Dissociation (ATD) [8, 9] with the absorption of more photons than the minimum required to reach the dissociation threshold, and Bond Softening (BS) [10] with the overall absorption of a single photon when the chemical bond is weakened by lowering the potential barrier preventing dissociation. In contrast, Vibrational Trapping (VT) [11–13] is the opposite process due to the transition from a dissociative to a bound potential, also caused by the coupling with an intense laser field. Both scenarios are phenomena of the vibrational dynamics described in the so-called dressed-states, or Floquet representation.

In addition, if the frequency of the field is comparable to the vibrational frequency of the molecule, it is possible to synchronize the phase of the field with the vibrations of the molecule in such a way that a laser-induced potential energy barrier to dissociation closes as the molecule reaches elongated geometries, reducing the probability of dissociation in an event called Dynamical Dissociation Quenching (DDQ) [14–18].

As to the ionization step itself, *i.e.* the preparation of H_2^+ from H_2, the simplest model refers to the Franck-Condon (FC) principle and considers the initial vibrational wave packet of the molecular ion as generated by the vertical promotion of the vibrational ground state of the parent H_2 molecule [19, 20]. This model was mainly invoked for practical purposes, since a non-FC distribution of the initial vibrational population of the ion is naturally expected to result from the nonlinear ionization rate dependence on the ionization potential, which depends on the internuclear distance [21–23].

To treat the ionization dynamics thoroughly, one has to solve the Time-Dependent Schrödinger Equation (TDSE). Because of the aforementioned many-body problem, the TDSE can only be solved for molecules with the use of approximations. These are generally divided into two categories: Grid-based approaches and function-based ones.

In grid-based approaches, to describe the motion of electrons in full dimensionality over long distances, the size of the spatial/momentum grid must be such that it corresponds to a complete basis, which requires a lot of computational power and memory. Grid-based approaches are thus mostly used for small and simple systems or complex systems in reduced dimensions. They have been used for instance for the electronic radial motion in atoms [24], 1D and 2D models of diatomic (such as bielectronic H_2 [25]), up to even triatomic molecules (such as bielectronic H_3^+ [26]).

As for function-based approaches, basis functions such as B-Splines [27–29] and

Sturmians [30] have been used in addition to Gaussians [31], or mixed with them to better fit bound and continuum orbitals [32].

Electron correlation is an additional difficulty for many-electron systems. The simplest treatment is the so-called Time-Dependent Hartree-Fock (TDHF) method [33, 34], which uses a single Slater determinant to represent the time-dependent wavefunction. The electrons are then regarded as independent from each other, since a Slater determinant is essentially a product of orbitals antisymmetrized to satisfy the Pauli principle. To include electron correlation, a multiconfiguration method is required, such as the Time-Dependent Configuration Interaction (TDCI) method [35–38], the Multiconfiguration Self-Consistent Field (TD-MCSCF) method [39], or the Multiconfiguration Time-Dependent Hartree-Fock (MCTDHF) method [40–44].

The challenges are already formidable when considering only the dynamics of correlated electrons at fixed nuclear geometry. The inclusion of nuclear motion along with an ab initio treatment of the ionization of a many-electron molecule is understandably much less accessible. For this reason, most dissociative ionization dynamics are studied on H_2^+ [45–48]. While such simulations are simplified by the fact that there is a single electron, nuclear vibrations become even more important because the light hydrogen nuclei are faster than other nuclei found in typical polyatomic systems, thus correlating the dynamics of ionization and dissociation even more strongly.

The inclusion of another electron to consider the neutral H_2 molecule represents a significant increase in the complexity of the problem, in the form of electronic correlation. The problem has been studied by Wu *et al.* in 2013 through a joint energy spectrum (JES) of the two dynamics [49], and more extensively recently with an experimental comparison done with the Cold Target Recoil Ion Momentum Spectroscopy (COLTRIMS) method [50], a tool that permitted the observation of high-order ATD energy peaks in coincidence with the ATI spectrum [51].

Heavier diatomics have also been studied, like the CO molecule by Zhang *et al.* [52] and Sun *et al.* [53], but few research groups have attempted to study double ionization events coupled to dissociation channels [54], one of the challenges that is addressed in this thesis. Indeed, the degrees of freedom of both nuclei and electrons quickly become computationally overwhelming, and even more so when electronic correlations are taken into account.

In view of these challenges, popular semi-classical (SC), semi-empirical theories of ionization, such as the Popov-Perelomov-Terent'ev (PPT) or the Ammosov-Delone-Kraïnov (ADK), offer an attractive possibility of simplifying the problem within the Strong Field Approximation (SFA), as discussed in section 1.3.1. Such

considerations stem from the early work of Landau and Lifshitz, who considered the tunnel ionization model applied to the ground state of the hydrogen atom in a static field [55], and established the ionization probability as a current of the wave function passing through the lowered potential barrier. From the case of the hydrogen atom, the Russian physicists Popov, Perelomov and Terent'ev extended the theory to any atomic asymptotic Coulomb wave function [56–58], allowing both the multiphoton (MPI) and tunnel regimes of ionization in a theory called 'PPT'. Specializing the PPT model to parameters allowing only tunnel ionization in a quasi-static field, Ammosov, Delone and Kraïnov elaborated the ADK theory [59, 60], a simplification of the PPT method that does not require the iterative calculation of rates depending on the number of absorbed photons for the MPI regime.

Since the PPT and ADK methods were generalized only to atomic systems, the equations had to be reworked to admit cases of small molecules, as shown for instance by the experimental comparison made by Cornaggia and Hering [61]. Molecular ADK (MO-ADK) was then developed by Tong, Zhao and Lin [62] to include diatomics such as the H_2 molecule studied here. For the multiphotonic ionization dynamics of diatomics, the molecular PPT (MO-PPT) model was then developed by Benis *et al.* [63], including Tong from the MO-ADK development. These approaches neglect the possibility of the photoelectron returning to the parent ion, but it is to be noted that other SC theories can also be used to describe recollision events. It is the case of recent researches conducted by A. T. Le *et al.* [64] through the Quantitative Rescattering (QRS) theory, a model that efficiently simulates Laser-Induced Electron Diffraction (LIED) and High-Order Harmonic Generation (HHG) [65, 66].

The present study on H_2 uses some of these different approaches to consider first the single and then the double ionization dynamics of the molecule, and ultimately couple them with nuclear motion to describe the complete molecular dynamics.

1.2 . Ionization Regimes

1.2.1 . The Keldysh Parameter

During ionization, the abundance of relatively low energy photons leads to a duality between two mechanisms: multiphoton (MPI) and tunnel ionization (TI). The Keldysh parameter γ [67] is widely used to estimate the regime into which ionization (and dissociative ionization) takes place in a strong laser field. This parameter helps to better describe the behavior of the molecular wave packets

under study during the dynamics. It is given by the formula

$$\gamma = \frac{\omega \sqrt{2I_P(R)}}{F(t)} = 2\,\frac{\tau_T}{\tau_F}\,, \tag{1.1}$$

where ω is the laser frequency, $F(t)$ is the electric field strength, and $I_P(R)$ the ionization potential which, for a diatomic molecule, is a function of the internuclear distance R. As suggested by Eq. (1.1), the Keldysh parameter is twice the ratio of the tunneling time τ_T to the period of a field oscillation $\tau_F = 1/\omega$ [68], so that it is lower for tunnel ionization and higher for multiphoton ionization, leading for example to Above-Threshold Ionization (ATI) [69–71]. An increase of the laser intensity I thus leads to a decrease of the Keldysh parameter γ and ultimately to more efficient tunneling, while on the contrary increasing the frequency ω leads to an increase of γ and tends to favour multiphoton ionization [72].

1.2.2 .Tunnel Ionization Regime

Unlike classical physics, quantum mechanics allow the partial passage of wave packets through potential barriers, rather than a definitive blockage. This allows the description of tunneling probabilities, which can be non-negligible depending on the barrier. This ability of the wave packet comes from its wave-like character, and the probability for the system to pass through said barrier depends on the energy and width of the barrier.

When an atom or molecule is irradiated by a strong laser field, the electric dipole coupling $-e\,\mathbf{r}\cdot\mathbf{F}(t)$ forces the Coulomb energy binding electrons with nuclei to decrease asymptotically in the direction of the field. Since the bound electronic and vibrational states lie within potential wells, such a linear decrease of the binding potential in the direction of the field induces the generation of transient barriers of decreasing height and width as the laser intensity increases. Thus, low frequency and high intensity conditions favour the tunneling regime (also known as the quasi-static ionization regime), since high intensities significantly lower the potential barrier, while low frequency increases the duration of the tunneling event.

In the case of a linearly polarized field, since the field amplitude oscillates from one orientation to its opposite during the pulse, the electronic wave packets ionized by tunnel ionization have the opportunity to be recaptured through the well-known three-step recollision mechanism [1]. Once ionized, the photoelectron wave packet gains momentum in the continuum before returning to the parent ion where it can be recaptured. This mechanism leads to High-Order

Harmonic Generation (HHG) [73, 74], which results from the emission of high-energy photons of odd harmonics. These harmonics were used in a molecular imaging technique called orbital tomography [75]. When the electronic wave packet recollides with the parent ion, the resulting interactions also give rise to Laser-Induced Electron Diffraction (LIED) [76–79] spectra, another tool for ultrafast molecular imaging.

1.2.3 . Multiphoton Ionization Regime

A peculiarity of atomic and molecular dynamics in strong laser fields is that, since the system is subjected to a high concentration of photons, it is quite possible for it to absorb multiple photons before eventually re-emitting some of them.

In this phenomenon, the combined energy of the absorbed photons can exceed the ionization potential of the target species, allowing the electrons to overcome the binding energy of the atom or molecule, sometimes reaching energies well above the ionization threshold. These events are referred to as ATI phenomena, for Above Threshold Ionization.

Multiphoton ionization is easily distinguished from quasi-static ionization by the resulting Kinetic Energy Distribution (KED) recorded in photoelectron spectra. In fact, in a multiphoton process, the electron KED is seen as a series of peaks separated by the energy of a discrete number of photons [71].

1.3 . Molecular Dynamics Approximations

Regardless of the ionization regime, the treatment of molecular dynamics is far from simple, even for the simplest molecule, and necessitates the use of approximations. Some of the most common in the literature in the field of attosecond physics are the Strong Field Approximation (SFA), the Single Active Electron (SAE), and the Born-Oppenheimer (BO) approximations.

1.3.1 . Strong Field Approximation (SFA)

As its name suggests, the Strong Field Approximation is a recurrent simplification model based on the fact that the molecular dynamics is largely dominated by the strong laser field. The theory relies on the premise that such a field is so strong that the Coulomb forces between the particles that constitute the molecule are negligible compared to the field's effect on those particles. As explained for example in the review by Amini *et al.* [80], the SFA has been at the heart of attosecond physics research for the last 25 years, going back to the sem-

inal works of Keldysh [67], Faisal [81] and Reiss [82], and to the electron-atom and atom-atom scattering models of Kroll and Watson [83, 84].

It is important to mention that the SFA underlies the popular work of Corkum's research group known as the Simple Man Model [85], and more formally the recollision or rescattering three-step model [86], where the so-called recollision mechanism is divided into three stages: the ionization of the system by tunneling effect, followed by the propagation of the free electron in the continuum, and finally its return to the parent ion under the effect of the laser field, leading to a collision with it. This three-step model is based on the use of both SFA and SAE; the former because the Coulomb attraction of the ion is not taken into account when calculating the acceleration of the ionized electron, and the latter because the interaction with other electrons is not taken into account, the interaction of the active electron with the strong electromagnetic field being considered as dominant.

The most significant work to assess non-SFA effects is the one by Ivanov, Spanner and Smirnova [87], who examined, within a semiclassical theoretic framework, the effects of the ionic core potential on the ionized electron dynamics through an eikonal (Eikonal-Volkov) approximation. That exploration is analytical while very recent explorations of the SFA limits carried out in the Nguyen-Dang group in the PhD thesis work of Hennani [88] are numerical and deal with non-SFA effects in the ionization dynamics of fully-correlated H_2. Such effects were brought to light by comparing the SFA dynamics—treating the ionized electron by Volkov waves [89]—with the results of bielectronic non-SFA wave packet calculations taking into account the interaction with the field and the Coulomb attraction potential of the ion, via the use of actual scattering states represented in a B-Splines basis.

Amini *et al.* [80] refer to the model using Volkov states as a primitive SFA, as opposed to the "standard SFA" which refers rather to a basis of scattering wavefunctions (as opposed to Volkov states) for the ionized electron, and which is formulated in such a way that (1) the strong field does not couple the ionized state to any bound state other than the ground state, and (2) the population of the ground state is assumed to be known and constant. The work cited above of the Nguyen-Dang group [76, 90, 91] already goes beyond this standard SFA definition, as initialized bound states are generated from a multi-electronic/multi-orbital basis, and its ground state population evolves according to the TDSE.

1.3.2 .Single Active Electron (SAE) Approximation

Since in a strong field molecular dynamics simulation most of the computational resources are devoted to the consideration of the electron interaction, the Single Active Electron (SAE) approximation turns out to be one of the most widely used models to simulate molecules in a strong laser field [92].

In this approximation, the ionization dynamics are assumed to be dominated by the force of the external laser field, which is then added to the Coulomb attraction potential of the cation represented by an effective average field, while the repulsion from the other electrons is neglected.

To refine the SAE approximation (and to study its limits of validity), a number of approaches have been developed. A common thread is to construct a model effective potential for the departing electron in the molecular ionization. The introduction of an empirical potential to capture the dynamic (field-induced) multielectron polarization effects [93–95] is an example of such a construct. The Correlated Strong-Field method [93, 96] provides a rigorous foundation to the idea through a Born-Oppenheimer type separation of the active electrons from the others. Such a separation is also proposed in the work of Schild and Gross [97].

One objective of this thesis is to identify the limitations of the SAE approximation through numerical simulations of strong-field ionization of a simple two-electron molecule. For this, we have access to an in-house *ab initio* code, Many-Electrons-Dynamics System (MEDYS), which already makes use of a non-SAE algorithm and takes into account full electron correlations within the Born-Oppenheimer approximation, *i.e.* at fixed nuclear geometries. With new implementations to the program, it is now possible to insert a modulation of the electron-repulsion term in the Hamiltonian that allows us to switch-off adiabatically this interaction, electron correlation, from the fully correlated model. As the field reaches a maximum of its amplitude in the beginning of the dynamic, bielectronic terms of the electronic Hamiltonian are slowly (via a sigmoïd function) brought down to zero, keeping only Coulomb attractions with the nuclei, simulating a SAE situation. Single ionization dynamics were compared for the case including full correlation, and the one with adiabatic switch-off, for different geometries of the H_2 molecule for which electron correlation is simply measured by the field-free mixing of the σ_g^2 and σ_u^2 configurations.

1.3.3 . Born-Oppenheimer (BO) Approximation in Strong Fields

To treat the complete ionization dynamics of multi-electron molecules, one has to include electronic correlation. The complexity of such a task increases with the number of particles involved, and since electrons typically move a thousand times faster than nuclei, the need to include vibrational dynamics is often subject to reconsideration from theoreticians, especially when the system is composed of heavy nuclei. To limit the computational power required for multi-electron simulations, the Born-Oppenheimer (BO) approximation is often invoked in the literature to separate the electronic dynamics from the nuclear dynamics [98], which also leads to the possibility of neglecting the latter by considering the nuclei as static: a R-fixed approximation.

For single-electron diatomic molecules, the use of the Born-Oppenheimer approximation is not essential, since nuclear motion within small molecules is manageable when considering a single-electron cloud subjected to the Coulomb attraction of relatively slower nuclei. In the case of H_2^+, the dissociative ionization dynamics can even be simulated exactly by solving the TDSE with non-BO methods; as achieved in an early work of Bandrauk *et al.*, who has succeeded to produce ATI and ATD kinetic energy spectra in agreement with those obtained experimentally [99].

While solving the TDSE exactly for more complex systems is presently inaccessible with our current technological means, non-BO quantum simulations have been used to obtain reasonable results of coupled electro-nuclear dynamics from simple molecular systems, such as H_2 found in the works of Li and He [100], and Saugout *et al.* [54, 101]; D_2 from the work of Ranitovic *et al.* [102]; or HF as seen in the work of Yonehara and Takatsuka [103].

In this thesis, we aim to go beyond the R-fixed Born-Oppenheimer approximation that was implicitly used in the calculations with the MEDYS program by adding nuclear motions to the molecular dynamics. Given the demanding resources required for this if we keep treating the ionization step using MEDYS, we have instead developed a program that (1) simplifies the ionization dynamics with semi-classical, quasi-analytical methods such as MO-ADK and MO-PPT and (2) introduces a Split-Operator (SO) propagation routine to simulate the evolution of wave packets within the neutral (H_2) and ionic (H_2^+) vibrational potentials of the molecule. Both stages of the program development are discussed in Chapters 5 and 6. This development is also motivated by the demand of the user community to have an accessible and physically transparent, simple electro-nuclear dynamics simulation code.

1.4 . Objectives

The following objectives have been addressed in this work:

1. Since the SAE approximation is widely used in the literature, it is necessary to evaluate its quantitative limits in terms of field parameters, a research that has been initiated with our *ab initio* program MEDYS.

2. To study the complete molecular dynamics of H_2, we aim to couple the electronic degrees of freedom to those of the nuclei. This requires to implement a simplification of the ionization dynamics, as *ab initio* methods are computationally demanding. A simplification of the approach using semi-classical methods has been done, in a newly coded program.

3. After implementing the MO-ADK and MO-PPT approximations to simulate the ionization dynamics, the nuclear motion was implemented to study the electro-nuclear dynamics of H_2 in a strong laser field, thus going beyond the R-fixed Born-Oppenheimer approximation. The phenomena of ionization and dissociation were analyzed up to the Coulomb explosion of the molecule, in terms of ionization probabilities and proton kinetic energy spectra. The latter arised from a need for plasma experimentalists to improve their atomic ADK representation towards a more realistic MO-ADK/PPT approach, including vibrational motion.

1.5 . Thesis Layout

The thesis is structured in **two parts**, exploring the main projects that were pursued during the PhD.

Part I – The first part is a preliminary study on the quantitative limits of the SAE approximation using the Time-Dependent Multi-Configurations Self-Consistent Field MEDYS program of the Nguyen-Dang laboratory at the Université Laval, developed in **Chapters 2** and **3**.

Chapter 2 introduces the theory behind the post-Hartree-Fock method used to solve the Time-Dependent Schrödinger Equation, followed by a description of the MEDYS algorithm used in the present work to simulate fully-correlated single ionization dynamics of the neutral H_2 molecule at fixed internuclear distances and using SFA considerations. The necessary basis for a reasonable representation of the ionization paths is then explained in the same chapter, ending with

a presentation of the parameters associated with the pulsed strong laser field, and the observables resulting from the dynamics.

Chapter 3 is the inserted published article "Strong-Field Molecular Ionization Beyond the Single Active Electron Approximation", which is the result of our exploration of the quantitative limits of the SAE approximation, comparing ionization dynamics with fully-correlated electrons or with an adiabatically switched-off correlation. The total ionization probability profiles as a function of the peak intensity of the field were plotted for both types of dynamics, and two main observations were made from these figures. The first (1) is that at the equilibrium geometry of the molecule, we have perceived a sudden jump towards total ionization past peak intensities over 10^{16} W/cm^2, which indicated an over-the-barrier ionization event. The other (2) is that while a relatively smooth increase of the probability was shown at equilibrium and dissociative geometries, the elongated molecule ionization dynamics denoted partial quenching and exaltation depending on the peak intensity, when the electrons were fully-correlated. Such parameter-dependent phenomena were attributed to a Resonance-Enhanced Multiphoton Ionization (REMPI) mechanism causing interference between excitation and ionization pathways. This article is followed by an annex, which presents an analysis going beyond what has been published, and provides results on the dynamics at elongated internuclear distances that support the fact that quenching and exaltation ionization events can also happen at R values surrounding the $R = 5.0$ a.u. presented in the article. To this end, population profiles of both eigenstates and configuration state functions are shown for events of quenching and exaltation of the population, for all three elongated configurations of H_2, including the one published in the original paper.

Part II – The second part is focused on the study of the complete dissociative ionization dynamics of the molecule, using semi-classical methods to describe the ionization events and to facilitate the implementation of the vibrational motion of the nuclei; a project that required the scripting of a completely new code in the Atabek & Charron research group at the Université Paris-Saclay, addressed in **Chapters 4** to **6**.

Chapter 4 covers the development of the different algorithms used in the semi-classical implementation of the ionization dynamics. From the time-dependent Schrödinger equation, the sequential ionization processes are represented in a way that involves complex exchanges of wave packet amplitudes, while successive population transfers are obtained from projections over eigenstates, corresponding to the Eur. Phys. J. Spec. Top. article "Strong Field Non-Franck-Condon Ionization of H_2: A Semiclassical Analysis" [104]. This chapter also presents the kinetic equations including the vibrational wave packet propagation to introduce

the model used in the J. Phys. Chem. A article "Electro-nuclear Dynamics of H_2 single and double ionization in ultrafast intense laser pulses" [105]. The split-operator method used for the propagation of the nuclear wave packets is then discussed, before explaining the generated observables that are analyzed during the dynamics.

Chapter 5 consists of a first step in the project, which is discussed in the inserted Eur. Phys. J. Spec. Top. article "Strong-Field Non-Franck-Condon Ionization of H_2: A Semi-Classical Analysis". This article covers in detail the equations used for ionization with the molecular Ammosov Delone Krainov (MO-ADK) method or the molecular Popov Perelomov Terent'ev (MO-PPT) method. Simulations of H_2 ionization dynamics in a strong field were compared between both methods, and for linear or circular polarizations of the field. For a similar fluence, the linear polarization was shown to saturate the ionization probability at lower peak intensities than the circular polarization. Non-Franck-Condon population distributions over eigenstates of H_2^+ were compared to the Franck-Condon distribution, and its shift of populations towards lower energy levels was attributed to the R-dependence of the ionization rate calculated from MO-ADK or MO-PPT. The article is followed by an annex that presents visual depictions of the anisotropic angular ionization and the fitted Padé function to the t_0 value that is necessary in the molecular PPT method. Linear and circular polarization are furthermore analyzed in term of ionization rates to explain how the two polarizations do not induce similar ionization probabilities over a same fluence.

Chapter 6 includes the inserted J. Phys. Chem. A article "Electro-nuclear Dynamics of H_2 single and double ionization in ultrafast intense laser pulses" and a subsequent annex that inquires about differences between the observables produced by the methods involving static or propagating nuclear wave packets, and the population transfers from eigenstate projections, subject of Chap. 5. Vibrational dynamics are put forward in this article that highlights their crucial role in the simulation of the dissociative ionization of H_2. The importance of nuclei motion is particularly demonstrated in second ionization processes, where static vibrational wave packets largely underestimate ionization probabilities. The suggested model of complete molecular dynamics is used to generate realistic results through the KED spectra of protons emitted via photodissociated H_2^+, encompassing events of Above-Threshold Dissociation, Bond Softening and, from double ionization, Coulomb Explosion of the remaining protons. The annex investigates the differences in population profiles, average internuclear distances and KED spectra, while returning to the principles of semi-classical ionization rates calculated in the annex of Chap. 5.

The thesis is concluded in **Chapter 7** with a brief summary of all chapters, and

some research directions and future plans, such as the development of analytical ionization rates from post-Hartree-Fock methods, plans to further investigate the quantitative limit of the SAE approximation, and the implementation of a new ionic continuum that would involve Gaussian propagation rather than plane waves.

Bibliography

[1] P. B. Corkum and F. Krausz. Attosecond science. *Nat. Phys.*, 3(6):381–387, 2007. URL: https://www.nature.com/articles/nphys620, doi:10.1038/nphys620.

[2] D. Strickland and G. Mourou. Compression of amplified chirped optical pulses. *Opt. Commun.*, 56(3):219–221, 1985. URL: https://www.sciencedirect.com/science/article/pii/0030401885901208, doi:10.1016/0030-4018(85)90120-8.

[3] G. A. Mourou, T. Tajima, and S. V. Bulanov. Optics in the relativistic regime. *Rev. Mod. Phys.*, 78:309–371, 2006. URL: https://journals.aps.org/rmp/abstract/10.1103/RevModPhys.78.309, doi:10.1103/RevModPhys.78.309.

[4] O. Atabek, R. Lefebvre, and T. T. Nguyen-Dang. Theory of intense laser-induced molecular dissociation: From simulation to control. In *Special Volume, Computational Chemistry*, volume 10 of *Handbook of Numerical Analysis*, pages 745–802. Elsevier, 2003. URL: https://www.sciencedirect.com/science/article/pii/S1570865903100142, doi:10.1016/S1570-8659(03)10014-2.

[5] G. Basnayake, P. Hoerner, B. Mignolet, M. K. Lee, Y. F. Lin, A. H. Winney, D. A. Debrah, L. Popaj, X. Shi, S. K. Lee, H. B. Schlegel, F. Remacle, and W. Li. Ellipticity controlled dissociative double ionization of ethane by strong fields. *Phys. Chem. Chem. Phys.*, 23:23537–23543, 2021. URL: https://pubs.rsc.org/en/content/articlelanding/2021/cp/d1cp03585a, doi:10.1039/D1CP03585A.

[6] A. Valentini, S. van den Wildenberg, and F. Remacle. Selective bond formation triggered by short optical pulses: quantum dynamics of a four-center ring closure. *Phys. Chem. Chem. Phys.*, 22:22302–22313, 2020. URL: https://pubs.rsc.org/en/content/articlelanding/2020/cp/d0cp03435e, doi:10.1039/D0CP03435E.

[7] D. J. Thouless, H. S. W. Massey, and R. W. Hellwarth. The Quantum Mechanics of Many-Body Systems. *Physics Today*, 15(7):52–52, 07 1962. URL: https://pubs.aip.org/physicstoday/article-abstract/15/7/52/423033/The-Quantum-Mechanics-of-Many-Body-Systems?redirectedFrom=fulltext, doi:10.1063/1.3058273.

[8] P. H. Bucksbaum, A. Zavriyev, H. G. Muller, and D. W. Schumacher. Softening of the H_2^+ molecular bond in intense laser fields. *Phys. Rev. Lett.*, 64:1883–1886, 1990. URL: https://link.aps.org/doi/10.1103/PhysRevLett.64.1883, doi:10.1103/PhysRevLett.64.1883.

[9] A. Giusti-Suzor, X. He, O. Atabek, and F. H. Mies. Above-threshold dissociation of H_2^+ in intense laser fields. *Phys. Rev. Lett.*, 64(5):515, 1990. URL: https://link.aps.org/doi/10.1103/PhysRevLett.64.515, doi:10.1103/PhysRevLett.64.515.

[10] A. Zavriyev, P. H. Bucksbaum, H. G. Muller, and D. W. Schumacher. Ionization and dissociation of H_2 in intense laser fields at 1.064 μm, 532 nm, and 355 nm. *Phys. Rev. A*, 42:5500–5513, Nov 1990. URL: https://link.aps.org/doi/10.1103/PhysRevA.42.5500, doi:10.1103/PhysRevA.42.5500.

[11] A. Giusti-Suzor and F. H. Mies. Vibrational trapping and suppression of dissociation in intense laser fields. *Phys. Rev. Lett.*, 68:3869–3872, Jun 1992. URL: https://link.aps.org/doi/10.1103/PhysRevLett.68.3869, doi:10.1103/PhysRevLett.68.3869.

[12] A. D. Bandrauk. *Molecules in laser fields*. M. Dekker, New York, 1994.

[13] L. J. Frasinski, J. Plumridge, J. H. Posthumus, K. Codling, P. F. Taday, E. J. Divall, and A. J. Langley. Counterintuitive alignment of H_2^+ in intense femtosecond laser fields. *Phys. Rev. Lett.*, 86:2541–2544, Mar 2001. URL: https://link.aps.org/doi/10.1103/PhysRevLett.86.2541, doi:10.1103/PhysRevLett.86.2541.

[14] F. Châteauneuf, T.-T. Nguyen-Dang, N. Ouellet, and O. Atabek. Dynamical quenching of field-induced dissociation of H_2^+ in intense infrared lasers. *J. Chem. Phys.*, 108(10):3974–3986, 1998. URL: https://pubs.aip.org/aip/jcp/article-abstract/108/10/3974/531892/Dynamical-quenching-of-field-induced-dissociation?redirectedFrom=fulltext, doi:10.1063/1.475800.

[15] H. Abou-Rachid, T. T. Nguyen-Dang, and O. Atabek. Dynamical quenching of laser-induced dissociations of heteronuclear diatomic molecules in intense infrared fields. *J. Chem. Phys.*, 110(10):4737–4749, 1999. URL: https://pubs.aip.org/aip/jcp/article-abstract/110/10/4737/476441/Dynamical-quenching-of-laser-induced-dissociations?redirectedFrom=fulltext, doi:10.1063/1.478361.

[16] H. Niikura, P. B. Corkum, and D. M. Villeneuve. Controlling vibrational wave packet motion with intense modulated laser fields. *Phys. Rev.*

Lett., 90(20):203601, 2003. URL: https://link.aps.org/doi/10.1103/PhysRevLett.90.203601, doi:10.1103/PhysRevLett.90.203601.

[17] C. Lefebvre, T. T. Nguyen-Dang, and O. Atabek. Intense laser-controlled quenching of molecular fragmentation. *Phys. Rev. A*, 75(2):023404, 2007. URL: https://journals.aps.org/pra/abstract/10.1103/PhysRevA.75.023404, doi:10.1103/PhysRevA.75.023404.

[18] F. Dion. *Dynamique de systèmes polyatomiques et polyélectroniques en champ laser intense*. PhD thesis, Université Laval, Québec, Canada, 2018.

[19] P. Dietrich, M. Yu. Ivanov, F. A. Ilkov, and P. B. Corkum. Two-electron dissociative ionization of H_2 and D_2 in infrared laser fields. *Phys. Rev. Lett.*, 77:4150–4153, Nov 1996. URL: https://link.aps.org/doi/10.1103/PhysRevLett.77.4150, doi:10.1103/PhysRevLett.77.4150.

[20] A. S. Alnaser, B. Ulrich, X. M. Tong, I. V. Litvinyuk, C. M. Maharjan, P. Ranitovic, T. Osipov, R. Ali, S. Ghimire, Z. Chang, C. D. Lin, and C. L. Cocke. Simultaneous real-time tracking of wave packets evolving on two different potential curves in $H_2{}^+$ and $D_2{}^+$. *Phys. Rev. A*, 72:030702, Sep 2005. URL: https://link.aps.org/doi/10.1103/PhysRevA.72.030702, doi:10.1103/PhysRevA.72.030702.

[21] X. Urbain, B. Fabre, E. M. Staicu-Casagrande, N. de Ruette, V. M. Andrianarijaona, J. Jureta, J. H. Posthumus, A. Saenz, E. Baldit, and C. Cornaggia. Intense-Laser-Field Ionization of Molecular Hydrogen in the Tunneling Regime and Its Effect on the Vibrational Excitation of H_2^+. *Phys. Rev. Lett.*, 92:163004, Apr 2004. URL: https://link.aps.org/doi/10.1103/PhysRevLett.92.163004, doi:10.1103/PhysRevLett.92.163004.

[22] E. Goll, G. Wunner, and A. Saenz. Formation of ground-state vibrational wave packets in intense ultrashort laser pulses. *Phys. Rev. Lett.*, 97:103003, Sep 2006. URL: https://link.aps.org/doi/10.1103/PhysRevLett.97.103003, doi:10.1103/PhysRevLett.97.103003.

[23] Th. Ergler, B. Feuerstein, A. Rudenko, K. Zrost, C. D. Schröter, R. Moshammer, and J. Ullrich. Quantum-phase resolved mapping of ground-state vibrational D_2 wave packets via selective depletion in intense laser pulses. *Phys. Rev. Lett.*, 97:103004, Sep 2006. URL: https://link.aps.org/doi/10.1103/PhysRevLett.97.103004, doi:10.1103/PhysRevLett.97.103004.

[24] J. S. Parker, K. J. Meharg, G. A. McKenna, and K. T. Taylor. Single-ionization of helium at Ti:Sapphire wavelengths: rates and scaling laws. *J. Phys. B*,

40(10):1729–1743, 2007. URL: https://iopscience.iop.org/article/10.1088/0953-4075/40/10/008, doi:10.1088/0953-4075/40/10/008.

[25] A. D. Bandrauk. Harmonic generation in a 1D model of H_2 with single and double ionization. *J. Phys. B*, 38(14):2529–2544, 2005. URL: https://iopscience.iop.org/article/10.1088/0953-4075/38/14/016, doi:https://doi.org/10.1088/0953-4075/38/14/016.

[26] D. S. Tchitchekova, H. Lu, S. Chelkowski, and A. D. Bandrauk. Molecular high-order harmonic generation in a nonlinear two-electron molecule: the equilateral H_3^+. *J. Phys. B*, 44(6):065601, 2011. URL: https://iopscience.iop.org/article/10.1088/0953-4075/44/6/065601, doi:10.1088/0953-4075/44/6/065601.

[27] Y. V. Vanne and A. Saenz. Ionisation of H_2 in intense ultrashort laser pulses: parallel versus perpendicular orientation. *J. Mod. Opt.*, 55(16):2665–2684, 2008. URL: http://www.tandfonline.com/doi/abs/10.1080/09500340802148979, doi:10.1080/09500340802148979.

[28] J. L. Sanz-Vicario, J. F. Pérez-Torres, F. Morales, E. Plésiat, and F. Martín. Molecular frame photoelectron angular distributions for H_2 ionization by single and trains of attosecond XUV laser pulses. *Int. J. Quantum Chem.*, 110(13):2462–2471, 2010. URL: https://onlinelibrary.wiley.com/doi/10.1002/qua.22586, doi:10.1002/qua.22586.

[29] C. M. Granados-Castro and J. L. Sanz-Vicario. Time-resolved resonant photoionization of He using a time-dependent Feshbach method with ultrashort laser pulses. *J. Phys. B*, 46(5):055601, February 2013. URL: https://iopscience.iop.org/article/10.1088/0953-4075/46/5/055601, doi:10.1088/0953-4075/46/5/055601.

[30] J. M. Ngoko Djiokap, S. X. Hu, W.-C. Jiang, L.-Y. Peng, and A. F Starace. Enhanced asymmetry in few-cycle attosecond pulse ionization of He in the vicinity of autoionizing resonances. *New J. Phys.*, 14(9):095010, 2012. URL: https://iopscience.iop.org/article/10.1088/1367-2630/14/9/095010, doi:10.1088/1367-2630/14/9/095010.

[31] M. Vacher, M. J. Bearpark, and M. A. Robb. Direct methods for non-adiabatic dynamics: connecting the single-set variational multi-configuration Gaussian (vMCG) and Ehrenfest perspectives. *Theoretical Chemistry Accounts*, 135(8):187, Jul 2016. URL: https://link.springer.com/article/10.1007/s00214-016-1937-2, doi:10.1007/s00214-016-1937-2.

[32] C. Marante, L. Argenti, and F. Martín. Hybrid Gaussian–B-spline basis for the electronic continuum: Photoionization of atomic hydrogen. *Phys. Rev. A*, 90:012506, Jul 2014. URL: https://link.aps.org/doi/10.1103/PhysRevA.90.012506, doi:10.1103/PhysRevA.90.012506.

[33] M. Horbatsch, H. J. Ludde, and R. M. Dreizler. Time-dependent variational approach for two-particle systems: photoionization of He $(1s^2)$. *J. Phys. B*, 25(15):3315, aug 1992. URL: https://dx.doi.org/10.1088/0953-4075/25/15/013, doi:10.1088/0953-4075/25/15/013.

[34] X. Li, S. M. Smith, A. N. Markevitch, D. A. Romanov, R. J. Levis, and H. B. Schlegel. A time-dependent Hartree–Fock approach for studying the electronic optical response of molecules in intense fields. *Phys. Chem. Chem. Phys.*, 7:233–239, 2005. URL: http://dx.doi.org/10.1039/B415849K, doi:10.1039/B415849K.

[35] P. Krause, T. Klamroth, and P. Saalfrank. Time-dependent configuration-interaction calculations of laser pulse driven many-electron dynamics: Controlled dipole switching in lithium cyanide. *J. Chem. Phys.*, 123(7):074105, 2005. URL: https://pubs.aip.org/aip/jcp/article-abstract/122/12/124102/950720/The-multiconfiguration-time-dependent-Hartree-Fock?redirectedFrom=fulltext, doi:10.1063/1.1862243.

[36] N. Rohringer, A. Gordon, and R. Santra. Configuration-interaction-based time-dependent orbital approach for ab initio treatment of electronic dynamics in a strong optical laser field. *Phys. Rev. A*, 74(4):043420, 2006. URL: https://link.aps.org/doi/10.1103/PhysRevA.74.043420, doi:10.1103/PhysRevA.74.043420.

[37] H. B. Schlegel, S. M. Smith, and X. Li. Electronic optical response of molecules in intense fields: Comparison of TD-HF, TD-CIS, and TD-CIS(D) approaches. *J. Chem. Phys.*, 126(24):244110, 2007. URL: https://pubs.aip.org/aip/jcp/article-abstract/126/24/244110/295899/Electronic-optical-response-of-molecules-in?redirectedFrom=fulltext, doi:10.1063/1.2743982.

[38] J. A. Sonk and H. B. Schlegel. TD-CI simulation of the strong-field ionization of polyenes. *J. Phys. Chem. A*, 116(26):7161–7168, July 2012. URL: https://pubs.acs.org/doi/10.1021/jp302389a, doi:10.1021/jp302389a.

[39] T. T. Nguyen-Dang, M. Peters, S. M. Wang, E. Sinelnikov, and F. Dion. Nonvariational time-dependent multiconfiguration

self-consistent field equations for electronic dynamics in laser-driven molecules. *J. Chem. Phys.*, 127(17):174107, 2007. URL: https://pubs.aip.org/aip/jcp/article-abstract/127/17/174107/958719/Nonvariational-time-dependent-multiconfiguration?redirectedFrom=fulltext, doi:10.1063/1.2774979.

[40] J. Zanghellini, M. Kitzler, C. Fabian, T. Brabec, and A. Scrinzi. An MCTDHF approach to multi–electron dynamics in laser fields. *Laser Phys.*, 13:1064, 2003. URL: https://www.semanticscholar.org/paper/An-MCTDHF-approach-to-multielectron-dynamics-in-Zanghellini-Kitzler/5462a6d588a18a5e8f187dbebda81629053ddd9b.

[41] J. Zanghellini, M. Kitzler, T. Brabec, and A. Scrinzi. Testing the multi-configuration time-dependent Hartree–Fock method. *J. Phys. B: At. Mol. Opt. Phys.*, 37(4):763–773, jan 2004. URL: https://iopscience.iop.org/article/10.1088/0953-4075/37/4/004, doi:10.1088/0953-4075/37/4/004.

[42] T. Kato and H. Kono. Time-dependent multiconfiguration theory for electronic dynamics of molecules in an intense laser field. *Chemical Physics Letters*, 392(4):533–540, 2004. URL: https://www.sciencedirect.com/science/article/pii/S0009261404008243, doi:10.1016/j.cplett.2004.05.106.

[43] M. Nest, T. Klamroth, and P. Saalfrank. The multiconfiguration time-dependent Hartree–Fock method for quantum chemical calculations. *J. Chem. Phys.*, 122(12):124102, 2005. URL: https://pubs.aip.org/aip/jcp/article-abstract/122/12/124102/950720/The-multiconfiguration-time-dependent-Hartree-Fock?redirectedFrom=fulltext, doi:10.1063/1.1862243.

[44] Z. Zhang, G. Fabien, and D. H. Zhang. Full-dimensional quantum mechanical calculations of the reaction probability of the $H + CH_4$ reaction based on a mixed Jacobi and Radau description. *J. Chem. Phys.*, 152(20):201101, 05 2020. arXiv:https://pubs.aip.org/aip/jcp/article-pdf/doi/10.1063/5.0009721/14907991/201101_1_online.pdf, doi:10.1063/5.0009721.

[45] C. B. Madsen, F. Anis, L. B. Madsen, and B. D. Esry. Multiphoton above threshold effects in strong-field fragmentation. *Phys. Rev. Lett.*, 109:163003, Oct 2012. URL: https://link.aps.org/doi/10.1103/PhysRevLett.109.163003, doi:10.1103/PhysRevLett.109.163003.

[46] R. E. F. Silva, F. Catoire, P. Rivière, H. Bachau, and F. Martín. Correlated electron and nuclear dynamics in strong field photoionization of H_2^+. *Phys. Rev. Lett.*, 110:113001, Mar 2013. URL: https://link.aps.org/doi/10.1103/PhysRevLett.110.113001, doi:10.1103/PhysRevLett.110.113001.

[47] K. Liu, P. Lan, C. Huang, Q. Zhang, and P. Lu. Revealing correlated electronic and nuclear dynamics in molecules with energy-resolved population imaging. *Phys. Rev. A*, 89:053423, May 2014. URL: https://link.aps.org/doi/10.1103/PhysRevA.89.053423, doi:10.1103/PhysRevA.89.053423.

[48] L. Yue and L. B. Madsen. Inter- and intracycle interference effects in strong-field dissociative ionization. *Phys. Rev. A*, 93:031401, Mar 2016. URL: https://link.aps.org/doi/10.1103/PhysRevA.93.031401, doi:10.1103/PhysRevA.93.031401.

[49] J. Wu, M. Kunitski, M. Pitzer, F. Trinter, L. Ph. H. Schmidt, T. Jahnke, M. Magrakvelidze, C. B. Madsen, L. B. Madsen, U. Thumm, and R. Dörner. Electron-nuclear energy sharing in above-threshold multiphoton dissociative ionization of H_2. *Phys. Rev. Lett.*, 111:023002, Jul 2013. URL: https://link.aps.org/doi/10.1103/PhysRevLett.111.023002, doi:10.1103/PhysRevLett.111.023002.

[50] R. Dörner, V. Mergel, O. Jagutzki, L. Spielberger, J. Ullrich, R. Moshammer, and H. Schmidt-Böcking. Cold target recoil ion momentum spectroscopy: a 'momentum microscope' to view atomic collision dynamics. *Physics Reports*, 330(2):95–192, 2000. URL: https://www.sciencedirect.com/science/article/pii/S037015739900109X, doi:10.1016/S0370-1573(99)00109-X.

[51] P. Lu, J. Wang, H. Li, K. Lin, X. Gong, Q. Song, Q. Ji, W. Zhang, J. Ma, H. Li, H. Zeng, F. He, and J. Wu. High-order above-threshold dissociation of molecules. *Proc. Natl. Acad. Sci. USA*, 115(9):2049–2053, 2018. URL: http://www.pnas.org/lookup/doi/10.1073/pnas.1719481115, doi:10.1073/pnas.1719481115.

[52] W. Zhang, Z. Li, P. Lu, X. Gong, Q. Song, Q. Ji, K. Lin, J. Ma, F. He, H. Zeng, and J. Wu. Photon energy deposition in strong-field single ionization of multielectron molecules. *Phys. Rev. Lett.*, 117:103002, Sep 2016. URL: https://link.aps.org/doi/10.1103/PhysRevLett.117.103002, doi:10.1103/PhysRevLett.117.103002.

[53] X. Sun, M. Li, Y. Shao, M.-M. Liu, X. Xie, Y. Deng, C. Wu, Q. Gong, and Y. Liu. Vibrationally resolved electron-nuclear energy sharing in above-threshold multiphoton dissociation of CO. *Phys. Rev. A*, 94:013425, Jul 2016. URL: https://link.aps.org/doi/10.1103/PhysRevA.94.013425, doi:10.1103/PhysRevA.94.013425.

[54] S. Saugout, C. Cornaggia, A. Suzor-Weiner, and E. Charron. Ultrafast Electronuclear Dynamics of H_2 Double Ionization. *Phys. Rev. Lett.*, 98:253003, Jun 2007. URL: https://link.aps.org/doi/10.1103/PhysRevLett.98.253003, doi:10.1103/PhysRevLett.98.253003.

[55] L. D. Landau and E. M. Lifshitz. *Quantum Mechanics: Non-Relativistic Theory*, volume 3. Pergamon Press, 3 edition, 1977.

[56] A. M. Perelomov, V. S. Popov, and M. V. Terent'ev. Ionization of atoms in an alternating electric field. *J. Exptl. Theoret. Phys. (U.S.S.R.)*, 50:1393–1409, 1966.

[57] A. M. Perelomov, V. S. Popov, and M. V. Terent'ev. Ionization of atoms in an alternating electric field II. *J. Exptl. Theoret. Phys. (U.S.S.R.)*, 51:309–326, 1966.

[58] A. M. Perelomov and V. S. Popov. Ionization of atoms in an alternating electric field III. *J. Exptl. Theoret. Phys. (U.S.S.R.)*, 52:514–526, 1967.

[59] M. V. Ammosov, N. B. Delone, and V. P Krainov. Tunnel ionization of complex atoms and of atomic ions in an alternating electromagnetic field. *Sov. Phys. JETP*, 64(6):1191, 1986.

[60] I. I. Fabrikant and G. A. Gallup. Semiclassical propagation method for tunneling ionization. *Phys. Rev. A*, 79:013406, Jan 2009. URL: https://link.aps.org/doi/10.1103/PhysRevA.79.013406, doi:10.1103/PhysRevA.79.013406.

[61] C. Cornaggia and Ph. Hering. Nonsequential double ionization of small molecules induced by a femtosecond laser field. *Phys. Rev. A*, 62:023403, Jul 2000. URL: https://link.aps.org/doi/10.1103/PhysRevA.62.023403, doi:10.1103/PhysRevA.62.023403.

[62] X. M. Tong, Z. X. Zhao, and C. D. Lin. Theory of molecular tunneling ionization. *Phys. Rev. A*, 66:033402, Sep 2002. URL: https://link.aps.org/doi/10.1103/PhysRevA.66.033402, doi:10.1103/PhysRevA.66.033402.

[63] E. P. Benis, J. F. Xia, X. M. Tong, M. Faheem, M. Zamkov, B. Shan, P. Richard, and Z. Chang. Ionization suppression of Cl_2 molecules in intense laser fields. *Phys. Rev. A*, 70:025401, Aug 2004. URL: https://link.aps.org/doi/10.1103/PhysRevA.70.025401, doi:10.1103/PhysRevA.70.025401.

[64] A.-T. Le, R. R. Lucchese, S. Tonzani, T. Morishita, and C. D. Lin. Quantitative rescattering theory for high-order harmonic generation from molecules. *Phys. Rev. A*, 80:013401, Jul 2009. URL: https://link.aps.org/doi/10.1103/PhysRevA.80.013401, doi:10.1103/PhysRevA.80.013401.

[65] A.-T. Le, H. Wei, C. Jin, and C. D. Lin. Strong-field approximation and its extension for high-order harmonic generation with mid-infrared lasers. *J. Phys. B*, 49(5):053001, Feb 2016. URL: https://iopscience.iop.org/article/10.1088/0953-4075/49/5/053001, doi:10.1088/0953-4075/49/5/053001.

[66] C. D. Lin, A.-T. Le, C. Jin, and H. Wei. Elements of the quantitative rescattering theory. *J. Phys. B*, 51(10):104001, Apr 2018. URL: https://iopscience.iop.org/article/10.1088/1361-6455/aabaa2, doi:10.1088/1361-6455/aabaa2.

[67] L. V. Keldysh. Ionization in the field of a strong electromagnetic wave. *Sov. Phys. JETP*, 20(5):1307–1314, 1965.

[68] C. Z. Bisgaard and L. B. Madsen. Tunneling ionization of atoms. *American Journal of Physics*, 72(2):249–254, Feb 2004. URL: https://pubs.aip.org/aapt/ajp/article-abstract/72/2/249/1039885, doi:10.1119/1.1603274.

[69] P. Agostini, F. Fabre, G. Mainfray, G. Petite, and N. K. Rahman. Free-free transitions following six-photon ionization of xenon atoms. *Phys. Rev. Lett.*, 42(17):1127–1130, 1979. URL: https://link.aps.org/doi/10.1103/PhysRevLett.42.1127, doi:10.1103/PhysRevLett.42.1127.

[70] P. B. Corkum, N. H. Burnett, and F. Brunel. Above-threshold ionization in the long-wavelength limit. *Phys. Rev. Lett.*, 62(11):1259, 1989. URL: https://link.aps.org/doi/10.1103/PhysRevLett.62.1259, doi:10.1103/PhysRevLett.62.1259.

[71] J. H. Eberly, J. Javanainen, and K. Rzazewski. Above-threshold ionization. *Phys. Rep.*, 204(5):331–383, 1991. URL: https://iopscience.iop.org/article/10.1088/0143-0807/9/4/004, doi:10.1088/0143-0807/9/4/004.

[72] S. V. Popruzhenko. Keldysh theory of strong field ionization: history, applications, difficulties and perspectives. *J. Phys. B*, 47(20):204001, 2014. URL: https://iopscience.iop.org/article/10.1088/0953-4075/47/20/204001/pdf, doi:10.1088/0953-4075/47/20/204001.

[73] A.-T. Le, R. R. Lucchese, and C. D. Lin. Quantitative rescattering theory of high-order harmonic generation for polyatomic molecules. *Phys. Rev. A*, 87(6):063406, June 2013. URL: https://link.aps.org/doi/10.1103/PhysRevA.87.063406, doi:10.1103/PhysRevA.87.063406.

[74] P. M. Paul, E. S. Toma, P. Breger, G. Mullot, F. Augé, Ph. Balcou, H. G. Muller, and P. Agostini. Observation of a train of attosecond pulses from high harmonic generation. *Science*, 292(5522):1689–1692, 2001. URL: https://www.science.org/doi/abs/10.1126/science.1059413, doi:10.1126/science.1059413.

[75] J. Itatani, J. Levesque, D. Zeidler, H. Niikura, H. Pépin, J. C. Kieffer, P. B. Corkum, and D. M. Villeneuve. Tomographic imaging of molecular orbitals. *Nature*, 432(7019):867–871, December 2004. URL: https://www.nature.com/articles/nature03183, doi:10.1038/nature03183.

[76] T. T. Nguyen-Dang, M. Peters, J. Viau-Trudel, E. Couture-Bienvenue, R. Puthumpally-Joseph, E. Charron, and O. Atabek. Laser-induced electron diffraction: alignment defects and symmetry breaking. *Mol. Phys.*, 115(15):1934–1943, 2017. URL: https://www.tandfonline.com/doi/full/10.1080/00268976.2017.1317858, doi:10.1080/00268976.2017.1317858.

[77] C. I. Blaga, J. Xu, A. D. DiChiara, E. Sistrunk, K. Zhang, P. Agostini, T. A. Miller, L. F. DiMauro, and C. D. Lin. Imaging ultrafast molecular dynamics with laser-induced electron diffraction. *Nature*, 483(7388):194–197, March 2012. URL: https://www.nature.com/articles/nature10820, doi:10.1038/nature10820.

[78] M. Peters, T. T. Nguyen-Dang, E. Charron, A. Keller, and O. Atabek. Laser-induced electron diffraction: A tool for molecular orbital imaging. *Phys. Rev. A*, 85(5):053417, 2012. URL: https://link.aps.org/doi/10.1103/PhysRevA.85.053417, doi:10.1103/PhysRevA.85.053417.

[79] T. Zuo, A.D. Bandrauk, and P.B. Corkum. Laser-induced electron diffraction: a new tool for probing ultrafast molecular dynamics. *Chem. Phys. Lett.*, 259(3):313–320, 1996. URL: https:

//linkinghub.elsevier.com/retrieve/pii/0009261496007865, doi:10.1016/0009-2614(96)00786-5.

[80] K. Amini, J. Biegert, F. Calegari, A. Chacón, M. F. Ciappina, A. Dauphin, D. K. Efimov, C. F. Morisson, K. Giergiel, P. Gniewek, A. S. Landsman, M. Lesiuk, M. Mandrysz, A. S. Maxwell, R. Moszyński, L. Ortmann, J. A. Pérez-Hernández, A. Picón, E. Pisanty, J. Prauzner-Bechcicki, K. Sacha, N. Suárez, A. Zaïr, J. Zakrzewski, and M. Lewenstein. Symphony on strong field approximation. *Rep. Prog. Phys.*, 82(3), 2019. URL: https://iopscience.iop.org/article/10.1088/1361-6633/ab2bb1, doi:10.1088/1361-6633/ab2bb1.

[81] F. H. M. Faisal. Multiple absorption of laser photons by atoms. *J. Phys. B*, 6(4):L89, apr 1973. URL: https://dx.doi.org/10.1088/0022-3700/6/4/011, doi:10.1088/0022-3700/6/4/011.

[82] H. R. Reiss. Effect of an intense electromagnetic field on a weakly bound system. *Phys. Rev. A*, 22:1786–1813, 1980. URL: https://link.aps.org/doi/10.1103/PhysRevA.22.1786, doi:10.1103/PhysRevA.22.1786.

[83] N. M. Kroll and K. M. Watson. Charged-particle scattering in the presence of a strong electromagnetic wave. *Phys. Rev. A*, 8:804–809, Aug 1973. URL: https://link.aps.org/doi/10.1103/PhysRevA.8.804, doi:10.1103/PhysRevA.8.804.

[84] N. M. Kroll and K. M. Watson. Inelastic atom-atom scattering within an intense laser beam. *Phys. Rev. A*, 13:1018–1033, Mar 1976. URL: https://link.aps.org/doi/10.1103/PhysRevA.13.1018, doi:10.1103/PhysRevA.13.1018.

[85] P. B. Corkum. Plasma perspective on strong field multiphoton ionization. *Phys. Rev. Lett.*, 71(13):1994–1997, 2013. URL: https://link.aps.org/doi/10.1103/PhysRevLett.71.1994, doi:10.1103/PhysRevLett.71.1994.

[86] M. Lewenstein, P. Balcou, M. Y. Ivanov, A. L'Huillier, and P. B. Corkum. Theory of high-harmonic generation by low-frequency laser fields. *Phys. Rev. A*, 49(3):2117–2132, 1994. URL: http://link.aps.org/doi/10.1103/PhysRevA.49.2117, doi:10.1103/PhysRevA.49.2117.

[87] O. Smirnova, M. Spanner, and M. Ivanov. Analytical solutions for strong field-driven atomic and molecular one- and two-electron continua and applications to strong-field problems. *Phys. Rev. A*, 77(3):033407, March

2008. URL: https://link.aps.org/doi/10.1103/PhysRevA.77.033407, doi:10.1103/PhysRevA.77.033407.

[88] S. Hennani. *Simulation numérique des processus d'excitation et d'ionisation des systèmes moléculaires à plusieurs électrons en champ laser intense*. PhD thesis, Université Laval, Québec, Canada, 2023.

[89] D. W. Wolkow. Über eine klasse von lösungen der diracschen gleichung. *Zeitschrift für Physik*, 94(3):250–260, Mar 1935. URL: https://link.springer.com/article/10.1007/BF01331022, doi:10.1007/BF01331022.

[90] T. T. Nguyen-Dang and J. Viau-Trudel. Multicomponent dynamics of coupled quantum subspaces and field-induced molecular ionizations. *J. Chem. Phys.*, 139(24):244102, 2013. URL: http://aip.scitation.org/doi/10.1063/1.4849755, doi:10.1063/1.4849755.

[91] T. T. Nguyen-Dang, É. Couture-Bienvenue, J. Viau-Trudel, and A. Sainjon. Time-dependent quantum chemistry of laser driven many-electron molecules. *J. Chem. Phys.*, 141(24):244116, 2014. URL: http://aip.scitation.org/doi/10.1063/1.4904102, doi:10.1063/1.4904102.

[92] M. Awasthi, Y. V. Vanne, A. Saenz, A. Castro, and P. Decleva. Single-active-electron approximation for describing molecules in ultrashort laser pulses and its application to molecular hydrogen. *Phys. Rev. A*, 77:063403, Jun 2008. URL: https://link.aps.org/doi/10.1103/PhysRevA.77.063403, doi:10.1103/PhysRevA.77.063403.

[93] Z. Zhao and T. Brabec. Tunnel ionization in complex systems. *J. Modern Optics*, 54:981, May 2007. URL: https://www.tandfonline.com/doi/abs/10.1080/09500340601043413, doi:10.1080/09500340601043413.

[94] B. Zhang, Y. Yuan, and Z. Zhao. Dynamic core polarization in strong-field ionization of CO molecules. *Phys. Rev. Lett.*, 111:163001, October 2013. URL: https://journals.aps.org/prl/abstract/10.1103/PhysRevLett.111.163001, doi:10.1103/PhysRevLett.111.163001.

[95] V.-H. Hoang, S. B. Zhao, V.-H. Le, and A.-T. Le. Influence of permanent dipole and dynamic core-electron polarization on tunneling ionization of polar molecules. *Phys. Rev. A*, 95:023407, 2017. URL: https://link.aps.org/doi/10.1103/PhysRevA.95.023407, doi:10.1103/PhysRevA.95.023407.

[96] S.-L. Hu, Z.-X. Zhao, and T.-Y. Shi. Alignment-dependent ionization of CO_2 in the intense laser fields: Single-Active-Electron approach. *Chin. Phys. Lett.*, 30(10):103103, oct 2013. URL: https://iopscience.iop.org/article/10.1088/0256-307X/30/10/103103, doi:10.1088/0256-307x/30/10/103103.

[97] A. Schild and E. K. U. Gross. Exact single-electron approach to the dynamics of molecules in strong laser fields. *Phys. Rev. Lett.*, 118:163202, Apr 2017. URL: https://link.aps.org/doi/10.1103/PhysRevLett.118.163202, doi:10.1103/PhysRevLett.118.163202.

[98] M. Born and R. Oppenheimer. Zur Quantentheorie der Molekeln. *Annalen der Physik*, 389(20):457–484, 1927. URL: https://onlinelibrary.wiley.com/doi/10.1002/andp.19273892002, doi:10.1002/andp.19273892002.

[99] A. D. Bandrauk, J. Levesque, and S. Chelkowski. *Laser-Phase Control of Dissociative Ionization of Molecules: Exact Non-Born-Oppenheimer Simulations for H2+*, volume 821 of *ACS Symposium Series*, pages 221–235. American Chemical Society, Jun 2002. URL: https://pubs.acs.org/doi/abs/10.1021/bk-2002-0821.ch015, doi:10.1021/bk-2002-0821.ch015.

[100] Z.-C. Li and F. He. Ab initio non-Born-Oppenheimer simulations of rescattering dissociation of H_2 in strong infrared laser fields. *Phys. Rev. A*, 90:053423, Nov 2014. URL: https://link.aps.org/doi/10.1103/PhysRevA.90.053423, doi:10.1103/PhysRevA.90.053423.

[101] S. Saugout, E. Charron, and C. Cornaggia. H_2 double ionization with few-cycle laser pulses. *Phys. Rev. A*, 77:023404, Feb 2008. URL: https://link.aps.org/doi/10.1103/PhysRevA.77.023404, doi:10.1103/PhysRevA.77.023404.

[102] P. Ranitovic, C. W. Hogle, P. Rivière, A. Palacios, X. Tong, N. Toshima, A. Gonzalez-Castrillo, L. S. Martin, F. Martin, M. M. Murnane, and H. C. Kapteyn. Attosecond vacuum uv coherent control of molecular dynamics. *Proceedings of the National Academy of Sciences*, 111:912–917, 2014. URL: https://www.pnas.org/doi/full/10.1073/pnas.1321999111, doi:10.1073/pnas.1321999111.

[103] T. Yonehara and K. Takatsuka. Non-Born-Oppenheimer quantum chemistry on the fly with continuous path branching due to nonadiabatic and intense optical interactions. *J. Chem. Phys.*, 132(24):244102, June 2010. URL: https://pubs.aip.org/aip/jcp/article-abstract/132/24/244102/

189085/Non-Born-Oppenheimer-quantum-chemistry-on-the-fly?redirectedFrom=fulltext, doi:10.1063/1.3439396.

[104] J.-N. Vigneau, O. Atabek, T.-T. Nguyen-Dang, and E. Charron. Strong field non-Franck–Condon ionization of H_2: a semi-classical analysis. *The European Physical Journal Special Topics*, 232(13):2081–2093, 2023. URL: https://link.springer.com/article/10.1140/epjs/s11734-022-00750-z, doi:10.1140/epjs/s11734-022-00750-z.

[105] J.-N. Vigneau, T.-T. Nguyen-Dang, and E. Charron. Electro-nuclear dynamics of single and double ionization of H_2 in ultrafast intense laser pulses. *The Journal of Physical Chemistry A*, 128(7):1375–1384, 2024. PMID: 38348852. URL: https://pubs.acs.org/doi/10.1021/acs.jpca.3c06525, doi:10.1021/acs.jpca.3c06525.

Annex: Atomic Units

All of the equations in this document are presented in atomic units, accordingly to Table 1.1, reproduced from the NIST website.

Quantity	Symbol	Value (SI Units)
Charge	e	$1.602\,176\,634 \times 10^{-19}$ **C**
Mass	m_e	$9.109\,383\,7015(28) \times 10^{-31}$ **kg**
Action	$\hbar$	$1.054\,571\,817... \times 10^{-34}$ **J.s**
Length (bohr)	a_0	$5.291\,772\,109\,03(80) \times 10^{-11}$ **m**
Energy (hartree)	E_h	$4.359\,744\,722\,2071(85) \times 10^{-18}$ **J**
Time	$\hbar/E_h$	$2.418\,884\,326\,5857(47) \times 10^{-17}$ **s**
Force	E_h/a_0	$8.238\,723\,4983(12) \times 10^{-8}$ **N**
Velocity	$a_0E_h/\hbar$	$2.187\,691\,263\,64(33) \times 10^{6}$ $\mathbf{m.s^{-1}}$
Momentum	$\hbar/a_0$	$1.992\,851\,914\,10(30) \times 10^{-24}$ $\mathbf{kg.m.s^{-1}}$
Current	$eE_h/\hbar$	$6.623\,618\,237\,510(13) \times 10^{-3}$ **A**
Charge density	e/a_0^3	$1.081\,202\,384\,57(49) \times 10^{12}$ $\mathbf{C.m^{-3}}$
Electric potential	E_h/e	$27.211\,386\,245\,988(53)$ **V**
Electric field	E_h/ea_0	$5.142\,206\,747\,63(78) \times 10^{11}$ $\mathbf{V.m^{-1}}$
Electric field gradient	E_h/ea_0^2	$9.717\,362\,4292(29) \times 10^{21}$ $\mathbf{V.m^{-2}}$
Electric dipole moment	ea_0	$8.478\,353\,6255(13) \times 10^{-30}$ **C.m**
Electric quadrupole moment	ea_0^2	$4.486\,551\,5246(14) \times 10^{-40}$ $\mathbf{C.m^2}$
Electric polarizability	$e^2a_0^2/E_h$	$1.648\,777\,274\,36(50) \times 10^{-41}$ $\mathbf{C^2.m^2.J^{-1}}$
1^{st} hyperpolarizability	$e^3a_0^3/E_h^2$	$3.206\,361\,3061(15) \times 10^{-53}$ $\mathbf{C^3.m^3.J^{-2}}$
2^{nd} hyperpolarizability	$e^4a_0^4/E_h^3$	$6.235\,379\,9905(38) \times 10^{-65}$ $\mathbf{C^4.m^4.J^{-3}}$
Magnetic flux density	$\hbar/ea_0^2$	$2.350\,517\,567\,58(71) \times 10^{5}$ **T**
Magnetic dipole moment	$\hbar e/m_e$	$1.854\,802\,015\,66(56) \times 10^{-23}$ $\mathbf{J.T^{-1}}$
Magnetizability	$e^2a_0^2/m_e$	$7.891\,036\,6008(48) \times 10^{-29}$ $\mathbf{J.T^{-2}}$
Permittivity	e^2/a_0E_h	$1.112\,650\,055\,45(17) \times 10^{-10}$ $\mathbf{F.m^{-1}}$

Table 1.1: Fundamental physical constants in atomic units (a.u.), reproduced from the National Institute of Standards and Technology (NIST) - Physical Measurement Laboratory (URL: https://physics.nist.gov/cgi-bin/cuu/Category?view=gif&Non-SI+units.x=101&Non-SI+units.y=14, accessed February 20^{th}, 2024.)

Chapter 2 Multi-Electron Dynamics and Strong Field Ionization

Contents

2.1 . Introduction

In this chapter, the part- Time-Dependent Multiconfiguration Self-Consistent Field (TD-MCSCF) and part- Time-Dependent Configuration Interaction (TDCI) algorithm that is used to resolve the Time-Dependent Schrödinger Equation under the Born-Oppenheimer and Strong Field approximations in fully-correlated, multi-electronic single ionization dynamics is presented. It constitutes MEDYS' algorithm that was applied in our research on the quantitative limitations of the Single Active Electron approximation usage in the ionization of H_2, the subject of next chapter's inserted article "Strong-Field Molecular Ionization Beyond the Single Active Electron Approximation." This chapter first explains the theory around resolving the TDSE with a multi-configuration method (Sec. 2.2), then its formulation within MEDYS' algorithm (Sec. 2.3), the basis that constitutes the neutral molecule and its ionic states (Sec. 2.4), and finally, the parameters of the field and resulting observables (Sec. 2.5).

2.2 . Theory

2.2.1 . The Time-Dependent Schrödinger Equation (TDSE)

Take any molecule (such as H_2) consisting of $N_n(=2)$ nuclei (n), and $N\ (=2)$ electrons (e), submitted to a strong electromagnetic field. It is described by a Hamiltonian ($\hat{H}$) of the form

$$\hat{H} = \hat{T}_n + \hat{T}_e + \hat{U}_{nn} + \hat{U}_{ee} + \hat{U}_{ne} + \hat{V}_{int}^{mol}(t), \tag{2.1}$$

comprising kinetic energy operators ($\hat{T}$) for all moving particles, intrinsic potential energies ($\hat{U}$) describing the mutual interactions of the particles, as well as an interaction energy with the external field ($\hat{V}$). In detail, each term of $\hat{H}$ is expressed, using atomic units, as

$$\hat{T}_n = -\sum_{\alpha=1}^{N_n} \frac{1}{2M_\alpha} \nabla^2_{\vec{R}_\alpha} \tag{2.2a}$$

$$\hat{T}_e = -\sum_{i=1}^{N} \frac{1}{2} \nabla^2_{\vec{r}_i} \tag{2.2b}$$

$$\hat{U}_{nn} = \frac{1}{2} \sum_{\alpha=1}^{N_n} \sum_{\beta(\neq\alpha)=1}^{N_n} \frac{Z_\alpha Z_\beta}{\left|\vec{R}_\alpha - \vec{R}_\beta\right|} \tag{2.2c}$$

$$\hat{U}_{ee} = \frac{1}{2}\sum_{i=1}^{N}\sum_{j(\neq i)=1}^{N}\frac{1}{|\vec{r}_i - \vec{r}_j|} \tag{2.2d}$$

$$\hat{U}_{ne} = -\sum_{\alpha=1}^{N_n}\sum_{i=1}^{N}\frac{Z_\alpha}{\left|\vec{R}_\alpha - \vec{r}_i\right|} \tag{2.2e}$$

$$\hat{V}_{int}^{mol}(t) = \left(\sum_{\alpha=1}^{N_n} Z_\alpha \vec{R}_\alpha - \sum_{i=1}^{N}\vec{r}_i\right)\cdot\vec{E}(t), \tag{2.2f}$$

where M_α is the mass of nucleus α, $\vec{R}_\alpha$ its position vector, $\vec{r}_i$ that of electron i, and Z_α the atomic number of nucleus α.

The Born-Oppenheimer Approximation

This exact operator takes into account the movement of all particles and the interactions between them, but as nuclei have masses at least 3 orders of magnitude greater than electrons, the electronic dynamics will take place at a significantly faster pace given a similar force. One could then assume the Born-Oppenheimer approximation to be adequate for such a system, considering nuclei as static ($\hat{T}_n = \hat{0}$) and their mutual interaction $\hat{U}_{nn}$ constant, and proceed with a purely electronic Hamiltonian

$$\hat{H}_{el} = \hat{T}_{el} + \hat{U}_{ne} + \hat{U}_{ee} + \hat{U}_{nn} + \hat{V}_{int}^{mol}(t). \tag{2.3}$$

For the particular case of molecular hydrogen, consisting of two protons stabilized by an electronic cloud of two electrons, the electronic Hamiltonian can be read as the sum of two terms: the one- ($\hat{H}_1$) and two-electrons ($\hat{H}_2$) operators, as well as the remaining nuclear function (C),

$$\hat{H}_{el} = \hat{H}_1(t) + \hat{H}_2 + C(t). \tag{2.4a}$$

The monoelectronic operator $H_1(t)$ is of a separable form given in Eq. (2.4b), of the sum of single electron Hamiltonians ($\hat{h}$) each of which includes the kinetic energy operator, and the interactions with nuclei and with the external field,

$$\hat{H}_1 = \sum_{i=1}^{N}\hat{h}(\vec{r}_i, t), \tag{2.4b}$$

where

$$\hat{h}(\vec{r}_i, t) = -\frac{1}{2}\nabla_{\vec{r}_i}^2 - \sum_{\alpha=1}^{N_n}\frac{Z_\alpha}{\left|\vec{R}_\alpha - \vec{r}_i\right|} - \vec{r}_i\cdot\vec{E}(t). \tag{2.4c}$$

The bielectronic operator stands entirely for the electron-electron interactions,

$$\hat{H}_2 = \hat{U}_{ee}, \tag{2.4d}$$

while the constant mutual interactions ($\hat{U}_{nn}$) between the nuclei and their interaction with the field is

$$C(t) = \hat{U}_{nn} + \sum_{\alpha=1}^{N_n} Z_\alpha \vec{R}_\alpha \cdot \vec{E}(t). \tag{2.4e}$$

Molecular Orbitals and Hartree-Fock Wave Function

We now introduce the molecular orbitals (MO) $|\phi_{ri}(i)\rangle$ (spin orbitals $|\eta_{ri}(i)\rangle = |\phi_{ri}(i), m_{s_i}\rangle$ if the electron spin is included), where ri and i are the subscripts associated with the corresponding MO and electron, respectively. These are one-electron wave functions, which can describe an actual physical state of a single electron (in the N electron system), or just a basis vector of the Hilbert space of that electron.

Orbitals refer to an independent-electron model. Thus, without $\hat{U}_{ee}$, the electronic Hamiltonian $\hat{H}_{el}$ of Eq. (2.4a) would reduce to $\hat{H}_1$, which is separable, and the N electron state would be a simple tensor product (Hartree product) of spin orbitals

$$|\Psi, t\rangle = |\eta_{r1}(1), t\rangle \otimes |\eta_{r2}(2), t\rangle \otimes \cdots \otimes |\eta_{rN}(N), t\rangle \tag{2.5a}$$

with the orbitals $|\phi_{ri}(i), t\rangle$ evolving from some one-electron initial state $|\phi^0_{ri}(i)\rangle$ under the one-electron Hamiltonian $\hat{h}(\vec{r}_i, t)$ of Eq. (2.4c) according to

$$i\frac{\partial}{\partial t}|\phi_{ri}(i), t\rangle = \hat{h}(\vec{r}_i, t)\,|\phi_{ri}(i), t\rangle\,, \quad |\phi_{ri}(i), 0\rangle = \left|\phi^0_{ri}(i)\right\rangle. \tag{2.5b}$$

This is without taking into account the Pauli principle, which requires that the N electron state (wave function) be antisymmetric with respect to permutations $\hat{P}_{ij}$ of any electron pair (i, j). Under this condition, one would rather write

$$|\Psi, t\rangle = \hat{A}\Big[\,|\eta_{r1}(1), t\rangle \otimes |\eta_{r2}(2), t\rangle \otimes \cdots \otimes |\eta_{rN}(N), t\rangle\,\Big] := |D^{\{m_{s_i}\}}_{\{ri\}}, t\rangle \tag{2.6a}$$

where $\hat{A}$ is the antisymmetrizer, and $|D_{\{ri\}}^{\{m_{s_i}\}}, t\rangle$ is the Slater determinant

$$|D_{\{ri\}}^{\{m_{s_i}\}}, t\rangle = \frac{1}{\sqrt{N!}} \begin{vmatrix} \phi_{r1}(\vec{r}_1,t)\omega_{m_{s_1}}(1) & \phi_{r2}(\vec{r}_1,t)\omega_{m_{s_2}}(1) & .. & \phi_{rN}(\vec{r}_1,t)\omega_{m_{s_N}}(1) \\ \phi_{r1}(\vec{r}_2,t)\omega_{m_{s_1}}(2) & \phi_{r2}(\vec{r}_2,t)\omega_{m_{s_2}}(2) & .. & \phi_{rN}(\vec{r}_2,t)\omega_{m_{s_N}}(2) \\ .. & .. & .. & .. \\ .. & .. & .. & .. \\ \phi_{r1}(\vec{r}_N,t)\omega_{m_{s_1}}(N) & \phi_{r2}(\vec{r}_N,t)\omega_{m_{s_2}}(N) & .. & \phi_{rN}(\vec{r}_N,t)\omega_{m_{s_N}}(N) \end{vmatrix}$$

$$:= \left| \phi_{r1}\omega_{m_{s_1}} \; \phi_{r2}\omega_{m_{s_2}} \; ... \; \phi_{rN}\omega_{m_{s_N}} \right| \tag{2.6b}$$

where $\omega_{m_{s_i}}(j)$ denotes the spin wave function of spin projection m_{s_i} for electron j. In this expression, $\{ri\}$ and $\{m_{s_i}\}$ represent the set of all possible values of ri and m_{s_i}, respectively.

Time-Dependent and Time-Independent Orbitals

In the above, the molecular orbitals $\phi_{ri}(\vec{r},t)$ are time-dependent, being governed by the one-electron TDSE (2.5b), and evolve from initial time-independent orbitals $\phi_{ri}^0(\vec{r})$.

These can be thought of as, and are often taken to be eigenstates of a field-free one-electron Hamiltonian $\hat{h}(\vec{r})$ according to

$$\hat{h}(\vec{r})\,\psi_k(\vec{r}) = \epsilon_k\,\psi_k(\vec{r})\,. \tag{2.7a}$$

This could be the Hamiltonian of Eq. (2.4c) taken at a time when $\vec{E}(t) = 0$, in which case it is called core Hamiltonian (core-H), and denoted $\hat{h}_{core}$ in quantum chemistry. Else, it could be the Fock operator of the Hartree-Fock theory (HF) [1–3], or the Kohn-Sham Hamiltonian in the Kohn-Sham implementation of Density-Functional Theory (KS-DFT) [4]. The Hamiltonian $\hat{h}(\vec{r})$ therefore reads

$$\hat{h}(\vec{r}) = -\frac{\nabla_r^2}{2} + \hat{U}_{ne}(\vec{r}) + \hat{v}_{eff}(\vec{r}) \tag{2.7b}$$

with

$$v_{eff}(\vec{r}) = \begin{cases} \sum_k \left[\hat{J}_k(\vec{r}) - \hat{K}_k(\vec{r})\right] & \text{(HF)} \\ \sum_k \left[\hat{J}_k(\vec{r})\right] + v_{xc}(\vec{r}) & \text{(KS-DFT)} \\ 0 & \text{(core-H)} \end{cases} \tag{2.7c}$$

In these expressions, $\hat{J}_k(\vec{r})$ and $\hat{K}_k(\vec{r})$ denote operators involved in the definition of an effective electron-electron interaction described as a mean field in the

HF method, and are called Coulomb and exchange integrals, respectively. These operators are defined as follows

$$\hat{J}_k(\vec{r}) := \int d^3r' \left[\frac{|\psi_k(\vec{r}')|^2}{|\vec{r} - \vec{r}'|} \right] \tag{2.7d}$$

and

$$\hat{K}_k(\vec{r})\, f(\vec{r}) := \int d^3r' \left[\frac{\psi_k^*(\vec{r}') f(\vec{r}')}{|\vec{r} - \vec{r}'|} \right] \psi_k(\vec{r})\,. \tag{2.7e}$$

Finally, the function $v_{xc}(\vec{r})$ is defined in the KS-DFT as the exchange-correlation potential, which is formally the functional derivative, with respect to the electron density ρ of an unknown functional of ρ called the exchange-correlation energy functional

$$v_{xc}(\vec{r}) := \frac{\delta E_{xc}[\rho]}{\delta \rho(\vec{r})}\,. \tag{2.7f}$$

The time-independent orbitals ψ_k may play the role of initial orbitals from which evolve the time-dependent orbitals $\phi_{ri}(\vec{r}, t)$, or can be considered as constituting a time-independent basis for the expansion of $\phi_{ri}(\vec{r}, t)$, and later for the construction of a time-independent configuration state functions (CSFs; explained in section 2.2.2) basis used in the TDCI expansion of the N-electron wave function.

2.2.2 . Post Hartree-Fock Methods: Multi-Configuration Ansatz

The Hartree-Fock method is an *ab initio* scheme based on the representation, in both time-dependent and time-independent cases, of the system wave function by a single Slater determinant, yielding a mean-field estimation of the electron repulsion through the Coulomb and exchange integrals.

To get a more exact description of the many-electron structure and/or dynamics, multiconfiguration theories such as the Multi-Configuration Self-Consistent-Field (MCSCF) method and its time-dependent counterpart, the TD-MCSCF approach, introduce a development over configuration state functions (CSFs) [5]. A CSF is a linear combination of Slater determinants, constructed out of a well-defined set (usually of finite dimension) of orbitals, to yield fixed total spin quantum numbers S and M_S

$$|\Phi_I^{S,M_S}\rangle = \sum_{\substack{\{m_{s_i}\} \\ \text{such that} \\ \sum_i m_{s_i} = M_S}} c_{\{m_{s_i}\}}^{S,M_s}\, |D_{\{ri\}}^{\{m_{s_i}\}}\rangle \tag{2.8}$$

The Slater determinants included in the sum on the right hand side of Eq. (2.8) use the same set of molecular orbitals indicated by $\{ri\}$, each possibly repeated,

in the same manner in all the included determinants, up to two times, defining an electron configuration with definite occupation numbers n_{ri} with $n_{ri} = 0, 1$ or 2, of the orbitals ϕ_{ri} with $ri = 1, 2, .., \nu_T$, and various ways of distributing the spin states $|m_{s_i}\rangle$ among them such as to give $\sum_i m_{s_i} = M_S$. The coefficients $c^{S,M_s}_{\{m_{s_i}\}}$ are spin-coupling coefficients, generalizations of Clebsh-Gordan coefficients from 2 to N ½ spins, ensuring that the total N-electron spin length is $\sqrt{S(S+1)}$. Using the occupation numbers n_{ri}, one can also denote the CSF as

$$|\Phi_I^{S,M_S}\rangle = |n_1, n_2, n_3, ..., n_{\nu_T}\rangle_{S,M_S} . \tag{2.9}$$

The wave function describing the N-electron state is then generated and evolved over time by combining the CSFs and pondering them with configuration interaction (CI) coefficients $A_I(t)$,

$$|\Psi, t\rangle = \sum_{I=1}^{N_{CSF}} A_I(t) \left|\Phi_I^{S,M_S}\right\rangle . \tag{2.10}$$

The CSFs $|\Phi_I^{S,M_S}\rangle$ may make use of time-dependent or time-independent orbitals. In the first case, we have a TD-MCSCF method, and in the second case, a TDCI method. It is to be noted that, in the TD-MCSCF case, while the $\{\phi_{ri}\}$ MOs are propagated under the effect of the monoelectronic, direct interaction with the field part of the Hamiltonian given in Eqs. (2.4b-2.4c), the CI coefficients evolve under the bielectronic part given in Eq. (2.4d), indirectly influenced by the field from its impact on the MO basis. No orbitals evolution is involved in the TDCI case, and the CI coefficients evolve under the full N-electron time-dependent Hamiltonian. Finally, considering ν_T molecular orbitals, N electrons and a total spin of S in the model, N_{CSF} CSFs are necessary to fully represent the system in the TD-MCSCF approach, which can be calculated as [5]

$$N_{CSF}(\nu_T, N, S) = \frac{2S+1}{\nu_T+1} \begin{pmatrix} \nu_T+1 \\ \frac{1}{2}N - S \end{pmatrix} \begin{pmatrix} \nu_T+1 \\ \frac{1}{2}N + S + 1 \end{pmatrix} . \tag{2.11}$$

2.2.3 . Ionization Continuum in the Strong Field Approximation (SFA) and Feshbach Partitioning

The number of required CSFs to meet the completeness criterion of the bound basis is computationally bearable while representing the bound states and the excitation pathways of the electrons in an atom or a small molecule, but one can see from Eq. (2.11) that including the ionization continuum instantly becomes problematic, as ensuring a quasi-complete representation of the photoelectron dynamics would require an excessive amount of CSFs. Such a computational problem would considerably restrict the orbitals basis onto which are constructed the CSFs.

To alleviate this demanding part of the method, most dynamics within a strong laser field will apply conditions of the Strong Field Approximation (SFA) [6–8], which establishes that the interactions between an ionized electron and the Coulomb potential from its source cation is negligible compared to its interaction with the field. Such an approximation implies that the photoelectron dynamics can be treated in a different regime neglecting the Coulomb potential once the particle reaches a certain distance from the cation, with a Volkov propagator [9].

The MO basis $\{\phi_{ri}\}$ is thus separated in two subspaces of the monoelectronic Hilbert space, $\mathcal{H}^{(1)}$, using the Feshbach partitioning method [10–13]. The first subspace is composed of ν_b square-integrable MOs, noted φ_i, while the other subspace is composed of ν_c plane wave orbitals limiting the continuum to a discretized basis, noted $\{\chi_\kappa\}$, all initially orthogonalized with the active $\{\varphi_i\}$ basis of bound MOs. We have therefore

$$\{\phi_{ri}\} = \{\varphi_i\}_{i=1}^{\nu_b} \cup \{\chi_\kappa\}_{\kappa=1}^{\nu_c}\,, \tag{2.12}$$

with

$$\nu_b + \nu_c = \nu_T\,.$$

Partitioning the complete MO basis with the orthogonal projection operators

$$\hat{q} = \sum_{i=1}^{\nu_b} |\varphi_i\rangle\langle\varphi_i|, \tag{2.13a}$$

and

$$\hat{p} = \sum\!\!\!\!\!\!\int_{\kappa}^{\infty} |\chi_\kappa\rangle\langle\chi_\kappa| = \mathbb{1} - \hat{q} \tag{2.13b}$$

(where $\mathbb{1}$ is the identity operator) renders the CSFs describable by their occupation number n_{ri} of subspace MOs ϕ_{ri} as

$$\begin{aligned} |\Phi_I^{S,M_S}\rangle &= |\underbrace{n_1, n_2, n_3, ..., n_{\nu_b}}_{\underline{n}_B}, \underbrace{n_{\nu_b+1}, ..., n_{\nu_b+\kappa}, ..., n_{\nu_b+\nu_c}}_{\underline{n}'_C}\rangle \\ &= |\underline{n}_B; \underline{n}'_C\rangle\,. \end{aligned} \tag{2.14}$$

Here, $|\underline{n}_B; \underline{n}'_C\rangle$ thus represents a particular distribution of n and n' electrons in the bound and continuum orbitals, respectively. The projection operator of CSFs associated with the neutral molecule basis, containing N bound electrons in the bound subgroup and no electron in the continuum, is written as

$$\begin{aligned} \hat{Q} &= \sum_{\underline{N}_B} |\underline{N}_B; \underline{0}_C\rangle\langle\underline{N}_B; \underline{0}_C| \\ &= \sum_I |I\rangle\langle I|\,, \end{aligned} \tag{2.15}$$

where the sum runs over all possible distributions of N electrons in ν_b bound orbitals. The projection operator associated with a single ionization in the plane wave continuum, while $N' = (N-1)$ electrons remain bound in the MO basis, is

$$\begin{aligned}\hat{P} &= \mathbb{1} - \hat{Q} \\ &= \sum_{\underline{N}'_B} \sum\!\!\!\!\!\!\int_{\kappa} |\underline{N}'_B; ..., 1_\kappa, ...\rangle\langle \underline{N}'_B; ..., 1_\kappa, ...| \\ &= \sum_{I^+} \sum\!\!\!\!\!\!\int_{\kappa} |I^+, \kappa\rangle\langle I^+, \kappa| \,, \end{aligned} \tag{2.16}$$

where the double sum runs over all possible distributions of N' electrons in ν_b bound orbitals and 1 electron in ν_c free orbitals. From these assumptions, it is possible to generate the time-dependent wave packet representing the electronic dynamics in both bound $|I\rangle$ and ionic $|I^+, \kappa\rangle$ states

$$|\Psi, t\rangle = \underbrace{\sum_I C_I(t)\,|I\rangle}_{|\Psi_Q(t)\rangle} + \underbrace{\sum_{I^+} \sum\!\!\!\!\!\!\int_{\kappa} \gamma_{I^+,\kappa}(t)\,|I^+, \kappa\rangle}_{|\Psi_P(t)\rangle} \,, \tag{2.17}$$

where $C_I(t)$ and $\gamma_{I^+,\kappa}(t)$ are the time-dependent coefficients representing the proportions of CSFs $|I\rangle$ and $|I^+, \kappa\rangle$, respectively. In so far as these CSFs make use of the time-independent orbitals, Eq. (2.17) represents the TDCI wave function.

2.2.4 .Solution to the Time-Dependent Schrödinger Equation

As mentioned in the section 2.2.3, the SFA implies that the photoelectron wave packet will not propagate the same way in the continuum as will do the wave packet constructed from bound states, so both fractions of the neutral $|\Psi_Q\rangle = \hat{Q}|\Psi\rangle$ and ionic $|\Psi_P\rangle = \hat{P}|\Psi\rangle$ molecule can be propagated separately, according to

$$i\partial_t|\Psi_Q(t)\rangle = H_{QQ}(t)|\Psi_Q(t)\rangle + H_{QP}(t)|\Psi_P(t)\rangle \tag{2.18}$$

and

$$i\partial_t|\Psi_P(t)\rangle = H_{PP}(t)|\Psi_P(t)\rangle + H_{PQ}(t)|\Psi_Q(t)\rangle, \tag{2.19}$$

$H_{QQ} = \hat{Q}\hat{H}\hat{Q}$ and $H_{PP} = \hat{P}\hat{H}\hat{P}$ being propagating operators within the partition, and $H_{PQ} = \hat{P}\hat{H}\hat{Q} = H^\dagger_{QP}$ being an exchange operator inducing wave packet injection from one partition to the other.

Over a time frame $t \in [t_n, t_{n+1}]$ that is chosen small enough to enclose an adia-

batic dynamic, the wave packet evolution matrices read as

$$\begin{pmatrix} |\Psi_Q(t)\rangle \\ |\Psi_P(t)\rangle \end{pmatrix} = \begin{pmatrix} U_{QQ}(t,t_n) & 0 \\ 0 & U_{PP}(t,t_n) \end{pmatrix} \begin{pmatrix} 1 & -\frac{i}{2}\bar{H}_{QP}(t_n) \\ -\frac{i}{2}\bar{H}_{PQ}(t_n) & 1 \end{pmatrix} \times \begin{pmatrix} 1 & \frac{i}{2}\bar{H}_{QP}(t_n) \\ \frac{i}{2}\bar{H}_{PQ}(t_n) & 1 \end{pmatrix}^{-1} \begin{pmatrix} |\Psi_Q(t_n)\rangle \\ |\Psi_P(t_n)\rangle \end{pmatrix}, \tag{2.20}$$

where U_{QQ} and U_{PP} are the propagators associated to H_{QQ} and H_{PP} respectively, and where the two central matrices of the right-hand term that include a summed inter-space interaction term

$$\bar{H}_{PQ}(t_n) = \int_{t_n}^{t} H_{PQ}(t')dt',$$

constitute the Crank-Nicolson propagator [14] for the H_{QP} and H_{PQ} interaction Hamiltonians.

The algorithm associated to each subspace can also be described more explicitly as

$$|\Psi_Q(t)\rangle = \hat{U}_{QQ}(t,t_n)\left\{\hat{\mathcal{L}}_Q^-(t_n)\left[\hat{\mathcal{L}}_Q^+(t_n)\right]^{-1}|\Psi_Q(t_n)\rangle - i\left[\hat{\mathcal{L}}_Q^+(t_n)\right]^{-1}\bar{H}_{QP}(t_n)|\Psi_P(t_n)\rangle\right\} \tag{2.21a}$$

and

$$|\Psi_P(t)\rangle = \hat{U}_{PP}(t,t_n)\left\{\left(\mathbb{1}_P + \frac{1}{2}\bar{H}_{PQ}(t_n)\left[\hat{\mathcal{L}}_Q^+(t_n)\right]^{-1}\bar{H}_{QP}(t_n)\right)|\Psi_P(t_n)\rangle - i\bar{H}_{PQ}(t_n)\left[\hat{\mathcal{L}}_Q^+(t_n)\right]^{-1}|\Psi_Q(t_n)\rangle\right\} \tag{2.21b}$$

with the simplification

$$\hat{\mathcal{L}}_Q^{\pm}(t_n) = \left[\mathbb{1}_Q \pm \frac{1}{4}\bar{H}_{QP}(t_n)\bar{H}_{PQ}(t_n)\right]. \tag{2.22}$$

Since the time-dependency of the wave packet dynamics can be basically reduced to the proportion coefficients of each CSF varying over time (see Eq. 2.17), it is convenient to regroup them into vectors $\underline{C}(t)$ of the bound Q subspace and $\underline{\Gamma}(t)$ of the ionic P subspace, such as

$$\underline{C}(t) = \mathbb{U}_{QQ}(t,t_n)\left\{\mathbb{L}_n^-(\mathbb{L}_n^+)^{-1}\underline{C}(t_n) - i(\mathbb{L}_n^+)^{-1}\mathbb{H}_{QP}\underline{\Gamma}(t_n)\right\} \tag{2.23}$$

and

$$\underline{\Gamma}(t) = \mathbb{U}_{PP}(t,t_n)\left\{\underline{\Gamma}(t_n) - \mathbb{H}_{PQ}\left[\frac{1}{2}(\mathbb{L}_n^+)^{-1}\mathbb{H}_{QP}\underline{\Gamma}(t_n) + i(\mathbb{L}_n^+)^{-1}\underline{C}(t_n)\right]\right\}, \tag{2.24}$$

where

$$\mathbb{U}_{QQ}(t,t_n) \leftrightarrow U_{QQ}(t,t_n), \quad \mathbb{U}_{PP}(t,t_n) \leftrightarrow U_{PP}(t,t_n), \quad \mathbb{L}_n^{\pm} \leftrightarrow \hat{\mathcal{L}}_Q^{\pm}(t_n),$$
$$\mathbb{H}_{QP} \leftrightarrow \bar{H}_{QP}(t_n), \quad \mathbb{H}_{PQ} \leftrightarrow \bar{H}_{PQ}(t_n).$$

2.3 . Many Electrons Dynamics System (MEDYS) Program

The algorithm explained in details in section 2.2.4 is the one that is used in the program MEDYS, developed and improved during the last decades in the laboratory of Prof. Nguyen-Dang [12, 15–17].

2.3.1 . Second Quantization

In the second quantization formalism [18–20], the mono- and bielectronic parts of the electronic Hamiltonian can be written as

$$\hat{H}_1(t) = \sum_r \sum_s h_{rs}(t)\hat{E}_{rs} \tag{2.25a}$$

$$\hat{H}_2(t) = \frac{1}{2}\sum_r \sum_s \sum_u \sum_v g_{rsuv}\hat{e}_{rsuv}, \tag{2.25b}$$

where

$$h_{rs} = \langle \phi_r(\vec{r})|\hat{h}(\vec{r},t)|\phi_s(\vec{r})\rangle \tag{2.26}$$

is the matrix element of the $\hat{h}(\vec{r}_i,t)$ matrix from Eq. (2.4c) in the MO basis $\{\varphi_s\}_{s=1}^{\nu_T}$, and

$$g_{rsuv} = \left\langle \psi_r(\vec{r_1})\psi_u(\vec{r_2}) \left| \frac{1}{r_{12}} \right| \psi_s(\vec{r_1})\psi_v(\vec{r_2}) \right\rangle \tag{2.27}$$

are the bielectronic integrals.

It is convenient to make use of the creation and annihilation operators $\hat{a}^\dagger_{r,\nu}$, $\hat{a}_{r,\nu}$ brought by the formalism to represent excitation from one spin orbital $\phi_{s,\nu}$ to the other $\phi_{r,\nu}$, with $\nu = \{\alpha,\beta\}$, i.e. $m_s = \{+\frac{1}{2}, -\frac{1}{2}\}$, as the monoelectronic generator

$$\hat{E}_{rs} = \hat{a}^\dagger_{r\alpha}\hat{a}_{s\alpha} + \hat{a}^\dagger_{r\beta}\hat{a}_{s\beta}\,, \tag{2.28}$$

and two instantaneous excitations as the bielectronic generator

$$\hat{e}_{rsuv} = \hat{E}_{rs}\hat{E}_{uv} - \hat{E}_{rv}\delta_{su}\,. \tag{2.29}$$

2.3.2 . Hamiltonian Matrix Elements

The matrix elements of the monoelectronic $\hat{H}_1$ and bielectronic $\hat{H}_2$ parts of the Hamiltonian in the CSF basis

$$\langle I|\hat{H}_1|J\rangle = \sum_r \sum_s h_{rs}(t)\langle I|\hat{E}_{rs}|J\rangle \tag{2.30a}$$

and

$$\langle I|\hat{H}_2|J\rangle = \frac{1}{2}\sum_r \sum_s \sum_u \sum_v g_{rsuv}\langle I|\hat{e}_{rsuv}|J\rangle, \tag{2.30b}$$

can be interpreted as projections that consider both the possibility and probability of electronic transfer from a CSF $|J\rangle$ to another, $|I\rangle$, independently of their bound or ionic nature.

As mentioned in section 2.2.2, CSFs are constructed antisymmetrized to any electron permutation, so that transitions of those fermions from CSF $|J\rangle$ to $|I\rangle$, $\langle I|\hat{E}_{rs}|J\rangle$, are only possible if (1) the MO ϕ_s represented in CSF $|J\rangle$ is occupied by at least one electron, with a maximum of two as per the Pauli exclusion principle [21], (2) the MO ϕ_r represented in CSF $|I\rangle$ is able to receive an electron of unchanged spin ν, so that if it already contains an electron, its spin should be $-\nu$, and (3) $|I\rangle$ and $|J\rangle$ only differ by the transfer of a sole electron. If all the conditions are met, the element of matrix shall be greater than zero, and pondered by the monoelectronic integral h_{rs} representing the transition probability from a molecular orbital ϕ_s to another ϕ_r (see Eq. 2.26).

The same conditions also apply to the bielectronic transitions, except that ϕ_u and ϕ_v must also satisfy the same requirements as ϕ_r and ϕ_s within $|I\rangle$ and $|J\rangle$ at the same time. The bielectronic integrals will also consider both electrons for the transition probabilities.

In this model of single ionization dynamics, when considering the recapture of an ionized electron, that is, when considering a transition from cation $|J^+,\kappa\rangle$ to neutral molecule $|I\rangle$, we can show exactly that the matrix element $\langle I|\hat{E}_{r\kappa}|J^+,\kappa\rangle$ does not vary with κ, and can be evaluated using any fixed reference value of κ, κ_0. The integrals of interest can therefore be calculated by

$$\langle I|H_{QP}(t)|J^+,\kappa\rangle \simeq \sum_r \langle I|\hat{E}_{r\kappa_0}|J^+,\kappa_0\rangle\ h_{r\kappa}(t)\ . \tag{2.31}$$

2.3.3 . Preliminary calculations

Quantum chemistry softwares are readily available online to help generate the data of molecular orbitals necessary to calculate the electronic integrals of the studied molecule, given initial approximations. COLUMBUS [22] is one of those programs, used prior to MEDYS to generate atomic orbitals (AOs), their Linear Combination of Atomic Orbitals (LCAO) coefficients as well as mono- and bi-electronic integrals via the restricted Hartree-Fock method, while neglecting the symmetry (the corresponding group symmetry is then C_1).

MEDYS then takes this information as input to convert it into the MO basis, which returns the time-independent integrals of the monoelectronic Hamiltonian without the field h^0_{rs}, the electronic dipole d_{rs} and the bielectronic integrals g_{rsuv}. Fourier transform of primitive gaussians [23] are then used to generate dipole monoelectronic integrals $d_{r\kappa}$ linking bound orbitals to the ones of the ionization

continuum. It is to be noted that the program in its actual state does not take into account bound with ionized electron interactions.

These calculations then allow us to proceed to the generation of partitioned Hamiltonian operators $\hat{H}_{QQ}$, $\hat{H}_{PP}$, $\hat{H}_{QP}$ and $\hat{H}_{PQ}$ via integrals $\langle I|\hat{E}_{rs}|J\rangle$ and $\langle I|\hat{E}_{rs}|J\rangle$.

2.3.4 .Time propagation

The exchange term $\bar{\mathbb{H}}_{QP}$ of the Hamiltonian has to be calculated for each time frame because of the time dependency of the field in its component

$$\bar{F}(t_n) = \frac{1}{t - t_n} \int_{t_n}^{t} E(t')dt' \,, \tag{2.32}$$

joined to dipole d_{QP}. From there, $\mathbb{L}_n^{\pm}$ are calculated to ultimately propagate interaction configuration vectors $\underline{C}(t)$ and $\underline{\Gamma}(t)$ within the timeframe $[t_n, t_{n+1}]$.

The propagation in the bound state of the neutral molecule is done by applying the unitary operator

$$\mathbb{U}_{QQ}(t, t_n) = \exp\{-i\mathbb{H}_{QQ}(t_n)\delta t\}, \quad \text{where } \delta t = t - t_n \tag{2.33}$$

and include coupling effects with the field as well as internal forces such as the electronic correlation.

Since the propagation of the bound electrons and of the photoelectron are done with different methods to characterize the cation, and since the correlation effects between the ionized electron and all the others are neglected, the unitary operator for the propagation of the cation will be constructed by two terms

$$\mathbb{U}_{PP}(t, t_n) \simeq \mathbb{U}^b_{PP}(t, t_n) \otimes \mathbb{U}^f_{PP}(t, t_n), \tag{2.34}$$

one for the bound electrons,

$$\mathbb{U}^b_{PP}(t, t_n) \simeq \exp\{-i\mathbb{H}^b_{PP}(t_n)\delta t\}, \tag{2.35}$$

that will propagate the $(N-1)$ remaining electrons exactly the same way as they are in the neutral molecule, and another term for the ionized electron

$$\left[\mathbb{U}^f_{PP}(t, t_n)\right]_{\kappa,\kappa'} = \left\langle \kappa \left| \hat{U}_{1e}(t, t_n) \right| \kappa' \right\rangle, \tag{2.36}$$

that induces evolution of the electronic wave packet independently of the Coulomb interactions with the cation, through a Volkov propagator brought by the Strong Field Approximation.

This operator acting within the electronic field $E(t)$ is written as

$$\hat{U}_{1e}(t,t_n) = e^{-i\Phi(t,t_n)}\, e^{i\vec{A}(t,t_n)\cdot\vec{r}}\, e^{-i\vec{\alpha}(t,t_n)\cdot\vec{p}}\, e^{-i\hat{p}^2\delta t/2}\,, \tag{2.37a}$$

with components

$$\vec{A}(t,t_n) = \int_{t_n}^{t} dt'\vec{E}(t')\,, \tag{2.37b}$$

$$\vec{\alpha}(t,t_n) = \int_{t_n}^{t} dt'\vec{A}(t',t_n)\,, \tag{2.37c}$$

and

$$\Phi(t,t_n) = \frac{1}{2}\int_{t_n}^{t} dt' A^2(t',t_n)\,. \tag{2.37d}$$

Even though the electron dynamics associated with the photoelectron are factorized from the dynamics of the bound electrons, one should note that the antisymmetric character of the configuration state functions renders electrons indistinguishable, as required by the Pauli principle. As the evolution of the wave packets are distinguished between both basis, Eq. (2.34) can be rewritten as

$$\hat{U}_{PP}(t,t_n) \simeq \left[\sum_P (-1)^P \hat{P}\right] \hat{U}^b_{PP}(t,t_n)\hat{U}_{1e}(t,t_n), \tag{2.38}$$

$\sum_P (-1)^P \hat{P}$ being the antisymmetrization operator.

2.4 . Case of H_2: Establishing the Basis of the Simplest Molecule

As mentioned in section 2.3.3, the quantum software COLUMBUS has been used to generate the atomic orbital basis, through Pople's 6-31G(d,p)—also known as 6-31G** [24, 25]. 10 MOs are generated using the atomic orbitals $1s$, $1s'$ (split-valence) and the 3 orbitals $2p_{(x,y,z)}$ of both hydrogen atoms, which are $1\sigma_{(g,u)}$, $1'\sigma_{(g,u)}$, $3\sigma_{(g,u)}$ generated from a combination of $2p_z$ AOs, and $1\pi_{(g,u;x,y)}$.

(a) $1\sigma_g$ (b) $1\sigma_u$ (c) $1\pi_{u(x)}$ (d) $1\pi_{g(x)}$

Figure 2.1: H_2 molecular orbitals in the 6-31G** basis at $R = 1.4\ a_0$.

(a) $1\sigma_g$ (b) $1\sigma_u$ (c) $1\pi_{u(x)}$ (d) $1\pi_{g(x)}$

Figure 2.2: H_2 molecular orbitals in the 6-31G** basis at $R = 5.0\ a_0$.

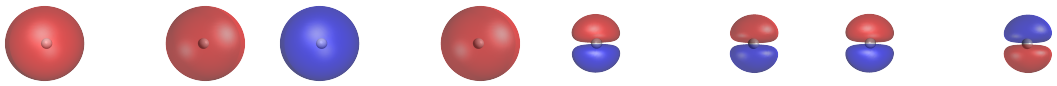

(a) $1\sigma_g$ (b) $1\sigma_u$ (c) $1\pi_{u(x)}$ (d) $1\pi_{g(x)}$

Figure 2.3: H_2 molecular orbitals in the 6-31G** basis at $R = 10.2\ a_0$.

From these MOs, only $1\sigma_g$, $1\sigma_u$, $1\pi_{u,x}$ and $1\pi_{g,x}$ (depicted on Figs. 2.1, 2.2 and 2.3, taken from the writer's master's thesis [26]) have been kept to represent the excitation and ionization of H_2, as selection rules are applicable depending on the angle between the field and the internuclear z axis, due to the variation in the dipolar interaction. For a transition to happen, the variation in the quantum number $\Lambda = |m|$ associated with the quantified value of the electron's angular momentum projected on the z axis (l_z) must be

$$\Delta\Lambda = \begin{cases} 0 & \text{Parallel field} \\ \pm 1 & \text{Perpendicular field} \end{cases}, \qquad g \longleftrightarrow u\,.$$

From the 4 active orbitals, 10 different electrons placement of inverse sign – and thus, singlet state ($S = 0, M_S = 0$) – are possible according to the Pauli principle. The 10 resulting CSFs that represent the Q subspace are

$$\begin{aligned}
|1\rangle &\leftrightarrow |\sigma_g\overline{\sigma}_g| & |6\rangle &\leftrightarrow |\pi_u\overline{\pi}_u| \\
|2\rangle &\leftrightarrow \frac{1}{\sqrt{2}}\Big\{\,|\sigma_g\overline{\sigma}_u| - |\sigma_u\overline{\sigma}_g|\,\Big\} & |7\rangle &\leftrightarrow \frac{1}{\sqrt{2}}\Big\{\,|\sigma_g\overline{\pi}_g| - |\pi_g\overline{\sigma}_g|\,\Big\} \\
|3\rangle &\leftrightarrow |\sigma_u\overline{\sigma}_u| & |8\rangle &\leftrightarrow \frac{1}{\sqrt{2}}\Big\{\,|\sigma_u\overline{\pi}_g| - |\pi_g\overline{\sigma}_u|\,\Big\} \\
|4\rangle &\leftrightarrow \frac{1}{\sqrt{2}}\Big\{\,|\sigma_g\overline{\pi}_u| - |\pi_u\overline{\sigma}_g|\,\Big\} & |9\rangle &\leftrightarrow \frac{1}{\sqrt{2}}\Big\{\,|\pi_u\overline{\pi}_g| - |\pi_g\overline{\pi}_u|\,\Big\} \\
|5\rangle &\leftrightarrow \frac{1}{\sqrt{2}}\Big\{\,|\sigma_u\overline{\pi}_u| - |\pi_u\overline{\sigma}_u|\,\Big\} & |10\rangle &\leftrightarrow |\pi_g\overline{\pi}_g|\,.
\end{aligned} \tag{2.39}$$

From the initial calculations, it was shown that one can get the $\hat{H}_{QQ}$ matrix containing energy data for each CSF. It is then possible to extract the eigenstates en-

ergy values by diagonalization of said matrix, as to get the 10 bound eigenstates $|E_I\rangle$, $I = 1, 10$, depicted on Fig. 2.4a for internuclear distances $R = [0, 12]\ a_0$.

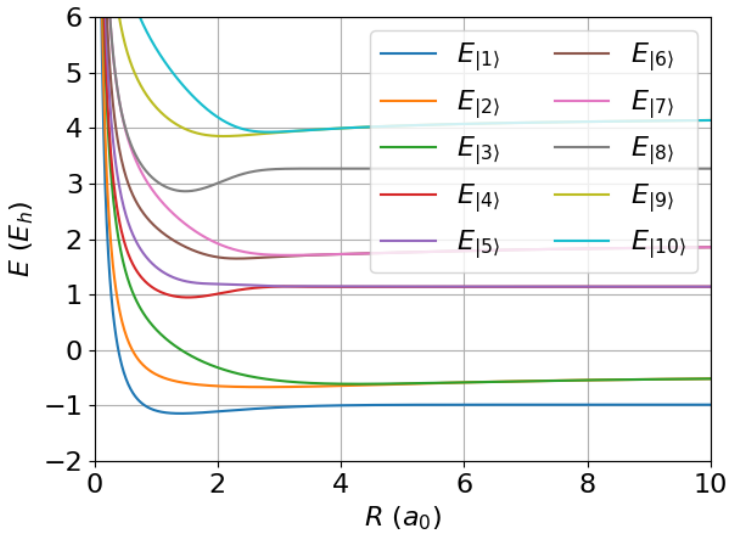

(a) Bound Subspace Q

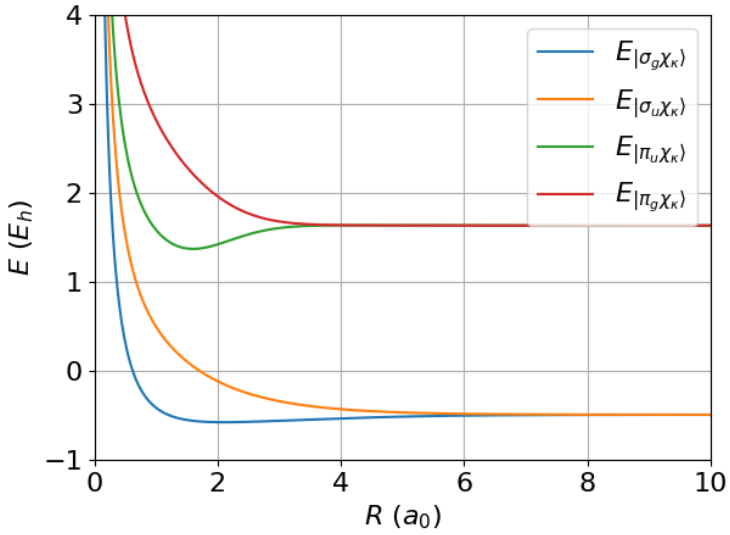

(b) Ionic Subspace P

Figure 2.4: Potential curves of the electronic eigenstates (a) $|E_I\rangle$ of H_2 and (b) $|E_{J^+,\kappa}\rangle$, $\kappa \leftrightarrow \vec{k} = 0$ of H_2^+, in atomic units.

To generate the basis for H_2^+, one has to consider that the remaining bound electron has to be placed within one of the four MOs while the ionized one is

in the ionization continuum, which in terms of plane waves basis is represented by vectors $\vec{k} \in \mathbb{R}^3$ – limited for computational reasons to a plane including the internuclear axis z and the possible perpendicular field polarization axis x. Considering a restriction to single ionization dynamics, the 4 continua generated to represent the 4 types of CSFs in the ionic P subspace is limited to

$$|\sigma_g, \kappa\rangle \leftrightarrow \frac{1}{\sqrt{2}}\Big\{ |\sigma_g \overline{\chi}_\kappa| - |\chi_\kappa \overline{\sigma}_g| \Big\} \qquad |\sigma_u, \kappa\rangle \leftrightarrow \frac{1}{\sqrt{2}}\Big\{ |\sigma_u \overline{\chi}_\kappa| - |\chi_\kappa \overline{\sigma}_u| \Big\}$$
$$|\pi_u, \kappa\rangle \leftrightarrow \frac{1}{\sqrt{2}}\Big\{ |\pi_u \overline{\chi}_\kappa| - |\chi_\kappa \overline{\pi}_u| \Big\} \qquad |\pi_g, \kappa\rangle \leftrightarrow \frac{1}{\sqrt{2}}\Big\{ |\pi_g \overline{\chi}_\kappa| - |\chi_\kappa \overline{\pi}_g| \Big\},$$

depicted for $\kappa \leftrightarrow \vec{k} = 0$ on Fig. 2.4b.

Lower potentials of neutral H_2 and its single ionization product H_2^+ were compared with interpolated potentials of the literature [27, 28]. The results were similar, as shown in Fig. 2.5, while reference datasets converged more rapidly towards asymptotic dissociation energies of $-1.0\ a.u.$ for the neutral molecule, and $-0.5\ a.u.$ for the ion. The perceived shift in energy from MEDYS' calculations can be attributed to the use of a 6-31G** Pople basis set for the generation of a restricted, quasi-complete electronic molecular orbitals basis.

While this basis set, developed for the description of the electronic structure of most molecules in which hydrogen atoms participate to bonding only via their $1s$ orbital, is convenient to represent σ_g ($\propto 1s_A + 1s_b$) and σ_u ($\propto 1s_A - 1s_b$) states of H_2 and H_2^+, it fails to represent the energetics of excited orbitals, and overestimates excitation energies, even to states correlating to the $n = 2$ hydrogenic levels at the dissociative limit, as seen in Fig. 2.4. It is to be noted that calculations in Chap. 3 do not consider molecular orbitals π_u and π_g, and thus do not make use of those anomalous potentials.

2.5 . Parameters and Observables

As mentioned in section 2.2.3, the wavepacket is separated in two subspaces, so its terms can be written, for H_2, as

$$\begin{aligned} |\Psi(t)\rangle &= |\Psi_Q(t)\rangle + |\Psi_P(t)\rangle \\ &= \sum_{I=1}^{10} c_I(t)\,|I\rangle + \sum_{I^+=1}^{4} \int d\kappa\, \gamma_{I^+,\kappa}(t)\,|I^+, \kappa\rangle\,, \end{aligned} \tag{2.40}$$

where $|I\rangle$ are the bound CSFs, $c_I(t)$ are the bound states coefficients, $|I^+, \kappa\rangle$ are the ionized CSFs and $\gamma_{I^+,\kappa}(t)$ are the ionized states coefficients.

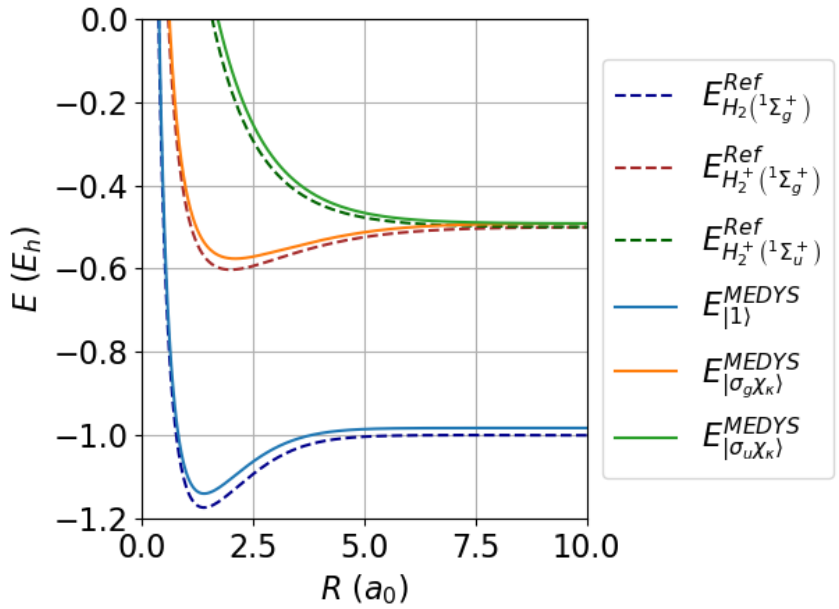

Figure 2.5: Comparison between lower potentials of H_2 and H_2^+ generated with the ab initio program MEDYS [23] (full lines) and the interpolated resulting energies from the work of Kolos and Wolniewicz on H_2 potentials [27] (dark blue dashed line) and the work of Madsen and Peek on H_2^+ potentials [28] (dark orange dashed line for $^1\Sigma_g^+$ and dark green dashed line for $^1\Sigma_u^+$).

In the MEDYS program, the time dependency of the wave function is given by the coefficients $c_I(t)$ and $\gamma_{I^+,\kappa}(t)$, respectively representing the subspaces Q and P. They are propagated over femtoseconds-long dynamics, using an iteration of attosecond timeframes, a duration short enough to converge the calculations.

2.5.1 . Parameters of the System and the Field

Initially, the molecule is in its ground state, without any external perturbation. To represent this state of the molecule, it is custom to use the first eigenstate $|E_1\rangle$ calculated for the system at rest. It is obtained by diagonalization of the $H_{QQ}(0)$ matrix at fixed R to get eigenvectors and their associated eigenvalues while $\gamma_{I^+,\kappa}(0) = 0, \forall I^+, \kappa$.

At any time during the dynamics, the eigenstates can be described as linear combinations of CSFs and vice versa. The initial states consist mainly of states $|1\rangle$ and $|3\rangle$, varying in proportion depending on the strength of the electronic correlation, which in turn depends on the internuclear distance R. At the equilib-

rium distance, $R = 1.4\ a_0$, the initial state consists almost entirely of $|\sigma_g\overline{\sigma}_g|$, as $|c_1(0)|^2 = 99.5\%$. As R increases towards regions where the σ_g and σ_u potentials are closer to each other and to the dissociative energy value, the distribution of CSFs within the eigenstates becomes comparable, with $|c_1(0)|^2 = 63\%$ for $R = 5.0\ a_0$ and $|c_1(0)|^2 = 50\%$ at $R = 10.2\ a_0$.

The electric field is described by the following equation

$$\mathcal{F}(t) = \mathcal{F}_0\ \sin^2\left(\frac{\pi\, t}{\tau}\right)\cos(\omega t)\,, \tag{2.41}$$

where $\mathcal{F}_0$ is the peak field amplitude, $\omega = 2\pi c/\lambda$ is the angular frequency, and τ is the total duration of the dynamics. It is of the form $\vec{\mathcal{F}} = \mathcal{F}(t)\,\hat{e}$, where $\hat{e}$ is the unit vector pointing in the polarization direction of the linear field.

For the purposes of my research, the parameters of the field were set to a total duration of $n_{per} = 4$ optical cycles, 2 cycles for the full width at half maximum (FWHM) of the pulse, which corresponds to approximately 9.34, 10.01 and 10.54 fs for wavelengths of $\lambda = 700$, 750 and 790 nm, respectively. These three different wavelengths were used to compare the effect of the frequency on the observables. They correspond to the frequencies of respectively $\omega = 6.51\times10^{-2}$, 6.08×10^{-2} and 5.77×10^{-2} a.u. (1.77, 1.65 and 1.57 eV), respectively. Each optical cycle is divided in $n_t = 2000$ time frames of similar duration $\delta t = \tau/(n_{per}n_t)$.

H_2 nuclei are considered static using the Born-Oppenheimer approximation, and thus molecules at the equilibrium, $R = 1.4\ a_0$, slightly elongated, $R = 5\ a_0$ and quasi-dissociated, $R = 10\ a_0$ are compared through our research. Electron-cation wave packets are represented on a plane wave's 2D grid over the k_z internuclear axis and the orthogonal k_x axis. The continuum is discretized using a total of 240 000 points: 400 on k_z and 600 on k_x, all spaced on the momentum grid by a factor $\delta k_z = \delta k_x = 0.0314\ {a_0}^{-1}$, which covers -6.27 to $6.27\ {a_0}^{-1}$ on k_z, and -9.41 to $9.41\ {a_0}^{-1}$ on k_x.

One aspect of the program that distinguishes it from other TD-MCSCF softwares is its recent addition of an "electronic interaction" parameter,

$$\eta(t) = \eta_i - \frac{\eta_i - \eta_f}{1 + \exp\left[\frac{-12(t-t_c)}{d}\right]}\,, \tag{2.42}$$

a sigmoid function applied to the electron repulsion potential $U_{ee} = 1/r_{12}$, from the electronic interaction part of the Hamiltonian described in Eq. (2.2d), that has the capacity to switch on or off the interaction over a certain period of time. As it is written in Eq. (2.42), $\eta(t)$ varies over time and can take any value between 0, where the electronic correlation is extinguished, to 1, where it is fully considered. Initially, its value is set to a weight of $\eta_i = 1$ and it will gradually change

towards a weight of $\eta_f = 0$, following a sigmoid of width d centred at the time t_c, ideally at a maximum of the field so that the dynamics is dominated by the strong field.

The purpose of this addition to the code is to explore the quantitative limitations of the Single Active Electron Approximation (SAE), an approximation widely used in the literature because it conveniently neglects the electronic interaction, so that each electron is considered independent of the others. As we will see in the next section, this approximation cannot be used under certain settings of the system and of the strong field, and our work constitutes a preliminary approach to the quantitative limits of some parameters. As such, it was necessary for our simulation program to be able to consider the same initial system, with full electronic correlation, and to compare situations in which the correlation is either kept total for the whole dynamics, or turned off during a maximum of the field.

Following a numerical study aimed at understanding the impact of the electronic correlation switch-off time, we decided to set the width parameter of the sigmoid to $d = 75$ a.u., corresponding to about 1.81 fs, so that it is large enough not to cause sudden excitation of the molecule, and small enough to be in a part of the dynamics where the field dominates Coulomb interactions. The sigmoid was centered at $t_c = 3\pi/2\omega$, right at the peak of the second maximum, so that the field is already strong enough to guide the dynamics during the cutoff of the electronic correlation, and at the earliest possible time to see the full effect of this cutoff.

2.5.2 .Ionization Probability and Photoelectron Spectra

Since population information is already stored in a channel-resolved fashion into the time-dependent coefficients $c_I(t)$ and $\gamma_{I^+,\kappa}(t)$, the information concerning the dynamics can be directly extracted from those.

The bound states composition of H_2 is of particular interest for the study, as transitions to excited states are able to either quench or exalt the ionization depending on the conditions of the simulation. It is possible to describe the eigenstates as linear combinations of CSFs, and vice-versa, such that if an eigenstate can be described as $|E_J\rangle = \sum_I D_{JI}|I\rangle$ (the result of diagonalizing $\mathbb{H}_{QQ}$ at $t = 0$) the populations within the said eigenstate during the dynamics can be written as

$$P_{E_J}(t) = \sum_I |D^*_{JI}\, c_I(t)|^2, \tag{2.43a}$$

and for their CSF counterpart as

$$P_I(t) = |c_I(t)|^2. \tag{2.43b}$$

Similarly, the time-dependent probability of ionization towards different ionic channels I^+ of H_2^+ can be calculated by

$$\Gamma_{I^+}(t) \propto \int |\gamma_{I^+,\kappa}(t)|^2 \, d^3\vec{k} - \sum_{i=1}^{2} \left| \int \langle \varphi_i | \vec{k} \rangle \, \gamma_{I^+,\kappa}(t) \, d^3\vec{k} \right|^2 , \tag{2.44}$$

where $\varphi_{\{1,2\}} = \sigma_{\{g,u\}}$, and the total ionization probability is given by

$$P_{ion}(t) = \sum_{I^+} \Gamma_{I^+}(t). \tag{2.45}$$

From those equations, one should always get a normalized total

$$P_{ion}(t) + \sum_{I} P_{E_I}(t) = 1 \, . \tag{2.46}$$

As stated in section 2.2.3, the ionic CSFs are constructed with the non-orthonormal $\{\chi_\kappa\}$ continuum orbitals, within the plane wave basis orthogonalized with the active bound MO basis $\{\varphi_i\}$. Asymptotically, those continuum orbitals can be effectively represented by their associated plane waves $|\chi_\kappa\rangle \to \left|\vec{k}\right\rangle$, and it is possible to extract from the ionic coefficient $\gamma_{I^+,\kappa}(t)$ the post-dynamic channel-resolved photoelectron spectra

$$f_{I^+}\left(\vec{k}\right) = |\gamma_{I^+,\kappa}(t_f)|^2, \tag{2.47}$$

distributed over the momentum plane associated with vectors $\vec{k}$.

Bibliography

[1] D. R. Hartree. The wave mechanics of an atom with a non-coulomb central field. part ii. some results and discussion. *Mathematical Proceedings of the Cambridge Philosophical Society*, 24(1):111–132, 1928. doi:10.1017/S0305004100011920.

[2] V. Fock. Näherungsmethode zur lösung des quantenmechanischen mehrkörperproblems. *Zeitschrift für Physik*, 61(1):126–148, 1930. URL: https://link.springer.com/article/10.1007/BF01340294, doi:10.1007/BF01340294.

[3] J. C. Slater. A simplification of the hartree-fock method. *Phys. Rev.*, 81:385–390, Feb 1951. URL: https://link.aps.org/doi/10.1103/PhysRev.81.385, doi:10.1103/PhysRev.81.385.

[4] W. Kohn and L. J. Sham. Self-consistent equations including exchange and correlation effects. *Phys. Rev.*, 140:A1133–A1138, Nov 1965. URL: https://link.aps.org/doi/10.1103/PhysRev.140.A1133, doi:10.1103/PhysRev.140.A1133.

[5] T. T. Nguyen-Dang, M. Peters, S. M. Wang, E. Sinelnikov, and F. Dion. Nonvariational time-dependent multiconfiguration self-consistent field equations for electronic dynamics in laser-driven molecules. *J. Chem. Phys.*, 127(17):174107, 2007. URL: https://pubs.aip.org/aip/jcp/article-abstract/127/17/174107/958719/Nonvariational-time-dependent-multiconfiguration?redirectedFrom=fulltext, doi:10.1063/1.2774979.

[6] L. V. Keldysh. Ionization in the field of a strong electromagnetic wave. *Sov. Phys. JETP*, 20(5):1307–1314, 1965.

[7] H. R. Reiss. Effect of an intense electromagnetic field on a weakly bound system. *Phys. Rev. A*, 22:1786–1813, 1980. URL: https://link.aps.org/doi/10.1103/PhysRevA.22.1786, doi:10.1103/PhysRevA.22.1786.

[8] D. B. Milošević. Phase space path-integral formulation of the above-threshold ionization. *J. Math. Phys.*, 54(4):042101, 2013. URL: https://pubs.aip.org/aip/jmp/article-abstract/54/4/042101/233329/Phase-space-path-integral-formulation-of-the-above?redirectedFrom=fulltext, doi:10.1063/1.4797476.

[9] D. W. Wolkow. Über eine klasse von lösungen der diracschen gleichung. *Zeitschrift für Physik*, 94(3):250–260, Mar 1935. URL: https://link.springer.com/article/10.1007/BF01331022, doi:10.1007/BF01331022.

[10] H. Feshbach. Unified theory of nuclear reactions. *Ann. Phys.*, 5(4):357–390, 1958. URL: https://www.sciencedirect.com/science/article/pii/0003491658900071, doi:10.1016/0003-4916(58)90007-1.

[11] B. Mignolet, R. D. Levine, and F. Remacle. Localized electron dynamics in attosecond-pulse-excited molecular systems: Probing the time-dependent electron density by sudden photoionization. *Phys. Rev. A*, 86:053429, Nov 2012. URL: http://link.aps.org/doi/10.1103/PhysRevA.86.053429, doi:10.1103/PhysRevA.86.053429.

[12] T. T. Nguyen-Dang and J. Viau-Trudel. Multicomponent dynamics of coupled quantum subspaces and field-induced molecular ionizations. *J. Chem. Phys.*, 139(24):244102, 2013. URL: http://aip.scitation.org/doi/10.1063/1.4849755, doi:10.1063/1.4849755.

[13] C. M. Granados-Castro and J. L. Sanz-Vicario. Time-resolved resonant photoionization of He using a time-dependent Feshbach method with ultrashort laser pulses. *J. Phys. B*, 46(5):055601, February 2013. URL: https://iopscience.iop.org/article/10.1088/0953-4075/46/5/055601, doi:10.1088/0953-4075/46/5/055601.

[14] J. Crank and P. Nicolson. A practical method for numerical evaluation of solutions of partial differential equations of the heat-conduction type. *Math. Proc. Cambridge*, 43(01):50–67, 1947. URL: http://journals.cambridge.org/abstract_S0305004100023197, doi:10.1017/S0305004100023197.

[15] T.-T. Nguyen-Dang, M. Peters, S.-M. Wang, E. Sinelnikov, and F. Dion. Nonvariational time-dependent multiconfiguration self-consistent field equations for electronic dynamics in laser-driven molecules. *J. Chem. Phys.*, 127:174107, 12 2007. URL: https://pubs.aip.org/aip/jcp/article-abstract/127/17/174107/958719/Nonvariational-time-dependent-multiconfiguration?redirectedFrom=fulltext, doi:10.1063/1.2774979.

[16] T. T. Nguyen-Dang, M. Peters, S.-M. Wang, and F. Dion. Toward ab-initio simulations of multiple ionization processes in intense laser field. *Chem. Phys.*, 366(1–3):71–84, 2009. URL: https://www.sciencedirect.com/science/article/abs/pii/S0301010409002766, doi:10.1016/j.chemphys.2009.09.007.

[17] J.-N. Vigneau, T.-T. Nguyen-Dang, E. Charron, and O. Atabek. Strong-field molecular ionization beyond the single active electron approximation. *The Journal of Chemical Physics*, 157(13):134304, 10 2022. URL: https://pubs.aip.org/aip/jcp/article-abstract/157/13/134304/2841883/Strong-field-molecular-ionization-beyond-the?redirectedFrom=fulltext, arXiv:https://pubs.aip.org/aip/jcp/article-pdf/doi/10.1063/5.0111636/16550642/134304_1_online.pdf, doi:10.1063/5.0111636.

[18] P. A. M. Dirac and N. H. D. Bohr. The quantum theory of the emission and absorption of radiation. *Proceedings of the Royal Society of London. Series A, Containing Papers of a Mathematical and Physical Character*, 114(767):243–265, 1927. URL: https://royalsocietypublishing.org/doi/abs/10.1098/rspa.1927.0039, arXiv:https://royalsocietypublishing.org/doi/pdf/10.1098/rspa.1927.0039, doi:10.1098/rspa.1927.0039.

[19] P. Jordan and E. Wigner. Über das paulische äquivalenzverbot. *Z. Phys.*,

47(9):631–651, Sep 1928. URL: https://link.springer.com/article/10.1007/BF01331938, doi:10.1007/BF01331938.

[20] V. A. Fock. Konfigurationsraum und zweite quantelung. *Z. Phys.*, 75(9):622–647, Sep 1932. URL: https://link.springer.com/article/10.1007/BF01344458, doi:10.1007/BF01344458.

[21] W. Pauli. Über den zusammenhang des abschlusses der elektronengruppen im atom mit der komplexstruktur der spektren. *Z. Phys.*, 31(1):765–783, Feb 1925. URL: https://link.springer.com/article/10.1007/BF02980631, doi:10.1007/BF02980631.

[22] H. Lischka, R. Shepard, I. Shavitt, R. M. Pitzer, M. Dallos, Th. Müller, P. G. Szalay, F. B. Brown, R. Ahlrichs, H. J. Böhm, A. Chang, D. C. Comeau, R. Gdanitz, H. Dachsel, C. Ehrhardt, M. Ernzerhof, P. Höchtl, S. Irle, G Kedziora, T. Kovar, V. Parasuk, M. J. M. Pepper, P. Scharf, H. Schiffer, M. Schindler, M. Schüler, M. Seth, E. A. Stahlberg, J.-G. Zhao, S. Yabushita, Z. Zhang, M. Barbatti, S. Matsika, M. Schuurmann, D. R. Yarkony, S. R. Brozell, E. V. Beck, J.-P. Blaudeau, M. Ruckenbauer, B. Sellner, F. Plasser, and J. J. Szymczak. Columbus, an ab initio electronic structure program, release 7.0, 2015.

[23] T. T. Nguyen-Dang, F. Dion, S. M. Wang, A. Sainjon, J. Viau-Trudel, M. Peters, and É. Couture-Bienvenue. Many-Electron-Dynamics System - MEDYS (v0.9), 2016.

[24] J. A. Pople and M. Gordon. Molecular orbital theory of the electronic structure of organic compounds. i. substituent effects and dipole moments. *J. Am. Chem. Soc.*, 89(17):4253–4261, Aug 1967. URL: https://pubs.acs.org/doi/abs/10.1021/ja00993a001, doi:10.1021/ja00993a001.

[25] R. Ditchfield, W. J. Hehre, and J. A. Pople. Self-Consistent Molecular-Orbital Methods. IX. An Extended Gaussian-Type Basis for Molecular-Orbital Studies of Organic Molecules. *J. Chem. Phys.*, 54(2):724–728, 01 1971. URL: https://pubs.aip.org/aip/jcp/article-abstract/54/2/724/757582/Self-Consistent-Molecular-Orbital-Methods-IX-An?redirectedFrom=fulltext, doi:10.1063/1.1674902.

[26] J.-N. Vigneau. *Dynamique d'ionisation dissociative du dihydrogène soumis à un champ laser intense*. Master thesis, Université Laval, 2020.

[27] W. Kolos and L. Wolniewicz. Potential-Energy Curves for the $\chi^1\Sigma_g^+$, $b^3\Sigma_u^+$, and $C^1\Pi_u$ States of the Hydrogen Molecule. *J. Chem. Phys.*, 43:2429, 1965. URL: https://pubs.aip.org/aip/jcp/article-abstract/43/7/

2429/81403/Potential-Energy-Curves-for-the-X-1-g-b3-u-and-C-1?redirectedFrom=fulltext, doi:10.1063/1.1697142.

[28] M. M. Madsen and J. M. Peek. Eigenparameters for the lowest twenty electronic states of the hydrogen molecule ion. *At. Data Nucl. Data Tables*, 2:IN3–204, 1970. URL: https://www.sciencedirect.com/science/article/pii/S0092640X70800080, doi:https://doi.org/10.1016/S0092-640X(70)80008-0.

Chapter 3 Strong-Field Molecular Ionization Beyond the SAE Approximation

This chapter is an authorized reproduction of an article that has been published in *The Journal of Chemical Physics*, Volume 157, Issue 13, pp. 134304 (2022). DOI: 10.1063/5.0111636.
The paper and its original bibliography are enriched by further explanations and analyses of unpublished, related results in an annex at the end of the chapter, after the article itself.

Contents

Strong-Field Molecular Ionization Beyond the Single Active Electron Approximation

J.-N. Vigneau,[1,2] **T.-T. Nguyen-Dang,**[2,a)] **E. Charron,**[1] **and O. Atabek**[1,b)]

[1]Institut des Sciences Moléculaires d'Orsay, Université Paris-Saclay, CNRS, 91405 Orsay, France
[2]Chemistry Department, Université Laval, Québec, QC, Canada

[a)]Correspondence: thanh-tung.nguyen-dang@chm.ulaval.ca
[b)]Deceased.

Résumé

Le présent travail explore les limites quantitatives de l'approximation du simple électron actif (SAE), souvent utilisée pour traiter l'ionisation en champ fort et la dynamique attoseconde ultérieure. En utilisant une approche multi-configurationnelle dépendante du temps, en particulier une méthode d'interaction de configurations dépendante du temps (TDCI), nous résolvons l'équation de Schrödinger dépendante du temps (TDSE) pour la molécule de dihydrogène à deux électrons, avec la possibilité de modifier l'interaction électron-électron par une fonction d'activation/désactivation adiabatique. Nous nous concentrons sur les signaux de l'ionisation simple de H_2 sous une impulsion laser intense à quatre cycles dans le proche infrarouge (NIR), à polarisation linéaire, d'intensité variable, et dans un modèle de molecule à vibration nucléaire gelée. Les observables que nous abordons sont des profils de probabilité d'ionisation totale post-impulsion en fonction de l'intensité maximale du laser. Trois valeurs de la distance internucléaire R sont prises en paramètre, $R = R_{eq} = 1.4$ a.u, la géométrie d'équilibre de la molécule, $R = 5.0$ a.u pour une molécule allongée et $R = 10.2$ a.u pour une molécule dissociée. L'observation la plus frappante est le comportement non monotone des profils de probabilité d'ionisation à des distances d'allongement intermédiaires avec un cas d'ionisation exaltée et un cas d'extinction partielle de l'ionisation. Nous donnons une interprétation de cela en termes d'un mécanisme d'ionisation multiphotonique exaltée par résonance (REMPI) avec des résonances superposées et interférentes résultant d'états électroniques excités.

Mots clés: Excitation en champ intense, corrélation électronique, ionisation tunnel, processus multiphotoniques, interférence de résonance, extinction de l'ionisation, interaction de configurations, partitionnement de Feshbach.

Abstract

The present work explores quantitative limits to the Single-Active Electron (SAE) approximation, often used to deal with strong-field ionization and subsequent attosecond dynamics. Using a time-dependent multiconfiguration approach, specifically a Time-Dependent Configuration Interaction (TDCI) method, we solve the time-dependent Schrödinger equation (TDSE) for the two-electron dihydrogen molecule, with the possibility of tuning at will the electron-electron interaction by an adiabatic switch-on/switch-off function. We focus on signals of the single ionization of H_2 under a strong near-infrared (NIR) four-cycle, linearly-polarized laser pulse of varying intensity, and within a vibrationally frozen molecule model. The observables we address are post-pulse total ionization probability profiles as a function of the laser peak intensity. Three values of the internuclear distance R taken as a parameter are considered, $R = R_{eq} = 1.4$ a.u, the equilibrium geometry of the molecule, $R = 5.0$ a.u for an elongated molecule and $R = 10.2$ a.u for a dissociating molecule. The most striking observation is the non-monotonous behavior of the ionization probability profiles at intermediate elongation distances with an instance of enhanced ionization and one of partial ionization quenching. We give an interpretation of this in terms of a Resonance-Enhanced-Multiphoton Ionization (REMPI) mechanism with interfering overlapping resonances resulting from excited electronic states.

Keywords: Strong-field excitation, electron correlation, tunnel ionization, multiphoton processes, resonance interference, ionization quenching, configuration interaction, Feshbach partitioning.

3.1 . Introduction

Intense-field dynamics features numerous phenomena that require radical assumptions or approximations in order to attain a simple yet comprehensive interpretation and/or to gain access to affordable quantitative simulations. Strong-field ionization [1] is one of these phenomena. It encompasses a wealth of processes and observable effects, such as High-order Harmonic Generation [2, 3] (HHG), Laser-Induced Electron Diffraction [4–6] (LIED) or Attosecond Electron Holography [7] for instance. When refering to molecules, these processes define Attosecond Molecular (photo-)Dynamics, and their measurements and simulations are highly non-trivial [8, 9]. Thus, the interpretation and simulations of these processes have often assumed that the properties of the ionization process depend essentially on the interaction of the departing electron with the

laser field and with the Coulomb field of the core, possibly screened by an effective, mean field associated with the Coulomb repulsion exerted by the remaining, bound electrons. This is the celebrated Single-Active Electron (SAE) approximation [10–12].

A number of approaches have been proposed to refine the SAE approximation, making it more quantitative, or to explore its validity. Constructing a model effective potential for the departing electron in the molecular ionization is a common thread of these works. This can take the form of the introduction of an empirical potential to capture the dynamic (field-induced) multielectron polarization effects [13–15]. Of note is the foundation of this in a rigorous Born-Oppenheimer like separation between the core and the departing electron, couched within a so-called Correlated Strong-Field (CSF) ansatz [13]. Else, in an alternative, not less fundamental approach [16], it was proposed to use, as a quantifier of electron correlation, the difference in the effective potential derived from the (laser-driven) time-evolution of the system's natural orbitals, as this evolution is calculated within a multiconfiguration time-dependent description (MCTDHF, for Time-Dependent Multiconfiguration Hartree-Fock) on one hand, and within a time-dependent mean-field description, (TDHF for Time-Dependent Hartree-Fock) on the other hand.

The present paper explores manifestations of effects that indicate the attainment of quantitative limits to the SAE approximation in H_2. Using an approach of the general time-dependent multiconfiguration class [17–21] specifically a Time-Dependent Configuration Interaction (TDCI) method [21–23], with a Feshbach partitioning of the many-electron state space [24, 25], we solve the time-dependent Schrödinger equation (TDSE) for the two-electron dihydrogen molecule, with the possibility of tuning at will the electron-electron interaction by an adiabatic switch on/off function. It is this possibility to modulate the electron-electron repulsion, during the laser-driven dynamics, which constitutes the distinctive trait of the present work. By doing so, we are probing phenomenological effects of the presence of V_{ee} during the laser-driven ionization dynamics, rather than trying to quantify electron correlation as proposed and illustrated nicely elsewhere [16].

Our TDCI methodology with Feshbach partitioning [24, 25] between neutral bound states and cationic (free) states shares the same philosophy as the Time Dependent Feshbach Close-Coupling (TDFCC) method of the literature [26–29] and differs from it only in the explicit use of configuration-state functions (CSF) as a basis, as opposed to eigenstates of the field-free two-electron Hamiltonian. We will focus on signals of the single ionization of H_2 under a strong NIR (wavelength $\lambda = 700, 750, 790$ nm) two-cycle FWHM, linearly-polarized laser pulse of varying

intensity. To assess the dynamical importance of the electron repulsion V_{ee}, we consider three values of the internuclear distance R taken as a parameter, the nuclei being frozen in each geometry in the spirit of the Born-Oppenheimer approximation: $R = R_{eq} = 1.4$ a.u, the equilibrium geometry of the molecule, represents a field-free situation of weak electronic correlation, while $R = 5.0$ a.u and 10.2 a.u, denoting respectively an elongated and a dissociating molecule, are situations of increasing field-free electronic correlation.

As expected, in the equilibrium geometry $R = R_{eq}$, tuning off the electron repulsion has little impact on the channel-resolved and total ionization probabilities exhibited as functions of the field-intensity. The total ionization probability vs. intensity profile is typical of a tunnel ionization (TI) process [1] except for the highest range of intensity, for which a sudden increase in the total ionization probability is observed and interpreted as due to the onset of an over-the-barrier ionization (OBI) mechanism [30]. At the elongated geometry $R = 5.0$ a.u, the ionization probability does not exhibit such a sudden increase as one approaches the high-intensity end, i.e. no over-the-barrier enhancement of the ionization is observed. The strong electronic correlation prevailing at this geometry now induces considerable modifications to the dynamics, and the ionization probability varies non-monotonously with I, passing through a peak (at I_{max}) then a dip (at I_{min}), denoting an enhancement and a quenching of the ionization, in a moderate intensity range, the value of which depends on the field frequency. A possible explanation is that the ionization is a mixture of a tunnel one (TI) from the (correlated) ground-state and multiphoton ionizations (MPI) through excited states, accessible from the ground state by multiphoton excitation. The dynamics thus proceeds through a Resonance Enhanced Multiphoton Ionization (REMPI) with interfering overlapping resonances resulting from excited electronic states. This non-monotonous behavior is not observed in the dissociative limit, $R = 10.2$ a.u, the strongest field-free correlation situation, where only subtle differences are observed between correlated and uncorrelated dynamics. This stunning observation is explained by the fact that no multiphoton transition to the excited states are possible from the correlated ground state, as these transitions between these states become dipole-forbidden in this geometry.

The manuscript is organized as follows: Section 3.2 is devoted to the model and to the computational approach chosen for solving the TDSE. The results concerning total ionization profiles are gathered in Section 3.3, with their interpretation and discussions. A summary and conclusion are found in Section 3.4.

3.2 . Model System and Computational Approach

3.2.1 . Model System: Orbital Basis and Configuration-State Functions (CSF)

The H_2 molecule is considered in a body-fixed coordinate system defined such as the z axis coincides with the internuclear axis of the molecule, at varying geometry given by specific values of the internuclear distance R. Calculations of the field-free electronic structure of the molecule at the HF-SCF (Hartree-Fock Self-Consistent Field) level, in the $6\text{-}31G^{**}$ basis and using the COLUMBUS program suite [31], yields 10 molecular orbitals. If kept in full, they would in turn generate a basis of $N_{\mathrm{CSF}} = 55$ two-electron singlet configuration states functions (CSF) [32]. The model we are using consists of the part of this basis corresponding to the various possible ways to distribute the two electrons in the lowest-lying molecular orbitals of σ symmetry, σ_g $(1s\sigma_g)$ and σ_u $(2p\sigma_u)$, respectively. In the language of multiconfiguration electronic-structure theories, this corresponds to a CAS(2,2) model of the molecule. These two active orbitals are the same pair of strongly interacting charge-resonance orbitals of H_2^+ that underlie all early works on the dynamics of the dihydrogen molecular ion in an intense laser field [33]. Their interactions give rise to several phenomena such as Above-Threshold Dissociation (ATD) [34], Bond Softening (BS) [35], Vibrational Trapping (VT) [36] and Charge-Resonance Enhanced Ionization (CREI) [37–40]. Note that the interpretation of the physics of the system using directly these orbitals' properties is possible only near the equilibrium geometry. Near the dissociative limit, the physics is more appropriately discussed in Valence-Bond theoretic language [41], using Heitler-London orbitals, which asymptotically, (as $R \longrightarrow \infty$), become atomic orbitals. We will occasionally evoke these in the discussion of the ionization dynamics at elongated geometries and in the dissociative limit.

The two active orbitals (σ_g, σ_u) give rise also to CSFs that are most fundamental in the discussion of correlation in the smallest two-electron molecule, H_2. Basically, with this active space, the CSF basis generated by these orbitals consists of three states, which will be denoted $|L\rangle$, with $L = 1, 2, 3$

$$|1\rangle = |\sigma_{g\uparrow}\, \sigma_{g\downarrow}| \tag{3.1a}$$

$$|2\rangle = \frac{1}{\sqrt{2}}\{|\sigma_{g\uparrow}\, \sigma_{u\downarrow}| - |\sigma_{u\uparrow}\, \sigma_{g\downarrow}|\} \tag{3.1b}$$

$$|3\rangle = |\sigma_{u\uparrow}\, \sigma_{u\downarrow}| \tag{3.1c}$$

where $|\xi_1\, \xi_2|$ designates a Slater determinant constructed out of the orthonormal spin-orbitals $\xi_1,\ \xi_2$, and $\uparrow$ and $\downarrow$ are for spin up or down respectively. These CSF will all be important in the discussion of the electronic excitation dynamics induced by the laser field, insofar as it is polarized along the z direction. In addi-

tion, we expect strong ionization to accompany these electronic excitations. To describe the ionization process, the bound orbital active space is augmented by a reasonably extended set of n_k continuum-type single-electron orbitals taken as plane-waves $|\vec{k}\rangle \equiv \exp\left(i\vec{k}.\vec{r}\right)$, pre-orthogonalized with respect to the bound active orbitals, and designated by

$$|\chi_{\vec{k}}\rangle \propto (1-\hat{q})\,|\vec{k}\rangle\,, \tag{3.2}$$

where $\hat{q}$ is the projection operator

$$\hat{q} = \sum_{i=1}^{2} |\varphi_i\rangle\langle\varphi_i| = |\sigma_g\rangle\langle\sigma_g| + |\sigma_u\rangle\langle\sigma_u|. \tag{3.3}$$

Laser-induced single ionization out of any of the bound-state CSF $|L\rangle,\ L=1,2,3$ will give ionized (singlet) CSFs of the form

$$|1^+,\vec{k}\rangle \;=\; \frac{1}{\sqrt{2}}\left\{\left|\sigma_{g\uparrow}\,\chi_{\vec{k}\downarrow}\right| - \left|\chi_{\vec{k}\uparrow}\sigma_{g\downarrow}\right|\right\} \tag{3.4a}$$

$$|2^+,\vec{k}\rangle \;=\; \frac{1}{\sqrt{2}}\left\{\left|\sigma_{u\uparrow}\,\chi_{\vec{k}\downarrow}\right| - \left|\chi_{\vec{k}\uparrow}\sigma_{u\downarrow}\right|\right\} \tag{3.4b}$$

where $\{J^+{=}1^+,2^+\}$ designate the cation CSFs $\{\sigma_g,\sigma_u\}$, respectively, here directly identifiable with the orbitals of H_2^+. With $\vec{k}\in\mathbb{R}^3$, these CSFs span two continua of two-electron states corresponding to the ionic channels 1^+, or σ_g, and 2^+, or σ_u.

The two-electron wave packet is at all time described by

$$|\Psi(t)\rangle = |\Psi_Q(t)\rangle + |\Psi_P(t)\rangle \tag{3.5}$$

with

$$|\Psi_Q(t)\rangle = \sum_{L=1}^{3} c_L(t)\,|L\rangle \tag{3.6a}$$

and

$$|\Psi_P(t)\rangle = \int d^3\vec{k} \sum_{J^+=1^+}^{2^+} \gamma_{J^+,\vec{k}}(t)\,|J^+,\vec{k}\rangle, \tag{3.6b}$$

denoting a Feshbach-Adams partitioning [42–44] of the two-electron state space, into two sub-spaces, the Q-subspace (dimension $N_Q = 3$) of bound states of the neutral molecule and the P-subspace (dimension $n_k \times N_P$, with $N_P = 2$) of singly-ionized states, *i.e.* states of the $\{H_2^+ + e^-\}$ system. Since it is the same partitioning of the many-electron Hilbert space as defined in TDFCC theory [26–29]

which refers explicitly to the basis of eigenstates of the field-free two-electron Hamiltonian, the same physical model, (for the same orbital active space), is involved here, although the Hamiltonian matrix is expressed in the CSF basis rather. In particular, the part of the partitioned Hamiltonian corresponding to the interaction between the two subspaces, $\hat{H}_{QP}$, is strictly defined by the radiative interaction potential, [see eq.(3.10a) below].

The configuration-interaction, (CI) coefficients $c_L(t)$ and $\gamma_{J^+,\vec{k}}(t)$ are to be obtained from their initial values by solving the electronic Time-Dependent Schrödinger Equation (TDSE) describing the electronic system driven by the laser pulse

$$i\partial_t|\Psi(t)\rangle = \hat{H}^{el}_{\eta}(R,t)|\Psi(t)\rangle\,, \tag{3.7}$$

where the 2-electron Hamiltonian is

$$\hat{H}^{el}_{\eta}(R,t) = \sum_{i=1}^{2}\hat{h}_i(R,t) + \frac{\eta(t)}{r_{12}}\,, \tag{3.8a}$$

with

$$\hat{h}_i(t) \;=\; -\frac{\nabla_i^2}{2} - \frac{1}{|\vec{r}_i - \vec{R}/2|} - \frac{1}{|\vec{r}_i + \vec{R}/2|} - \vec{r}_i\cdot\vec{\mathcal{F}}(t), \tag{3.8b}$$

containing the spin-conserving electric-dipole interaction (written in the length gauge) between the molecule and the electric component of the laser field $\vec{\mathcal{F}}(t)$. Note the presence, in Eq. (3.8a), of the factor $\eta(t)$ multiplying the electron repulsion potential $V_{ee} = 1/r_{12}$. It allows us to artificially switch the electron interaction on ($\eta = 1$) and off ($\eta = 0$) at will, thereby assessing the role (or effect) of electron correlation on the strong-field dynamics.

3.2.2 . Many-electron TDSE

The TDSE, Eq. (3.7), is solved by the algorithm of Refs. [24] and [25]. The time-evolution operator is factorized into a product of a block-diagonal (or intra subspace) and off-diagonal (inter-subspace) parts associated with the Feshbach partitioning defined above. This factorization gives the following structure of the solutions to the partitioned TDSE, here written explicitly, (for t in one of the short time-slices $[t_{n-1}, t_n]$ into which the total time evolution is divided), in terms of the vectors $\underline{c}(t)$, $\underline{\gamma}(t)$ of CI coefficients $c_L(t)$ and $\gamma_{J^+,\vec{k}}(t)$,

$$\underline{c}(t) \;=\; \mathbb{U}_{QQ}\Big\{\mathbb{L}_0^-[\mathbb{L}_0^+]^{-1}\,\underline{c}(t_{n-1}) - i[\mathbb{L}_0^+]^{-1}\mathbb{H}_{QP}\,\underline{\gamma}(t_{n-1})\Big\} \tag{3.9a}$$

$$\underline{\gamma}(t) \;=\; \mathbb{U}_{PP}\Big\{\Big(\mathbb{I}_P - \frac{1}{2}\mathbb{H}_{PQ}[\mathbb{L}_0^+]^{-1}\mathbb{H}_{QP}\Big)\underline{\gamma}(t_{n-1}) + i[\mathbb{L}_0^+]^{-1}\,\underline{c}(t_{n-1})\Big\}. \tag{3.9b}$$

In this pair of equations, $\mathbb{H}_{QP}(=\mathbb{H}^{\dagger}_{PQ})$ is a $N_Q \times (n_k N_P)$ rectangular matrix, with elements

$$(\mathbb{H}_{QP})_{L,\{J^+,\vec{k}\}} = \langle L|\sum_i \vec{r}_i|J^+,\vec{k}\rangle.\vec{E}(t_n)\delta t, \tag{3.10a}$$

and $\mathbb{L}_0^{\pm}$ are $(N_Q \times N_Q)$ matrices defined by

$$\mathbb{L}_0^{\pm} = \mathbb{I}_Q \pm \frac{1}{4}\mathbb{H}_{QP}\mathbb{H}_{PQ}. \tag{3.10b}$$

$\mathbb{I}_{Q(P)}$ in the above is the unit matrix in the $Q(P)$ subspace. The parts containing the matrices $\mathbb{L}_0^{\pm}$ and $\mathbb{H}_{QP}$, $\mathbb{H}_{PQ}$ in Eqs. (3.9a) and (3.9b) correspond to the off-diagonal, inter-subspace propagator, whereas $\mathbb{U}_{QQ}$ and $\mathbb{U}_{PP}$ represent intra-subspace propagators.

In the basis of the CSFs $|L\rangle$ of the neutral molecule M $\equiv$ H_2, $\mathbb{U}_{QQ}$ is given by ($t \in [t_n, t_{n-1}]$)

$$\mathbb{U}_{QQ} = \exp\Big\{\{-i\mathbb{H}^M(t-t_{n-1})\}\Big\}, \tag{3.11}$$

while the propagator $\mathbb{U}_{PP}$ of the ionized system $M^+ \equiv \{H_2^+ + e^-\}$ is factorized approximately into the product of a propagator for the bound cation and one for the ionized electron

$$\mathbb{U}_{PP} = \exp\Big\{\{-i\mathbb{H}^{M+}(t-t_{n-1})\Big\}\} \otimes u^f(t,t_{n-1}). \tag{3.12}$$

In these equations $\mathbb{H}^X$ denotes the (time-dependent) Hamiltonian matrices describing the dynamics of the bound-states of the two-electron molecular system X, represented in the bound-CSF basis of that system. For H_2, it is a (3×3) matrix (in the basis of the bound CSF $|L\rangle$), while for the cation H_2^+ system, it is a (2×2) matrix in the basis of the bound CSFs J^+ of the cation, *i.e.* of the H_2^+ $\sigma_{g(u)}$ orbitals. The one-electron propagator $u^f(t,t_{n-1})$ describes the motion of the ionized electron in the combined action of the Coulomb forces of the ion and that of the field. Given that the strong-field effect is dominant, we use the well-known Volkov form of this propagator, [see Ref. [24] *e.g.*, for details], corresponding to the strong-field approximation (SFA) [45, 46].

The initial conditions used are given by

$$c_L(0) = c_L^{gs}(R), \tag{3.13a}$$

$$\gamma_{J^+,\vec{k}}(0) = 0,\ \forall\ J^+,\ \forall\ \vec{k}, \tag{3.13b}$$

where $c_L^{gs}(R)$ are the CI coefficients of the ground-state of the fully interacting two-electron neutral molecule at internuclear distance R, as obtained by diagonalizing the matrix representing the field-free Hamiltonian, i.e. $\hat{H}_{\eta}^{el}(R,t)$ of

Eq. (3.8a) with $\vec{\mathcal{F}} = 0$, and $\eta = 1$, in the CSF basis of the Q-subspace. In other words, the initial state is systematically constructed as the ground-state of H_2 described at the CISD (Configuration Interaction including Single and Double excitations) level with the 2-orbital active space described above.

The system then evolves under a two-cycle FWHM pulse, (for a total width of four cycles), of the form $\vec{\mathcal{F}} = \mathcal{F}(t)\,\hat{e}$, where $\hat{e}$ is a unit vector pointing in the (linear) polarization direction of the field, and where

$$\mathcal{F}(t) = \mathcal{F}_0\,\sin^2\!\left(\frac{\pi t}{\tau}\right)\cos(\omega t) \tag{3.14}$$

with a frequency $\omega = 2\pi\,c/\lambda$ corresponding to a wavelength λ ranging from 700 to 790 nm. The pulse duration (total width) is τ.

The novelty of the numerical simulations presented here lies in the introduction of the parameter $\eta(t)$ multiplying the electron repulsion potential $V_{ee} = 1/r_{12}$ in the Hamiltonian of Eq. (3.8a), more precisely in the intra-subspace parts $\hat{H}_{QQ}$, $\hat{H}_{PP}$ of this Hamiltonian. We will be comparing results of calculations with $\eta(t) = 1$ at all t, corresponding to the normal H_2 molecule with the two electrons fully interacting with each other, and those of calculations in which $\eta(t)$ is

$$\eta(t) = 1 - \frac{1}{1 + e^{-(12/d)(t-t_c)}}, \tag{3.15}$$

with the width parameter $d = 75$ a.u, (about three quarters of the optical cycle), chosen sufficiently long to make sure that no non-adiabatic effects in the time-resolved dynamics are induced by this V_{ee} switch-off process. The center of this sigmoïd, $t_c = 3\pi/2\omega$, is positioned at the second maximum of $\mathcal{F}(t)$. With this choice, the V_{ee} switch-off process comes into play when the field already acquires important amplitudes, so that the usual assumption of radiative interactions dominating electron correlation can be meaningfully tested. The calculations reported in the following use a two-dimensional k-grid defining the plane-wave basis. For a field polarized in the same z axis as the molecule alignment, the k_x grid contains $n_x = 600$ points with a step-size of $\delta k_x = 0.0314$ a.u while the k_z grid has $n_z = 400$ points.

From the propagated time-dependent CI coefficients $c_L(t)$ and $\gamma_{J^+,\vec{k}}(t)$, a number of observables can be calculated. The central one in the following is the final, total ionization probability.

First, let $|E_J\rangle = \sum_L D_{JL}|L\rangle$ describe the composition of the energy eigenstate $|E_J\rangle$ in terms of the CSF, as obtained by diagonalizing $\mathbb{H}_{QQ}$ at the initial time $t = 0$. Then the population of that energy eigenstate $|E_J\rangle$ can be calculated

from the $c_L(t)$'s by

$$P_{E_J}(t) = \sum_L |D^*_{LJ}\, c_L(t)|^2. \tag{3.16}$$

The channel-resolved ionization time-profile, *i.e.* the time-dependent probability of ionization into an ionic channel (ionic CSF) J^+, is defined by

$$\Gamma_{J^+}(t) \quad \propto \quad \int d^3\vec{k}\, |\gamma_{J^+,\vec{k}}(t)|^2 - \sum_{i=1}^{2} \left| \int d^3\vec{k}\, \langle\varphi_i|\vec{k}\rangle\, \gamma_{J^+,\vec{k}}(t) \right|^2 \tag{3.17}$$

where $\varphi_{1/2} = \sigma_{g/u}$. The total ionization probability is then the sum of all $\Gamma_{J^+}(t)$,

$$P_{ion}(t) = \sum_{J^+} \Gamma_{J^+}(t), \tag{3.18}$$

and the proportionality constant implicit in Eq. (3.17) is such that

$$P_{ion}(t) + \sum_L P_{E_L}(t) = 1$$

at all times. These definitions of channel-resolved and total ionization probabilities reflect the fact that the CI coefficients $\gamma_{J^+,\vec{k}}(t)$ refer to ionic CSF that are constructed with the non-orthonormal $\{\chi_{\vec{k}}\}$ continuum orbitals (orthogonalized plane-waves) basis, as defined in Eq. (3.2). However, since asymptotically, $|\chi_{\vec{k}}\rangle \to |\vec{k}\rangle$, the channel-resolved photoelectron asymptotic momentum distributions (spectra) are obtained directly from

$$f_{J^+}(\vec{k}) = |\gamma_{J^+,\vec{k}}(t_f)|^2. \tag{3.19}$$

3.3 . Results and discussions

Observables of two types could be used to identify deviations from expected SAE behaviors. In the following we will focus on scalar observables provided by the populations of various two-electron channels, both in the Q and the P subspaces, (*i.e.* neutral and ionic channels). Signatures of the same deviations from the SAE model found for vectorial observables, in photoelectron momentum spectra, will be presented and discussed in a forthcoming publication. The results will systematically be reported for three fixed internuclear distances corresponding to the equilibrium geometry, $R = 1.4$ a.u., a geometry corresponding to an elongated but bound (undissociated) molecule $R = 5.0$ a.u., and at a sufficiently large distance $R = 10.2$ a.u., where the molecule is almost dissociated. We wish to emphasize that, in all calculations, the two-electron multi-channel

wave packet is propagated starting from the same initial state of the molecular system, (cf. Eqs. (3.13a) and (3.13b)), precisely its fully correlated electronic ground state. While the radiative coupling of the molecule with the electromagnetic field is being introduced by the laser pulse, we adiabatically switch off the electron repulsion V_{ee}, *i.e.* we modulate the electronic correlation from its natural level at the considered geometry to zero. This allows us to check the validity of SAE approximation, and to find cases where electron correlation effects are in competition with strong field couplings.

The total ionization probability $P_{ion}(t_f)$ is displayed in Fig. 3.1, as a function of the laser pulse peak intensity, for three values of the carrier-wave frequency, corresponding to wavelengths λ within the interval $700 - 790$ nm. The figure is organized so that the dynamics with the electron interaction V_{ee} switched off is shown in the upper row, while the lower row pertains to the normal fully correlated dynamics. The laser polarization axis $\hat{e}$ is parallel to the internuclear axis.

The first observation that can be made is that the SAE approximation appears to fail in the case of ionization from H_2 in an elongated, non-dissociative geometry, as typified by the case $R = 5.0$ a.u., where the ionization probability shows a non-monotonous behavior for the fully correlated calculation (lower row), while it (the ionization probability) increases monotonously with the field intensity when the electron interaction is switched off. For $R = 1.4$ a.u. (equilibrium geometry) and $R = 10.2$ a.u. (dissociative limit), the ionization profiles in the correlated dynamics are rather smooth, monotonously growing with the laser peak intensity.

Let us now examine in detail how these results can be interpreted. A part of the interpretation is based on the Keldysh parameter for the identification of the dominant ionization mechanism underlying the situation in consideration, the other part is based on the energy positioning of the field-free energy levels with respect to various ionization thresholds. Let us review these two aspects.

The Keldysh parameter is defined as $\gamma = \sqrt{I_p/2U_p}$, where I_p is the ionization potential and $U_p = \mathcal{F}_0^2/(4\omega^2)$ is the ponderomotive energy, with $\mathcal{F}_0$ the maximum electric-field amplitude. Processes involving $\gamma \ll 1$ are commonly referred to as tunnel ionizations (TI), where the electron tunnels through and escapes from the barrier resulting from the field-distorted Coulomb nuclear attraction potential (in a quasi-static picture). In the opposite limit of $\gamma \gg 1$, the electron is thought to be ionized after absorption of several photons, *i.e.* by multiphoton ionization (MPI). Defining a borderline between TI and MPI, for values of the Keldysh parameter in the intermediate range $\gamma \sim 1$, is a challenging issue [47]. The value of γ therefore remains an indicator of the dominant mechanism, its increase

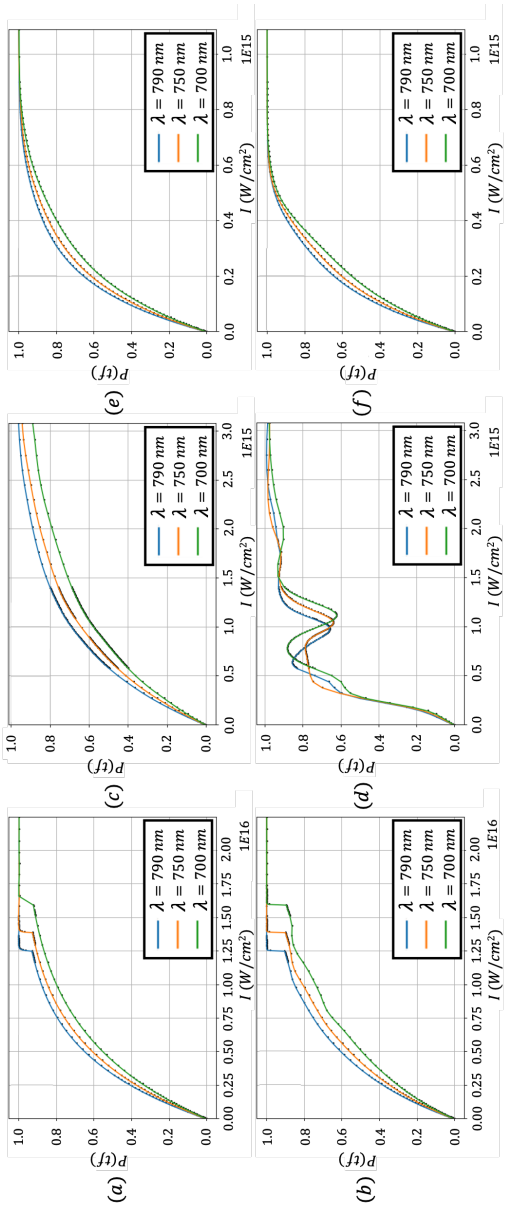

Figure 3.1: Total ionization probability profiles given as a function of the laser pulse leading intensity, for three excitation frequencies: $\lambda = 790\,$nm blue line, $\lambda = 750\,$nm orange line, and $\lambda = 700\,$nm green line. The first column [panels (a) and (b)] is for $R = 1.4\,$a.u., the second [panels (c) and (d)] for $R = 5.0\,$a.u., and the third [panels (e) and (f)] for $R = 10.2\,$a.u. The upper row [panels (a), (c) and (e)] corresponds to the adiabatic switch-off of V_{ee}, while the lower one [panels (b), (d) and (f)] is for the full dynamical calculation including the electron correlation.

R (au)	State	I_p (au)	I (W/cm^2)	γ	Mechanism
1.4	$\|E_1\rangle$	0.60	10^{15}	0.37	TI
			10^{16}	0.12	OBI
	$\|E_1^0\rangle$	1.25	10^{15}	0.53	
			10^{16}	0.16	TI
5.0	$\|E_1\rangle$	0.49	5×10^{14}	0.47	MPI
			3×10^{15}	0.19	
	$\|E_1^0\rangle$	0.75	5×10^{14}	0.59	MPI
			3×10^{15}	0.16	
10.2	$\|E_1\rangle$	0.52	10^{14}	1.09	MPI
			10^{15}	0.35	

Table 3.1: Keldysh parameter values γ for the three different molecular geometries $R = 1.4, 5.0$ and 10.2 a.u. In all cases, the ionization potential I_p corresponds to the energy of the two-electron molecule's ground state, ($|E_1\rangle$ in the fully correlated case, $|E_1^0\rangle$ in the uncorrelated case), relative to the threshold of the ionic channel $1^+ \leftrightarrow |\sigma_g, \vec{k}\rangle$. I are some selected laser peak intensities. The last column is an indication for the possible ionization mechanism (tunnel TI or multiphoton MPI) adopted for the interpretation.

signaling a change in mechanism from TI to MPI.

Table 3.1 collects the values of the Keldysh parameter for a number of important conditions as defined by specific values of the laser peak intensity and ionization potential I_p. The value of the latter depends on which initial bound state of the neutral molecule one is considering, in the presence or not of V_{ee}. For the three internuclear distances, the table actually considers the I_p of the molecule's ground state only, $|E_1\rangle$ with V_{ee} and $|E_1^0\rangle$ without V_{ee}. Note that I_p changes strongly with R, following closely the change in the degree of field-free electronic correlation.

3.3.1 . Equilibrium geometry

It is for the equilibrium geometry ($R = 1.4$ a.u.) that the value of the ionization potential is largest, advocating for an MPI reading in a modest intensity range. However, the laser intensities in play here lead to Keldysh parameters as small as $\gamma = 0.12$, and we can affirm that the ionization regime is mainly Tunnel Ionization (TI). The monotonous rise of the ionization probability as a function of the field intensity is reminiscent of ionization rate curves deriving from theories such as the ADK model [48], and is typical of tunnel ionization. However, one notes a striking probability jump at a wavelength-dependent critical intensity I_{cr} ($I_{cr} = 1.25\times10^{16}$ W/cm^2 for $\lambda = 790$ nm), as seen from Fig. 3.1. We interpret this

as marking the onset of an over-the-barrier ionization (OBI) mechanism [30], a natural high-intensity transformation of TI. In the simple static model, the barrier evoked is that created by the deformation of the nuclear Coulomb potential, with its two wells centered at $z = \pm R/2$, distorted by the radiative coupling. To estimate the barrier height, consider this distorted Coulomb potential along the laser polarization (z direction). Close to $z \simeq R/2$, neglecting the effect of the nucleus at $-R/2$, such a potential is given by

$$V(z) = -\frac{q_{\text{eff}}}{|z - R/2|} - z\mathcal{F}_0, \tag{3.20}$$

where q_{eff} represents an effective nuclear charge, (rather, a nuclear charge number), possibly representing a screening effect of V_{ee} in a simple, semi-empirical mean-field model. This produces a barrier of height $V_{max} = -2\sqrt{q_{\text{eff}}\mathcal{F}_0} - (R/2)\mathcal{F}_0$ positioned at $z_{max} = R/2 + \sqrt{q_{\text{eff}}/\mathcal{F}_0}$. For a critical intensity of 1.25×10^{16} W/cm^2 we get, from the naked Coulomb potential ($q_{\text{eff}} = 1$) with $R = 1.4$ a.u., a barrier height of $V_{max} = -1.9$ a.u, located at $z_{max} = 1.99$ a.u. This is to be compared with the ground state energy, $-I_p = -0.6$ a.u. with V_{ee} on, *i.e.* for the actual interacting electrons system, and $-I_p = -1.25$ a.u. without V_{ee}, *i.e.* for the a non-interacting two-electron molecule, as indicated in Table 3.1. The height of the barrier being well below the ground state energy, this explains the over-the-barrier ionization mechanism.

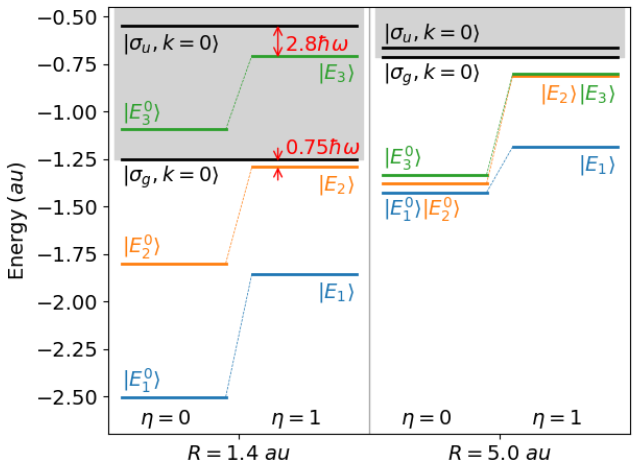

Figure 3.2: Field-free eigenenergies of H_2 with (right side labeled as $\eta = 1$) and without (left side labeled as $\eta = 0$) the electronic interaction potential V_{ee}, at the equilibrium $R = 1.4$ a.u. and extended $R = 5.0$ a.u. geometries. The origin of energies is taken as the second ionization threshold. The gray rectangles correspond to ionization from the first σ_g or σ_u channels.

This information on I_p can also be read from Fig. 3.2 which shows how the three lowest energy levels $|E_1\rangle$, $|E_2\rangle$ and $|E_3\rangle$ of the two-electron system are positioned depending on whether the electrons are considered interacting or not. For the non-interacting electronic system, the ground state is the CSF $|\sigma_g^2\rangle$ with an energy which is twice the σ_g orbital energy calculated by diagonalizing the strictly one-electron core Hamiltonian. On the other hand, for the actual interacting two-electrons system, the molecule's energy eigenstates are obtained in a full CI calculation, by diagonalizing the two-electron Hamiltonian matrix in the CSF basis, within the $\{\sigma_g, \sigma_u\}$ active space. This gives

$$|E_1\rangle = -0.99\,|\sigma_g^2\rangle + 0.06\,|\sigma_u^2\rangle \tag{3.21a}$$

$$|E_2\rangle = |\sigma_g^1\sigma_u^1\rangle \tag{3.21b}$$

$$|E_3\rangle = 0.06\,|\sigma_g^2\rangle + 0.99\,|\sigma_u^2\rangle \tag{3.21c}$$

at the equilibrium geometry. The state $|E_1\rangle$ is almost a pure CSF, being dominated by $|\sigma_g^2\rangle$. It is this fact that confers to the situation at $R = 1.4$ a.u its qualification as a weak-correlation situation. It may come as a surprise that when including the electron repulsion $V_{ee} = 1/r_{12}$ we see a large shift in the ground-state energy (a strong reduction of I_p), and yet electron correlation is said to be weak. In this respect, it is important to recall that correlation is to be understood as the correction from the Hartree-Fock limit, where a part of V_{ee} was already included as a mean field (Coulomb and exchange integrals) [49], so that the orbital energies are different from the $V_{ee} = 0$ values. Thus this large shift seen in Fig. 3.2 is mainly due to the inclusion of V_{ee} as a mean-field in the HF limit.

Returning to our discussion, with the I_p quoted above, it can be concluded that, with or without V_{ee}, the ground electronic state $|E_1\rangle$ is already well above the barrier for tunnel ionisation. Actually, using the expression of V_{max} given above, a laser field intensity of 4×10^{15} W/cm^2 would be sufficient to lower the barrier for the OBI mechanism to operate with respect to ionization from the (correlated) ground state $|E_1\rangle$. The observed critical intensity for the onset of OBI is three times this. There are many reasons for this: (i) The laser electric field being oscillatory, the static model fails when considering the ionization process only at the maximum intensity reached within an optical cycle, and the actual barrier would be, in average, higher than the calculated V_{max}. (ii) The Coulomb potential should take into account the presence of the second well located at $z = -R/2$. (iii) The screening effect of the second electron should also be introduced. In addition to these corrections that would affect the barrier height by increasing its value, one should also consider corrections that would affect the energy positioning of $|E_1\rangle$. The most important is the radiative Stark effect that would lower the molecular orbital energy level by a non-negligible amount, roughly equal to $-\mathcal{F}_0 R/2 \simeq -0.44$ a.u.

Concerning the two points (ii) and (iii) made above, we have actually conducted a simple investigation and found that the second nuclear Coulomb attraction center, at $z = -R/2$, with $R = 1.4$ a.u., tends to lower the barrier down, while a screening factor q_{eff} estimated by $q_{\text{eff}}^2 = E_1/E_1^0 = 0.6/1.25 \simeq 0.5$, in the spirit of the Quantum Defect Theory [50], would have an opposite effect, raising the barrier height to a somewhat larger value. Figure 3.3 shows the distorted Coulomb potential obtained, at $R = 1.4$ a.u., with $q_{\text{eff}} = 1$ and an intensity of 1.25×10^{16} W/cm^2. The ground-state energies E_1 (interacting electrons) and E_1^0 (non-interacting electrons system), placed with respect to the σ_g ionization threshold, are indicated by the dotted horizontal line in green and the dashed line in magenta respectively. Thus, taking $|E_1\rangle$ as the initial state, we will be way above the barrier for TI, at this value of $\mathcal{F}_0$, corresponding to the critical intensity observed for $\lambda = 790$ nm. Adding the Stark shift would give an effective I_p of $\simeq 1$ a.u., which is still 0.9 a.u. above the barrier. The cycle-averaging of the barrier height is thus the only remaining effect that can explain the higher critical intensity found in the calculations.

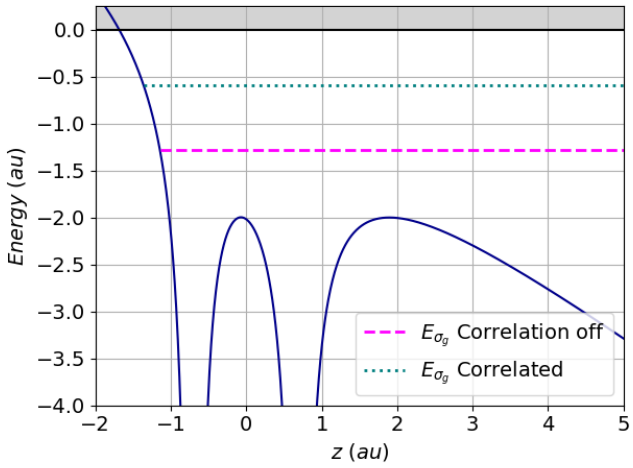

Figure 3.3: Field-distorted Coulomb potential, as defined by Eq. (3.20), with $R = 1.4$ a.u., $q_{eff} = 1$ and $\mathcal{F}_0$ corresponding to an intensity of 1.25×10^{16} W/cm^2. The ground state level at $-I_p$ is indicated by the green dotted and the magenta dashed horizontal lines, respectively for the calculations with and without electron repulsion.

Another observation to be accounted for is the frequency dependence of the critical intensity marking the onset of OBI. Figure 3.1 shows that a higher critical intensity is required when the field frequency increases. From a time-dependent viewpoint, one can argue that, since the potential barrier oscillates at the field frequency, for the lowest frequency ($\lambda = 790$ nm), corresponding to the longest oscillation period $T = 2\pi/\omega$, the barrier would stay lowered longer, and a low

critical intensity $I_c = 1.25 \times 10^{16}$ W/cm^2 would be required for OBI to set in, since this intensity is felt on a longer duration. On the other hand, a higher frequency ($\lambda = 700$ nm) corresponds to a faster oscillating barrier, offering less chance for ionization by OBI.

3.3.2 . Elongated geometries

Turning now to elongated geometries, we will focus on two typical examples, namely $R = 5.0$ a.u. and $R = 10.2$ a.u. The ionization potential I_p for the ground state decreases progressively as R increases. One notes that the field intensity, I_{sat}, where the ionization probabilities saturates to $\simeq 1$, also decreases. Actually, as can be seen from Fig. 3.1, I_{sat} is, at these elongated geometries, an order of magnitude less than at the equilibrium geometry implying smaller ponderomotive energies at saturation, and a generally larger Keldysh parameter. As seen in Table 3.1, $\gamma \simeq 0.5$, for an intensity $I = 5 \times 10^{14}$ W/cm^2 at $R = 5.0$ a.u., and $\gamma \simeq 1.1$, for $I = 10^{14}$ W/cm^2 at $R = 10.2$ a.u. Such values correspond to an intermediate regime for the Keldysh parameter, and an MPI interpretation of the processes in consideration is possible.

The profile of the ionization probability $P_{ion}(t_f)$ as a function of the field intensity exhibits, at $R = 5.0$ a.u, an intriguing behavior around $I = 5 \times 10^{14}$ W/cm^2, in the fully correlated dynamics (cf. Fig. 3.1, panel (d)). The total ionization probability follows at first a smooth rising curve at low intensity, to deviate from this curve at around 3×10^{14} W/cm^2, exhibiting from then on a rather strong oscillatory pattern (localized around $0.5 - 1.5 \times 10^{15}$ W/cm^2). This behavior is not observed in the uncorrelated (V_{ee} switched off) case (shown on panel (c) of Fig. 3.1), for which the ionization regime is TI at high intensity. It is not observed either in the dissociative limit, $R = 10.2$ a.u. It appears to be correlated with the degree of excitations to the bound excited states, $|E_j\rangle, j = 2, 3$, which in the correlated system are found much closer to the ionization thresholds than in the non-interacting electrons system, (cf. Fig. 3.4). We will see that these excitations are extinguished completely at $R = 10.2$ a.u.

The energy diagram for the lowest three energy eigenstates is displayed in Fig. 3.4, together with the first $|\sigma_g, k = 0\rangle$ and second $|\sigma_u, k = 0\rangle$ ionization thresholds. The full CI calculation in field-free condition gives the composition of these energy eigenstates at $R = 5.0$ a.u as

$$|E_1\rangle = -0.79\,|\sigma_g^2\rangle + 0.61\,|\sigma_u^2\rangle \quad \text{(3.22a)}$$

$$|E_2\rangle = |\sigma_g^1 \sigma_u^1\rangle \quad \text{(3.22b)}$$

$$|E_3\rangle = -0.61\,|\sigma_g^2\rangle - 0.79\,|\sigma_u^2\rangle \quad \text{(3.22c)}$$

Contrary to what is observed in the case of the equilibrium geometry (Eqs. (3.21a) to (3.21c)), we have an important configuration mixing, a signature of a strong electron correlation. The expansion coefficients in Eq. (3.22a) denote an uneven (asymmetric) distribution of population among the configurations σ_g^2 and σ_u^2 in $|E_1\rangle$, the σ_g^2 configuration still dominating at 64%.

At this range of R, the symmetry allowed $\sigma_g \leftrightarrow \sigma_u$ transition dipole moments in $z-$linear polarization, acquires important values, (it is well known that it increases linearly with R, and this is confirmed by the preparatory *ab initio* calculations), and the ground state $|E_1\rangle$ is directly and strongly coupled to the first excited state $|E_2\rangle$. The excitation of this state, which is the configuration $\sigma_g^1\sigma_u^1$, either from the $|\sigma_g^2\rangle$ or $|\sigma_u^2\rangle$ components of the ground state $|E_1\rangle$, instantly debalances this initial state in its CI content, amounting to populating (suddenly) the other excited state $|E_3\rangle$ as well, by the same multiphoton process that has prepared $|E_2\rangle$.

This dynamics of laser-driven excitation among the bound states is well illustrated by Fig. 3.5, panel (b), which shows the time evolution, during the $I = 10^{15}$ W/cm^2, $\lambda = 790$ nm laser pulse, of the populations of the energy eigenstates at $R = 5.0$ a.u, to be compared to the same bound-states dynamics for the $R = 1.4$ a.u in panel (a). In the equilibrium geometry, the two bound states that have appreciable populations during the pulse are $|E_1\rangle$ and $|E_2\rangle$. Their populations oscillate in phase with the field oscillations, with only the ground state population exhibiting a decay in the mean, due to ionization. In contrast, at $R = 5.0$ a.u, all three eigenstates are populated appreciably, with the populations of $|E_2\rangle$ and $|E_3\rangle$ of equal magnitude and tracking each other, throughout the pulse, and all three decay in the mean. Superimposed on this mean decay curve denoting the ionization out of the designated eigenstate, one notes population oscillations or rather beating at two frequencies, the lowest being $\omega_{32} = E_3 - E_2$, the highest $\omega_{31} = E_3 - E_1$. The fact that the bound-state dynamics is strongly driven by the two states $|E_1\rangle$ and $|E_3\rangle$ is further seen in the dynamics of the bound CSFs.

Fig. 3.6 shows, for the $\lambda = 790$ nm case, the populations $|c_I(t)|^2, (I = 1, 2, 3)$ of these CSFs as a function of time for $I = 6.25 \times 10^{14}$ W/cm^2, and $I = 10^{15}$ W/cm^2, corresponding to a maximum and minimum in the ionization probability profile of Fig. 3.1, panel (d). In the two cases, the populations of the two CSFs σ_g^2 and σ_u^2 that compose $|E_1\rangle$ and $|E_3\rangle$ exhibit very strong oscillations in phase opposition at the two frequencies identified above. In all, these results show clearly how strongly and coherently the two excited states $|E_2\rangle$ and $|E_3\rangle$ are accessed from the ground state, giving a dynamics that is strongly dependent on the excitation energies $E_j - E_1,\ j = 2, 3$ (6-7 photons) and the difference between them, $E_3 -$

E_2. We will come back to this Fig. 3.6 later, to discuss how comparing panels (a) and (b) can explain the different ionization yields at these two intensities.

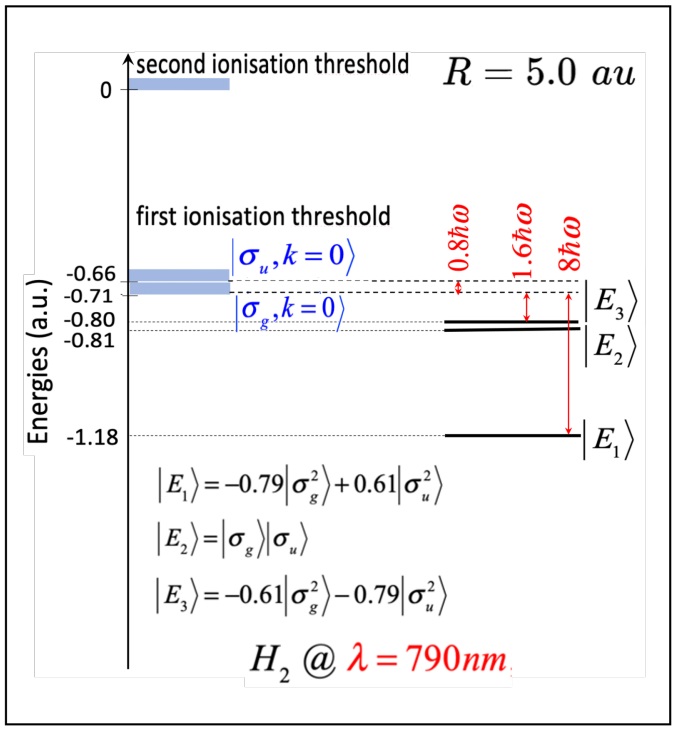

Figure 3.4: Field-free eigenenergies of H_2 at $R = 5.0$ au (solid thick black lines) and the ionization thresholds (thick blue rectangles and dashed black lines). The origin of energies is taken as the second ionization threshold. Indicated in thin red arrows are the number of ($\lambda = 790$ nm) photons needed to ionize.

The interpretation we have in mind for the observed oscillatory behavior in the ionization probability profile, in the case $R = 5.0$ a.u, is based on a Fano [51] type picture, involving two interfering routes. While the initial population on $|E_1\rangle$ can be ionized (by TI) directly, it can also be first transferred on $|E_2\rangle$ through a seven-photon absorption process. An additional photon is sufficient to ionize the molecule from $|E_2\rangle$ to the $|\sigma_g, \chi_k\rangle$ channel. With two photons, the ionization would ionize the system to the $|\sigma_u, \chi_k\rangle$ channel instead. This route is a Resonance-Enhanced-Multiphoton-Ionization (REMPI) [52]. Else, the state $|E_3\rangle$ can also be populated strongly once $|E_2\rangle$ is, (recall Fig. 3.5). From $|E_3\rangle$, which is composed of the same CSF as $|E_1\rangle$, we may also have a single-photon (two-photon) ionization to the $\sigma_g(\sigma_u)$ ionic channel. We are thus facing a situation with two field-dressed resonances (E_2 and E_3), close in energy and decaying into the same ionization continua $|\sigma_g(\sigma_u), \chi_k\rangle$. These overlapping resonances have almost the same energy (real part of the complex resonance energy), but dif-

ferent widths. We can expect that one of these resonances have a much larger width than the other one[1]. Referring to the discussion to be found in the following paragraph, we can identify the resonance with the largest width as an ionic doorway state, while the stabilizing resonance is a covalent state. Now, these resonance states with energies and widths defined within the Floquet representation [53, 54], would be transported adiabatically in time during the time-development of the pulse envelope. Through non-Abelian Berry phases associated with this adiabatic transport [55], these overlapping resonances may thus interfere with each other to give an intensity-dependent ionization rate: some intensities would lead to the ionic doorway state (more ionizing) being more populated at pulse-end, some others to the preponderance of the covalent (less ionizing) state, producing the Stückelberg-type oscillations [56] in the ionization profiles of Fig. 3.1, panel (d). We have assumed adiabatic transport of the resonances under the pulse. Given the relatively short duration of the pulse, we expect non-adiabatic effects to be non-negligible both on the rising and the descending sides of the pulse. These could further impact the resonance population dynamics, again in a strongly intensity-dependent manner.

It is also important to note that in the absence of electron correlation this specific resonance overlapping mechanism cannot happen. This is clear from Fig. 3.2, where the lowest three eigenstates, $|E_1^0\rangle$, $|E_2^0\rangle$, $|E_3^0\rangle$, are seen well separated, and lie much lower in energy, beside the fact that in compositions, they are pure CSFs, completely different from the fully correlated states $|E_1\rangle$, $|E_3\rangle$ which denote strong mixing of CSFs.

An alternative explanation, in a time-dependent semi-classical approach, can also be attempted using the electron trajectory view of the three-step rescattering mechanism [57]. At such a geometry, the intensity and frequency dependent ionized electron quiver radius is roughly comparable to the size of the elongated molecule. In other words, contrary to the situation where the ionized electron feels an almost point-like molecule, (the case at $R = 1.4$ a.u), or one where it rather sees two almost separated, also point-like atoms (the case at $R = 10.2$ a.u), in the case of an intermediate elongated geometry, the electron trajectory would somehow remain within a “cage of the molecule", not being able to leave it. This could explain at least an ionization quenching, as observed at certain values of the field intensity. Actually that extended “cage of the molecule" exists only in so far as it corresponds to the covalent elongated molecule, *i.e.* the covalent part of the initial correlated wavefunction at $R = 5.0$ a.u. That wave-

[1] One can think of the same effect in this electron (ionization) dynamics as the one which gives rise to Zero-Width Resonances (ZRW) in the context of vibrational, i.e laser-driven dissociation dynamics [53].

function has an ionic part (which would tend asymptotically to a H^- + H^+ dissociation state), for which the system again reduces to a point-like two-electron H^- anion accompanied by a bare proton. That ionic part is known to be a doorway state for enhanced ionization (CREI) of this two-electron molecule [39, 40]. It could be increased or decreased by a time-dependent admixture of the excited $|E_2\rangle$, $|E_3\rangle$ states. The dominance of the ionic or covalent component, during the time-dependent dynamics at certain intensity could give rise to an enhancement or a quenching of the ionization probability, as observed.

This can be clearly seen in Fig. 3.6. We first note that only the CSFs $|1\rangle \equiv |\sigma_g^2\rangle$ and $|3\rangle \equiv |\sigma_u^2\rangle$ can give an asymptotically covalent configuration $1s_A 1s_B$, where $1s_{A(B)}$ denotes a Heitler-London, or rather Coulson-Fischer orbital of Valence-Bond theory [41] that becomes the $1s$ atomic orbital centered on proton H_A or H_B. A purely covalent state is attained when the oscillating populations of these two CSFs are equal, i.e. when the time-profiles of their populations cross each other. It is clear, from perusal of Fig. 3.6, that at $I = 10^{15}$ W/cm^2, this state acquires a higher population in average, (giving a stabilization with respect to ionization), than at $I = 6.25 \times 10^{14}$ W/cm^2. In both panels, the coherent fast oscillations of the populations of CSFs $|1\rangle$ and $|3\rangle$ would give roughly a small average contribution, to the (asymptotically) ionic configuration ($1s_A^2 + 1s_B^2$) at both intensities. This contribution is to be added to the contribution of CSF $|2\rangle \equiv |\sigma_g \sigma_u\rangle$ whose population clearly rises to larger average values during the pulse at $I = 6.25 \times 10^{14}$ W/cm^2, the intensity of a maximum in the ionization probability profile of Fig. 3.1, panel (d), than at $I = 10^{15}$ W/cm^2, where $P_{ion}(t_f)$ is at a minimum.

To summarize, just as for the interpretation in terms of resonance interferences discussed above, the strong electron correlation plays a central role in this alternative interpretation. This electron correlation is already manifest through the strong CI mixing in the initial state, perturbed by field-driven excitations to $|E_2\rangle$.

3.3.3 . Dissociation limit

For the largest internuclear distance $R = 10.2$ a.u, we are practically in the dissociative limit. The electron correlation is strongest, as testified by the CI composition of the three two-electron eigenstates

$$|E_1\rangle = -0.71\,|\sigma_g^2\rangle + 0.71\,|\sigma_u^2\rangle \quad (3.23a)$$

$$|E_2\rangle = |\sigma_g^1 \sigma_u^1\rangle \quad (3.23b)$$

$$|E_3\rangle = -0.71\,|\sigma_g^2\rangle - 0.71\,|\sigma_u^2\rangle \quad (3.23c)$$

featuring equal (even) but anti symmetric contributions of the CSFs $|\sigma_g^2\rangle$ and $|\sigma_u^2\rangle$ to the ground-state. The configuration mixing is maximal, denoting the highest electron correlation effect. The energy diagram of Fig. 3.7 suggests that an even stronger resonances overlap situation should occur, as the levels $|E_2\rangle$ and $|E_3\rangle$ are closer than for $R = 5.0$ a.u. Yet the ionization probability profiles are smooth curves, monotonously increasing with the field intensity. No oscillations due to resonances overlap is observed. This can be understood by the fact that the transition dipole moments μ_{12} from $|E_1\rangle$ to $|E_2\rangle$ vanishes identically, due to the anti-symmetric contributions of the $|\sigma_g^2\rangle$ and $|\sigma_u^2\rangle$ CSFs to $|E_1\rangle$. Indeed, using Condon-Slater rules in Ref. [49], p.321, it can easily be shown that

$$\langle \sigma_g^1 \sigma_u^1 | \mu | \sigma_g^2 \rangle = \langle \sigma_g^1 \sigma_u^1 | \mu | \sigma_u^2 \rangle \tag{3.24}$$

so that

$$\mu_{12} \propto \Big[\langle \sigma_g^1 \sigma_u^1 | \mu | \sigma_g^2 \rangle - \langle \sigma_g^1 \sigma_u^1 | \mu | \sigma_u^2 \rangle) \Big] = 0. \tag{3.25}$$

No transition to the excited states is thus possible, and the ionization is a direct 9-photon ionization or tunnel ionization from the ground-state only. The interference process we are referring to for the intermediate internuclear distance $R = 5.0$ a.u. no longer holds, and the ionization profile smoothly increases without any oscillation, saturating for an intensity close to 7×10^{14} W/cm^2.

A number of remarks ought to be made at this point. First, the apparent lack of excitation at the dissociative limit in the fully correlated calculation is due to the fact that, within the simplified model considered, as resulting from the choice of the minimal orbital active space, the ground state is that of a H atom located either at $\pm R/2$, and that in this model, H has only one orbital, $1s$. In a complete model, the parallel laser field can give transition to higher lying states of the atom, (e.g. $2p_z$), corresponding to the dissociative limit of higher energy MOs. These are simply not included (intentionally) in the active space of the present model. Without excitation to $|E_2\rangle$ or $|E_3\rangle$ possible from the $|E_1\rangle$, ionization at $R = 10.2$ a.u. can occur only from the ground state, and corresponds to tunnel ionization or 9-photon ionization from the $1s$ atomic orbital. With V_{ee} switched off, we have exactly the same tunnel ionization from the same initial state as in the fully correlated case, hence the transferability of the ionization profiles from one case to another, as seen on the last column of Fig. 3.1. The effect of electron correlation to produce an energy level scheme among which laser-induced excitations correspond to interfering REMPI processes and/or overlapping and interacting multiphoton ATI (Above-Threshold Ionization) [58] resonances, giving rise to non-monotonous ionization vs. intensity profiles, is only seen in elongated geometries not too close to the dissociative limit. This non-monotonous

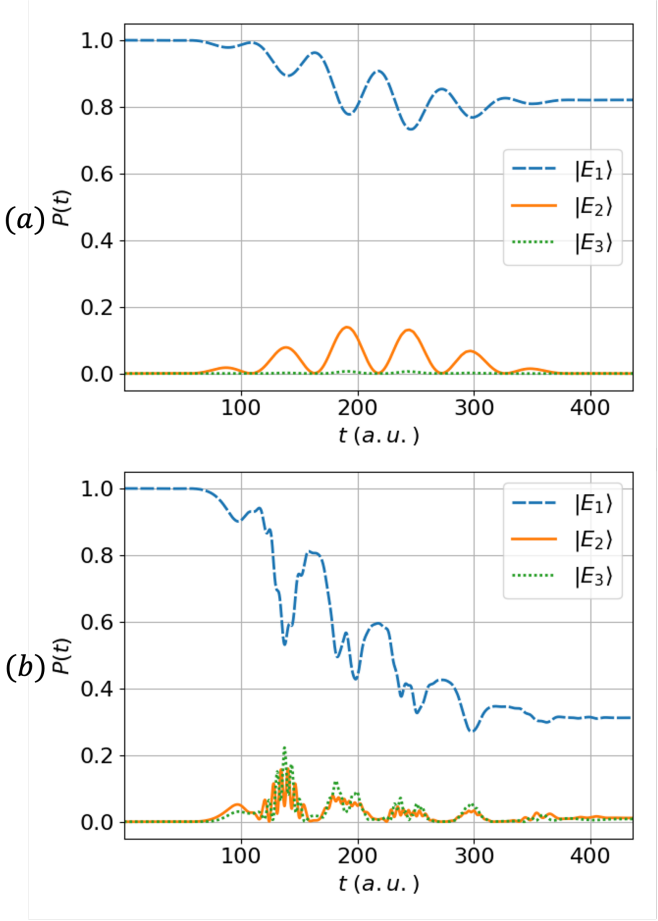

Figure 3.5: Time evolution, during the $I = 10^{15}$ W/cm^2, $\lambda = 790$ nm laser pulse, of the populations of the energy eigenstates at (a) $R = 1.4$ a.u., and (b) $R = 5.0$ a.u.

ionization probability profile deviates strongly from a single electron TI profile and constitutes a clear signature of a non-SAE behavior.

3.3.4 . Experimental considerations

How to experimentally observe the non trivial behavior of the ionization probabilities at an elongated (but non-dissociative geometry) as a function of the field intensity? Our primary purpose here has been to understand how strong electronic correlation could modulate the strong-field ionization dynamics. The simplicity of the model used here, with the nuclear motion frozen and the electronic excitation dynamics reduced to its essential elements, helps in this respect. We have, in particular, shown that strong Stückelberg type of oscillations are present at $R = 5.0$ a.u. The same oscillations in the intensity profile of the

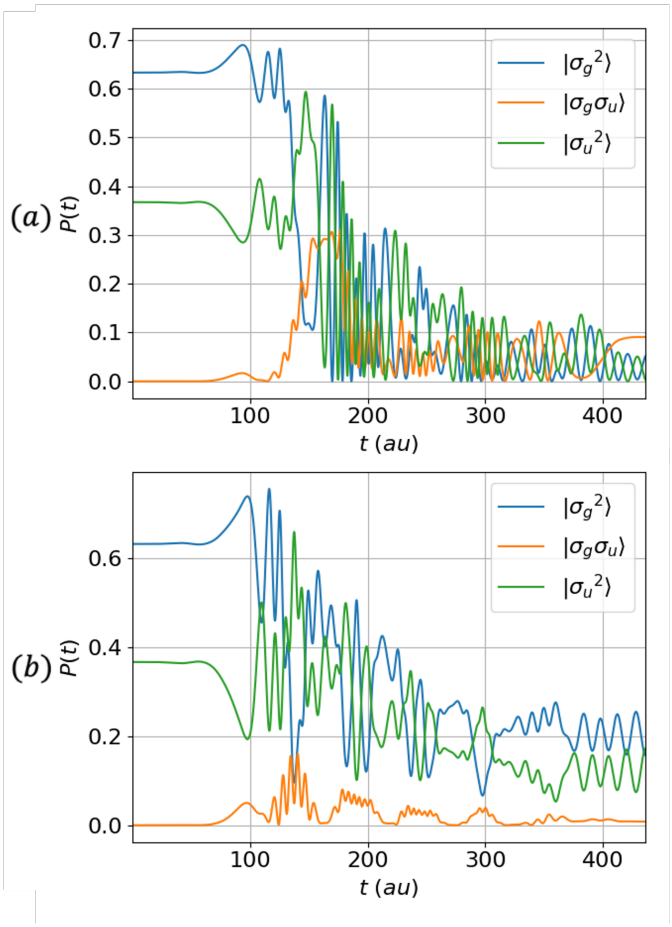

Figure 3.6: Time evolution of the populations of CSFs $|\sigma_g^2\rangle$, $|\sigma_g\sigma_u\rangle$ and $|\sigma_u^2\rangle$ of H_2 at $R = 5.0$ a.u during a $\lambda = 790$ nm laser pulse, at (a) $I = 6.25 \times 10^{14}$ W/cm^2, where ionization is enhanced, and (b) $I = 1.00 \times 10^{15}$ W/cm^2, where ionization is quenched.

ionization probability are found, although with different amplitudes, for other values of R (in the range $4 - 6$ a.u.) that have also been considered in our calculations (not showed here). This electron-correlation driven behavior of the ionization dynamics is thus not an artifact of the case $R = 5.0$ a.u that was discussed in length in the text. That it does not appear in the strongest correlation case at $R = 10.2$ a.u is due to the extinction of the coupling between the correlated ground and excited states, an interference effect, as it is conditioned by the opposite phases of the $|\sigma_g^2\rangle$ and $|\sigma_u^2\rangle$ components of the ground state. As the electron-correlation driven behavior of the ionization probability typified by the $R = 5.0$ a.u case appears to set in as soon as one departs from R_{eq} in the higher R range, it would be encountered to some extend during the vibrational motion of the molecule. Thus the non-monotonous variation of $P_{ion}(t_f)$ with

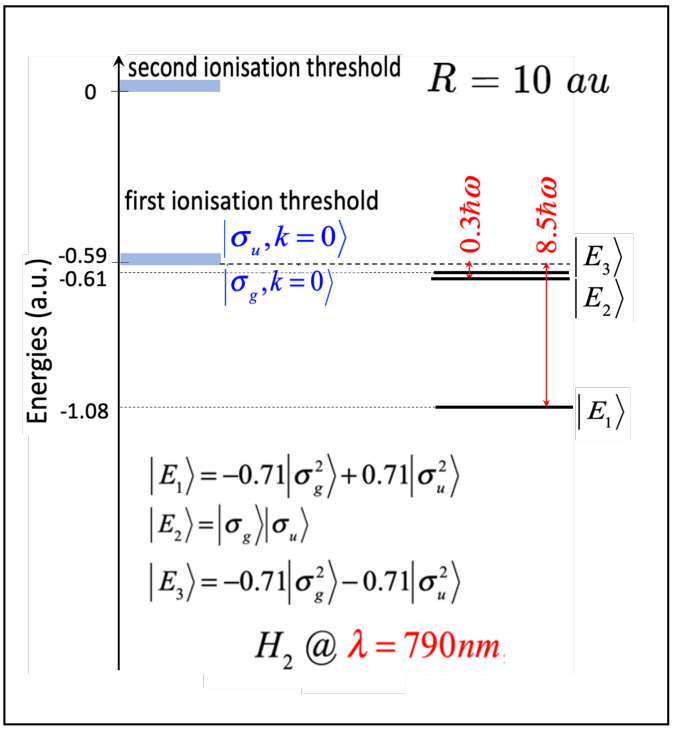

Figure 3.7: Same as for figure (3.4) but for the internuclear distance $R = 10.2$ a.u.

I, though expected to be weaker within the support of the vibrational ground state of the molecule, and somewhat washed out by the averaging over the vibrational motion, may still be observable. This remains to be assessed by more detailed calculations, including vibrational motions.

We can also imagine that the range of large values of R, where the oscillations in $P_{ion}(t_f)$ *vs.* I are strong, could be accessed by a Raman vibrational excitation of the molecule, using a first laser pulse operating in the XUV (pump pulse). With a proper time-delay, the NIR laser as considered here, (probe pulse), can then interrogate the ionization dynamics at an elongated geometry. It is to be noted that a vibrational excitation exceeding the $v = 10$ level of H_2 would be necessary to expect an average value of R reaching 5.0 a.u. and beyond.

Still another way to prepare the molecule in an elongated geometry is to exploit long-range and long-lived scattering Feshbach resonances resulting from a bound state embedded in the translational energy continuum, associated with the laser-controlled collision between a pair of free H atoms [53]. We have recently studied such laser bound H_2^+ molecules (LBM) in the context of laser cooling [59]. It was shown that such a laser bound quasi-stable hydrogen molecular system LBM (as opposite to the usual chemically bound molecule CBM), can be

obtained using a THz laser with a wavelength of $\lambda = 25\,\mu$m and an intensity of about 3 GW/cm^2. The associated wavefunction has a spatial extension which can grow up to an average internuclear distance $\langle R \rangle \simeq 13$ a.u.

These schemes for probing the molecule's ionization dynamics at an elongated but non-dissociative geometry, in a strong correlation regime, can become more interesting if we can record in coincidence photoelectron spectra taken at a sub-femtosecond time scale and providing a snapshot of the molecule undergoing dissociation. Such channel-resolved photoelectron or LIED spectra, if emanating strictly from a single molecular orbital, as implied by the SAE [5, 60], would exhibit equally spaced interference fringes from which the internuclear distance R can be inferred. In addition, this fringe pattern comes with a definite, clear nodal structure that is a signature of the molecular orbital from which the photoelectron is ionized [60–62]. The part of our research dealing with these photoelectron spectra, within the thematic of the present work (correlation effects in strong-field ionization), shows that, precisely at $R = 5.0$ a.u., this pattern of equidistant interference fringes is shifted and distorted, and the nodal structure blurred as the photoelectron spectrum carries the signature of a multi-orbital ionization. The detailed analysis of these spectra, with a comparison with those associated with the SAE, or a non-correlated dynamics, is too long to be presented here, and exceeds the scope of the present paper. It will be presented in a separate contribution. It suffices to say that observation of this non-SAE signature in the channel-resolved photoelectron or LIED spectra in coincidence with the observation of a non-monotonous behaviour of the total ionization probability as a function of the field intensity would suffice to establish this electron-correlation driven ionization dynamics.

3.4 . Conclusions

We have set out to explore possible manifestations of the limit of the SAE approximation in the description of the intense-field ionization of H_2. To this end, we used a model of the molecule in a finite function basis, as customarily done in Quantum Chemistry, specifically the 6-31G** basis set. It corresponds to a time-dependent version of a quantum chemical full-CI representation with an active space of two-electron CSFs spanned by the most relevant molecular orbitals, the charge-resonance pair σ_g and σ_u. The TDCI (with Feshbach partitioning) algorithm that we have access to [24, 25] allows one to solve the many-electron TDSE, here with the possibility of tuning at will the electron correlation, through the introduction of an adiabatic switching-off of the two-electron interaction potential V_{ee}. The effect of switching off this interaction depends on the strength of

electron correlation and this depends on R. We have focused on three values of R typical of three regions of progressively increasing electron correlation. The equilibrium one $R = 1.4$ a.u, an elongated geometry $R = 5.0$ a.u, and a geometry at the dissociation limit $R = 10.2$ a.u.

The observable we have addressed is the total ionization probability profile as a function of the field intensity. This profile follows a regular and nearly smooth increasing behavior, both at the equilibrium geometry and at the dissociative limit. A sudden probability jump in the highest range of the field intensity, is observed however at $R = 1.4$ a.u. This sudden increase of the total ionization probability is interpreted as the onset of an over-the-barrier ionization regime. The most striking observation is however found in an elongated, (but not dissociative), geometry, such as $R \simeq 5$ a.u. There, the total ionization probability profile exhibits a non-monotonous behavior, passing through a rise to a maximum then a dip, denoting a partial quenching of the ionization, at some moderate intensity, the value of which depends on the field frequency. The value of the Keldysh parameter for ionization out of the ground-state then pertains to the intermediate regime ($\gamma \sim 0.5$), indicating a possible competition between tunnel and multiphoton ionizations. We provide an interpretation of this non-monotonous variation of $P_{ion}(t_f)$ with I, referring to an interference mechanism among two overlapping resonances, corresponding to the autoionization of a pair of dressed excited states, reached by a multi-photon REMPI process. Note that this interpretation is based on considerations of the correlation-dependent molecular energy spectrum, where the positions of the excited states with respect to the ionization threshold matter as well as the strong transition moments linking them to the ground state.

Acknowledgments

Dr. O. Atabek passed away on 27 June 2022. He was the most ardent proponent of the present study of electron correlation effects through an artificial switching-off of the electron repulsion. The interpretation of the results of Sec. 3.3.2 of the present article is based on the experience of Dr. Atabek with Zero-Width Resonances (ZWR) (Refs. [53] and [60]). Dr. O. Atabek was a great mentor for J.-N.V., and a most enthusiastic, insightful collaborator to us all in this endeavor.

Jean-Nicolas Vigneau is grateful to the French MESRI (French Ministry of Higher Education, Research and Innovation) for funding his PhD grant through a scholarship from EDOM (Ecole Doctorale Ondes et Matière, Université Paris-Saclay,

France). JNV also acknowledges partial funding from the Choquette Family Foundation - Mobility Scholarship and the Paul-Antoine Giguère Scholarship. Numerical calculations conducted in Canada used HPC resources of the Compute Canada and Calcul Québec Consortia (group CJT-923). This work was also performed using HPC resources from the "Mésocentre" computing center of CentraleSupélec and École Normale Supérieure Paris-Saclay supported by CNRS and Région Île-de-France. We finally acknowledge the use of the computing cluster MesoLum/GMPCS of the LUMAT research federation (FR 2764 at Centre National de la Recherche Scientifique). T.T.N.D. acknowledges partial funding of this research by the Natural Science and Research Council of Canada (NSERCC) through grant 05369-2015.

Data Availability Statement

The data that support the findings of this study are available from the corresponding author upon request.

Bibliography

[1] M. Y. Ivanov, M. Spanner, and O. Smirnova. Anatomy of strong field ionization. *J. Mod. Opt.*, 52(2-3):165–184, 2005. URL: https://www.tandfonline.com/doi/abs/10.1080/0950034042000275360, doi:10.1080/0950034042000275360.

[2] M. Lewenstein, Ph. Balcou, M. Yu. Ivanov, Anne L'Huillier, and P. B. Corkum. Theory of high-harmonic generation by low-frequency laser fields. *Phys. Rev. A*, 49:2117–2132, Mar 1994. URL: https://link.aps.org/doi/10.1103/PhysRevA.49.2117, doi:10.1103/PhysRevA.49.2117.

[3] P. M. Paul, E. S. Toma, P. Breger, G. Mullot, F. Augé, Ph. Balcou, H. G. Muller, and P. Agostini. Observation of a train of attosecond pulses from high harmonic generation. *Science*, 292(5522):1689–1692, 2001. URL: https://www.science.org/doi/abs/10.1126/science.1059413, doi:10.1126/science.1059413.

[4] T. Zuo, A.D. Bandrauk, and P.B. Corkum. Laser-induced electron diffraction: a new tool for probing ultrafast molecular dynamics. *Chem. Phys. Lett.*, 259(3):313–320, 1996. URL: https://www.sciencedirect.

com/science/article/abs/pii/0009261496007865?via%3Dihub, doi:10.1016/0009-2614(96)00786-5.

[5] M. Peters, T. T. Nguyen-Dang, C. Cornaggia, S. Saugout, E. Charron, A. Keller, and O. Atabek. Ultrafast molecular imaging by laser-induced electron diffraction. *Phys. Rev. A*, 83:051403, May 2011. URL: https://link.aps.org/doi/10.1103/PhysRevA.83.051403, doi:10.1103/PhysRevA.83.051403.

[6] R. Puthumpally-Joseph, J. Viau-Trudel, M. Peters, T.-T. Nguyen-Dang, O. Atabek, and E. Charron. Inversion of strong-field photoelectron spectra for molecular orbital imaging. *Phys. Rev. A*, 94:023421, 2016. URL: https://link.aps.org/doi/10.1103/PhysRevA.94.023421, doi:10.1103/PhysRevA.94.023421.

[7] G. Porat, G. Alon, S. Rozen, O. Pedatzur, M. Krüger, D. Azoury, A. Natan, G. Orenstein, B. D. Bruner, M. J. J. Vrakking, and N. Dudovich. Attosecond time-resolved photoelectron holography. *Nat. Commun.*, 9(1):2805, 2018. URL: https://www.nature.com/articles/s41467-018-05185-6, doi:10.1038/s41467-018-05185-6.

[8] G. Sansone, F. Calegari, and M. Nisoli. Attosecond technology and science. *J. Sel. Top. Quantum Electron.*, 18(1):507–519, 2012. URL: https://ieeexplore.ieee.org/document/6012549, doi:10.1109/JSTQE.2011.2153181.

[9] M. Nisoli, P. Decleva, F. Calegari, A. Palacios, and F. Martín. Attosecond electron dynamics in molecules. *Chem. Rev.*, 117(16):10760–10825, 2017. URL: https://pubs.acs.org/doi/10.1021/acs.chemrev.6b00453, doi:10.1021/acs.chemrev.6b00453.

[10] M. Awasthi, Y. V. Vanne, A. Saenz, A. Castro, and P. Decleva. Single-active-electron approximation for describing molecules in ultrashort laser pulses and its application to molecular hydrogen. *Phys. Rev. A*, 77:063403, Jun 2008. URL: https://link.aps.org/doi/10.1103/PhysRevA.77.063403, doi:10.1103/PhysRevA.77.063403.

[11] A. Schild and E. K. U. Gross. Exact single-electron approach to the dynamics of molecules in strong laser fields. *Phys. Rev. Lett.*, 118:163202, Apr 2017. URL: https://link.aps.org/doi/10.1103/PhysRevLett.118.163202, doi:10.1103/PhysRevLett.118.163202.

[12] A. I. Pegarkov, E. Charron, and A. Suzor-Weiner. Nonlinear single and double ionization of molecules by strong laser pulses.

J. Phys. B: At., Mol. Opt. Phys., 32(14):L363–L369, jul 1999. URL: https://iopscience.iop.org/article/10.1088/0953-4075/32/14/104, doi:10.1088/0953-4075/32/14/104.

[13] Z. Zhao and T. Brabec. Tunnel ionization in complex systems. *J. Modern Optics*, 54:981, May 2007. URL: https://www.tandfonline.com/doi/abs/10.1080/09500340601043413, doi:10.1080/09500340601043413.

[14] B. Zhang, Y. Yuan, and Z. Zhao. Dynamic core polarization in strong-field ionization of CO molecules. *Phys. Rev. Lett.*, 111:163001, October 2013. URL: https://journals.aps.org/prl/abstract/10.1103/PhysRevLett.111.163001, doi:10.1103/PhysRevLett.111.163001.

[15] V.-H. Hoang, S. B. Zhao, V.-H. Le, and A.-T. Le. Influence of permanent dipole and dynamic core-electron polarization on tunneling ionization of polar molecules. *Phys. Rev. A*, 95:023407, 2017. URL: https://link.aps.org/doi/10.1103/PhysRevA.95.023407, doi:10.1103/PhysRevA.95.023407.

[16] S. Ohmura, H. Ohmura, T. Kato, and H. Kono. Manipulation of multielectron dynamics of molecules by fourier-synthesized intense laser pulses: Effective potential analysis of CO. *Front. Phys.*, 9:9:677671, July 2021. URL: https://journals.aps.org/prl/abstract/10.1103/PhysRevLett.111.163001, doi:10.1103/PhysRevLett.111.163001.

[17] J. Zanghellini, M. Kitzler, T. Brabec, and A. Scrinzi. Testing the multi-configuration time-dependent Hartree–Fock method. *J. Phys. B: At. Mol. Opt. Phys.*, 37(4):763–773, jan 2004. URL: https://iopscience.iop.org/article/10.1088/0953-4075/37/4/004, doi:10.1088/0953-4075/37/4/004.

[18] M. Nest, T. Klamroth, and P. Saalfrank. The multiconfiguration time-dependent Hartree–Fock method for quantum chemical calculations. *J. Chem. Phys.*, 122(12):124102, 2005. URL: https://pubs.aip.org/aip/jcp/article-abstract/122/12/124102/950720/The-multiconfiguration-time-dependent-Hartree-Fock?redirectedFrom=fulltext, doi:10.1063/1.1862243.

[19] T. Kato and H. Kono. Time-dependent multiconfiguration theory for describing molecular dynamics in diatomic-like molecules. *Chem. Phys. Lett.*, 392:533, 2004. URL: http://ac.els-cdn.com/S0009261404008243/1-s2.0-S0009261404008243-main.pdf?_tid=df0c110a-f934-11e2-a539-00000aab0f6c&acdnat=1375201805_831cca1bb91b0d7743a195701e7c42c5.

[20] T. T. Nguyen-Dang, M. Peters, S. M. Wang, E. Sinelnikov, and F. Dion. Nonvariational time-dependent multiconfiguration self-consistent field equations for electronic dynamics in laser-driven molecules. *J. Chem. Phys.*, 127(17):174107, 2007. URL: https://pubs.aip.org/aip/jcp/article-abstract/127/17/174107/958719/Nonvariational-time-dependent-multiconfiguration?redirectedFrom=fulltext, doi:10.1063/1.2774979.

[21] H. B. Schlegel, S. M. Smith, and X. Li. Electronic optical response of molecules in intense fields: Comparison of TD-HF, TD-CIS, and TD-CIS(D) approaches. *J. Chem. Phys.*, 126(24):244110, 2007. URL: https://pubs.aip.org/aip/jcp/article-abstract/126/24/244110/295899/Electronic-optical-response-of-molecules-in?redirectedFrom=fulltext, doi:10.1063/1.2743982.

[22] N. Rohringer, A. Gordon, and R. Santra. Configuration-interaction-based time-dependent orbital approach for ab initio treatment of electronic dynamics in a strong optical laser field. *Phys. Rev. A*, 74(4):043420, 2006. URL: https://link.aps.org/doi/10.1103/PhysRevA.74.043420, doi:10.1103/PhysRevA.74.043420.

[23] P. Krause, T. Klamroth, and P. Saalfrank. Time-dependent configuration-interaction calculations of laser pulse driven many-electron dynamics: Controlled dipole switching in lithium cyanide. *J. Chem. Phys.*, 123(7):074105, 2005. URL: https://pubs.aip.org/aip/jcp/article-abstract/122/12/124102/950720/The-multiconfiguration-time-dependent-Hartree-Fock?redirectedFrom=fulltext, doi:10.1063/1.1862243.

[24] T. T. Nguyen-Dang and J. Viau-Trudel. Multicomponent dynamics of coupled quantum subspaces and field-induced molecular ionizations. *J. Chem. Phys.*, 139(24):244102, 2013. URL: http://aip.scitation.org/doi/10.1063/1.4849755, doi:10.1063/1.4849755.

[25] T.-T. Nguyen-Dang, E. Couture-Bienvenue, J. Viau-Trudel, and A. Sainjon. Time-dependent quantum chemistry of laser driven many-electron molecules. *J. Chem. Phys.*, 141(24):244116, 2014. URL: https://pubs.aip.org/aip/jcp/article-abstract/141/24/244116/915500/Time-dependent-quantum-chemistry-of-laser-driven?redirectedFrom=fulltext, doi:10.1063/1.4904102.

[26] J. L. Sanz-Vicario, H. Bachau, and F. Martín. Time-dependent theoretical description of molecular autoionization produced by femtosecond xuv laser

pulses. *Phys. Rev. A*, 73:033410, Mar 2006. URL: https://link.aps.org/doi/10.1103/PhysRevA.73.033410, doi:10.1103/PhysRevA.73.033410.

[27] A. Palacios, H. Bachau, and F. Martín. Step-ladder Rabi oscillations in molecules exposed to intense ultrashort VUV pulses. *Phys. Rev. A*, 74:031402, Sep 2006. URL: https://link.aps.org/doi/10.1103/PhysRevA.74.031402, doi:10.1103/PhysRevA.74.031402.

[28] A. Palacios, J. L. Sanz-Vicario, and F. Martín. Theoretical methods for attosecond electron and nuclear dynamics: applications to the H_2 molecule. *J. Phys. B: At., Mol. Opt. Phys.*, 48(24):242001, 2015. URL: https://iopscience.iop.org/article/10.1088/0953-4075/48/24/242001, doi:10.1088/0953-4075/48/24/242001.

[29] C. F. Pauletti, E. Coccia, and E. Luppi. Role of exchange and correlation in high-harmonic generation spectra of H_2, N_2, and CO_2: Real-time time-dependent electronic-structure approaches. *J. Chem. Phys.*, 154(1):014101, 2021. URL: https://pubs.aip.org/aip/jcp/article-abstract/154/1/014101/307830/Role-of-exchange-and-correlation-in-high-harmonic?redirectedFrom=fulltext, doi:10.1063/5.0033072.

[30] V. S. Popov. Tunneling and above-barrier ionization of atoms in a laser radiation field. *J. Exp. Theor. Phys.*, 91(1):48–66, 2000. URL: https://link.springer.com/article/10.1134/1.1307233, doi:10.1134/1.1307233.

[31] H. Lischka, R. Shepard, I. Shavitt, R. M. Pitzer, M. Dallos, Th. Müller, P. G. Szalay, F. B. Brown, R. Ahlrichs, H. J. Böhm, A. Chang, D. C. Comeau, R. Gdanitz, H. Dachsel, C. Ehrhardt, M. Ernzerhof, P. Höchtl, S. Irle, G Kedziora, T. Kovar, V. Parasuk, M. J. M. Pepper, P. Scharf, H. Schiffer, M. Schindler, M. Schüler, M. Seth, E. A. Stahlberg, J.-G. Zhao, S. Yabushita, Z. Zhang, M. Barbatti, S. Matsika, M. Schuurmann, D. R. Yarkony, S. R. Brozell, E. V. Beck, J.-P. Blaudeau, M. Ruckenbauer, B. Sellner, F. Plasser, and J. J. Szymczak. Columbus, an ab initio electronic structure program, release 7.0, 2015.

[32] R. Shepard. *Ab-Initio Methods in Quantum Chemistry*, volume II. John Wiley and Sons, Inc., New York, 1986.

[33] A. Giusti-Suzor, F. H. Mies, L. F. DiMauro, E. Charron, and B. Yang. Dynamics of H_2^+ in intense laser fields. *J. Phys. B: At. Mol. Opt. Phys.*, 28(3):309–339, Feb 1995. doi:10.1088/0953-4075/28/3/006.

[34] A. Giusti-Suzor, X. He, O. Atabek, and F. H. Mies. Above-threshold dissociation of H_2^+ in intense laser fields. *Phys. Rev. Lett.*, 64:515–518, Jan 1990.

URL: https://link.aps.org/doi/10.1103/PhysRevLett.64.515, doi:10.1103/PhysRevLett.64.515.

[35] G. Jolicard and O. Atabek. Above-threshold-dissociation dynamics of H_2^+ with short intense laser pulses. *Phys. Rev. A*, 46:5845–5855, Nov 1992. URL: https://link.aps.org/doi/10.1103/PhysRevA.46.5845, doi:10.1103/PhysRevA.46.5845.

[36] A. Giusti-Suzor and F. H. Mies. Vibrational trapping and suppression of dissociation in intense laser fields. *Phys. Rev. Lett.*, 68:3869–3872, Jun 1992. URL: https://link.aps.org/doi/10.1103/PhysRevLett.68.3869, doi:10.1103/PhysRevLett.68.3869.

[37] T. Zuo and A. D. Bandrauk. Charge-resonance-enhanced ionization of diatomic molecular ions by intense lasers. *Phys. Rev. A*, 52:R2511–R2514, Oct 1995. URL: https://link.aps.org/doi/10.1103/PhysRevA.52.R2511, doi:10.1103/PhysRevA.52.R2511.

[38] A. D. Bandrauk and J. Ruel. Charge-resonance-enhanced ionization of molecular ions in intense laser pulses: Geometric and orientation effects. *Phys. Rev. A*, 59:2153–2162, Mar 1999. URL: https://link.aps.org/doi/10.1103/PhysRevA.59.2153, doi:10.1103/PhysRevA.59.2153.

[39] I. Kawata, H. Kono, Y. Fujimura, and A. D. Bandrauk. Intense-laser-field-enhanced ionization of two-electron molecules: Role of ionic states as doorway states. *Phys. Rev. A*, 62:031401, Aug 2000. URL: https://link.aps.org/doi/10.1103/PhysRevA.62.031401, doi:10.1103/PhysRevA.62.031401.

[40] K. Harumiya, H. Kono, Y. Fujimura, I. Kawata, and A. D. Bandrauk. Intense laser-field ionization of H_2 enhanced by two-electron dynamics. *Phys. Rev. A*, 66:043403, Oct 2002. URL: https://link.aps.org/doi/10.1103/PhysRevA.66.043403, doi:10.1103/PhysRevA.66.043403.

[41] S. Shaik, D. Danovich, and P. C. Hiberty. On the nature of the chemical bond in valence bond theory. *J. Chem. Phys.*, 157(9):090901, 09 2022. URL: https://pubs.aip.org/aip/jcp/article/157/9/090901/2841680/On-the-nature-of-the-chemical-bond-in-valence-bond, arXiv:https://pubs.aip.org/aip/jcp/article-pdf/doi/10.1063/5.0095953/18026532/090901_1_5.0095953.pdf, doi:10.1063/5.0095953.

[42] H. Feshbach. Unified theory of nuclear reactions. *Ann. Phys.*, 5(4):357–390, 1958. URL: https://www.sciencedirect.com/science/article/pii/0003491658900071, doi:10.1016/0003-4916(58)90007-1.

[43] P.-O. Löwdin. Studies in perturbation theory. iv. solution of eigenvalue problem by projection operator formalism. *J. Math. Phys.*, 3(5):969–982, 1962. URL: http://link.aip.org/link/?JMP/3/969/1, doi:10.1063/1.1724312.

[44] W. H. Adams. Correction of configuration-interaction wavefunctions by perturbation theory. *J. Chem. Phys.*, 45(9):3422–3424, 1966. URL: https://pubs.aip.org/aip/jcp/article-abstract/45/9/3422/210699/Correction-of-Configuration-Interaction?redirectedFrom=fulltext, doi:10.1063/1.1728122.

[45] L. V. Keldysh. Ionization in the field of a strong electromagnetic wave. *Sov. Phys. JETP*, 20(5):1307–1314, 1965.

[46] H. R. Reiss. Effect of an intense electromagnetic field on a weakly bound system. *Phys. Rev. A*, 22:1786–1813, 1980. URL: https://link.aps.org/doi/10.1103/PhysRevA.22.1786, doi:10.1103/PhysRevA.22.1786.

[47] R. Wang, Q. Zhang, D. Li, S. Xu, P. Cao, Y. Zhou, W. Cao, and P. Lu. Identification of tunneling and multiphoton ionization in intermediate keldysh parameter regime. *Opt. Express*, 27(5):6471–6482, Mar 2019. URL: http://opg.optica.org/oe/abstract.cfm?URI=oe-27-5-6471, doi:10.1364/OE.27.006471.

[48] M.V. Ammosov, N.B. Delone, and V.P. Krainov. Tunnel ionization of complex atoms and of atomic ions in an alternating electromagnetic field. *Sov. Phys. JETP*, 64:1191, 1986.

[49] I. N. Levine. *Quantum Chemistry, 7th ed.* Pearson, NJ, USA, 2014.

[50] M. J. Seaton. Quantum defect theory i. general formulation. *Proc. Phys. Soc.*, 88(4):801–814, aug 1966. URL: https://iopscience.iop.org/article/10.1088/0370-1328/88/4/302, doi:10.1088/0370-1328/88/4/302.

[51] U. Fano. Effects of configuration interaction on intensities and phase shifts. *Phys. Rev.*, 124:1866–1878, Dec 1961. URL: https://link.aps.org/doi/10.1103/PhysRev.124.1866, doi:10.1103/PhysRev.124.1866.

[52] L. Zandee and R. B. Bernstein. Resonance-enhanced multiphoton ionization and fragmentation of molecular beams: NO, I_2, benzene, and butadiene. *J. Chem. Phys.*, 71(3):1359–1371, 1979. URL: https://pubs.aip.org/aip/jcp/article-abstract/71/3/1359/458927/Resonance-enhanced-multiphoton-ionization-and?redirectedFrom=fulltext, doi:10.1063/1.438436.

[53] O. Atabek, R. Lefebvre, C. Lefebvre, and T. T. Nguyen-Dang. Intense-field zero-width resonances and control of molecular photodissociation. *Phys. Rev. A*, 77:043413, 2008. URL: https://journals.aps.org/pra/abstract/10.1103/PhysRevA.77.043413, doi:10.1103/PhysRevA.77.043413.

[54] T. T. Nguyen-Dang, C. Lefebvre, H. Abou-Rachid, and O. Atabek. Floquet representation of absolute phase and pulse-shape effects on laser-driven molecular photodissociation. *Phys. Rev. A*, 71:023403, 2005. URL: https://journals.aps.org/pra/abstract/10.1103/PhysRevA.71.023403, doi:10.1103/PhysRevA.71.023403.

[55] M. V. Berry. Quantal phase factors accompanying adiabatic changes. *Proc. R. Soc. A*, 392:45, 1984. URL: https://journals.aps.org/pra/abstract/10.1103/PhysRevA.78.052109, doi:10.1103/PhysRevA.78.052109.

[56] E. C. G. Stückelberg. Theory of inelastic collisions between atoms. *Helv. Phys. Acta*, 5:369–423, 1932.

[57] P. B. Corkum. Plasma perspective on strong field multiphoton ionization. *Phys. Rev. Lett.*, 71:1994–1997, Sep 1993. URL: https://link.aps.org/doi/10.1103/PhysRevLett.71.1994, doi:10.1103/PhysRevLett.71.1994.

[58] J. H. Eberly, J. Javanainen, and K. Rzążewski. Above-threshold ionization. *Phys. Rep.*, 204(5):331–383, 1991. URL: https://www.sciencedirect.com/science/article/pii/0370157391901315, doi:https://doi.org/10.1016/0370-1573(91)90131-5.

[59] R. Lefebvre and O. Atabek. Progress toward full optical control of ultracold-molecule formation: Role of scattering feshbach resonances. *Phys. Rev. A*, 101:063406, Jun 2020. URL: https://link.aps.org/doi/10.1103/PhysRevA.101.063406, doi:10.1103/PhysRevA.101.063406.

[60] R. Puthumpally Joseph. *Quantum Interferences in the Dynamics of Atoms and Molecules in Electromagnetic Fields*. Theses, Université Paris-Saclay, 2016. URL: https://tel.archives-ouvertes.fr/tel-01301505.

[61] R. Puthumpally-Joseph, J. Viau-Trudel, M. Peters, T.-T. Nguyen-Dang, O. Atabek, and E. Charron. Laser-induced electron diffraction: inversion of photo-electron spectra for molecular orbital imaging. *Mol. Phys.*, 115(15-16):1889–1897, 2017. URL: https://www.tandfonline.com/doi/full/10.1080/00268976.2017.1290837, doi:10.1080/00268976.2017.1290837.

[62] T.-T. Nguyen-Dang, M. Peters, J. Viau-Trudel, E. Couture-Bienvenue, R. Puthumpally-Joseph, E. Charron, and O. Atabek. Laser-induced electron

diffraction: alignment defects and symmetry breaking. *Mol. Phys.*, 115(15-16):1934–1943, 2017. URL: https://www.tandfonline.com/doi/full/10.1080/00268976.2017.1317858, doi:10.1080/00268976.2017.1317858.

Annex to: Strong-Field Molecular Ionization Beyond the Single Active Electron Approximation

To verify that the REMPI effect observed at an elongated internuclear distance was not an isolated case for $R = 5.0$ a.u., calculations for the H_2 molecule for two values of R around this distance, $R = 4.0$ and $R = 6.0$ a.u., were also analyzed. The profiles of the total ionization probability vs. field-intensity are shown in Fig. A3.1, along with the corresponding results at the internuclear distances included in the article, i.e. at $R = 1.4$, $R = 5.0$ and $R = 10.2$ a.u.

Neglecting electronic correlation, the single ionization BO dynamics at the new elongated geometries bear the same λ and R dependencies as shown in the article. Higher field wavelengths, implying longer dynamics durations, (as all the simulations were conducted for a total of four optical cycles), require lower intensities to reach ionization saturation to H_2^+. The saturation intensity is also shifted towards lower values as the internuclear distance is increased.

Results shown also adhere to the physical description of the frequency and intensity dependent enhancement and quenching of the ionization. Elongated but non-dissociative distances increases the correlation between $|\sigma_g^2\rangle$ and $|\sigma_u^2\rangle$ compositions of the eigenstates and their energy states, hence amplifying Fano resonances given specific parameters of the field, while also admitting constructive interferences between the phases due to the remaining differences in the composition of the said eigenstates. It can be seen in Fig. A3.1h that once the internuclear distance reaches values where the compositions of the CSFs in the eigenstates reach relatively close proportions in $|\sigma_g^2\rangle$ and $|\sigma_u^2\rangle$, the amplification of the ionization is not as powerful as it was with shorter internuclear distances, which can be attributed to destructive interference between phases of the wave packets once promoted to excited and ionized states. Indeed, the proportions

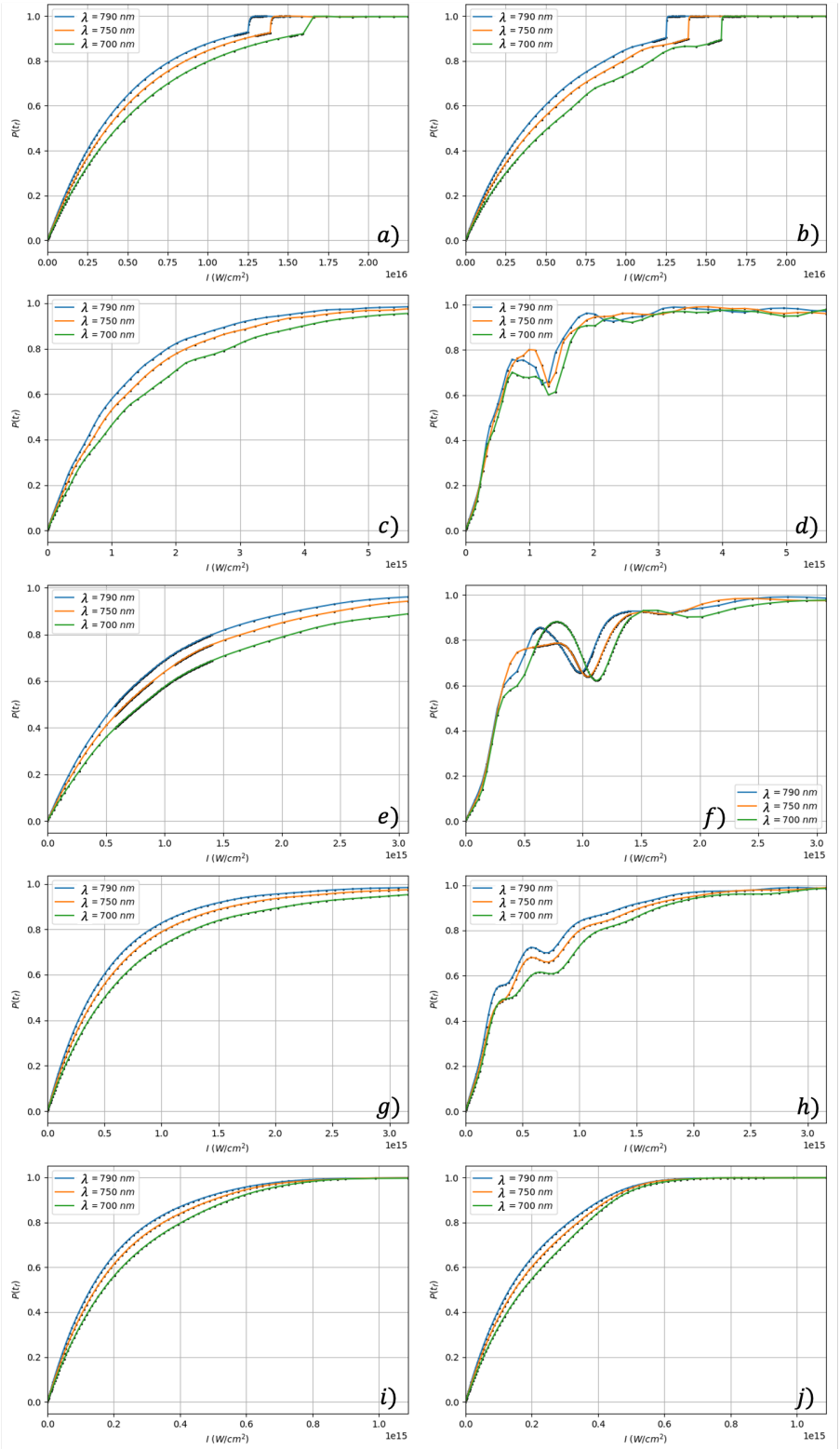

Figure A3.1: Ionization probability as a function of the peak intensity at $\lambda = 790$ nm (blue), 750 nm (orange), and 700 nm (green). The first row [(a), (b)] is for $R = 1.4$ a.u., the second [(c) , (d)] for $R = 4.0$ a.u., the third [(e) , (f)] for $R = 5.0$ a.u., the fourth [(g), (h)] for $R = 6.0$ a.u., and the fifth [(i) , (j)] for $R = 10.2$ a.u. The left column corresponds to the adiabatic switch-off of V_{ee}, while the right one is for the full dynamical calculation including V_{ee}.

of $|\sigma_g^2\rangle$ and $|\sigma_u^2\rangle$ pass from

$$|E_1^{(R=4.0\,a.u.)}\rangle = -0.87\,|\sigma_g^2\rangle + 0.49\,|\sigma_u^2\rangle \quad \text{(A3.1a)}$$
$$|E_2^{(R=4.0\,a.u.)}\rangle = |\sigma_g^1\sigma_u^1\rangle \quad \text{(A3.1b)}$$
$$|E_3^{(R=4.0\,a.u.)}\rangle = -0.49\,|\sigma_g^2\rangle - 0.87\,|\sigma_u^2\rangle \quad \text{(A3.1c)}$$

at $R = 4.0\,a.u.$ to

$$|E_1^{(R=6.0\,a.u.)}\rangle = -0.75\,|\sigma_g^2\rangle + 0.66\,|\sigma_u^2\rangle \quad \text{(A3.2a)}$$
$$|E_2^{(R=6.0\,a.u.)}\rangle = |\sigma_g^1\sigma_u^1\rangle \quad \text{(A3.2b)}$$
$$|E_3^{(R=6.0\,a.u.)}\rangle = -0.66\,|\sigma_g^2\rangle - 0.75\,|\sigma_u^2\rangle \quad \text{(A3.2c)}$$

at $R = 6.0\,a.u.$, a near-equal distribution of the CSFs population made possible by the narrowing of the gap between energies of the eigenstates, a phenomenon visually depicted in Fig. A3.2.

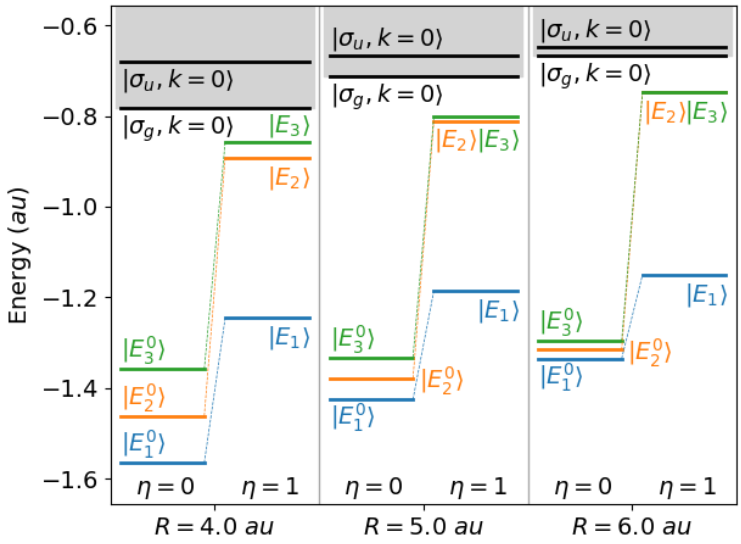

Figure A3.2: Field-free eigenenergies of H_2 with (right side labeled as $\eta = 1$) and without (left side labeled as $\eta = 0$) the electronic interaction potential V_{ee}, at the extended geometries $R = 4.0$, $R = 5.0$ and $R = 6.0$ a.u. The origin of energies is taken as the second ionization threshold. The gray rectangles correspond to ionization from the first σ_g or σ_u channels.

As can be seen in Fig. A3.1, the ionization enhancement events shown in the article at intensities $I = 6.0 \times 10^{14}$ and 1.4×10^{15} W/cm^2 for a wavelength of

790 nm at $R = 5.0$ a.u., are now shifted to higher intensities $I = 8.0 \times 10^{14}$ and 1.9×10^{15} W/cm^2 at $R = 4.0$ a.u., and lower intensities $I = 6.0 \times 10^{14}$ and 1.0×10^{15} W/cm^2 at $R = 6.0$ a.u. The same applies to the quenching events: the most remarkable ionization restraint, centered at $I = 1.0 \times 10^{15}$ W/cm^2 for the elongated model geometry $R = 5.0$ a.u. at $\lambda = 790$ nm, is shifted to $I = 1.2 \times 10^{15}$ W/cm^2 for $R = 4.0$ a.u. and to $I = 7.0 \times 10^{14}$ W/cm^2 for $R = 6.0$ a.u.

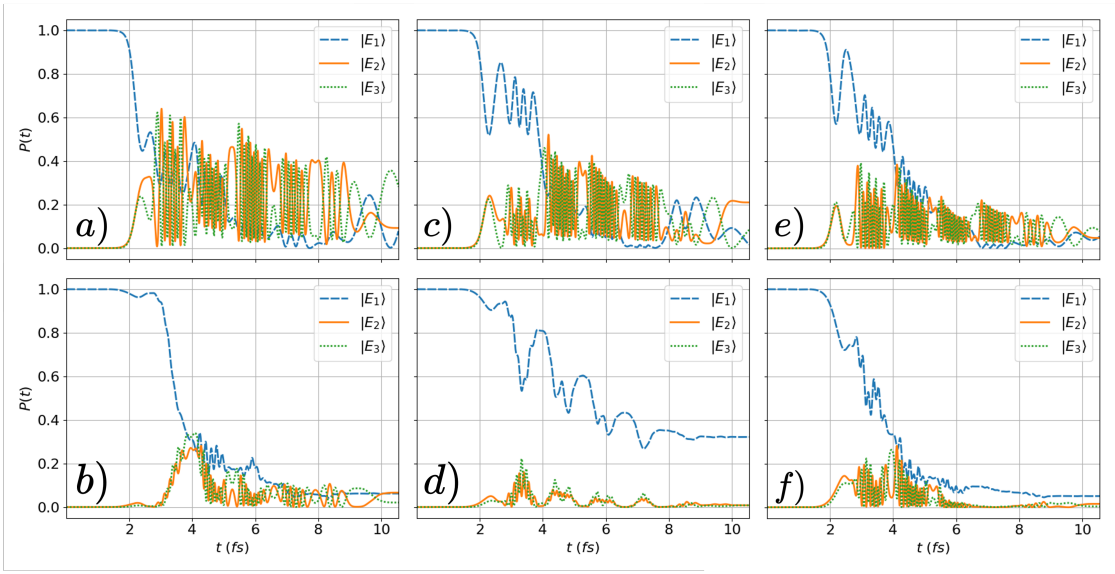

Figure A3.3: Energy eigenstate populations evolution during the $\lambda = 790$ nm laser pulse at $R = 5.0$ a.u., for dynamics with electronic correlation switched off in the upper row (a, c and e) and kept fully correlated in the lower row (b, d and f), at intensities $I = 6.67 \times 10^{14}$ W/cm^2 in the left column (a and b), $I = 1.00 \times 10^{15}$ W/cm^2 in the middle column (c and d) and $I = 1.50 \times 10^{15}$ W/cm^2 in the right column (e and f). Left and right columns show populations evolution during REMPI-induced enhancement of the ionization, and the middle column shows dynamics of a quenched ionization.

These shifts in intensity can be explained by taking a look at the field-free eigenenergies diagram of H_2, added for internuclear distances $R = 4.0, 5.0$ and $6.0\, a.u.$ in Fig. A3.2. While all geometries dynamics including electron correlation require approximately 8 photons to reach the first ionization barrier from their fundamental state, it is only when eigenenergies of excited eigenstates $|E_2\rangle$ and $|E_3\rangle$ are close —which is to say that the internuclear distance is at its longest while still involving constructive interference during electronic dynamics— that the Fano resonance is amplified. From the initial, ground state, the molecule can either excite to $|E_2\rangle$ and/or $|E_3\rangle$ simultaneously or sequentially to reach one of the two ionic states $|\sigma_g, \kappa\rangle$ or $|\sigma_u, \kappa\rangle$. Furthermore, paths are more diversified at longest R values as ionic states threshold get closer to one another, hence the direct

ionization to $|\sigma_u, \kappa\rangle$ becoming a more reachable option for the system. The increase in path options enhances the REMPI effect taking place in the ionization, which in turn reduces the global necessity in intensity to induce ionization.

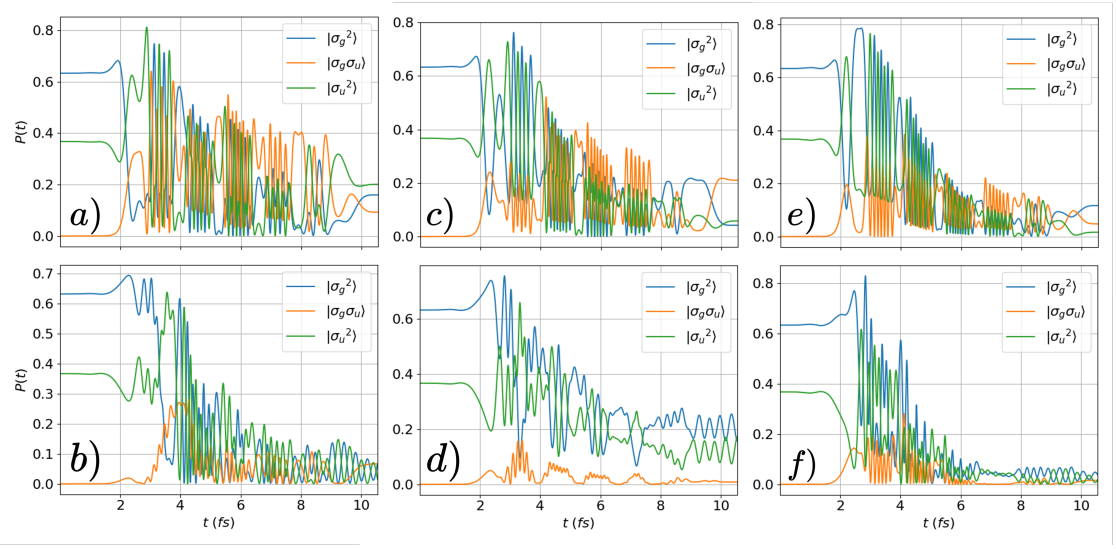

Figure A3.4: Time evolution of the CSFs populations $|\sigma_g^2\rangle$, $|\sigma_g\sigma_u\rangle$ and $|\sigma_u^2\rangle$ of H_2 at $R = 5.0$ a.u during the $\lambda = 790$ nm laser pulse for dynamics with electronic correlation switched off in the upper row (a, c and e) and kept fully correlated in the lower row (b, d and f), at intensities $I = 6.67 \times 10^{14}$ W/cm^2 in the left column (a and b), $I = 1.00 \times 10^{15}$ W/cm^2 in the middle column (c and d) and $I = 1.50 \times 10^{15}$ W/cm^2 in the right column (e and f). Left and right columns show populations evolution during REMPI-induced enhancement of the ionization, and the middle column shows dynamics of a quenched ionization.

To better understand the underlying mechanics taking place during the ionization dynamics of H_2 at enhancement- and quenching-inducing intensities, population profiles of the bound eigenstate states are presented in Fig. A3.3 at $R = 5.0\, a.u.$ for intensities $I = 6.67 \times 10^{14}$ and 1.50×10^{15} W/cm^2 to consider the enhancement events, and $I = 1.00 \times 10^{15}$ W/cm^2 to consider quenching events. Dynamics switching off the electronic correlation, Figs. A3.3a,c,e, denote a tendency in the profiles for the fundamental population to quickly mix with excited states, and consequentially with the maximum intensity of the field, partially ionize. When the electronic correlation is kept fully on during the ionization dynamics, as in Figs. A3.3b,f, excited states are generally less populated than is the fundamental state. These changes in the populations exchanges are due to the REMPI effect while correlation is kept on, as once the fundamental population has gained enough photons to get excited to states $|E_2\rangle$ and $|E_3\rangle$, it is quasi-instantly ionized to H_2^+, the excited and ionic states being close to one another.

The case when V_{ee} is kept fully on in a simulation where field parameters induce quenching of the ionization, as seen in Fig. A3.3d, has been covered in the article (see paragraphs related to Fig. 3.5b in the article).

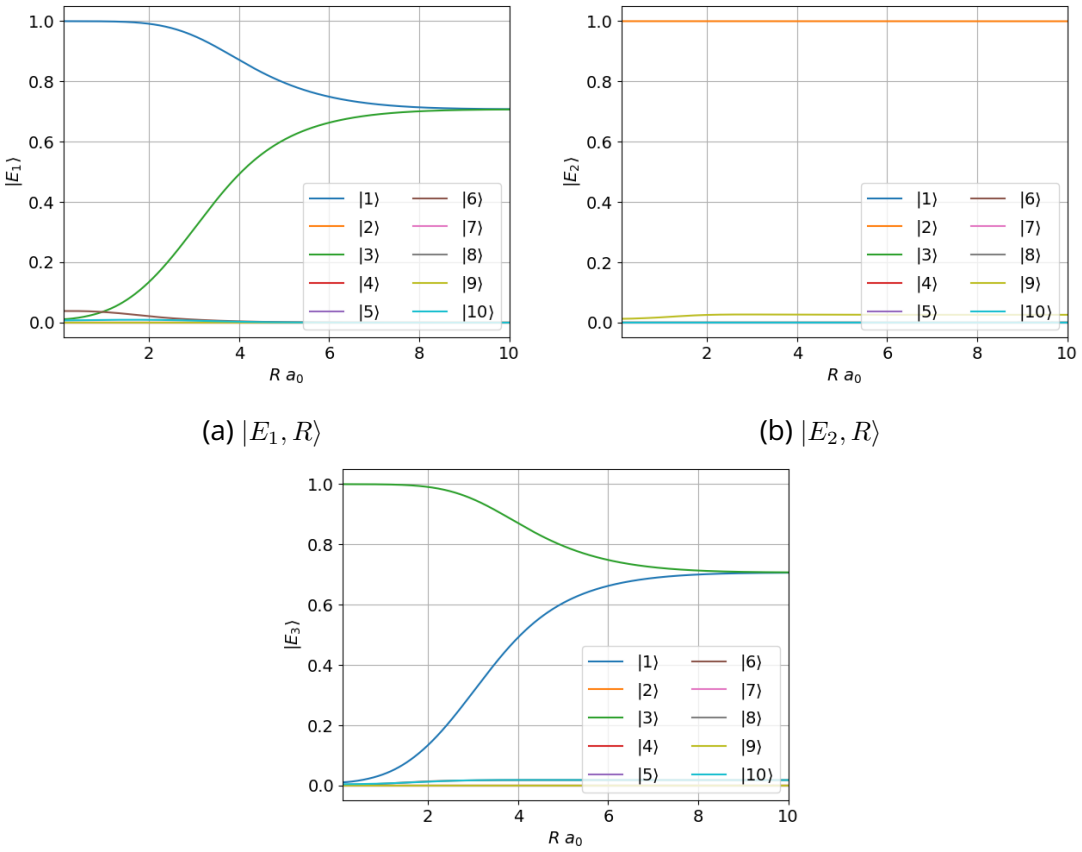

(a) $|E_1, R\rangle$

(b) $|E_2, R\rangle$

(c) $|E_3, R\rangle$

Figure A3.5: Composition of eigenstates $|E_1\rangle$ (a), $|E_2\rangle$ (b) and $|E_3\rangle$ (c) in generated CSFs (see Eqs. 2.39 for equivalences) over non-dissociative R values.

As eigenstates are linear combinations of CSFs, population exchanges can be analysed for selected configuration states $|\sigma_g^2\rangle$, $|\sigma_g\sigma_u\rangle$ and $\sigma_u^2\rangle$, a depiction that has been done in Fig. A3.4. Since $|E_2\rangle = |\sigma_g\sigma_u\rangle \equiv |2\rangle$, as shown in Fig. A3.5b, the population profiles of $|\sigma_g\sigma_u\rangle$ and $|E_2\rangle$ in Figs. A3.3 and A3.4 are the same. But the population profiles for $|\sigma_g^2\rangle$ and $|\sigma_u^2\rangle$ are quite different, though, as eigenstates $|E_1\rangle$ and $|E_3\rangle$ are combinations of the two CSFs at internuclear distances $R = 4$ and 6 a.u., as shown in Figs. A3.5a and A3.5c. As the mix of the two CSFs converges towards similar values at dissociative R values, populations of the associated eigenstates mingle together in the depiction of CSFs population profiles,

and it becomes increasingly difficult to distinguish parts of the CSFs associated with the fundamental state and the ones associated with the excited state.

Chapter 4

Strong Field Dissociative Ionization Dynamics

Contents

4.1 . Introduction

Including dissociation dynamics in the simulation of molecular ionization (i.e. freeing oneself from the Born-Oppenheimer approximation and taking into account the vibrational motion of the nuclei) is a non-trivial task, especially in terms of the computational resources needed to accommodate the new dimensions of the molecular wave packet and its propagation. Since running a full molecular dynamics simulation at the same level as the ab initio treatment of its ionization dynamics would require an enormous amount of computational time and memory, some simplifications are introduced in the representation of the ionization part. This alternative, simplified treatment of the ionization dynamics and the implementation of the added nuclear dynamics are explained in this chapter.

We begin with the hypothesis that there is an analytical expression for the (real-valued, possibly measurable) ionization rate at fixed nuclear geometry (R for H_2), and we explore how this type of information can be used to devise a complete electro-nuclear wave packet propagation scheme. The hope is that this scheme will be able to capture all dissociative ionization events, including the final breakup of the molecule in the Coulomb explosion channel.

This scheme is first applied to single ionization in Chapter 5, where simulations are performed on H_2 using linear and circular polarizations. We review the foundations, strengths and weaknesses of these semi-classical representations of the ionization rates embodied in the molecular ADK (MO-ADK) and PPT (MO-PPT) approaches, which are described in detail in Chapter 5, Section 5.2. The results obtained are discussed in terms of the ionization probability and of the non-Franck-Condon distributions of the vibrational populations formed in H_2^+. This model is based on a set of kinetic equations whose origin is explained in the present Chapter, in sections 4.2 and 4.3.

Finally, in Chapter 6 this scheme is used in full to evaluate the performance of the popular semi-classical MO-PPT expressions of the first and second ionization rates of H_2, taking into account the vibrational motion that takes place in the intermediate molecular ion H_2^+. This model is based on a set of quantum dynamical equations whose origin is explained in the present Chapter, especially in Section 4.4.

4.2 . H_2 vibronic basis up to Coulomb explosion

Adding vibrational dynamics to electronic (ionization) dynamics to account for the possibility of dissociation in a molecule comes at a considerable computational cost. For this reason, we turn to resource-efficient semiclassical (SC) methods to estimate the ionization rate over time within an electro-vibrational dynamics simulation. The principles of SC rates began with the work of Landau and Lifshitz on the tunnel ionization of the ground state of the hydrogen atom in a static field [1], and the idea behind it is to calculate an ionization probability current of the wavefunction passing through the potential barrier during the irradiation of the studied system, taking into account parameters of both the system and the field. This theory was then generalized to any atomic asymptotic Coulomb wave function in the competing regimes of multiphoton and tunnel ionization by the work of Popov, Perelomov and Terent'ev (PPT) [2–4]. An application of this model by Ammosov, Delone and Kraïnov (ADK) [5, 6] to the case of a quasi-static field (i.e., in the tunnel regime) then allowed the emergence of a simplified, non-iterative formulation, called ADK, of ionization rates in linear and circular polarizations.

These methods, while practical for atoms, were only partially suitable for small molecules, as demonstrated by the experimental work of C. Cornaggia and Ph. Hering [7], and would generally require adaptations to better represent the full ionization dynamics of diatomics. To alleviate these limitations, Tong, Zhao and Lin extended the ADK method to a molecular ADK (MO-ADK) [8] and Benis et al., including Tong from the MO-ADK development, formulated a new algorithm for molecular PPT, called MO-PPT [9].

The implementation of these semiclassical methods for the ionization parts in a complete (electro-nuclear) molecular wave packet simulation requires starting from the basic TDSE formulation. Our system of interest, H_2, is first singly-ionized to H_2^+ (eventually treated as a two-state system at the level of its electronic dynamics), and then second-ionized to protons $2H^+$, in the final Coulomb explosion channel. The total electro-nuclear wave function is thus of the form

$$\Psi(\mathbf{r}_1, \mathbf{r}_2, R, t) = \Psi_0(\mathbf{r}_1, \mathbf{r}_2, R, t) + \Psi_1(\mathbf{r}_1, \mathbf{r}_2, R, t) + \Psi_2(\mathbf{r}_1, \mathbf{r}_2, R, t) \tag{4.1}$$

where the indices 0, 1 and 2 stand respectively for

$$\begin{aligned} 0 &\longleftrightarrow \mathrm{H}_2 \\ 1 &\longleftrightarrow \mathrm{H}_2^+ + e^- \\ 2 &\longleftrightarrow \mathrm{H}^+ + \mathrm{H}^+ + e^- + e^- \end{aligned}$$

In Ψ_0, the two electrons are bound, whereas in Ψ_1 one electron is in the ioniza-

tion continuum and the other is in a bound state. Finally, in Ψ_2 the two electrons are in the ionization continuum.

These electro-nuclear wave functions Ψ_0, Ψ_1 and Ψ_2 are then expressed in a Born-Oppenheimer form

$$\Psi_0(\mathbf{r}_1,\mathbf{r}_2,R,t) = \psi_{\mathrm{H}_2}(R,t)\,\Phi_0(\mathbf{r}_1,\mathbf{r}_2;R) \tag{4.2a}$$

$$\begin{aligned}\Psi_1(\mathbf{r}_1,\mathbf{r}_2,R,t) &= \psi^g_{\mathrm{H}_2^+}(R,t)\,\Phi^g_1(\mathbf{r}_1,\mathbf{r}_2;R) + \psi^u_{\mathrm{H}_2^+}(R,t)\,\Phi^u_1(\mathbf{r}_1,\mathbf{r}_2;R)\\ &= \left[\psi^g_{bound}(R,t) + \psi^g_{diss}(R,t)\right]\Phi^g_1(\mathbf{r}_1,\mathbf{r}_2;R)\\ &\quad + \psi^u_{\mathrm{H}_2^+}(R,t)\,\Phi^u_1(\mathbf{r}_1,\mathbf{r}_2;R)\end{aligned} \tag{4.2b}$$

$$\Psi_2(\mathbf{r}_1,\mathbf{r}_2,R,t) = \psi_{2\mathrm{H}^+}(R,t)\,\Phi_2(\mathbf{r}_1,\mathbf{r}_2;R) \tag{4.2c}$$

Note that there are two nuclear wave packets $\psi^\sigma_{\mathrm{H}_2^+}(R,t)$ for H_2^+, associated with the coupled electronic states Φ^g_1 ($\sigma = g$) and Φ^u_1 ($\sigma = u$). Also, in Eq. (4.2b), the g-state wave packet is further decomposed into bound and dissociative components

$$\psi^g_{bound}(R,t) = \sum_{v_+}\beta_{v_+}(t)\,\chi_{v_+}(R) \tag{4.3a}$$

$$\psi^g_{diss}(R,t) = \int d\varepsilon\;\beta_\varepsilon(t)\,\chi^g_\varepsilon(R), \tag{4.3b}$$

where $\chi_{v_+}(R)$, for $v_+ = 0-18$, are vibrational eigenstates of the g channel, and $\chi^g_\varepsilon(R)$ are continuum eigenstates of the same channel. The purely dissociative wave packet $\psi^u_{\mathrm{H}_2^+}$ and the one associated with the Coulomb explosion (CE) channel are likewise expressed as in Eq. (4.3b) in terms of continuum wavefunctions defined by the corresponding repulsive potential. For example

$$\psi_{2\mathrm{H}^+}(R,t) = \int d\varepsilon\;\gamma_\varepsilon(t)\,\chi^{\mathrm{CE}}_\varepsilon(R) \tag{4.4}$$

for the CE channel.

In principle, the wave packet $\psi_{\mathrm{H}_2}(R,t)$ of the neutral molecule in its ground-state should also be expanded in terms of vibrational eigenstates of that ground-state manifold. In the simplified model of Chapter 5, only the ground vibrational state is considered to be involved, and we simply write

$$\psi_{\mathrm{H}_2}(R,t) = \alpha_0(t)\,\chi_0(R)\,. \tag{4.5}$$

Finally, in the above, $\alpha_0(t)$, $\beta_{v_+}(t)$, $\beta_\varepsilon(t)$ and $\gamma_\varepsilon(t)$ are complex amplitudes, functions of time.

Note that here we completely ignore the continuum of energies (or momenta) of the ionized electrons by writing Ψ_1 and Ψ_2 in Eqs. (4.2b) and (4.2c). In this respect, the present approach is compatible with the ADK and PPT formulations. For simulation purposes, the basis set is considered complete with a single vibrational state of the ground electronic state of H_2, all the bound and dissociative states of the $^1\Sigma_g^+$ configuration of H_2^+, and the dissociative states of both the H_2^+ $^1\Sigma_u^+$ configuration and the Coulomb Explosion channel.

Nuclear motions: Eigenstates

The vibrational potentials of H_2 and H_2^+, which are the starting point for our basis, have been quantitatively studied in the work of Kolos and Wolniewicz [10], Madsen and Peek [11, 12] respectively, and are widely considered to be exact in the literature. These potentials are not analytical, and calculations of eigenstates and eigenvalues based on them therefore require a numerical algorithm such as the Numerov method. This well-known method, which is based on a finite difference approach, was derived by the Russian astronomer Boris Numerov. It is an iterative algorithm [13–15] capable of predicting the value of a wave function $\chi(R_{n+1})$ at the next point $R_{n+1} = R_n + dR$, given the potential $V(R)$, the two values of the wave function at the two previous points $\chi(R_n)$ and $\chi(R_{n-1})$, and an estimated energy E as the eigenvalue. This approach can be used to calculate both bound eigenstates with discrete energies within a potential well and dissociative states associated to the continuum of energies above that well. The calculation starts at a point ($n = 1$) of the grid corresponding to a classically forbidden region of the potential, say before the left turning point at the guessed value of the energy. At such a point, it is safe to assume a vanishing value of the wave function at the two initial positions. The value of the wave function at each grid point is then obtained iteratively. For a bound discrete energy level that is yet to be found, the procedure is repeated by starting from a point in the classically forbidden region lying beyond the right turning point at the guessed energy, and propagating inward on the grid. If the guessed energy is a bound level, then the wavefunction propagated inward must match the one propagated outward at an intermediate point of the grid. To find the discrete-energy eigenstates, the Numerov algorithm must iterate over several energy guesses until it finds the correct quantized energy for a state. For a potential well with a single minimum, such as that for the vibration of H_2, the ground state will have no node. Each subsequent eigenstate gains a node, up to the last bound state. The generated bound eigenstates are automatically orthogonal to each other, so the last step is to normalize them. The 19 vibrational wave functions calculated in the $^1\Sigma_g^+$ electronic state of H_2^+ are shown in Fig. 4.1. Above

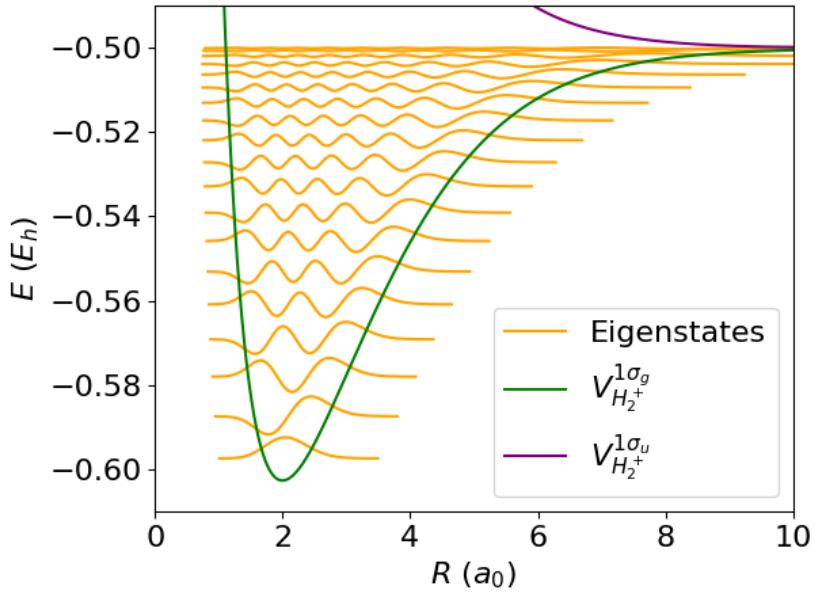

Figure 4.1: Vibrational Eigenstates (orange lines) generated within the bound potential $V_{\mathrm{H}_2^+}^{1\sigma_g}(R)$ (green line) of H_2^+ using Numerov's method.

the threshold, the states are dissociative, and their energies constitute a continuum. Their calculation by the Numerov algorithm requires only an outward propagation on the grid. It is impossible to compute numerically the complete basis of continuum dissociative states, so one must ensure that the discretization includes enough functions at energies within a range that is sufficient to construct the dissociative wave packet according to the field parameters used. These dissociated molecular states, normalized in energy, have the usual oscillatory asymptotic behavior [16]

$$\chi_\varepsilon(R) \xrightarrow[R\to\infty]{} e^{-i\xi}\sqrt{\frac{2\mu}{\hbar^2\pi k}}\,\frac{\sin(kR+\xi)}{R}\,, \tag{4.6}$$

where ξ is the asymptotic phase shift introduced by the scattering on the potential energy curve at the prescribed energy $\varepsilon = \hbar^2k^2/(2\mu)$, μ being the reduced mass of the diatomic molecule.

4.3 . TDSE and Simplification of the Ionization Dynamics via Semi-Classical Methods

The time-dependent Schrödinger equation (TDSE) is

$$i\hbar\,\partial_t\Psi(\mathbf{r}_1,\mathbf{r}_2,R,t) = \Big[\hat{H}_{el}+\hat{T}_R+1/R+V_{\rm int}(\mathbf{r}_1,\mathbf{r}_2,t)\Big]\Psi(\mathbf{r}_1,\mathbf{r}_2,R,t) \tag{4.7}$$

where $\hat{H}_{el}(\mathbf{r}_1,\mathbf{r}_2,R)$ is the electronic field-free Hamiltonian, $\hat{T}_R$ is the nuclear kinetic energy operator and

$$V_{\rm int}(\mathbf{r}_1,\mathbf{r}_2,t) = -e(\mathbf{r}_1+\mathbf{r}_2)\cdot\mathrm{F}(t) \tag{4.8}$$

is the field-molecule interaction energy, written here in the length gauge using the dipole approximation.

Substituting the expression of $\Psi(\mathbf{r}_1,\mathbf{r}_2,R,t)$ given in Eqs. (4.1) and (4.2a-4.2c), and projecting onto the ground electronic state Φ_0 yields

$$i\hbar\,\partial_t\,\psi_{\mathrm{H}_2}(R,t) = \Big[\hat{T}_R+V_{\mathrm{H}_2}(R)\Big]\,\psi_{\mathrm{H}_2}(R,t)+\hbar\,W_0^1(R,t)\,\psi^g_{\mathrm{H}_2^+}(R,t)\,, \tag{4.9}$$

where

$$\hbar\,W_0^1(R,t) = \iint \Phi_1^g(\mathbf{r}_1,\mathbf{r}_2;R)\,V_{\rm int}(\mathbf{r}_1,\mathbf{r}_2,t)\,\Phi_0(\mathbf{r}_1,\mathbf{r}_2;R)\,d\mathbf{r}_1 d\mathbf{r}_2\,. \tag{4.10}$$

Equation (4.9) is obtained by assuming *i*) that there is no radiative coupling between the ground electronic state of H_2 and H_2^+ first excited electronic state of $^1\Sigma_u^+$ configuration, and *ii*) that the radiative coupling terms between H_2 and the double electronic continuum are negligible.

Further projecting (4.9) on the ground vibrational state $\chi_0(R)$ of H_2 with the help of Eqs. (4.3a), (4.3b) and (4.5) yields

$$i\hbar\,\dot{\alpha}_0(t) = E_0\,\alpha_0(t)+\sum\!\!\!\!\!\!\int_{v_+(\varepsilon)}\hbar\,W_{00}^{1v_+(\varepsilon)}(t)\,\beta_{v_+(\varepsilon)}(t)\,, \tag{4.11}$$

where E_0 is the total electronic plus vibrational energy of the state $\chi_0\Phi_0$, and where

$$W_{00}^{1v_+(\varepsilon)}(t) = \int \chi_{v_+(\varepsilon)}(R)\,W_0^1(R,t)\,\chi_0(R)\,dR\,. \tag{4.12}$$

Similarly, for the second ionization we define

$$\hbar\,W_1^2(R,t) = \iint \Phi_2(\mathbf{r}_1,\mathbf{r}_2;R)\,V_{\rm int}(\mathbf{r}_1,\mathbf{r}_2,t)\,\Phi_1^g(\mathbf{r}_1,\mathbf{r}_2;R)\,d\mathbf{r}_1 d\mathbf{r}_2\,, \tag{4.13a}$$

with matrix elements between the vibrational states χ_{v_+} of H_2^+ and the scattering states $\chi_\varepsilon^{\rm CE}$ of the CE channel

$$W_{1v_+}^{2\varepsilon}(t) = \int \chi_\varepsilon^{\rm CE}(R)\, W_1^2(R,t)\, \chi_{v_+}(R)\, dR\,. \tag{4.13b}$$

It is the quantities $W_0^1(R,t)$, $W_1^2(R,t)$ that will be calculated later on using either the ADK or PPT theory. Equating the transition probabilities associated with the approach described above with the transition probabilities of the semi-classical ADK or PPT models, we naturally obtain

$$\left[W_0^1(R,t)\,\delta t\right]^2 = W_{\rm H_2}^{\rm SC}(R,t)\,\delta t \tag{4.14a}$$

$$\left[W_1^2(R,t)\,\delta t\right]^2 = W_{\rm H_2^+}^{\rm SC}(R,t)\,\delta t \tag{4.14b}$$

where δt denotes a short time interval and where the quantities $W_{\rm H_2}^{\rm SC}(R,t)$ and $W_{\rm H_2^+}^{\rm SC}(R,t)$ are identified with the ADK or PPT semiclassical (SC) ionization rates calculated at the internuclear distance R and at time t. These definitions transform Eq. (4.11) into

$$\dot\alpha_0(t) = -i\,\frac{E_0}{\hbar}\,\alpha_0(t) - i \sum\!\!\!\!\!\!\int_{v_+(\varepsilon)} \left[\Gamma_0^{v_+(\varepsilon)}(t)/\delta t\right]^{\frac{1}{2}} \beta_{v_+(\varepsilon)} \tag{4.15}$$

where

$$\Gamma_0^{v_+(\varepsilon)}(t) = \left| \int \chi_{v_+(\varepsilon)}(R) \left[W_{\rm H_2}^{\rm SC}(R,t)\right]^{\frac{1}{2}} \chi_0(R)\, dR \right|^2 \tag{4.16}$$

is the state-resolved single ionization rate. Similarly, for the second ionization, we can define the state-resolved second ionization rate

$$\Gamma_{v_+}^{\varepsilon}(t) = \left| \int \chi_\varepsilon^{\rm CE}(R) \left[W_{\rm H_2^+}^{\rm SC}(R,t)\right]^{\frac{1}{2}} \chi_{v_+}(R)\, dR \right|^2 . \tag{4.17}$$

Using a simple first-order finite difference, Eq. (4.15) leads to an iterative short-time solution written as

$$\alpha_0(t+\delta t) = \left[1 - i\,\frac{E_0}{\hbar}\,\delta t\right] \alpha_0(t) - i \sum\!\!\!\!\!\!\int_{v_+(\varepsilon)} \left[\Gamma_0^{v_+(\varepsilon)}(t)\,\delta t\right]^{\frac{1}{2}} \beta_{v_+(\varepsilon)}\,. \tag{4.18}$$

Ignoring for the moment the coupling between the Φ_1^g and Φ_1^u states, the projection of the TDSE (4.7) onto Φ_1^g (for the H_2^+ σ_g channel) yields

$$\begin{aligned} i\hbar\,\partial_t\,\psi_{\rm H_2^+}^g(R,t) = &\left[\hat T_R + V_{\rm H_2^+}^g(R)\right] \psi_{\rm H_2^+}^g(R,t) + \hbar\, W_0^1(R,t)\,\psi_{\rm H_2}(R,t) \\ &+ \hbar\, W_1^2(R,t)\,\psi_{\rm 2H^+}(R,t)\,, \end{aligned} \tag{4.19}$$

which, upon further projection onto the vibrational state χ_{v_+} of that channel, gives

$$\dot{\beta}_{v^+}(t) = -i\,\frac{E_{v^+}}{\hbar}\,\beta_{v^+}(t) - i\,\left[\Gamma_0^{v_+}(t)/\delta t\right]^{\frac{1}{2}}\,\alpha_0(t) - i\int\left[\Gamma_{v_+}^{\varepsilon}(t)/\delta t\right]^{\frac{1}{2}}\,\gamma_\varepsilon(t)\,d\varepsilon\,, \quad (4.20)$$

where E_{v^+} is the total electronic plus vibrational energy of the state $\chi_{v^+}\Phi_1$. For $\beta_{v^+}(t)$ the iterative (short-time) first-order finite difference solution is therefore

$$\begin{aligned}\beta_{v^+}(t+\delta t) = \left[1 - i\,\frac{E_{v^+}}{\hbar}\,\delta t\right]\beta_{v^+}(t) - i\,\left[\Gamma_0^{v_+}(t)\delta t\right]^{\frac{1}{2}}\,\alpha_0(t)\\ - i\int\left[\Gamma_{v_+}^{\varepsilon}(t)\delta t\right]^{\frac{1}{2}}\,\gamma_\varepsilon(t)\,d\varepsilon\,.\end{aligned} \quad (4.21)$$

Finally, projecting the TDSE (4.7) on the electro-nuclear eigenstate $\chi_\varepsilon^{\mathrm{CE}}\Phi_2$ yields

$$\dot{\gamma}_\varepsilon(t) = -i\,\frac{\varepsilon}{\hbar}\,\gamma_\varepsilon(t) - i\,\sum_{v^+}\left[\Gamma_{v_+}^{\varepsilon}(t)/\delta t\right]^{\frac{1}{2}}\,\beta_{v^+}(t)\,, \quad (4.22)$$

with the short-time first-order solution

$$\gamma_\varepsilon(t+\delta t) = \left[1 - i\,\frac{\varepsilon}{\hbar}\,\delta t\right]\gamma_\varepsilon(t) - i\sum_{v^+}\left[\Gamma_{v_+}^{\varepsilon}(t)\delta t\right]^{\frac{1}{2}}\,\beta_{v^+}(t)\,. \quad (4.23)$$

Note that in this last equation ε corresponds to the pure Coulomb nuclear kinetic energy, with the origin of the energy chosen as the asymptotic $(R \to \infty)$ energy of the Coulomb explosion potential energy curve.

Static Molecular Dynamics from Population Transfers

The thesis work went through two stages of development aimed at merging ADK and PPT semiclassical treatments of ionization (in lieu of actual quantum electron dynamics) with nuclear wave packet propagation. The first stage focuses on the evaluation of population transfer rates, using kinetic-type rate equations, as resulting from single and double ionization of the molecule.

The kinetic equations, given in the next chapter, Eqs.(5.1a)-(5.1c) are based on the simple premise that, for example, the variations of the population on a given vibrational level of H_2^+ would be equivalent to the sum of losses and gains to and from other molecular states, according to the population available in the

originating state. In integral forms, to the first-order in δt, they are

$$P_{\mathrm{H}_2}(t+\delta t) = \left[1 - \sum_{v_+} \Gamma_0^{v_+}(t)\delta t\right] P_{\mathrm{H}_2}(t)\,, \tag{4.24a}$$

$$P_{\mathrm{H}_2^+}(t+\delta t) = \sum_{v_+}\left[1 - \int \Gamma_{v_+}^{\varepsilon}(t)\delta t\, d\varepsilon\right] P_{v_+}(t) + \sum_{v_+}\left[\Gamma_0^{v_+}(t)\delta t\right] P_{\mathrm{H}_2}(t)\,, \tag{4.24b}$$

$$P_{2\mathrm{H}^+}(t+\delta t) = \int \left(P_{\varepsilon}(t) + \sum_{v_+} \Gamma_{v_+}^{\varepsilon}(t)\delta t\, P_{v_+}(t)\right) d\varepsilon\,, \tag{4.24c}$$

where Γ_i^j are the population transfer rates from state i to j, as given in Eqs. (4.16) and (4.17) in terms of the MO-ADK/PPT ansatz. These kinetic equations describe the time evolution of the diagonal part of the system's density matrix, as resulting from the TDSE given above, ignoring coherences in this density matrix.

Rate equation for $\mathbf{P}_{\mathrm{H}_2}(\mathbf{t}) = |\alpha_{\mathbf{0}}(\mathbf{t})|^{\mathbf{2}}$

Multiplying both sides of Eq. (4.15) by $\alpha_0^*(t)$, then summing the result with its complex conjugate expression, noting that $\Gamma_0^{v_+(\varepsilon)}$ is real, we have

$$\frac{dP_{\mathrm{H}_2}(t)}{dt} = \sum\!\!\!\!\!\!\int_{v_+(\varepsilon)} \left[\Gamma_0^{v_+(\varepsilon)}(t)/\delta t\right]^{\frac{1}{2}} \mathrm{Im}\left[\alpha_0^* \beta_{v_+(\varepsilon)}\right] \tag{4.25}$$

On the other hand, solving Eq. (4.21) for β_{v_+} using a short-time approximation with initial condition $\beta_{v_+}(0) = 0$ and for a negligible double ionization, we obtain

$$\beta_{v^+} \sim -i\left[\Gamma_0^{v_+}(t)\delta t\right]^{\frac{1}{2}} \alpha_0\,. \tag{4.26}$$

Substituting this expression into Eq. (4.25) then yields

$$\frac{dP_{\mathrm{H}_2}(t)}{dt} = -\sum\!\!\!\!\!\!\int_{v_+(\varepsilon)} \Gamma_0^{v_+(\varepsilon)} P_{\mathrm{H}_2}(t)\,. \tag{4.27}$$

This is the first kinetics equation, Eq.(5.1a), in Chapter 5 (or Eq. 1a of [17]), with $\Gamma_0^+ = \sum\!\!\!\!\!\!\int_{v_+(\varepsilon)} \Gamma_0^{v_+(\varepsilon)}$.

Rate equation for $\mathbf{P}_{\mathbf{v}_+}(\mathbf{t}) = |\beta_{\mathbf{v}_+}(\mathbf{t})|^{\mathbf{2}}$

In a similar way to what was done previously for H_2, if we multiply Eq. (4.20) by $\beta_{v_+}^*$ and add the result to its complex conjugate we obtain

$$\frac{dP_{v^+}(t)}{dt} = \left[\Gamma_0^{v_+}(t)/\delta t\right]^{\frac{1}{2}} \mathrm{Im}\left[\beta_{v_+}^* \alpha_0\right] + \int \left[\Gamma_{v_+}^{\varepsilon}(t)/\delta t\right]^{\frac{1}{2}} \mathrm{Im}\left[\beta_{v_+}^* \gamma_{\varepsilon}\right] d\varepsilon \tag{4.28}$$

Using Eq. (4.26) to express β_{v_+} in the first term of the right hand side of Eq. (4.28) gives the source term $+\Gamma_0^{v_+} P_{\mathrm{H}_2}(t)$ corresponding to the gain of population of the v_+ vibrational state by ionization from the neutral molecule ground-state with rate constant $\Gamma_0^{v_+}(t)$.

As for the expression of $\gamma_\varepsilon(t)$ to be inserted in the second term of the right hand side of Eq. (4.28), it can be estimated by the short-time solution (4.23) as

$$\gamma_\varepsilon \sim -i \sum_{v^+} \left[\Gamma^\varepsilon_{v_+}(t)\delta t\right]^{\frac{1}{2}} \beta_{v^+} \tag{4.29}$$

Upon substitution in the second term of the right hand side of Eq. (4.28), and ignoring the cross products $\beta^*_{v_+}\beta_{v'_+}$ between different v_+ and v'_+ levels (terms corresponding to coherences in the density matrix), we obtain

$$\frac{dP_{v^+}}{dt} = \Gamma_0^{v_+}(t)\, P_{\mathrm{H}_2}(t) - \int \Gamma^\varepsilon_{v_+}(t) d\varepsilon \; P_{v^+}(t)\,. \tag{4.30}$$

This is the second kinetics equation, Eq. (5.1b), of Chapter 5 (or Eq. 1b of [17]), with

$$\Gamma^{\mathrm{CE}}_{v_+}(t) = \int \Gamma^\varepsilon_{v_+}(t) d\varepsilon\,. \tag{4.31}$$

Rate equation for $\mathbf{P_{CE}(t) = \int |\gamma_\varepsilon(t)|^2\, d\varepsilon}$

The demonstration of the last kinetic equation of Chapter 5, Eq. (5.1c), follows the same line of reasoning, starting from Eq. (4.22) to express the time derivative of $|\gamma_\varepsilon(t)|^2$, followed by using Eq. (4.29) as a short-time approximation of γ_ε and neglecting cross-products (coherences) of the form $\beta^*_{v_+}(t)\beta_{v'_+}(t)$ with $v_+ \neq v'_+$. The end result is

$$\frac{d}{dt} P_{\mathrm{CE}}(t) = \sum_{v_+} \Gamma^{\mathrm{CE}}_{v_+}(t) P_{v_+}(t) \tag{4.32}$$

This is Eq.(5.1c) of Chapter 5 (or Eq. 1c of [17]).

4.4 . From R-Parameterized Population Transfer to Full Molecular Wave Packets

From the eigenstate population transfer algorithm presented in the previous section, the molecular dynamics simulation was then extended with implementations of propagating vibrational wave packets, which could be analyzed to extract, for example, the single- and double-ionization probabilities, but also the

kinetic energy distributions of the emitted protons in the course of a dissociation process. This section describes the methodology that led us to the quantum dynamical equations describing the vibrational motion, which are consistent with the semiclassical approximations such as MO-ADK and MO-PPT used for the description of the ionization dynamics.

4.4.1 .Vibrational Motion

The time-dependent Schrödinger equation applied to the nuclear wave packet $\psi_{\mathrm{H_2}}(R,t)$ of $\mathrm{H_2}$ was obtained in the previous section, Eq. (4.9). This equation has an exact formal solution in the form of the formula

$$\begin{aligned}\psi_{\mathrm{H_2}}(R,t) = e^{-i\,[\hat{H}_n^0\,t/\hbar]}\;\psi_{\mathrm{H_2}}(R,0) \\ - i\int_0^t e^{-i\,[\hat{H}_n^0\,(t-t')/\hbar]}\;W_0^1(R,t')\,\psi^g_{\mathrm{H_2^+}}(R,t')\,dt'\,,\end{aligned} \tag{4.33}$$

where the nuclear Hamiltonian of the neutral $\mathrm{H_2}$ molecule is $\hat{H}_n^0 = \hat{T}_R + V_{\mathrm{H_2}}(R)$. In Eq. (4.33), $\psi_{\mathrm{H_2^+}}(R,t)$ is the nuclear wave packet associated with the g electronic ground state of $\mathrm{H_2^+}$. If we neglect its coupling to the first excited electronic state u of $\mathrm{H_2^+}$, its dynamics is governed by Eq. (4.19). This also has an exact formal solution in the form

$$\begin{aligned}\psi_{\mathrm{H_2^+}}(R,t) = e^{-i\,[\hat{H}_n^{1g}\,t/\hbar]}\;\psi_{\mathrm{H_2^+}}(R,0) \\ - i\int_0^t e^{-i\,[\hat{H}_n^{1g}\,(t-t')/\hbar]}\Big(W_0^1(R,t')\,\psi_{\mathrm{H_2}}(R,t') \\ + W_1^2(R,t')\,\psi_{\mathrm{2H^+}}(R,t')\Big)\,dt'\,,\end{aligned} \tag{4.34}$$

where $\hat{H}_n^{1g} = \hat{T}_R + V^g_{\mathrm{H_2^+}}(R)$. We see in Eq. (4.34) that the nuclear wave packet $\psi_{\mathrm{H_2^+}}(R,t)$ evolving on the $1s\sigma_g$ potential of $\mathrm{H_2^+}$ is coupled to both the nuclear wave packet $\psi_{\mathrm{H_2}}(R,t)$ describing the neutral H_2 molecule and the wave packet $\psi_{\mathrm{2H^+}}(R,t)$ describing the doubly ionized Coulomb explosion channel. The latter evolves according to the time-dependent Schrödinger equation

$$i\hbar\,\partial_t\psi_{\mathrm{2H^+}}(R,t) = \hat{H}_n^{\mathrm{CE}}\,\psi_{\mathrm{2H^+}}(R,t) + \hbar\,W_1^2(R,t)\,\psi_{\mathrm{H_2^+}}(R,t), \tag{4.35}$$

where $\hat{H}_n^{\mathrm{CE}} = \hat{T}_R + 1/R$, leading to the exact formal solution

$$\begin{aligned}\psi_{\mathrm{2H^+}}(R,t) = e^{-i\,[\hat{H}_n^{\mathrm{CE}}\,t/\hbar]}\;\psi_{\mathrm{2H^+}}(R,0) \\ - i\int_0^t dt' e^{-i\,[\hat{H}_n^{\mathrm{CE}}\,(t-t')/\hbar]}W_1^2(R,t')\,\psi_{\mathrm{H_2^+}}(R,t')\,.\end{aligned} \tag{4.36}$$

Applying the propagation (4.33) between t and $(t+\delta t)$ over a very short time interval $\delta t \to 0$, we obtain

$$\psi_{\mathrm{H}_2}(R,t+\delta t) \simeq e^{-i\,[\hat{H}_n^0\,\delta t/\hbar]}\left(\psi_{\mathrm{H}_2}(R,t) - i\int_t^{t+\delta t} W_0^1(R,t')\,\psi^g_{\mathrm{H}_2^+}(R,t')\,dt'\right). \quad (4.37)$$

Furthermore, for a sufficiently small value of δt, we can assume that the integrant does not change much between t and $(t+\delta t)$, and therefore we get

$$\psi_{\mathrm{H}_2}(R,t+\delta t) \simeq e^{-i\,[\hat{H}_n^0\,\delta t/\hbar]}\left(\psi_{\mathrm{H}_2}(R,t) - i\,[W_0^1(R,t')\delta t]\,\psi^g_{\mathrm{H}_2^+}(R,t')\right), \quad (4.38)$$

where $t' = t + \delta t/2$ is the average time value between t and $t+\delta t$. Using the same approach to express the nuclear wave packet of electronic symmetry g associated with the H_2^+ ion, and neglecting for the moment the coupling with the u state of H_2^+ and with the double ionization continuum, we obtain

$$\psi^g_{\mathrm{H}_2^+}(R,t+\delta t) \simeq e^{-i\,[\hat{H}_n^{1g}\,\delta t/\hbar]}\left(\psi^g_{\mathrm{H}_2^+}(R,t) - i\,[W_0^1(R,t')\delta t]\,\psi_{\mathrm{H}_2}(R,t')\right). \quad (4.39)$$

Rewriting Eqs. (4.38) and (4.39) to express $\psi_{\mathrm{H}_2}(R,t')$ and $\psi^g_{\mathrm{H}_2^+}(R,t')$, and keeping only the 0^{th}-order term in the series development of the evolution operators of Eqs. (4.38) and (4.39) for the short time interval $(t'-t=\delta t/2)$ involved, we get

$$\psi_{\mathrm{H}_2}(R,t') \simeq \psi_{\mathrm{H}_2}(R,t) - i\,[W_0^1(R,t')\delta t/2]\,\psi^g_{\mathrm{H}_2^+}(R,t)\,, \quad (4.40a)$$

$$\psi^g_{\mathrm{H}_2^+}(R,t') \simeq \psi^g_{\mathrm{H}_2^+}(R,t) - i\,[W_0^1(R,t')\delta t/2]\,\psi_{\mathrm{H}_2}(R,t)\,. \quad (4.40b)$$

Inserting Eq. (4.40b) in Eq. (4.38) we get at second order in δt

$$\psi_{\mathrm{H}_2}(R,t+\delta t) \simeq e^{-i\,[\hat{H}_n^0\,\delta t/\hbar]}\left(\left[1-X^2/2\right]\psi_{\mathrm{H}_2}(R,t) - i\,X\,\psi^g_{\mathrm{H}_2^+}(R,t)\right), \quad (4.41a)$$

$$\simeq e^{-i\,[\hat{H}_n^0\,\delta t/\hbar]}\left(\left[1-X^2\right]^{\frac{1}{2}}\psi_{\mathrm{H}_2}(R,t) - i\,X\,\psi^g_{\mathrm{H}_2^+}(R,t)\right), \quad (4.41b)$$

where, for simplicity, we have defined $X = W_0^1(R,t')\,\delta t$. In equation (4.41b), the first term on the right corresponds to the loss of population due to ionization, while the second term accounts for the possibility of recapturing an electron after it has been ionized. Since this recapture probability is small, it is neglected in Chapter 6. Now, taking into account Eq. (4.14a), which relates W_0^1 to the semi-classical ionization rate $W^{\mathrm{SC}}_{\mathrm{H}_2}$, we finally obtain

$$\psi_{\mathrm{H}_2}(R,t+\delta t) \simeq e^{-i\,[\hat{H}_n^0\,\delta t/\hbar]}\left(1 - W^{\mathrm{SC}}_{\mathrm{H}_2}(R,t')\delta t\right)^{\frac{1}{2}}\psi_{\mathrm{H}_2}(R,t) \quad (4.42)$$

This brings ψ_{H_2} in line with the formulation proposed in Chapter 6, Eqs. (6.2) and (6.3). Inserting now Eq. (4.40a) in Eq. (4.39) we get at the lowest order in δt

$$\psi^g_{H_2^+}(R, t+\delta t) \simeq e^{-i\,[\hat{H}_n^{1g}\,\delta t/\hbar]} \left(\psi^g_{H_2^+}(R,t) - i \left[W^{SC}_{H_2}(R,t')\delta t \right]^{\frac{1}{2}} \psi_{H_2}(R,t) \right). \quad (4.43)$$

This brings this expression in a form that is very similar to the one used in Chap. 6

$$\psi^g_{H_2^+}(R, t+\delta t) \simeq e^{-i\,[\hat{H}_n^{1g}\,\delta t/\hbar]} \left(\psi^g_{H_2^+}(R,t) - i\,\alpha(t) \left[W^{SC}_{H_2}(R,t)\delta t \right]^{\frac{1}{2}} \psi_{H_2}(R,t) \right), \quad (4.44)$$

as can be seen in Eqs. (6.5) and (6.7).

The only two differences between Eqs. (4.43) and (4.44) are as follows: *i*) In Chapter 6, the ionization rate $W^{SC}_{H_2}$ is assumed to be constant over the short time interval between the times t and $t+\delta t$. Thus, $W^{SC}_{H_2}(R,t')$ in Eq. (4.43) is replaced by $W^{SC}_{H_2}(R,t)$ in Eq. (4.44). *ii*) An additional parameter $\alpha(t)$ has been introduced in Eq. (4.44), in comparison with Eq. (4.43). This parameter $\alpha(t)$ is a normalization factor calculated numerically at each time step so as to impose a population gain in H_2^+ which exactly compensates, at each time step δt, the loss in H_2 given by Eq. (4.42). A similar approximation of the TDSE equations has been implemented in the MEDYS code discussed in Chapter 2 to ensure the conservation of the norm during the evolution through exchanges of the bound Ψ_Q and ionic Ψ_P wave packets.

Calculation of the normalization factor $\alpha(t)$

The Born-Oppenheimer approximation allows the eigenstates projection ionization method to disregard the explicit evolution of wave packets (e.g. in Chapter 5), but this point becomes critical in an algorithm that considers both ionization and vibrations (e.g. in Chapter 6). As mentioned above, in the latter case it is necessary to introduce an additional normalization parameter $\alpha(t)$, the calculation of which is explained below.

We start by defining from Eq. (4.42) the variation of population in H_2 as

$$\Delta P_{H_2}(t) = \int |\Psi_{H_2}(R, t+\delta t)|^2\, dR - \int |\Psi_{H_2}(R,t)|^2\, dR \quad (4.45a)$$

$$= -\int \left|\Phi(R,t)\right|^2 dR \quad (4.45b)$$

where

$$\Phi(R,t) = \left[W^{SC}_{H_2}(R,t')\delta t \right]^{\frac{1}{2}} \psi_{H_2}(R,t)\,. \quad (4.46)$$

Then from Eq. (4.44) we see that the variation of population in H_2^+ is

$$\Delta P_{H_2^+}(t) = \int |\Psi^g_{H_2^+}(R, t+\delta t)|^2 \, dR - \int |\Psi^g_{H_2^+}(R,t)|^2 \, dR \tag{4.47a}$$

$$= -\Delta P_{H_2}(t)\, \alpha^2(t) + B(t)\, \alpha(t) \tag{4.47b}$$

where

$$B(t) = 2 \int \mathrm{Im}\Big[\Phi(R,t)\, \psi^{g*}_{H_2^+}(R,t)\Big] \, dR \,. \tag{4.48}$$

Finally, the conservation of the total norm $\Delta P_{H_2}(t) + \Delta P_{H_2^+}(t) = 0$ leads to the following quadratic equation

$$\Delta P_{H_2}(t)\, \alpha^2(t) - B(t)\, \alpha(t) - \Delta P_{H_2}(t) = 0 \tag{4.49}$$

that we solve numerically at each time step to extract the real-valued normalization parameter

$$\alpha(t) = \frac{B(t) + \Big[B^2(t) + 4\, \Delta P^2_{H_2}(t)\Big]^{\frac{1}{2}}}{2\, \Delta P_{H_2}(t)} \,, \tag{4.50}$$

$B(t)$ being evaluated using the expressions (4.48) and (4.46).

Finally, the approach described here by Eq. (4.42) to describe the ionization of H_2 is also used in Chapter 6, as can be seen in Eq. (6.10), to describe the ionization of H_2^+.

4.4.2 . Vibrational Propagation: Split-Operator Method

As can be seen from Eqs. (4.42) and (4.44) describing the nuclear dynamics of the H_2 and H_2^+ system during its interaction with the laser fields, the vibrational wave packets are made to evolve in time on their potential, thus ensuring complete molecular dynamics of ionization and dissociation. The method used for this is the Split-Operator (SO) method [18], which separates the kinetic and potential parts of the Hamiltonian into three terms that are applied symmetrically, to limit the errors generated [19]. In addition, it is necessary to take into account the radiative coupling between the two firsts electronic states of H_2^+. For a time interval between t and $t+\delta t$, the SO is written as

$$\begin{bmatrix} \psi^g_{H_2^+}(R, t+\delta t) \\ \psi^u_{H_2^+}(R, t+\delta t) \end{bmatrix} = \mathcal{F}^{-1} \, \exp\left[-i \frac{\hbar k^2}{4\mu} \delta t\right] \, \mathcal{F} \, \exp\left[-i \frac{\hat{V}}{\hbar} \delta t\right]$$

$$\times \, \mathcal{F}^{-1} \, \exp\left[-i \frac{\hbar k^2}{4\mu} \delta t\right] \, \mathcal{F} \, \begin{bmatrix} \psi^g_{H_2^+}(R,t) \\ \psi^u_{H_2^+}(R,t) \end{bmatrix} \tag{4.51}$$

where $\mathcal{F}$ and $\mathcal{F}^{-1}$ are the Fourier transform and the inverse Fourier transform, respectively, applied to the wave packets, to transpose them back and forth from coordinate space to momentum space, where the kinetic operator takes a simpler (non-differential) form. In Eq. (4.51), k is the nuclear momentum, μ is the reduced mass of the molecule, and the potential matrix $\hat{V}$ is written as

$$\hat{V} = \begin{bmatrix} V^{g}_{H_2^+}(R) & -\mu_{ug}(R)\,F(t) \\ -\mu_{ug}(R)\,F(t) & V^{u}_{H_2^+}(R) \end{bmatrix}, \tag{4.52}$$

where $\mu_{ug}(R)$ is the electronic transition dipole between the g and u electronic states of H_2^+ and $F(t)$ is the time-dependent electric field.

4.4.3 . Generated observables

From the evolution of the nuclear wave packets it is possible to extract the time evolution of the probabilities:

i) of remaining in the neutral H_2 form of the molecule, $P_{H_2}(t)$,

ii) of being ionized once to give rise to the molecular ion H_2^+, $P_{H_2^+}(t)$,

iii) of being ionized twice to initiate a Coulomb explosion process, $P_{2H^+}(t)$.

These probabilities are presented in the following Chapters 5 and 6 in the form of time profiles of the population evolution.

In the "static" approach of Chapter 5, which does not take vibrational dynamics into account, these probabilities are written as follows

$$P_{H_2}(t) = |\alpha_0(t)|^2 \tag{4.53a}$$

$$P_{H_2^+}(t) = \sum_{v^+} |\beta_{v^+}(t)|^2 \tag{4.53b}$$

$$P_{2H^+}(t) = \int |\gamma_\varepsilon(t)|^2 \, d\varepsilon \,. \tag{4.53c}$$

Note that if we don't integrate the Coulomb explosion probability (4.53c) on the energy, we obtain directly by $|\gamma_\varepsilon(t)|^2$ a differential probability, resolved in time and dissociation energy.

In the "dynamical" approach of Chapter 6, which takes into account vibrational dynamics, the probability of being being bound in H_2 or in H_2^+ are written as follows

$$P_{H_2}(t) = \int |\psi_{H_2}(R,t)|^2 \, dR \tag{4.54a}$$

$$P_{H_2^+}(t) = \int |\psi^{g}_{H_2^+}(R,t)|^2 \, dR + \int |\psi^{u}_{H_2^+}(R,t)|^2 \, dR \,. \tag{4.54b}$$

In H_2^+, however, part of the population is bound and part is dissociated. To separate the probability of forming bound H_2^+ from the probability of forming the fragments H^+ + H(1s), we can project the $\psi^g_{H_2^+}(R, t_f)$ wave packet obtained at the end of propagation $(t = t_f)$ onto the bound vibrational states of the molecular ion, but this procedure does not give access to the energy-resolved kinetic energy release (KER) spectrum. To compute this spectrum, we project the $\psi^g_{H_2^+}(R, t_f)$ and $\psi^u_{H_2^+}(R, t_f)$ wave packets obtained at the end of the propagation onto the field-free dissociative molecular states associated with the $V^g_{H_2^+}(R)$ and $V^u_{H_2^+}(R)$ potentials, respectively.

The Coulomb explosion KER spectrum, on the other hand, is obtained by direct projection of the H_2^+ nuclear wave packets, taking into account the variation with R of the semiclassical ionization probabilities. We start by calculating, for each time interval δt, the spatial distribution $P_{CE}(R), t$ projected onto the Coulomb explosion channel according to

$$P_{CE}(R,t) = \left[W^{SC}_{H_2^+,g}(R,t)\delta t\right] |\psi^g_{H_2^+}(R,t)|^2 + \left[W^{SC}_{H_2^+,u}(R,t)\delta t\right] |\psi^u_{H_2^+}(R,t)|^2 \quad (4.55)$$

and from this spatial distribution, an energy-resolved KER spectrum is then extracted thanks to the simple law relating the internuclear distance R to the dissociation energy E in this Coulomb explosion channel, $E = 1/R$, as explained in Chapter 6, Eqs. (6.12) and (6.13).

Summary

In this chapter we have attempted to reduce complex ionization dynamics including electron correlation to more efficient semiclassical simulations of ionization rates, in order to save computational resources that can then be used to consider vibrational dynamics and thus achieve a more realistic description of the molecular double ionization dynamics of H_2 in strong laser fields. To this end, two possible approximations are explored: the simpler MO-ADK approximation, which gives satisfactory results in the wavelength and intensity ranges associated with dominant tunnel ionization, and the more complex MO-PPT approximation, which allows to explore larger ranges of laser intensity and field frequency.

Adding the dissociation dynamics to the simulation implied generating a vibrational basis to our wave packet, which was made possible with the use of Numerov's method to generate eigenstates and their associated eigenvalues (energies) from the potentials. To get a better estimation of the molecular dynamics,

a shift from an algorithm using only population transfers to a global wave packet ionization including conservation of their phase was done, which as we will see in the next chapters, will considerably alter the resulting dynamics in a way that brings observables to values closer to reality. To induce propagation of the wave packet during the simulation, a split-operator method is used, composed of alternating kinetic and potential operators applied on the wave packets.

Bibliography

[1] L. D. Landau and E. M. Lifshitz. *Quantum Mechanics: Non-Relativistic Theory*, volume 3. Pergamon Press, 3 edition, 1977.

[2] A. M. Perelomov, V. S. Popov, and M. V. Terent'ev. Ionization of atoms in an alternating electric field. *J. Exptl. Theoret. Phys. (U.S.S.R.)*, 50:1393–1409, 1966.

[3] A. M. Perelomov, V. S. Popov, and M. V. Terent'ev. Ionization of atoms in an alternating electric field II. *J. Exptl. Theoret. Phys. (U.S.S.R.)*, 51:309–326, 1967.

[4] A. M. Perelomov and V. S. Popov. Ionization of atoms in an alternating electric field III. *J. Exptl. Theoret. Phys. (U.S.S.R.)*, 52:514–526, 1967.

[5] M. V. Ammosov, N. B. Delone, and V. P Krainov. Tunnel ionization of complex atoms and of atomic ions in an alternating electromagnetic field. *Sov. Phys. JETP*, 64(6):1191, 1986.

[6] I. I. Fabrikant and G. A. Gallup. Semiclassical propagation method for tunneling ionization. *Phys. Rev. A*, 79:013406, Jan 2009. URL: https://link.aps.org/doi/10.1103/PhysRevA.79.013406, doi:10.1103/PhysRevA.79.013406.

[7] C. Cornaggia and Ph. Hering. Nonsequential double ionization of small molecules induced by a femtosecond laser field. *Phys. Rev. A*, 62:023403, Jul 2000. URL: https://link.aps.org/doi/10.1103/PhysRevA.62.023403, doi:10.1103/PhysRevA.62.023403.

[8] X. M. Tong, Z. X. Zhao, and C. D. Lin. Theory of molecular tunneling ionization. *Phys. Rev. A*, 66:033402, Sep 2002. URL: https://link.aps.org/doi/10.1103/PhysRevA.66.033402, doi:10.1103/PhysRevA.66.033402.

[9] E. P. Benis, J. F. Xia, X. M. Tong, M. Faheem, M. Zamkov, B. Shan, P. Richard, and Z. Chang. Ionization suppression of Cl_2 molecules in intense laser fields. *Phys. Rev. A*, 70:025401, Aug 2004. URL: https://link.aps.org/doi/10.1103/PhysRevA.70.025401, doi:10.1103/PhysRevA.70.025401.

[10] W. Kolos and L. Wolniewicz. Potential-Energy Curves for the $\chi^1\Sigma_g^+$, $b^3\Sigma_u^+$, and $C^1\Pi_u$ States of the Hydrogen Molecule. *J. Chem. Phys.*, 43:2429, 1965. URL: https://pubs.aip.org/aip/jcp/article-abstract/43/7/2429/81403/Potential-Energy-Curves-for-the-X-1-g-b3-u-and-C-1?redirectedFrom=fulltext, doi:10.1063/1.1697142.

[11] J. M. Peek. Eigenparameters for the $1s\sigma_g$ and $2p\sigma_u$ Orbitals of H_2^+. *J. Chem. Phys.*, 43:3004, 1965. URL: https://pubs.aip.org/aip/jcp/article-abstract/43/9/3004/82697/Eigenparameters-for-the-1s-g-and-2p-u-Orbitals-of?redirectedFrom=fulltext, doi:10.1063/1.1697265.

[12] M. M. Madsen and J. M. Peek. Eigenparameters for the lowest twenty electronic states of the hydrogen molecule ion. *At. Data Nucl. Data Tables*, 2:IN3–204, 1970. URL: https://www.sciencedirect.com/science/article/pii/S0092640X70800080, doi:https://doi.org/10.1016/S0092-640X(70)80008-0.

[13] B. V. Noumerov. A Method of Extrapolation of Perturbations. *Monthly Notices of the Royal Astronomical Society*, 84(8):592–602, 06 1924. URL: https://academic.oup.com/mnras/article/84/8/592/1064858?login=false, doi:10.1093/mnras/84.8.592.

[14] B. Numerov. Note on the numerical integration of $d^2x/dt^2 = f(x,t)$. *Astronomische Nachrichten*, 230(19):359–364, 1927. URL: https://onlinelibrary.wiley.com/doi/abs/10.1002/asna.19272301903, doi:https://doi.org/10.1002/asna.19272301903.

[15] I. N. Levine. *Quantum Chemistry*. Pearson Education, Inc., London, England, 7 edition, 2014.

[16] S. J. Singer, K. F. Freed, and Y. B. Band. Theory of diatomic molecule photodissociation: Electronic angular momentum influence on fragment and fluorescence cross sections. *The Journal of Chemical Physics*, 79(12):6060–6085, 12 1983. URL: https://pubs.aip.org/aip/jcp/article-abstract/79/12/6060/88036/Theory-of-diatomic-molecule-photodissociation?redirectedFrom=fulltext, doi:10.1063/1.445788.

[17] J.-N. Vigneau, O. Atabek, T.-T. Nguyen-Dang, and E. Charron. Strong field non-Franck–Condon ionization of H_2: a semi-classical analysis. *The European Physical Journal Special Topics*, 232(13):2081–2093, 2023. URL: https://link.springer.com/article/10.1140/epjs/s11734-022-00750-z, doi:10.1140/epjs/s11734-022-00750-z.

[18] M. D. Feit, J. A. Fleck, and A. Steiger. Solution of the Schrödinger equation by a spectral method. *Journal of Computational Physics*, 47(3):412–433, 1982. URL: https://www.sciencedirect.com/science/article/pii/0021999182900912, doi:https://doi.org/10.1016/0021-9991(82)90091-2.

[19] A. D. Bandrauk and H. Shen. Exponential split operator methods for solving coupled time-dependent Schrödinger equations. *The Journal of Chemical Physics*, 99(2):1185–1193, 07 1993. URL: https://pubs.aip.org/aip/jcp/article-abstract/99/2/1185/688669/Exponential-split-operator-methods-for-solving?redirectedFrom=fulltext, doi:10.1063/1.465362.

Chapter 5 Strong Field Non-Franck-Condon Ionization of H_2: A Semiclassical Analysis

This chapter is an authorized reproduction of an article that has been published in *The European Physical Journal Special Topics* (2023).
DOI: 10.1140/epjs/s11734-022-00750-z

The paper and its original bibliography are enriched by further explanations and analyses of unpublished, related results in an annex at the end of the chapter, after the article itself.

Contents

Strong Field Non-Franck-Condon Ionization of H_2: A Semi-Classical Analysis

Jean-Nicolas Vigneau,[1,2*] **Osman Atabek,**[1] **Thanh-Tung Nguyen-Dang**[2*)] **and Eric Charron**[1*]

[1]Université Paris-Saclay, CNRS, Institut des Sciences Moléculaires d'Orsay, 91405, Orsay, France.
[2]Département de chimie, COPL, Université Laval, 1045 av. de la Médecine, Québec, G1V 0A6, Québec, Canada.

*Corresponding author(s). E-mail(s): jean-nicolas.vigneau@universite-paris-saclay.fr; thanh-tung.nguyen-dang@chm.ulaval.ca; eric.charron@universite-paris-saclay.fr;

Résumé

L'ionisation simple de la molécule H_2 exposée à une impulsions laser intense et ultrabrève est étudiée par une méthode semi-classique. Trois caractéristiques du laser sont considérées : i) La fréquence de l'onde porteuse correspondant aux longueurs d'onde couvrant et reliant les deux régimes d'ionisation : De l'ionisation tunnel (TI) à 800 nm à l'ionisation multiphotonique (MPI) à 266 nm. ii) Les valeurs de l'intensité maximale sont choisies dans une fenêtre pour éliminer les processus d'ionisation double en compétition. iii) Une attention particulière est portée à la polarisation du champ laser, qui peut être polarisée de manière linéaire ou circulaire. Les résultats et leur interprétation concernent deux observables : la probabilité d'ionisation totale à la fin de l'impulsion et la distribution des populations vibrationnelles générée dans le cation H_2^+. Les résultats les plus marquants sont une efficacité d'ionisation accrue en polarisation linéaire et une distribution vibrationnelle du cation qui favorise les niveaux plus bas que ceux qui seraient peuplés dans une ionisation verticale (Franck-Condon), conduisant à des distributions non Franck-Condon, à la fois en polarisation linéaire et circulaire.

Mots clés: Photoionisation de H_2, Impulsions laser courtes et intenses, Polarisation linéaire versus circulaire, Profils d'ionisation, Distributions non-Franck-Condon, Méthodes ADK et PPT moléculaires.

Abstract

Single ionization of H_2 molecules exposed to strong and short laser pulses is investigated by a semi-classical method. Three laser characteristics are considered: i) The carrier-wave frequency corresponds to wavelengths covering and bridging the two ionization regimes: From tunnel ionization (TI) at 800 nm to multiphoton ionization (MPI) at 266 nm. ii) Values of the peak intensity are chosen within a window to eliminate competing double ionization processes. iii) Particular attention is paid to the polarization of the laser field, which can be linearly or circularly polarized. The results and their interpretation concern two observables, namely the end-of-pulse total ionization probability and vibrational distribution generated in the cation H_2^+. The most prominent findings are an increased ionization efficiency in linear polarization and a vibrational distribution of the cation that favors lower-lying levels than those that would be populated in a vertical (Franck-Condon) ionization, leading to non Franck-Condon distributions, both in linear and circular polarizations.

Keywords: H_2 photoionization, Short intense laser pulses, Linear versus circular polarization, Ionization profiles, Non-Franck-Condon distributions, Molecular ADK and PPT methods.

5.1 . Introduction

Imaging and controlling correlated electronic and nuclear dynamics in their natural time scales is a difficult challenge of ultrafast science [1]. This is because irradiating a molecule with intense, short laser pulses will lead to a competition between ionization and dissociation processes. Even though these dynamics are expected to evolve on different time scales, a strong field phenomenon such as Coulomb explosion can bring them together and in competition, especially in multi-electron systems. Experimental observations has been reported recently [2] of molecular above-threshold dissociation (ATD) during the time scale of the strong-field ionization of dihydrogen, giving rise to concomitant Above-Threshold Ionization spectra (ATI). Experimental spectroscopic and imaging techniques based on the celebrated three-step rescattering mechanism [3, 4], such as attosecond pump-probe spectroscopy [5], high-order harmonic spectroscopy [6] and laser-induced electron diffraction [7–10] can unravel the intricate interplay of electronic and nuclear motions, but they depend on its understanding and control for an optimal functioning of these as ultrafast analytical tools.

From a theoretical and computational viewpoint, a full quantum description of dissociative ionization of multi-electron molecules taking into account electron correlation as well as nuclear motions is highly desirable, and represents a huge technical challenge, scarcely attempted [11] in the strong-field litterature. Even for the simplest many-electron molecular system H_2, solving the full multi-dimensional time-dependent Schrödinger equation (TDSE) for all electronic and nuclear degrees of freedom represents a formidable computational task. For this molecule, reduced-dimension models have been used, and allow partial captures of the coupled electron-nuclear dynamics and even of essential features of the double ionization of the molecule [12–15].

No matter the approach one has in mind for the electronic part of the laser-driven molecular dynamics, it is the description of ionization steps, strong bound-to-free transitions, that is limiting, and resource-demanding. In view of this, there is an interest to adapt existing analytical theories of ionization, in particular semi-classical theories such as the Ammosov-Delone-Krainov (ADK) [16, 17] and the Perelomov-Popov-Terent'ev (PPT) [18–20] models, into an algorithm for the numerical calculations of ionization amplitudes out of an arbitrary initial molecular orbital (MO). The ultimate aim would be to incorporate this simplified ionization algorithm into a code treating the full laser-induced electronic dynamics, coupled to vibrational degrees of freedom. There is thus a need to explore how the ionization rate expressions derived in these semi-classical theories can be used to calculate and understand the ionization dynamics of the molecule at a fixed nuclear geometry, (or in a range of nuclear geometries) considered as a parameter, before including these as parts of a complete quantum dynamical model.

The present theoretical work is such a preliminary study devoted specifically to the ionization of H_2 molecules exposed to moderately intense laser pulses, investigated by the ADK and PPT approximations in their adaptations to molecular systems to give the MO-ADK [21] and MO-PPT [22] theories respectively. Concentrating on the first ionization of the two-electron molecule, we consider two electronic states: the initial ground state $X^1\Sigma_g^+$ of H_2 and the $X^2\Sigma_g^+$ $(1s\sigma_g)$ state of H_2^+. More specifically, we are interested in the initial preparation of the cation, in a superposition of its vibrational levels, by an ionizing laser pulse. It is the subsequent dissociation process of the cation that involves the field coupling of the $1s\sigma_g$ and $2p\sigma_u$ states of H_2^+, and this post-ionization dynamics is not considered here. The radiative coupling to the excited $2p\sigma_u$ state of the cation is therefore neglected. Still another simplification we will eventually make is the neglect of the double ionization process, leading to the Coulomb Explosion of the molecule. This is justified if we stay in a rather moderate laser intensity

range, the double ionization entering into competition only for intensities exceeding certain thresholds (above a few 10^{14} W/cm^2 at 800 nm, to fix the ideas). The effect of various parameters of the laser field, in particular its wavelength (in the IR and UV spectral regions), peak intensity and polarization, is analysed in terms of two calculated observables: the total ionization probability, and the distribution of populations on the vibrational states of the field-free cation, all taken at the final time of the laser pulse. The last observable highlights deviations from the usually assumed Franck-Condon distribution. We will discuss the origin of this non-Franck-Condon distribution in an assessment of the semiclassical ionization model used.

The manuscript is organized as follows. Section 5.2 starts with the equations governing the time-evolution of the populations of the two-electron molecule in the basis of relevant vibronic states of the neutral H_2, the cation H_2^+, and the Coulomb Explosion channel $H^+ + H^+$. In physical terms, they are kinetic rate equations describing the relative population gains and losses among these states during the single and double ionization processes. The ionization rates driving these equations have the form of rate constants, and are obtained from the MO-ADK or the MO-PPT theories, and carry a parametric dependence on the internuclear distance R of the molecule through the molecular ionization potential. Section 5.3 gives the results concerning the two observables of interest, discussed in terms of the distinction between tunnel or multiphoton ionization regimes. The most important conclusions of this section are: (i) for a given fluence, the linearly polarized field is more efficient than a circular one in terms of the ionization yield. (ii) The molecular ion vibrational distribution as prepared by the ionization step is shifted from $v_+ = 2$ (as predicted by a vertical Franck-Condon preparation) to lower vibrational v_+ levels. When comparing the respective roles of the laser polarization, the differences between linear and circular polarizations in terms of non-Franck-Condon ionization are small.

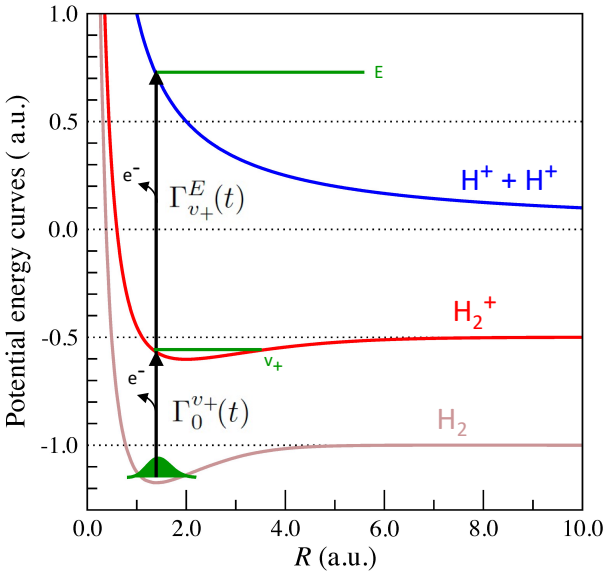

Figure 5.1: Depiction of the ionization paths of the H_2 vibrational state $v = 0$ (wave function depicted in green) from its initial potential well (brown) into its ionized vibrational states v_+ (green) in the H_2^+ ground electronic potential (red), and ultimately to its Coulomb explosion potential H^++H^+ (blue) with the kinetic energy E (green).

5.2 . Methods

The dynamics of single and double ionization of H_2 in a time-dependent laser field $F(t)$ is treated by solving the rate equations

$$\left.\frac{dP_{\mathrm{H_2}}}{dt}\right|_t = -\Gamma_0^+(t)\, P_{\mathrm{H_2}}(t) \tag{5.1a}$$

$$\left.\frac{dP_{v_+}}{dt}\right|_t = \Gamma_0^{v_+}(t)\, P_{\mathrm{H_2}}(t) - \Gamma_{v_+}^{\mathrm{CE}}(t)\, P_{v_+}(t) \tag{5.1b}$$

$$\left.\frac{dP_{\mathrm{CE}}}{dt}\right|_t = \sum_{v_+} \Gamma_{v_+}^{\mathrm{CE}}(t)\, P_{v_+}(t) \tag{5.1c}$$

where $P_{\mathrm{H_2}}(t)$ is the total population of H_2, $P_{v_+}(t)$ is the population of the vibrational level v_+ in the ground electronic state of H_2^+ and $P_{\mathrm{CE}}(t)$ is the total population in the [H^+ + H^+] (Coulomb Explosion) dissociation continuum. As a consequence, the total population of H_2^+, expressed as

$$P_{\mathrm{H_2^+}}(t) = \sum_{v_+} P_{v_+}(t), \tag{5.2}$$

is calculated within the state-resolved complete ionization dynamics of the molecule, which includes both the gain of population of the cation from the (first) ionization of the neutral H_2 molecule, and its loss due to the second ionization. The passage of the population from H_2 to its ionized states is represented schematically in Fig. 5.1.

The instantaneous molecular ionization rates $\Gamma_0^+(t)$, $\Gamma_0^{v_+}(t)$ and $\Gamma_{v_+}^{\mathrm{CE}}(t)$ are obtained as described hereafter using the molecular ADK or PPT approximations. The total single ionization rate $\Gamma_0^+(t)$ is expressed as a sum over all accessible vibrational levels v_+ as

$$\Gamma_0^+(t) = \sum_{v_+} \Gamma_0^{v_+}(t) \tag{5.3}$$

with

$$\Gamma_0^{v_+}(t) = \left| \int \chi_{v_+}^*(R) \Big(W_{\mathrm{H}_2}[R,t] \Big)^{\frac{1}{2}} \chi_0(R)\, dR \right|^2 \tag{5.4}$$

where $W_{\mathrm{H}_2}[R,t]$ is the instantaneous molecular ADK or PPT ionization rate at the internuclear distance R and at time t given by

$$W_{\mathrm{H}_2}[R,t] = W_{\mathrm{ADK/PPT}}\Big[I_{\mathrm{H}_2}(R), F(t) \Big]. \tag{5.5}$$

The molecular ADK and PPT ionization rates W_{ADK} and W_{PPT} used here are given in Eqs. (5.11) and (5.15), and are calculated for the H_2 ionization potential $I_{\mathrm{H}_2}(R)$ and the electric field amplitude $F(t)$. The ionization potential is taken as the energy separating the ground electronic states of H_2 and H_2^+. In Eq. (5.4), $\chi_0(R)$ is the wave function associated with the ground vibrational state of H_2 and $\chi_{v_+}(R)$ is the wave function associated with the vibrational level v_+ of the ground electronic state of the cation. These are calculated numerically using a Numerov type of algorithm [23], to solve for eigenstates supported by the potential energy curves for the ground electronic states of H_2 and H_2^+, themselves taken from Refs. [24] and [25, 26] respectively.

Similarly, the total ionization rate of the v_+ vibrational level of the cation H_2^+, $\Gamma_{v_+}^{\mathrm{CE}}(t)$, is expressed as a sum over all Coulomb Explosion energies E as

$$\Gamma_{v_+}^{\mathrm{CE}}(t) = \int \Gamma_{v_+}^{E}(t)\, dE \tag{5.6}$$

with

$$\Gamma_{v_+}^{E}(t) = \left| \int \chi_E^*(R) \Big(W_{\mathrm{H}_2^+}[R,t] \Big)^{\frac{1}{2}} \chi_{v_+}(R)\, dR \right|^2 \tag{5.7}$$

where

$$W_{\mathrm{H}_2^+}[R,t] = W_{\mathrm{ADK/PPT}}\Big[I_{\mathrm{H}_2^+}(R), F(t) \Big] \tag{5.8}$$

and where $\chi_E(R)$ represents the wave function of the energy normalized Coulomb Explosion dissociative continuum at energy E. It is calculated numerically using the Numerov algorithm also, with the Coulomb $1/R$ repulsion as potential energy curve. The ionization potential $I_{H_2^+}(R)$ is taken here as the energy separating the $1/R$ Coulomb repulsion energy potential curve from the ground electronic potential curve of H_2^+.

At time $t = 0$, the system is in the ground vibrational level of the ground electronic state of H_2, with

$$\begin{aligned} & P_{H_2}(0) &=& \ 1, \\ \forall v_+, \quad & P_{v_+}(0) &=& \ 0, \\ & P_{CE}(0) &=& \ 0, \end{aligned} \tag{5.9}$$

and since the sum of Eqs. (5.1a), (5.1b) and (5.1c) is zero, one can note that the total population

$$P_{H_2}(t) + P_{H_2^+}(t) + P_{CE}(t) = 1 \tag{5.10}$$

is naturally conserved throughout the entire ionization process.

The molecular ADK (or MO-ADK) ionization rate is given by [21]

$$W_{ADK}\Big[I_p, F\Big] = B_0^2 \left(\frac{2\kappa^2}{F}\right)^{\xi} \exp\left(-\frac{2\kappa^3}{3F}\right), \tag{5.11}$$

where $\kappa = \sqrt{2I_p}$, $\xi = (2Z/\kappa) - 1$, and

$$B_0(\theta) = \sum_l \sqrt{\frac{2l+1}{2}}\, C_l\, P_l(\cos\theta)\,. \tag{5.12}$$

Z is the effective Coulomb charge seen asymptotically by the electron and θ is the angle between the laser field and the molecular axis. In the case of linear polarization, the time dependent electric field amplitude is given by $F(t) = |\mathbf{F}(t)|$, where

$$\mathbf{F}(t) = F_0\, f(t) \cos(\omega t)\, \mathbf{e}_\theta \tag{5.13}$$

ω is the carrier frequency and F_0 the electric-field amplitude. $f(t) = \sin^2(\pi t/t_f)$ denotes the temporal envelope of the pulse, t_f being the total pulse duration, $\mathbf{e}_\theta = [\cos\theta\, \mathbf{e}_z + \sin\theta\, \mathbf{e}_x]$ is the unit vector along the direction of the fixed polarization of the field, which makes an angle θ with respect to the molecular axis. In this case of linear polarization, we will limit ourselves to the angle $\theta = 0$, corresponding to a situation where the molecule is aligned with the field. In the case of circular polarization, the time dependent electric field is given by

$$\mathbf{F}(t) = F_0\, f(t) \Big[\, \cos(\omega t)\, \mathbf{e}_z + \sin(\omega t)\, \mathbf{e}_x \Big]\,, \tag{5.14}$$

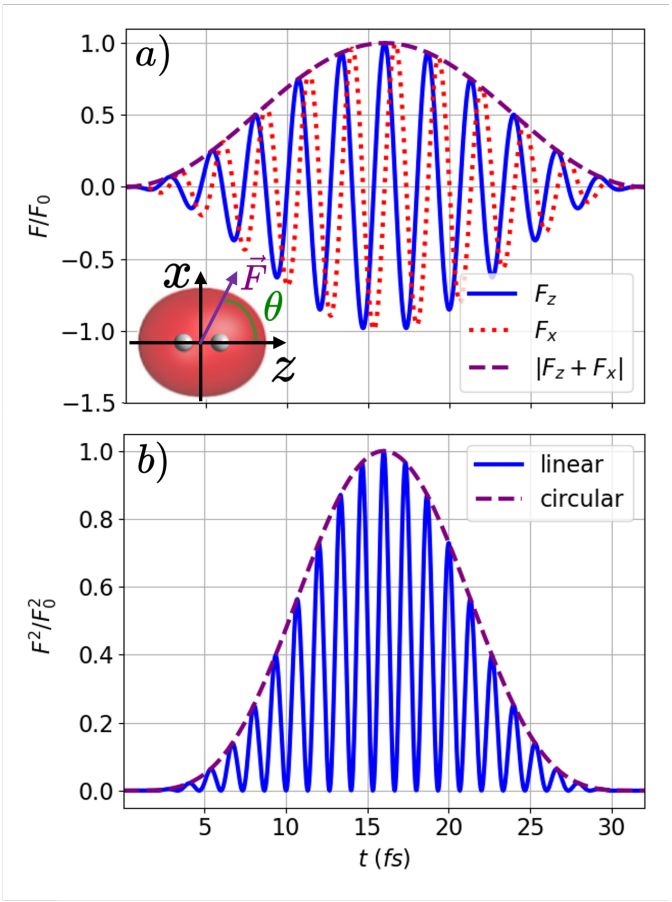

Figure 5.2: Panel (a): 800 nm circularly polarized laser electric field components along the z-axes ($F_z(t)$, full blue line), and along the x-axes ($F_x(t)$, dotted red line) as a function of time. The H_2 molecular axis is aligned along z-axis. θ is the angle between the intermolecular axis and the instantaneous field direction. Panel (b): Square modulus of the linear (full blue line) and circular (dashed purple line) fields as a function of time.

i.e. the angle θ becomes time-dependent, with $\theta(t) = \omega t$. It is to be noted that the field amplitude F_0 for the circular polarization case is chosen as the one for the linear case divided by $\sqrt{2}$, such that the average value of $F^2(t)$ over an optical cycle is identical in linear and circular polarization. The coefficients C_l in Eq. (5.12) ensure the anisotropy of the ionization by the different weighting of the spherical harmonics-related Legendre polynomials $P_l(\cos\theta)$ of quantum number l. The values of the coefficients C_l are experimentally fitted in Refs. [27] and [28], and are provided in Table 5.1 for both the ionization of H_2 and of H_2^+. Figure 5.2 shows the electric field components F_z and F_x and their square modulus for circular polarization along the z and x axes. The linear polarization cor-

responds solely to F_z. The upper panel also illustrates the angular positioning of the H_2 molecule assumed to lie on the z-axis.

Table 5.1: Anisotropy coefficients C_l for H_2 [27] and H_2^+ [28]

l	C_l for H_2	C_l for H_2^+
0	2.4350	4.52
2	0.1073	0.62
4	0.0010	0.03

In the molecular PPT (or MO-PPT) approach, the ionization rate is given by [22]

$$W_{\mathrm{PPT}}\big[I_p, F\big] = B_0^2 \left(\frac{2\kappa^2}{F\sqrt{1+\gamma^2}}\right)^{\xi} \exp\left(-\frac{2\kappa^3}{3F} g(\gamma)\right) \times A_0(\omega,\gamma)\,(1+2\gamma)^{-2Z/\kappa}\,, \quad (5.15)$$

when taking into account the Coulomb correction factor [29]. In this expression $\gamma = \omega\sqrt{2I_p}/F$ is the (frequency dependent) Keldysh parameter [30, 31]. The expressions of $g(\gamma)$ and $A_0(\omega,\gamma)$ differ in linear and circular polarizations. For the case of linear polarization, $A_0(\omega,\gamma)$ is given by

$$A_0(\omega,\gamma) = \frac{\beta^2(\gamma)}{\sqrt{3\pi}} \sum_{\tilde{n}>\nu}^{\infty} \Omega_0\Big(\sqrt{\tilde{n}'\beta(\gamma)}\Big) e^{-\tilde{n}'\alpha(\gamma)} \quad (5.16)$$

where $\tilde{n}' = \tilde{n} - \nu$ with $\nu = \frac{I_p}{\omega}\left(1 + \frac{1}{2\gamma^2}\right)$. The sum therefore runs over the number of photons $\tilde{n}$ absorbed above the ionization threshold. In practice, in the numerical evaluation of $A_0(\omega,\gamma)$, we considered the sum (5.16) converged when its relative gain over an iteration was less than 10^{-10} of the current sum value. In addition, we have

$$\Omega_0(x) = \frac{x}{2}\int_0^1 \frac{e^{-x^2 t}}{\sqrt{1-t}}dt\,, \quad (5.17a)$$

$$\alpha(\gamma) = 2\,\mathrm{Arsh}(\gamma) - \beta(\gamma)\,, \quad (5.17b)$$

$$\beta(\gamma) = \frac{2\gamma}{\sqrt{1+\gamma^2}}\,, \quad (5.17c)$$

$$g(\gamma) = \frac{3}{2\gamma}\left[\left(1+\frac{1}{2\gamma^2}\right)\mathrm{Arsh}(\gamma) - \frac{1}{\beta(\gamma)}\right] \quad (5.17d)$$

Finally, in the case of circular polarization A_0 is a a function of γ only, and the expressions of $A_0(\gamma)$ and $g(\gamma)$ involved in the MO-PPT ionization rate (5.15) become

$$A_0(\gamma) = (1-t_0)\left[\frac{\gamma^2(1+\gamma^2)(1-t_0^2)}{(\gamma^2+t_0^2)(1+t_0^2+2t_0^2/\gamma^2)}\right]^{\frac{1}{2}} \quad (5.18)$$

and

$$g(\gamma) = \frac{3t_0}{\gamma^2(1-t_0^2)}\left[(1+\gamma^2)\left(1+\frac{t_0^2}{\gamma^2}\right)\right]^{\frac{1}{2}} \tag{5.19}$$

where t_0 function of γ, is a real positive root, in the interval [0,1], of the following equation [18]

$$\mathrm{Arth}\left(\sqrt{\frac{t_0^2+\gamma^2}{1+\gamma^2}}\right) = \frac{1}{1-t_0}\sqrt{\frac{t_0^2+\gamma^2}{1+\gamma^2}}\,. \tag{5.20}$$

For practical reasons, it is convenient to fit $t_0(\gamma)$ using a simple analytical function. Indeed, one can very accurately fit this variation with γ using an eighth order Padé approximant [32] in the form

$$t_0(\gamma) = \left(\sum_{i=0}^{8} a_i\,\gamma^i\right) \Big/ \left(\sum_{i=0}^{8} b_i\,\gamma^i\right) \tag{5.21}$$

The corresponding fitting parameters a_i and b_i are provided in table 5.2. We have verified that the relative error made when using this simplified analytic expression is always less than 6×10^{-4} on the interval $\gamma\in[0,100]$.

Table 5.2: Padé approximant parameters for t_0.

i	a_i	b_i
0	0	1
1	0	1.97454
2	1/3	2.50994
3	6.58161×10^{-1}	2.46203
4	6.29483×10^{-1}	1.55840
5	4.09872×10^{-1}	7.56738×10^{-1}
6	1.41151×10^{-1}	1.97492×10^{-1}
7	9.97954×10^{-3}	1.23464×10^{-2}
8	1.02588×10^{-4}	1.17511×10^{-4}

5.3 . Results

In this section we first justify the consideration of the first step of the complete ionization dynamics of H_2, the first ionization of the two-electron molecule, by

referring to an intensity range which allows one to separate its single and double ionizations. We then analyze the performances of the two semi-classical approaches, MO-ADK and MO-PPT, by comparing the ionization yields they predicted to results of full quantum mechanical TDSE calculations. We confirm through this comparison that MO-PPT is actually a rather good approximation for describing ionizations both in tunnel or multiphoton regimes. Finally, we discuss and interpret results of MO-PPT calculations on two observables, namely the final ionization probability vs. intensity profiles and the non Franck-Condon vibrational distributions of H_2^+ as a function of the field intensity and polarization characteristics.

5.3.1 .Single versus double ionization

The laser-induced complete dissociative ionization of H_2, in a full quantum description, should consider the two electrons and the two protons on an equal footing, through a wavefunction evolution taking electron correlation fully into account and involving both the single and double ionization processes, together with the nuclear dynamics. Such a full quantum treatment remains a formidable methodological challenge. Depending on the laser pulse duration and leading intensity, the complete dissociative ionization dynamics can be described by steps of increasing sophistication. In particular, the two time scales of ionization and nuclear dynamics being very different, the possibility is offered to treat separately the two fragmentation processes, focusing as a first step solely on the ultra-fast ionization. Depending on the intensity of the laser, this will give rise to single, and sequential (or non-sequential) double ionization processes [15, 33, 34]. Neglecting all vibrational wave packet evolution during the pulse, all the ultra-fast ionization dynamics is encapsulated in the rate $W_{\mathrm{H_2}}[R,t]$ appearing in Eq. (5.4) which, as stated above, is obtained within a semi-classical approach either the simple, commonly used MO-ADK approach [21] or the more complete MO-PPT theory [22].

Figure 5.3 illustrates how the final population, (evaluated at the final time t_f of the laser pulse), of the initial neutral H_2 molecule, $P_{\mathrm{H_2}}(t_f)$, that of the molecular cation H_2^+ resulting from the first ionization, $P_{\mathrm{H_2^+}}(t_f)$, and the population of the Coulomb Explosion channel accessed from the second ionization, $P_{\mathrm{CE}}(t_f)$, vary as a function of the laser peak intensity I. For this illustrative purpose we are showing the results for a $\lambda = 800$ nm linearly or circularly polarized IR pulse extending over 12 optical cycles, for a total duration of about 32 fs. Results obtained by doubling or halving the pulse duration show that changing the pulse duration only scales up or down the total ionization probability without changing the relative populations of the different vibrational levels produced in H_2^+.

These results are collected in the Supplementary Information.

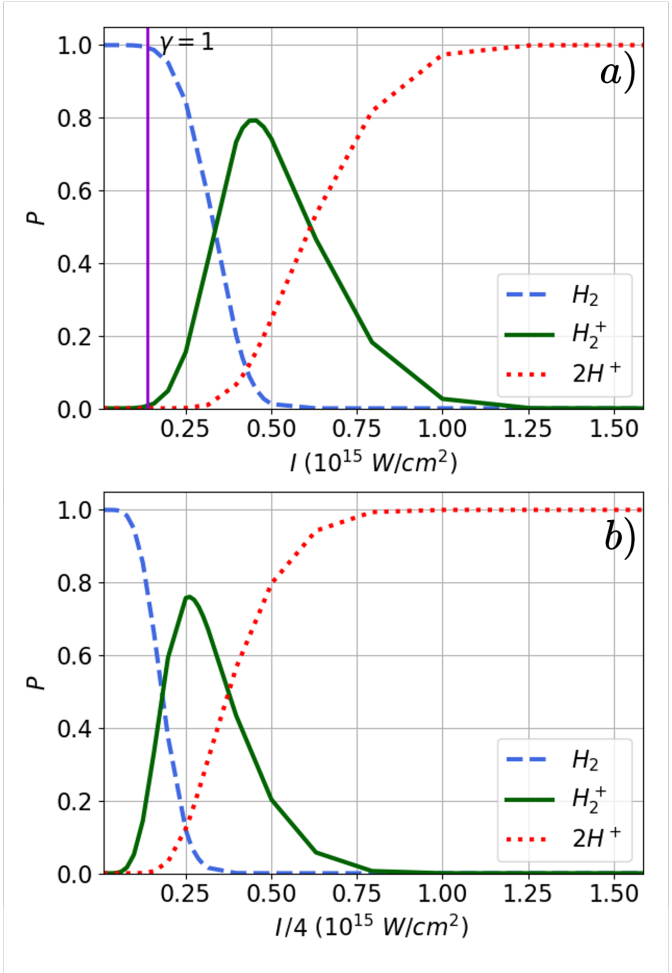

Figure 5.3: Final populations of H_2 ($P_{H_2}(t_f)$; dashed blue line), H_2^+ ($P_{H_2^+}(t_f)$; full green line) and $H^+ + H^+$ ($P_{CE}(t_f)$; Coulomb Explosion, red dotted line), using a 800 nm (a) linearly and (b) circularly polarized field, and the MO-PPT approach for a $\sin^2$ pulse envelope of total duration 32 fs corresponding to 12 optical cycles (16 fs FWHM). The vertical purple line in panel (a) indicates the value of the intensity at which the Keldysh parameter is $\gamma = 1$.

In Fig. 5.3, the first ionization is observed for peak intensities of about 10^{14} W/cm^2, with the precise onset intensity depending on the polarization of the field. There, the initial population of the neutral molecule starts to decrease while the H_2^+ cation's population increases up to about 0.8. It is only for field intensities typically larger than 4×10^{14} W/cm^2 in linear polarization and 10^{15} W/cm^2 in circular polarization that the second ionization process comes into play and the initial

state population decreases below 0.2. Note that this onset of second ionization would be shifted to a higher intensity for a shorter pulse (see Supplementary Information for details). It is worthwhile to note that this second ionization sets in basically by depleting the population of the H_2^+ cation. It is precisely in that respect that we can at least partly separate the two (first and second) ionization processes, defining the physical frame for our focus on the single ionization as a dominant process for intensities typically less than about 5×10^{14} W/cm^2 at 800 nm. This thus fixes the general framework of the present study which will concern from now on only the first ionization of H_2.

To be complete, a few additional observations are in order: (i) For intensities exceeding 10^{15} W/cm^2 the molecule is completely ionized both for linear or circular polarizations. (ii) An identification as to whether the ionization follows a tunnel or multiphoton regime can be given in terms of the already defined Keldysh parameter γ. The regime with $\gamma \ll 1$ is referred to as the tunnel ionization (TI) regime, where the electron escapes by tunneling through the barrier resulting from a field-distorted Coulomb potential. In the opposite limit of $\gamma \gg 1$, the electron ionizes after absorption of several photons, a regime termed multiphoton ionization (MPI). The field intensity value giving $\gamma = 1$ for the first ionization process is indicated by a vertical line in Fig. 5.3(a). It roughly delimits the two ionization regimes (TI and MPI). For a given ionization potential and field frequency, the Keldysh parameter takes on values less than 1 for field intensities higher than the limit indicated by the corresponding vertical line. In other words, basically all intensities within the first ionization profile studied here allow at 800 nm an interpretation of the dynamics in terms of the TI regime, where semi-classical approaches are normally rather well adapted. (iii) Finally, linear and circular polarizations give slightly different results. More precisely, switching the polarization from linear to circular, the first ionization $P_{H_2^+}$ vs. I profile is shifted towards higher intensities and acquires a broader extension. This could be interpreted by the fact that for the circularly polarized pulse, the electric field amplitude is lower, as opposed to the linearly polarized one at equal fluence.

5.3.2 .Validation of the semi-classical approaches

We proceed now to a quantitative assessment of the performances of the two semi-classical approximations MO-ADK and MO-PPT with respect to the first ionization of H_2, by comparing the calculated $P_{H_2^+}(t_f)$ with that predicted by a full quantum mechanical calculation [27, 35, 36], in which the two-electron TDSE was solved at a (full) Time-Dependent Configuration Interaction (TDCI) level, using CI wavefunctions comprising of thousands of configurations using Kohn-Sham (DFT) molecular orbitals expressed in an extended B-spline basis. The TDCI data

used here are those of figures 3, 5, 7 of Ref. [27] explicitly marked TDCI (as opposed to SAE-CI, based on a more limited CI expansion of the two-electron system eigenstates, as per the description of it in Ref. [27]). Note that this paper (Ref. [27]) assesses the validity of the SAE by comparing SAE calculations' results with the aforementioned TDCI results. It is the latter however that are relevant here. The comparison is made for a series of laser peak intensities ranging from 10^{13} W/cm^2 up to 10^{15} W/cm^2, and for three wavelengths, $\lambda = 266$ nm, 400 nm, 800 nm. The number of optical cycles are adjusted, for each value of λ, in such a manner as to have the same pulse duration. Both polarization cases, linear and circular, are considered. Figure 5.4 displays, for the linear polarization case, the final ionization probability as a function of intensity on a logarithmic scale to better enhance the large scale differences. The corresponding results for circular polarization are displayed in Fig. 5.5.

On numerical grounds, the present semi-classical calculations are in close agreement (graphical estimation) with those of the Fig. 5 of Ref. [37], despite a difference in the models for the calculation of the rate: averaged over H_2^+ vibrational states in this work (Eq. 5.4), and taken at H_2^+ equilibrium distance for Ref. [37]. We note that for the highest frequency considered ($\lambda = 266$ nm, panel (a) of Fig. 5.4) the ionization is basically in the multiphoton (MPI) regime, as all considered values of the field intensity I up to 10^{15} W/cm^2 give a Keldysh parameter $\gamma > 1$. In this case, the frequency-independent MO-ADK description fails by orders of magnitude in producing the correct H_2^+ population, at least up to $I = 3 \times 10^{14}$ W/cm^2. The MO-PPT model is a much better approximation, and gives results that basically follow the exact TDCI results. Semi-classical approximations are in better agreement among them and with the exact results for lower frequencies ($\lambda = 400$ nm, 800 nm, Fig. 5.4, panels (b), (c) respectively), where the tunnel mechanism becomes progressively dominant. This is indicated by the shift of the vertical line $\gamma = 1$ towards lower intensities in panels (b) and (c). In particular, a rather good agreement between MO-ADK and MO-PPT results is obtained at $\lambda = 800$ nm.

Although no TDCI calculations results are available for the case of circular polarization, we can still offer a reasonable interpretation of two observations in Fig. 5.5: (i) for the three wavelength considered, the threshold intensity for the H_2^+ population saturation is higher for the case of a circular polarization as compared to the linear polarization case, due to the lower circularly polarized field amplitude argument advanced previously; (ii) the slope of the rise of the ionization probability curve is much higher for $\lambda = 800$ nm than for $\lambda = 266$ nm. This is due to the fact that $\lambda = 800$ nm corresponds to the TI regime where the ionization yield is exponentially increasing with the intensity, as opposed to the

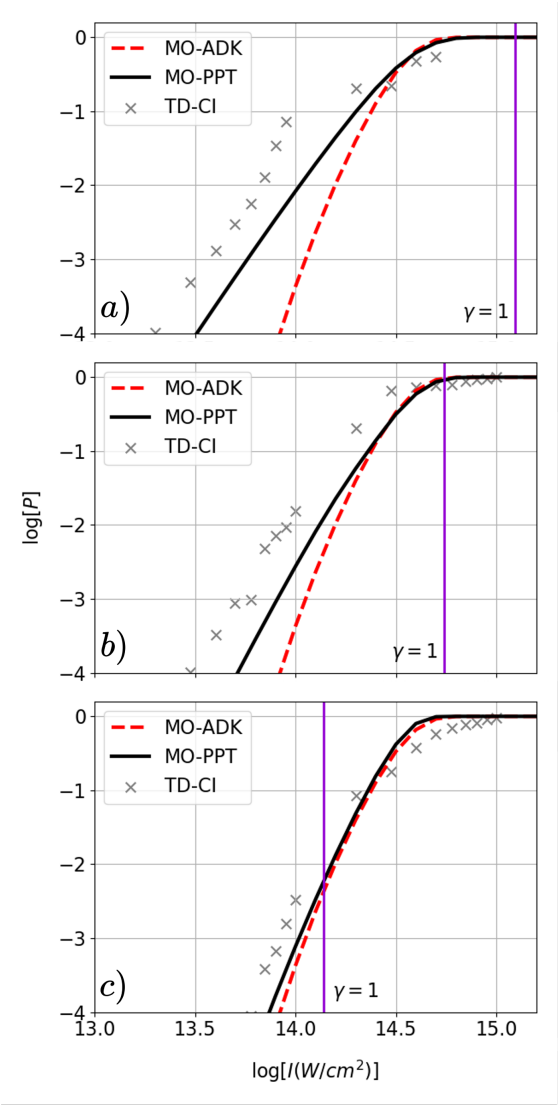

Figure 5.4: Final ionization probability of H_2 (in logarithmic scale) using a linearly polarized field of peak intensity I (in logarithmic scale), as given by MO-ADK (dashed red line), MO-PPT (full black line) and TDCI [27] (grey crosses) methods, with wavelengths of (a) 266 nm over 36 optical cycles, (b) 400 nm over 24 optical cycles and (c) 800 nm over 12 optical cycles. The total pulse duration is therefore fixed at the value 32 fs (16 fs FWHM).

$\lambda = 266$ nm case where the MPI regime is the leading one, giving rise to a slower power-type increase.

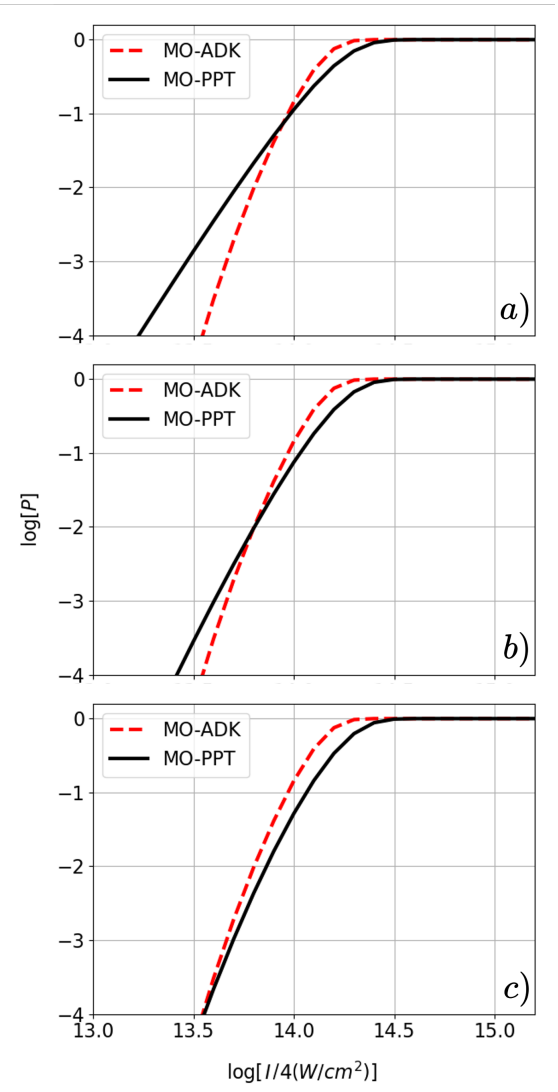

Figure 5.5: Final ionization probability of H_2 (in logarithmic scale) using a circularly polarized field of peak intensity I (in logarithmic scale), as given by MO-ADK (dashed red line) and MO-PPT (full black line) methods, with wavelengths of (a) 266 nm over 36 optical cycles, (b) 400 nm over 24 optical cycles and (c) 800 nm over 12 optical cycles. The total pulse duration is therefore fixed at the value 32 fs (16 fs FWHM).

5.3.3 . Non-Franck-Condon ionization

An interesting way of presenting the results of the integration of Eq. (5.1b) without the last term on the right hand side (since we are considering only the first ionization process, ignoring the Coulomb Explosion channel) is to plot, as a normalized function of v_+, in the form of a histogram, the populations $f^{nFC}(v_+)$ of

various vibrational states v_+ of the cation, relative to the final total population of cation $P_{H_2^+}(t_f)$, accumulated during the ionizing action of the laser pulse

$$\begin{aligned} f^{nFC}(v_+) &= \frac{P_{v_+}(t_f)}{P_{H_2^+}(t_f)} \\ &= \frac{1}{P_{H_2^+}(t_f)} \int_0^{t_f} \Gamma_0^{v_+}(t) P_{H_2}(t) dt \end{aligned} \tag{5.22}$$

This kind of plot gives the composition of the vibrational wave packet created in the cation as it is formed by the ionization of the neutral molecule H_2. It is often assumed that the ionization is a Franck-Condon (FC) process, *i.e.* the vertical promotion of the ground vibrational state $\chi_0(R)$ of H_2 onto the cation electronic ground-state manifold. This Franck-Condon principle corresponds to assume that $W_{H_2}[R,t]$ in Eq. (5.4) does not depend on the internuclear distance R. Eq. (5.22) then becomes

$$f^{FC}(v_+) = \frac{|\langle \chi_{v_+} | \chi_0 \rangle|^2}{\sum_{v_+} |\langle \chi_{v_+} | \chi_0 \rangle|^2} \tag{5.23}$$

Now, by the mere fact that the rate $W_{H_2}[R,t]$ as described by the MO-ADK formula for tunnel ionization, or by the more general MO-PPT expression, depends on the internuclear distance R through the first ionization potential $I_{H_2}(R)$ (see Eq. 5.5), we expect that the vibrational distribution in the cation does not follow the Franck-Condon principle. Indeed, the onset of a non-Franck-Condon behavior has been related to a sharp increase of the tunnel ionization rate as a function of the internuclear distance R by a number of authors [38, 39]. Such an increase in the ionization rate is expected when I_p decreases, and this is the case when R increases in the range $0 < R < 3.5$ a.u which is of interest to us, hence the relationship between $\Gamma_0^{v_+}$ and R. Another form of deviation from the Franck-Condon principle has been discussed in the literature [40], and pertains more to the field-induced deformation of the cation vibrational states onto which the initial (also deformed) vibrational wavefunction of the parent neutral molecule is projected. The ADK or PPT ionization rates used in this work contain the R-dependent ionization potential, and this does contribute in part to the non-Franck-Condon effect demonstrated therein. We also extend the analysis of non-Franck-Condon ionization to circular polarization, and to several wavelengths covering the TI and MPI regimes.

The R dependence of the square root of the ionization rate W_{PPT}, as it enters Eq. (5.4), is displayed in Fig. 5.6, panels (c) and (d) together with a pair of H_2^+ vibrational wavefunctions $\chi_{v_+}(R)$, with $v_+ = 1$ in (c) and $v_+ = 2$ in (d). The FC

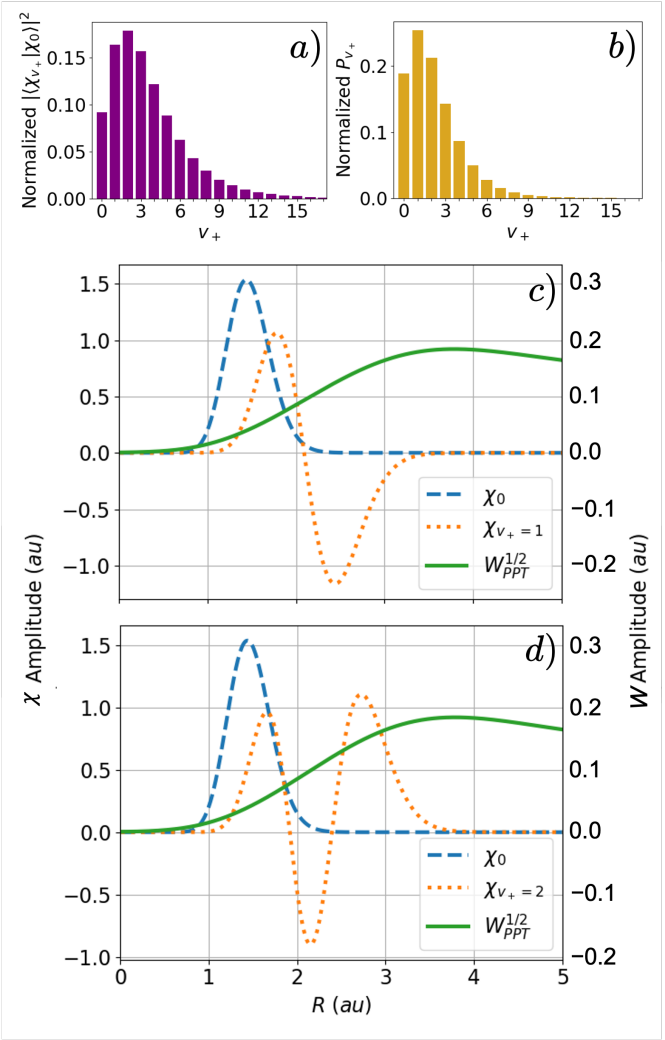

Figure 5.6: Franck-Condon projection of the H_2 ground state on the H_2^+ vibrational states v_+ (upper panel a), and the non-Franck-Condon population resulting from a MO-PPT circularly-polarized 800 nm field of peak intensity 6.4×10^{14} W/cm^2 (upper panel b). The lower panels display the wavefunctions of H_2 ground state (χ_0), together with the ones of the vibrational states (c) $v_+ = 1$ and (d) $v_+ = 2$ of H_2^+ (χ_{v_+}). The square root of the ionization amplitude calculated from the MO-PPT method ($W_{\rm PPT}^{1/2}$, from Eq. 5.15) using a 800 nm circularly polarized field and a typical peak intensity, is given as the solid green line, with a scale indicated on the right vertical axis.

distribution, $f^{FC}(v_+)$ is given by the histogram of panel (a), while that in panel (b) gives an example of non-Franck-Condon (non-FC) distribution, $f^{nFC}(v_+)$, as given in Eq. (5.22) with $\Gamma_0^{v_+}$ therein defined by Eq. (5.4) using $W_{\rm PPT}$. The distribution shown in panel (b) is for the specific case of a $\lambda = 800\,$nm, $I = 6.4 \times$

10^{14} W/cm^2 circularly polarized pulse.

The first general observation that can be made when comparing the FC with the non-FC distributions is that the maximum population is shifted from the $v_+ = 2$ level to the $v_+ = 1$ level, the ground $v_+ = 0$ population increasing also with respect to its FC value. The second observation is that the distribution stops at a lower value of v_+ than in the FC distribution: While the FC distribution in panel (a) extends to the last v_+ level ($v_+ = 18$) supported by the ground-state potential energy curve of H_2^+, the non-FC distribution in panel (b) acquires negligible values past $v_+ \simeq 10$. The quantitative details of these deviations with respect to the vertical FC ionization results depend on the specific values of the laser pulse parameters. We will give later a more detailed discussion of how these variations with respect to the FC distribution depend on the field polarization. For now, it suffices to say that the non-FC distribution that the MO-PPT ionization model affords is more compact, more restricted to the low-lying vibrational levels of the cation.

We can understand these salient traits of the non-Franck-Condon distributions by referring to panels (c) and (d) of Fig. 5.6. One first notes that a rather fast variation from almost zero to 0.17 is observed for $W_{\rm PPT}^{1/2}$ as R goes from 0 to ca. 3 a.u. This has a double effect: first, recalling Eq. (5.4), we see that with respect to high v_+ vibrational wavefunctions of H_2^+, it filters out almost completely the left turning point amplitudes of this wavefunction, which normally (i.e. in the FC case) would presents some overlap with the $\chi_0(R)$ H_2 ground vibrational state, while the amplitudes of this high v_+ wavefunction found at the right turning point lies completely outside the range of $\chi_0(R)$ and gives a zero overlap with it. The consequence is that, from a broad vibrational population distribution extending up to $v_+ = 18$ as obtained for the vertical FC ionization, we now have, with the non trivial dependence of $W_{\rm PPT}$ on R, a narrower distribution (up to $v_+ \simeq 10$).

The fact that this non-FC distribution is peaked at $v_+ = 1$ rather than at $v_+ = 2$ can also be understood by this rise of $W_{\rm PPT}^{1/2}$ in the region where $\chi_0(R)$ is peaking, though things here depend on a rather delicate balance between various portions of the variation of $W_{\rm PPT}^{1/2}$ around its value at the equilibrium internuclear distance R_e of the neutral molecule. In the interval of R where $\chi_0(R)$ overlaps well with $\chi_{v_+=1}(R)$ (traced in orange in panel (c)), *i.e.* on the right of the equilibrium geometry, $W_{\rm PPT}^{1/2}$ is larger than its value at R_e. Thus the overlap between the $v_+ = 1$ state and the H_2 ground vibrational wavefunction is enhanced with respect to the FC situation. The same thing can be said for the overlap between the cation ground vibrational wavefunction. This nodeless $\chi_{v_+=0}(R)$ wavefunction is centered at the node of the $\chi_{v_+=1}(R)$ function just discussed and its overlap

with the H_2 ground vibrational state $\chi_0(R)$ lies in the region where $W_{\rm PPT}^{1/2}$ is larger than its value at R_e. As a consequence, the weights of the $v_+ = 0$ and $v_+ = 1$ vibrational states are increased when using the more realistic PPT approach as compared to the FC approximation.

The case of the vibrational state $v_+ = 2$ is more delicate: In the interval of R where $\chi_0(R)$ overlaps well with $\chi_{v_+=2}(R)$ (traced in orange in panel (d)), $W_{\rm PPT}^{1/2}$ is smaller than its value at R_e on the left of this equilibrium geometry, diminishing the contribution to the overlap there. The subsequent rise of $W_{\rm PPT}^{1/2}$ in the region of the first maximum of $\chi_{v_+=2}(R)$ contributes to enhance the (positive) overlap there. However, the continued rise of $W_{\rm PPT}^{1/2}$ past this range enhances the previously small negative overlap between the tail of $\chi_0(R)$ and the negative lobe of $\chi_{v_+=2}(R)$. All this gives a slight decrease in the overlap between the two functions when the R-dependent $W_{\rm PPT}^{1/2}$ is inserted.

A closer look at how the non-FC character affects the lowest v_+ states' populations is given in Fig. 5.7, for two values of the wavelengths, 266 nm and 800 nm. The field intensity is 1.6×10^{14} W/cm^2. The histogram with striped pink bars is for the linear polarization case, while that with full brown bars is for the case of a circularly polarized pulse. The horizontal purple line drawn at each value of v_+ marks the expected height of the population for that level in the FC distribution. We see that there is depletion of population with respect to the FC distribution starting for the highest v_+ levels. The $v_+ = 2$ population actually increases, but less so than the $v_+ = 0$ and 1 populations. The non-FC character seems a little stronger for circularly polarized fields in the TI regime ($\lambda = 800$ nm, panel (b)).

In summary, the ionization of H_2 within a MO-PPT model description, enhances the populations of the lowest levels $v_+ = 0 - 4$ of H_2^+ to the detriment of levels close to the dissociation limit. A number of remarks ought to be made at this point. First, although the above results were obtained for rather long pulses, they are representative of the vibrational excitation of the cation as it is formed, in an attosecond time-scale, as the MO-PPT semi-classical model sees the time as merely a parameter governing the instantaneous value of the field under which the molecular ionization is produced. Basically, the consideration of the long pulse is irrelevant in the discussion of the non-FC character of the ionization, as it merely amplifies the collected ionization signal while the non-FC character is defined relative to the total final ionization probability, (see Eqs. (5.22, 5.23)). Thus, the v_+-state population distributions shown here represent the vibrational wave packet of the cation as it is formed. This absence of dependence of the calculated non-FC distributions with the pulse duration was confirmed by calculations performed with shorter (8 fs FWHM) and longer (32 fs FWHM) pulses at

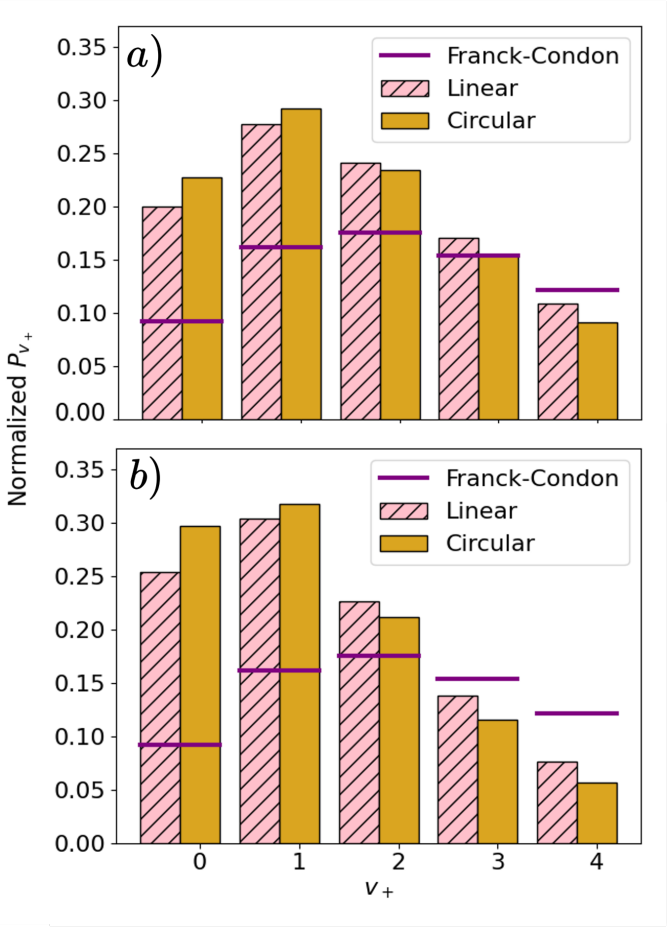

Figure 5.7: Non-FC final H_2^+ populations using linearly (striped pink bars) and circularly (full brown bars) polarized fields, calculated at a peak intensity of $I = 1.6 \times 10^{14}$ W/cm^2 by the MO-PPT method. The upper and lower panels are for comparing wavelengths of (a) 266 nm over 36 optical cycles and (b) 800 nm over 12 optical cycles. FC projections are indicated by horizontal purple lines.

the 3 considered wavelengths (266, 400 and 800 nm). This distribution is thus to be viewed as the initial state of a subsequent vibrational dynamics, be it with or without an external field.

Imagine for example that the external field is the probe pulse in a pump-probe experiment. The outcome of this vibrational dynamics, often discussed by assuming a FC preparation of the molecular ion, will be affected by this non-FC character. In the IR spectral region, a dynamical control of the dissociation probability can be exerted by tuning the carrier-envelope phase of the probe pulse, by a mechanism called Dynamical Dissociation Quenching (DDQ) [41, 42]. The

non-FC wave packet would modify the optimized parameters for this type of control. In the UV-Visible region, an intense probe pulse gives rise to ATD signals in the proton kinetic energy release (KER) spectrum, with possible signatures of Bond-Softening and/or Vibrational Trapping effects [43]. All this depends delicately on the content of the initial vibrational wave packet. A non-FC preparation of this wave packet will surely be manifest in these spectra.

The last comment to be made on these non-FC ionization considerations is that the semi-classical expressions of the ionization rate depend on R only through the ionization potential, as they are basically adapted from a theory of atomic ionization. By considering the core potential as felt by the ionizing electron as a single-centered one, MO-ADK and MO-PPT, as well as CS-ADK, the recent adaptation of ADK theory to complex systems [44], ignore the LCAO (Linear Combination of Atomic Orbitals) form of the molecular orbital out of which the ionization takes place. A study that takes into account the form of this potential [45], using a reformulation of the tunneling ionization theory [46] do reveal this dependence that would further enhance the non-Franck-Condon character of the cation initial vibrational wave packet. Various considerations, of short-time projections of the initial (molecular) orbitals onto the ionization continuum, or of exact molecular symmetry conservation in the case of ionization under a perpendicularly polarized field [10], indicate the existence of diffraction-like factors in the exact ionization probability amplitude, the R-dependence of which would contribute to a stronger non-FC behaviour, in particular for a high ionized electron momentum. This aspect of the non-Franck-Condon strong field ionization is yet to be explored using a more detailed, albeit numerically exact description of the strong-field ionization.

5.4 . Conclusion

In this paper, we consider the dynamical process of laser-induced strong field ionization of H_2, treated within semi-classical models which include the internuclear degree of freedom as a mere parameter. We verified that for laser peak intensities not exceeding a few 10^{14} W/cm^2 the single (first) ionization is by far the dominant process in the tunnel ionization regime. For those intensities the first ionization process can be considered by itself, separated from the slower vibrational motions, thus allowing us to concentrate on the ionization dynamics. Concerning the models, we refer to semi-classical treatments comparing the relative performances of MO-ADK and MO-PPT approximations. In that respect, we show that the popular MO-ADK method performs well in the tunnel ionization (TI) regime, that is for the corresponding Keldysh parameter $\gamma \ll 1$, *i.e.*

for high intensities and long wavelengths. The MO-PPT formula is characterized by a more extended validity domain, at least partially covering the multiphoton ionization (MPI) regime with $\gamma \gg 1$. As typical examples of the TI and MPI regimes, we considered two wavelengths, one in the near IR domain (800 nm) and the other one in the UV spectral region (266 nm). We compared the results for the two types of field polarizations: linear and circular. For any wavelength, the threshold intensity for the H_2^+ population saturation is higher for the case of a circular polarization as compared to the linear polarization case. This is mainly a fluence effect. We also noted that the slope of the rise of the ionization probability vs. intensity curve is higher for $\lambda = 800$ nm than for $\lambda = 266$ nm. This is coherent with the identification of the first case as typical of the TI regime, and the second of the MPI regime.

Concerning the vibrational populations of the ion as it is formed, we have shown that the strong field ionization of H_2 does not follow the Franck-Condon principle, contrary to the simplified view of an ultrafast ionization mechanism with the nuclear motions frozen on the ionization time scale. Indeed, in this simplified view the vibrational initial state of the neutral molecule would simply be transported vertically onto the cation's ground-state manifold. The deviation from a Franck-Condon behaviour is to be understood in terms of the R-dependence of the ionization rate, which increases rapidly with the internuclear distance, whatever the polarization. The resulting so-called non-FC distributions are peaked at lower vibrational levels than the FC ones, and are more limited in v_+ range than the Franck-Condon one, levels above $v_+ = 4$ being only weakly populated.

It is worthwhile noting that non-FC distributions have already been experimentally observed in the literature using a 800 nm excitation in linear polarization, and interpreted with a theoretical approach at the ADK level of approximation [40]. This study concluded also that the ionization process was favoring the production of the lowest v_+ levels, but the comparison cannot be pushed further, not only because our study is performed at the PPT level of approximation, but also because the individual vibrational levels of H_2^+ referred to in Ref. [40] take into account the laser-induced modifications of the two field-dressed potential energy curves of the $1s\sigma_g$ and $2p\sigma_u$ states of the cation. As such, the distribution is necessarily non-FC, not because of a non-vertical ionization, but because the distribution is one over a different basis of vibrational states.

The study we have presented here, describing the creation of a vibrational wave packet in the electronic ground state of the molecular ion H_2^+, is a first step towards the development of a more complete model that will take into account the subsequent nuclear dynamics, by solving the time-dependent Schrödinger equation describing the dynamics of the nuclear wave packet thus formed in

the electronic state $1s\sigma_g$ and coupled to the first excited and dissociative electronic state $2p\sigma_u$ of the H_2^+ ion. This will complete the inclusion of a semi-classical MO-ADK or MO-PPT scheme in the full description of the dissociative ionization process leading to a useful observable such as the kinetic energy distribution of protons emitted in the dissociative continuum associated with the asymptotic [H(1s) + H^+] channel. This approach should allow an accurate and realistic evaluation of the low energy part of these proton spectra, while the description of higher kinetic energies will require the consideration of the double ionization process leading to the [H^+ + H^+] Coulomb Explosion occurring for stronger laser fields. Work is thus in progress in our group to treat the complete dynamics that can take place, from the ionization of H_2 to its Coulomb Explosion, based on a semi-classical approach for the ionization and a fully quantum description for the vibrational dynamics.

Supplementary information

Results of calculations with varying pulse durations, as mentioned and discussed in section 5.3.1, are shown in a separate Supplementary Information file.

Acknowledgments

This work has been performed within the French GDR UP number 3754 of CNRS. Jean-Nicolas Vigneau is grateful to the French MESRI (French Ministry of Higher Education, Research and Innovation) for funding his PhD grant through a scholarship from EDOM (Ecole Doctorale Ondes et Matière, Université Paris-Saclay, France). JNV also acknowledges partial funding from the Choquette Family Foundation - Mobility Scholarship and the Paul-Antoine-Giguère Scholarship.

Declarations

Competing interests

All authors certify that they have no affiliations with or involvement in any organization or entity with any financial interest or non-financial interest in the subject matter or materials discussed in this manuscript.

Data availability statement

The datasets generated during and/or analysed during the current study are available from the corresponding author on reasonable request.

Code availability

The Fortran codes developed by us and used in this work are available on request from the authors.

Authors' contributions

All authors contributed to the study conception and design. The numerical simulations were performed by Jean-Nicolas Vigneau. The first draft of the manuscript was written by Osman Atabek and all authors commented on previous versions of the manuscript. All authors read and approved the final manuscript.

Bibliography

[1] P. B. Corkum and F. Krausz. Attosecond science. *Nat. Phys.*, 3(6):381–387, 2007. URL: https://www.nature.com/articles/nphys620, doi:10.1038/nphys620.

[2] P. Lu, J. Wang, H. Li, K. Lin, X. Gong, Q. Song, Q. Ji, W. Zhang, J. Ma, H. Li, H. Zeng, F. He, and J. Wu. High-order above-threshold dissociation of molecules. *Proc. Natl. Acad. Sci. USA*, 115(9):2049–2053, 2018. URL: http://www.pnas.org/lookup/doi/10.1073/pnas.1719481115, doi:10.1073/pnas.1719481115.

[3] P. B. Corkum. Plasma perspective on strong field multiphoton ionization. *Phys. Rev. Lett.*, 71(13):1994, 1993. URL: http://link.aps.org/doi/10.1103/PhysRevLett.71.1994, doi:10.1103/PhysRevLett.71.1994.

[4] M. Lewenstein, P. Balcou, M. Y. Ivanov, A. L'Huillier, and P. B. Corkum. Theory of high-harmonic generation by low-frequency laser fields. *Phys. Rev. A*, 49(3):2117–2132, 1994. URL: http://link.aps.org/doi/10.1103/PhysRevA.49.2117, doi:10.1103/PhysRevA.49.2117.

[5] T. Okino, Y. Furukawa, Y. Nabekawa, S. Miyabe, A. A. Eilanlou, E. J. Takahashi, K. Yamanouchi, and K. Midorikawa. Direct observation of an attosecond electron wave packet in a nitrogen molecule. *Sci. Adv.*, 1(8):e1500356, 2015. URL: https://www.science.org/doi/abs/10.1126/sciadv.1500356, doi:10.1126/sciadv.1500356.

[6] S. Sukiasyan, S. Patchkovskii, O. Smirnova, T. Brabec, and M. Y. Ivanov. Exchange and polarization effect in high-order harmonic imaging of molecular structures. *Phys. Rev. A*, 82:043414, Oct 2010. URL: https://link.

aps.org/doi/10.1103/PhysRevA.82.043414, doi:10.1103/PhysRevA.82.043414.

[7] T. Zuo, A. D. Bandrauk, and P. B. Corkum. Laser-induced electron diffraction: a new tool for probing ultrafast molecular dynamics. *Chem. Phys. Lett.*, 259(3):313–320, 1996. doi:https://doi.org/10.1016/0009-2614(96)00786-5.

[8] C. I. Blaga, J. Xu, A. D. DiChiara, E. Sistrunk, K. Zhang, P. Agostini, T. A. Miller, L. F. DiMauro, and C. D. Lin. Imaging ultrafast molecular dynamics with laser-induced electron diffraction. *Nature*, 483(7388):194–197, March 2012. URL: https://www.nature.com/articles/nature10820, doi:10.1038/nature10820.

[9] M. Peters, T. T. Nguyen-Dang, C. Cornaggia, S. Saugout, E. Charron, A. Keller, and O. Atabek. Ultrafast molecular imaging by laser-induced electron diffraction. *Phys. Rev. A*, 83:051403, May 2011. URL: https://link.aps.org/doi/10.1103/PhysRevA.83.051403, doi:10.1103/PhysRevA.83.051403.

[10] T. T. Nguyen-Dang, M. Peters, J. Viau-Trudel, E. Couture-Bienvenue, R. Puthumpally-Joseph, E. Charron, and O. Atabek. Laser-induced electron diffraction: alignment defects and symmetry breaking. *Mol. Phys.*, 115(15-16):1934–1943, 2017. URL: https://www.tandfonline.com/doi/full/10.1080/00268976.2017.1317858, doi:10.1080/00268976.2017.1317858.

[11] S. Patchkovskii and M. S. Schuurman. Full-dimensional treatment of short-time vibronic dynamics in a molecular high-order-harmonic-generation process in methane. *Phys. Rev. A*, 96:053405, Nov 2017. URL: https://link.aps.org/doi/10.1103/PhysRevA.96.053405, doi:10.1103/PhysRevA.96.053405.

[12] A. I. Pegarkov, E. Charron, and A. Suzor-Weiner. Nonlinear single and double ionization of molecules by strong laser pulses. *J. Phys. B: At., Mol. Opt. Phys.*, 32(14):L363–L369, jul 1999. URL: https://iopscience.iop.org/article/10.1088/0953-4075/32/14/104, doi:10.1088/0953-4075/32/14/104.

[13] A. D. Bandrauk. Harmonic generation in a 1D model of H_2 with single and double ionization. *J. Phys. B*, 38(14):2529–2544, 2005. URL: https://iopscience.iop.org/article/10.1088/0953-4075/38/14/016, doi:https://doi.org/10.1088/0953-4075/38/14/016.

[14] S. Saugout, C. Cornaggia, A. Suzor-Weiner, and E. Charron. Ultrafast Electronuclear Dynamics of H_2 Double Ionization. *Phys. Rev. Lett.*, 98:253003, Jun 2007. URL: https://link.aps.org/doi/10.1103/PhysRevLett.98.253003, doi:10.1103/PhysRevLett.98.253003.

[15] S. Saugout, E. Charron, and C. Cornaggia. H_2 double ionization with few-cycle laser pulses. *Phys. Rev. A*, 77:023404, Feb 2008. URL: https://link.aps.org/doi/10.1103/PhysRevA.77.023404, doi:10.1103/PhysRevA.77.023404.

[16] M. V. Ammosov, N. B. Delone, and V. P Krainov. Tunnel ionization of complex atoms and of atomic ions in an alternating electromagnetic field. *Sov. Phys. JETP*, 64(6):1191, 1986.

[17] I. I. Fabrikant and G. A. Gallup. Semiclassical propagation method for tunneling ionization. *Phys. Rev. A*, 79:013406, Jan 2009. URL: https://link.aps.org/doi/10.1103/PhysRevA.79.013406, doi:10.1103/PhysRevA.79.013406.

[18] A. M. Perelomov, V. S. Popov, and M. V. Terent'ev. Ionization of atoms in an alternating electric field. *J. Exptl. Theoret. Phys. (U.S.S.R.)*, 50:1393–1409, 1966.

[19] A. M. Perelomov, V. S. Popov, and M. V. Terent'ev. Ionization of atoms in an alternating electric field II. *J. Exptl. Theoret. Phys. (U.S.S.R.)*, 51:309–326, 1966.

[20] A. M. Perelomov and V. S. Popov. Ionization of atoms in an alternating electric field III. *J. Exptl. Theoret. Phys. (U.S.S.R.)*, 52:514–526, 1967.

[21] X. M. Tong, Z. X. Zhao, and C. D. Lin. Theory of molecular tunneling ionization. *Phys. Rev. A*, 66:033402, Sep 2002. URL: https://link.aps.org/doi/10.1103/PhysRevA.66.033402, doi:10.1103/PhysRevA.66.033402.

[22] E. P. Benis, J. F. Xia, X. M. Tong, M. Faheem, M. Zamkov, B. Shan, P. Richard, and Z. Chang. Ionization suppression of Cl_2 molecules in intense laser fields. *Phys. Rev. A*, 70:025401, Aug 2004. URL: https://link.aps.org/doi/10.1103/PhysRevA.70.025401, doi:10.1103/PhysRevA.70.025401.

[23] B. Numerov. Note on the numerical integration of $d^2x/dt^2 = f(x,t)$. *Astron. Nachr.*, 230(19):359–364, 1927. URL: https://onlinelibrary.wiley.com/doi/abs/10.1002/asna.19272301903, doi:https://doi.org/10.1002/asna.19272301903.

[24] W. Kolos and L. Wolniewicz. Potential-Energy Curves for the $\chi^1\Sigma_g^+$, $b^3\Sigma_u^+$, and $C^1\Pi_u$ States of the Hydrogen Molecule. *J. Chem. Phys.*, 43:2429, 1965. URL: https://pubs.aip.org/aip/jcp/article-abstract/43/7/2429/81403/Potential-Energy-Curves-for-the-X-1-g-b3-u-and-C-1?redirectedFrom=fulltext, doi:10.1063/1.1697142.

[25] J. M. Peek. Eigenparameters for the $1s\sigma_g$ and $2p\sigma_u$ Orbitals of H_2^+. *J. Chem. Phys.*, 43:3004, 1965. URL: https://pubs.aip.org/aip/jcp/article-abstract/43/9/3004/82697/Eigenparameters-for-the-1s-g-and-2p-u-Orbitals-of?redirectedFrom=fulltext, doi:10.1063/1.1697265.

[26] M. M. Madsen and J. M. Peek. Eigenparameters for the lowest twenty electronic states of the hydrogen molecule ion. *At. Data Nucl. Data Tables*, 2:IN3–204, 1970. URL: https://www.sciencedirect.com/science/article/pii/S0092640X70800080, doi:https://doi.org/10.1016/S0092-640X(70)80008-0.

[27] M. Awasthi, Y. Vanne, A. Saenz, A. Castro, and P. Decleva. Single-active-electron approximation for describing molecules in ultrashort laser pulses and its application to molecular hydrogen. *Phys. Rev. A*, 77(6):063403, 2008. URL: https://journals.aps.org/pra/abstract/10.1103/PhysRevA.77.063403, doi:10.1103/PhysRevA.77.063403.

[28] S.-F. Zhao, C. Jin, A.-T. Le, T. F. Jiang, and C. D. Lin. Determination of structure parameters in strong-field tunneling ionization theory of molecules. *Phys. Rev. A*, 81:033423, Mar 2010. URL: https://link.aps.org/doi/10.1103/PhysRevA.81.033423, doi:10.1103/PhysRevA.81.033423.

[29] S. V. Popruzhenko, V. D. Mur, V. S. Popov, and D. Bauer. Strong field ionization rate for arbitrary laser frequencies. *Phys. Rev. Lett.*, 101:193003, Nov 2008. URL: https://link.aps.org/doi/10.1103/PhysRevLett.101.193003, doi:10.1103/PhysRevLett.101.193003.

[30] L. V. Keldysh. Ionization in the field of a strong electromagnetic wave. *Sov. Phys. JETP*, 20(5):1307–1314, 1965.

[31] S. V. Popruzhenko. Keldysh theory of strong field ionization: history, applications, difficulties and perspectives. *J. Phys. B*, 47(20):204001, 2014. URL: https://iopscience.iop.org/article/10.1088/0953-4075/47/20/204001/pdf, doi:10.1088/0953-4075/47/20/204001.

[32] H. Padé. Sur la représentation approchée d'une fonction par des fractions rationnelles. *Ann. Sci. ENS*, 9:3–93, 1892. URL: http://www.numdam.org/articles/10.24033/asens.378/, doi:10.24033/asens.378.

[33] B. Walker, B. Sheehy, L. F. DiMauro, P. Agostini, K. J. Schafer, and K. C. Kulander. Precision measurement of strong field double ionization of helium. *Phys. Rev. Lett.*, 73:1227–1230, Aug 1994. URL: https://link.aps.org/doi/10.1103/PhysRevLett.73.1227, doi:10.1103/PhysRevLett.73.1227.

[34] F. Mauger, A. Kamor, C. Chandre, and T. Uzer. Mechanism of delayed double ionization in a strong laser field. *Phys. Rev. Lett.*, 108:063001, Feb 2012. URL: https://link.aps.org/doi/10.1103/PhysRevLett.108.063001, doi:10.1103/PhysRevLett.108.063001.

[35] M. Awasthi, Y. V. Vanne, and A. Saenz. Non-perturbative solution of the time-dependent Schrödinger equation describing H_2 in intense short laser pulses. *J. Phys. B*, 38(22):3973, oct 2005. URL: https://iopscience.iop.org/article/10.1088/0953-4075/38/22/005, doi:10.1088/0953-4075/38/22/005.

[36] Y. V. Vanne and A. Saenz. Numerical treatment of diatomic two-electron molecules using a B-spline based CI method. *J. Phys. B*, 37(20):4101, oct 2004. URL: https://iopscience.iop.org/article/10.1088/0953-4075/37/20/005, doi:10.1088/0953-4075/37/20/005.

[37] S.-F. Zhao, A.-T. Le, C. Jin, X. Wang, and C. D. Lin. Analytical model for calibrating laser intensity in strong-field-ionization experiments. *Phys. Rev. A*, 93:023413, Feb 2016. URL: https://link.aps.org/doi/10.1103/PhysRevA.93.023413, doi:10.1103/PhysRevA.93.023413.

[38] A. Saenz. On the influence of vibrational motion on strong-field ionization rates in molecules. *J. Phys. B*, 33(20):4365–4372, sep 2000. URL: https://iopscience.iop.org/article/10.1088/0953-4075/33/20/313, doi:10.1088/0953-4075/33/20/313.

[39] J. H. Posthumus, L. J. Frasinski, and K. Codling. *Tunnelling ionization and the Franck-Condon principle*, page 171. Springer, Dordrecht: Kluwer, 2001.

[40] X. Urbain, B. Fabre, E. M. Staicu-Casagrande, N. de Ruette, V. M. Andrianarijaona, J. Jureta, J. H. Posthumus, A. Saenz, E. Baldit, and C. Cornaggia. Intense-Laser-Field Ionization of Molecular Hydrogen in the Tunneling Regime and Its Effect on the Vibrational Excitation of H_2^+. *Phys. Rev. Lett.*, 92:163004, Apr 2004. URL: https://link.aps.org/doi/10.1103/PhysRevLett.92.163004, doi:10.1103/PhysRevLett.92.163004.

[41] F. Châteauneuf, T.-T. Nguyen-Dang, N. Ouellet, and O. Atabek. Dynamical quenching of field-induced dissociation of H_2^+ in intense infrared lasers. *J. Chem. Phys.*, 108(10):3974–3986, 1998. URL: https://pubs.aip.org/aip/jcp/article-abstract/108/10/3974/531892/Dynamical-quenching-of-field-induced-dissociation?redirectedFrom=fulltext, doi:10.1063/1.475800.

[42] H. Abou-Rachid, T.-T. Nguyen-Dang, and O. Atabek. Dynamical quenching of laser-induced dissociations of diatomic molecules in intense infrared fields: Effects of molecular rotations and misalignments. *J. Chem. Phys.*, 114(5):2197–2207, 2001. URL: https://pubs.aip.org/aip/jcp/article-abstract/114/5/2197/444182/Dynamical-quenching-of-laser-induced-dissociations?redirectedFrom=fulltext, doi:10.1063/1.1328378.

[43] A. Giusti-Suzor and F. H. Mies. Vibrational trapping and suppression of dissociation in intense laser fields. *Phys. Rev. Lett.*, 68:3869–3872, Jun 1992. URL: https://link.aps.org/doi/10.1103/PhysRevLett.68.3869, doi:10.1103/PhysRevLett.68.3869.

[44] S.-L. Hu, Z.-X. Zhao, and T.-Y. Shi. Alignment-dependent ionization of CO_2 in the intense laser fields: Single-Active-Electron approach. *Chin. Phys. Lett.*, 30(10):103103, oct 2013. URL: https://iopscience.iop.org/article/10.1088/0256-307X/30/10/103103, doi:10.1088/0256-307x/30/10/103103.

[45] R. Murray. *Tunnel Ionization in Strong-Field in Atoms and Molecules and its Applications*. PhD thesis, University of Waterloo, Waterloo, Ontario, Canada, 2011.

[46] R. Murray, W.-K. Liu, and M. Y. Ivanov. Partial Fourier-transform approach to tunnel ionization: Atomic systems. *Phys. Rev. A*, 81:023413, 2010. URL: https://link.aps.org/doi/10.1103/PhysRevA.81.023413, doi:10.1103/PhysRevA.81.023413.

Supplementary Information

Effect of the pulse duration on the ionization probability

To illustrate the effect of pulse duration, we present here, for $\lambda = 800$ nm, the results of calculations made for a pulse of 8 fs FWHM, corresponding to half the pulse duration considered in the main text, and of 32 fs FWHM, i.e. the double of the pulse duration in the main text. The results for the shorter pulse, 8 fs FWHM (6 optical cycles), and those for the longer pulse, 32 fs FWHM (24 optical cycles) are given in Fig. S5.1 for a linearly polarized field, and in Fig. S5.2 for a circularly polarized field.

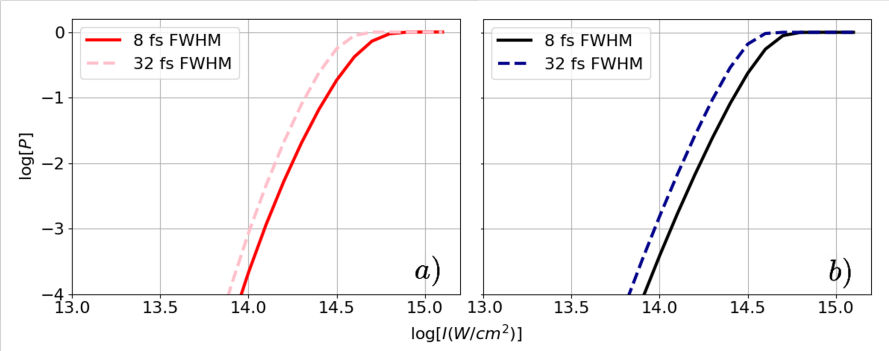

Figure S5.1: Final ionization probability of H_2 (in logarithmic scale) using a linearly polarized field of peak intensity I (in logarithmic scale), as given by (a) MO-ADK (red and pink) and (b) MO-PPT (black and blue) methods, with wavelengths of 800 nm over 6 optical cycles (8 fs FWHM; full red and black lines) and 24 optical cycles (32 fs FWHM; dashed pink and blue lines).

Compared with panel (c) of Fig. 4 of the main text, it is clearly seen that the ionization probability at t_f decreases (increases) globally with the pulse compression (stretching), and the saturation intensity (where $P_{ion}(t_f) = 1$) is shifted to higher (lower) values.

The effect of the pulse duration shortening or stretching on the second ionization follows the same trend, causing a shift of the H_2^+ (or H_2^{++}) apparition curve(s) to a higher (lower) intensity, i.e. to the right (left) of its value in Fig. 3 of the main text, in both the linear and circular polarization results. Fig. S5.3 shows the results for the pulse compression case (6 optical cycles, 8 fs FWHM), using the same layout as Fig. 3 of the main text.

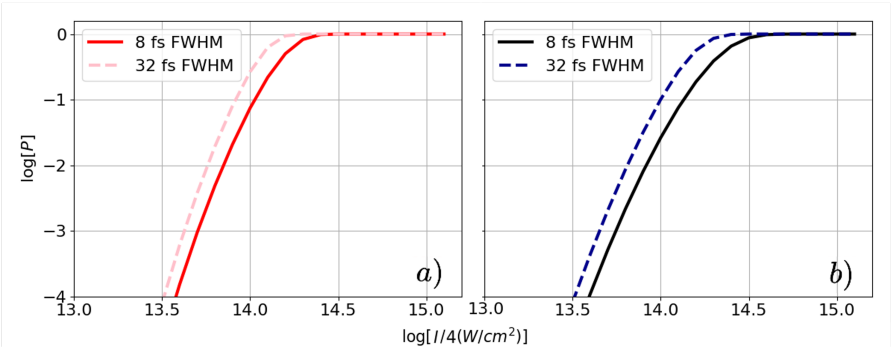

Figure S5.2: Final ionization probability of H_2 (in logarithmic scale) using a circularly polarized field of peak intensity I (in logarithmic scale), as given by (a) MO-ADK (red and pink) and (b) MO-PPT (black and blue) methods, with wavelengths of 800 nm over 6 optical cycles (8 fs FWHM; full red and black lines) and 24 optical cycles (32 fs FWHM; dashed pink and blue lines).

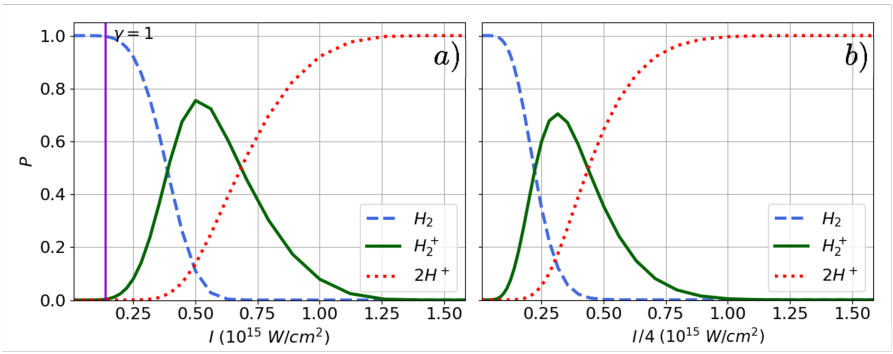

Figure S5.3: Final populations of H_2 ($P_{H_2}(t_f)$; dashed blue line), H_2^+ ($P_{H_2^+}(t_f)$; full green line) and H^+ + H^+ ($P_{CE}(t_f)$; Coulomb Explosion, red dotted line), using a 800 nm (a) linearly and (b) circularly polarized field, and the MO-PPT approach for a $\sin^2$ pulse envelope of total duration 16 fs corresponding to 6 optical cycles (8 fs FWHM). The vertical purple line in panel (a) indicates the value of the intensity at which the Keldysh parameter is $\gamma = 1$.

Annex to the Article: Strong-Field Non-Franck-Condon Ionization of H_2: A Semi-Classical Analysis

To help visualize the θ-dependence of the anisotropy parameter of the semi-classical methods, its squared form $B_0^2(\theta)$, as seen in Eq. (5.12), is depicted in Fig. A5.1 as a polar plot for H_2 (Fig. A5.1a) and H_2^+ (Fig. A5.1b). In this figure, $\theta = 0$ corresponds to an alignment of the field with the internuclear axis of the molecule, and $\theta = \pi/2$ to a perpendicular polarization. In Fig. A5.1c, which compares these two anisotropies, the graph shows that, as expected, the angular anisotropy of the ground state molecular orbital is more pronounced in H_2^+ than in H_2, since in the neutral molecule the electron repulsion tends to produce a more ovoid structure of the orbital.

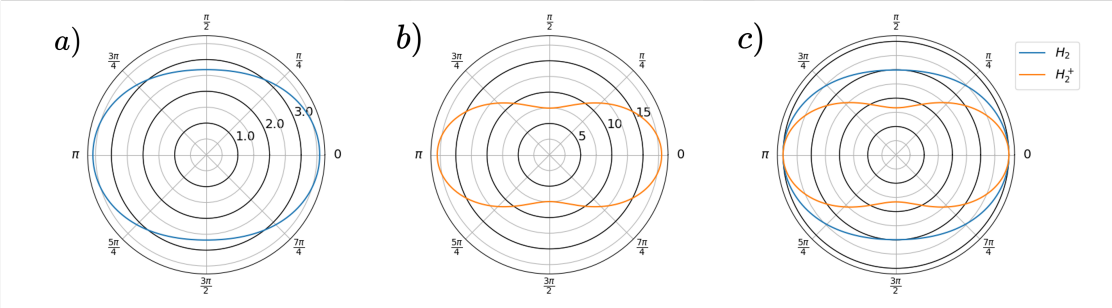

Figure A5.1: Polar plots of $B_0^2(\theta)$ for the ionization of H_2 (a), H_2^+ (b), and both values normalized for comparison purposes (c).

Also, to better represent the Padé approximant that has been used to fit the MO-PPT $t_0(\gamma)$ function, it has been plotted as a function of the Keldysh parameter γ in Fig. A5.2.

As shown in the article, for an equivalent fluence, a linearly polarized field ionizes at lower intensities than a circularly polarized field. In the light of these results, one might wonder why the linear polarization is more efficient at ionizing the molecule, considering that the amplitude of the linear field is brought to zero

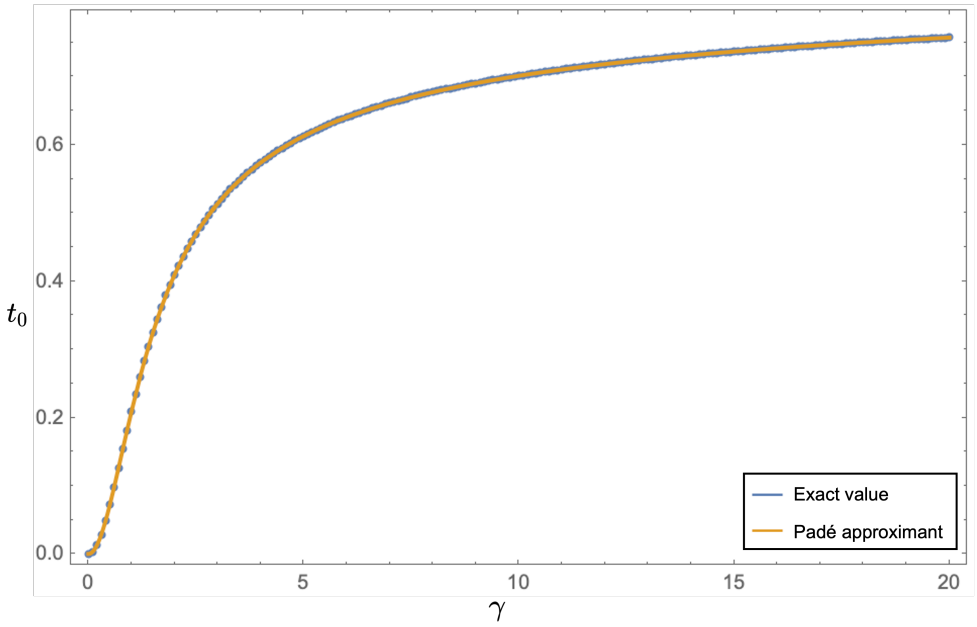

Figure A5.2: $t_0(\gamma)$ values used in the MO-PPT calculation in a circular field as the result of solving Eq. (5.20) for specific values of γ (blue scatter points), and as the analytical Padé approximant given in Eq. (5.21) (orange line).

several times during the dynamics, while the circular field is constantly active during the pulse. To better answer this question, H_2 ionization rates summed over all H_2^+ eigenstates were plotted as a function of time, for linearly-polarized and circularly-polarized fields, considering the three wavelengths of interest $\lambda = 266$ nm in Fig. A5.3, 400 nm in Fig. A5.4 and 800 nm in Fig. A5.5, within field parameters similar to those in the article.

These figures show that for linear polarization the ionization rate $\sum_{v_+} \Gamma_0^{v_+}(t)$ fluctuates from high values to zero according to the time variation of the field amplitude (see e.g. Fig. 5.2 for $\lambda = 800$ nm). However, the peak values of the linearly polarized field are $\sqrt{2}$ higher than those of the circularly polarized field. This contrast between the two polarizations is due to the adjusted circular field intensity, which is $I_{\text{circ}} = I_{\text{lin}}/2$ to maintain identical fluence, a difference large enough to significantly reduce the intensity threshold at which ionization starts when the polarization is linear. If all field parameters were equal, including peak intensity, then the circular field could be observed to be more efficient at ionizing the molecule, since the peak ionization rates would be similar to those of a linearly polarized field, and the amplitude would be non-zero throughout the dynamics.

As the effect of the pulse duration on the ionization probability was shown in

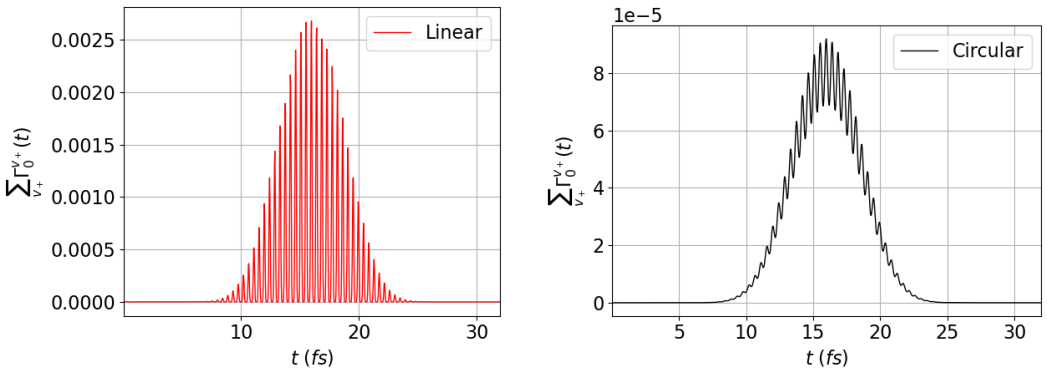

(a) Linear polarization (b) Circular polarization

Figure A5.3: Single ionization rate profile, summed over all H_2^+ eigenstates, as a function of time, during a 32 fs dynamics with a pulsed, (a) linearly- and (b) circularly-polarized field of wavelength $\lambda = 266$ nm.

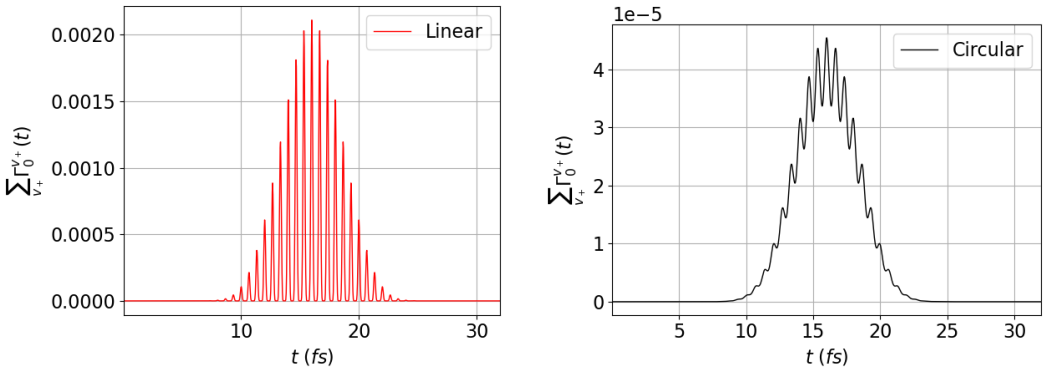

(a) Linear polarization (b) Circular polarization

Figure A5.4: Single ionization rate profile, summed over all H_2^+ eigenstates, as a function of time, during a 32 fs dynamics with a pulsed, (a) linearly- and (b) circularly-polarized field of wavelength $\lambda = 400$ nm.

Figs. S5.1-S5.3 in the Supplementary Information section of the article, but not its effect on the non-FC distributions mentioned in the article, plots of these calculations with shorter ($8\ fs$ FWHM) and longer ($32\ fs$ FWHM) pulses at the 3 considered wavelengths (266, 400 and 800 nm) for linearly- and circularly-polarized fields, along with the studied duration of $16\ fs$ FWHM, are shown in Fig. A5.6 for $\lambda = 266$ nm, Fig. A5.7 for $\lambda = 400$ nm and Fig. A5.8 for $\lambda = 800$ nm.

It is evident from these figures that for all field parameters studied at a similar intensity of 1.6×10^{14} W/cm^2, the non-FC distribution of the H_2^+ vibrational pop-

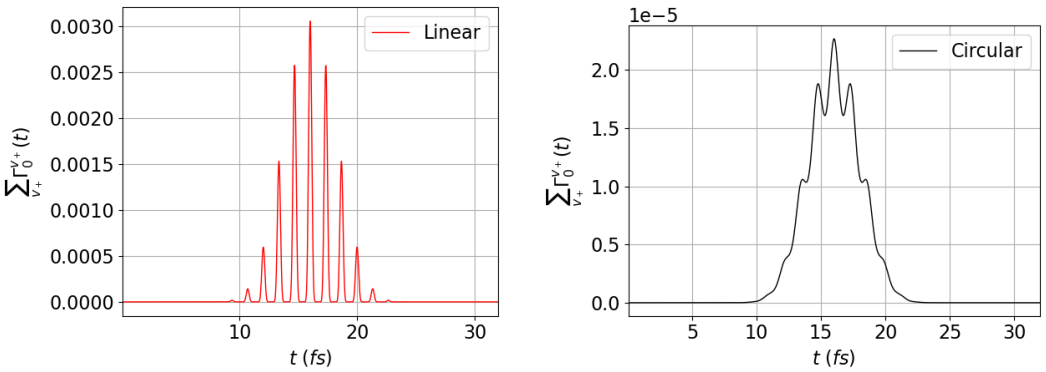

(a) Linear polarization

(b) Circular polarization

Figure A5.5: Single ionization rate profile, summed over all H_2^+ eigenstates, as a function of time, during a 32 fs dynamics with a pulsed, (a) linearly- and (b) circularly-polarized field of wavelength $\lambda = 800$ nm.

ulations is independent of the pulse duration and of the field frequency. These results can be explained by the fact that, according to Eq. (5.15), the MO-PPT ionization rate only depends on (1) the angle θ and polarization of the field, (2) the internuclear distance R between the nuclei, (3) the field intensity I and (4) the angular frequency ω of the field. For a given field strength, what affects most the vibrational populations of H_2^+ is the dependence on R. However, this dependence is identical regardless of the pulse duration and of the field frequency. Thus, in our simulations, the main dependence factor for the vibrational populations of the molecular ion is the field strength.

Within a certain range of optical cycles, shortening or lengthening the pulse duration will not affect the non-FC distribution, or in other words, the fraction of ionized H_2^+ vibrational populations. This phenomenon occurs only after a certain number of optical cycles, because the more optical cycles you consider at the beginning, the smaller will be the difference in the "perceived intensity" when you add or remove optical cycles. One can consider a distribution of the intensities perceived by the molecule during the dynamics, ranging from zero to the maximum intensity of 1.6×10^{14} W/cm^2 in this case, with each intensity given a certain weight according to the time spent at that intensity. This distribution, in terms of percentages, converges to a certain value as more cycles are added, and past a certain point this value doesn't vary much anymore. This stagnation of the "perceived intensity distribution" is observed here in terms of the vibrational population distribution, since the peak intensity of the field remains the only parameter on which this distribution depends.

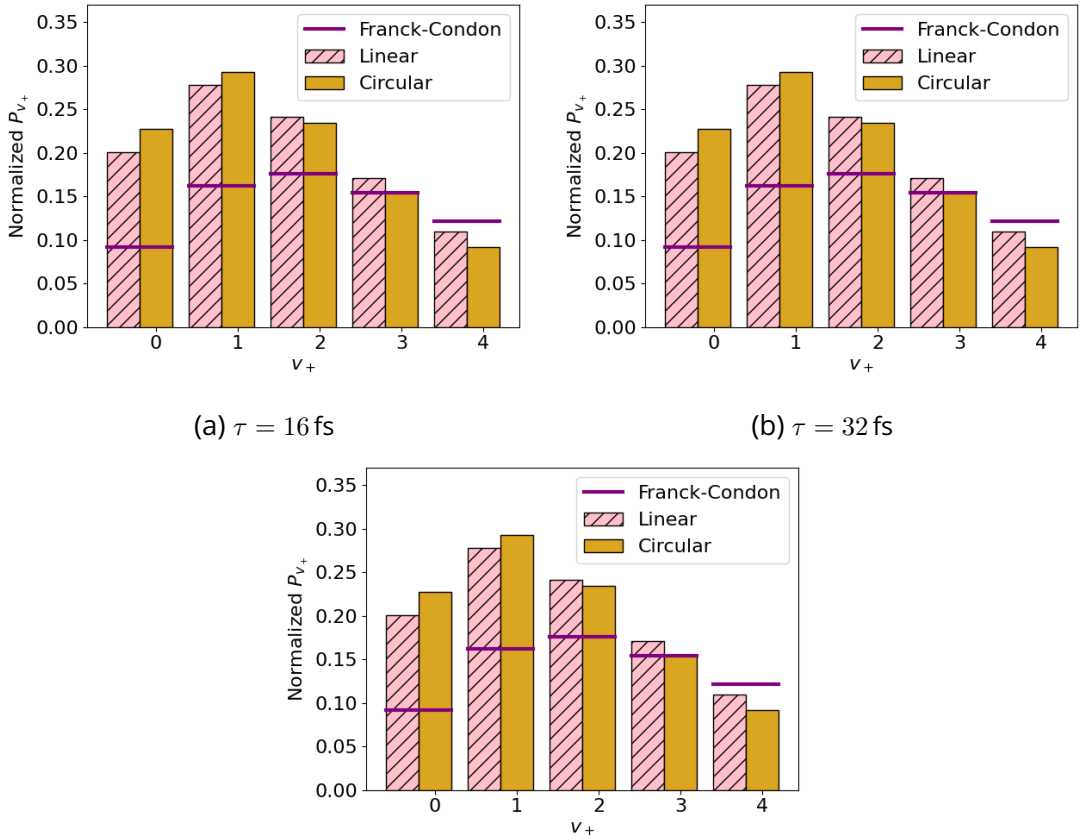

(a) $\tau = 16\,\text{fs}$ (b) $\tau = 32\,\text{fs}$

(c) $\tau = 64\,\text{fs}$

Figure A5.6: Non-FC final H_2^+ populations using linearly (striped pink bars) and circularly (full brown bars) polarized fields, calculated at a peak intensity of $I = 1.6 \times 10^{14}\,\text{W/cm}^2$ by the MO-PPT method. The panels compare pulses with durations of (a) 8 fs FWHM (18 optical cycles), (b) 16 fs FWHM (36 optical cycles) and (c) 32 fs FWHM (72 optical cycles), and a wavelength of 266 nm. FC projections are indicated by horizontal purple lines.

This result is confirmed in the three Figures A5.9 to A5.11, where we see that, within the dynamics restricted to single ionization, the final relative vibrational $(v_+ = 0, ..., 4)$ population distributions of H_2^+ are completely independent of the pulse duration, whether for linear or circular polarization of the field, or for a wavelength varying, in this study, from 266 to 800 nm. Although the relative distributions are quasi-identical, looking at the y-axis corresponding to the absolute population distribution, it becomes clear that the pulse duration has a direct effect on the total ionization probability of the molecule. Since the simulations for this article are performed with a peak intensity low enough to neglect second ionization, the ionization probabilities will vary proportionally with the pulse

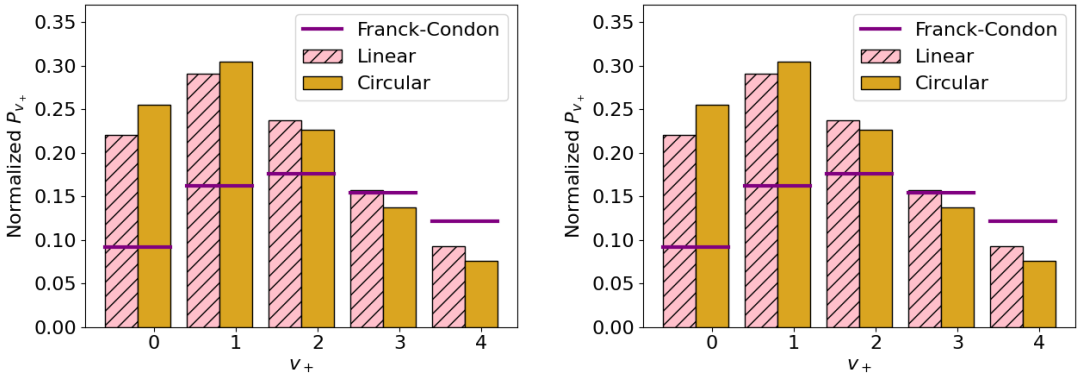

(a) $\tau = 16$ fs (b) $\tau = 32$ fs

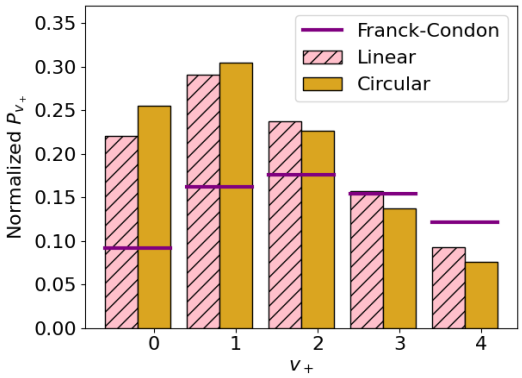

(c) $\tau = 64$ fs

Figure A5.7: Non-FC final H_2^+ populations using linearly (striped pink bars) and circularly (full brown bars) polarized fields, calculated at a peak intensity of $I = 1.6 \times 10^{14}$ W/cm^2 by the MO-PPT method. The panels compare pulses with durations of (a) 8 fs FWHM (12 optical cycles), (b) 16 fs FWHM (24 optical cycles) and (c) 32 fs FWHM (48 optical cycles), and a wavelength of 400 nm. FC projections are indicated by horizontal purple lines.

duration and won't saturate within a relatively short dynamic range.

While the population distribution converges to fixed values as the pulse duration is increased, one must keep in mind that the single ionization model cannot give credible results if the field intensity and duration are large enough to induce a significant probability of double ionization, i.e., Coulomb explosion of the molecule. Indeed, for a given peak field intensity, one can only increase the pulse duration up to a certain number of optical cycles before the bound population of H_2^+ is ionized to form $2H^+$.

Looking at the single ionization process, Fig. A5.12 shows that in both cases of

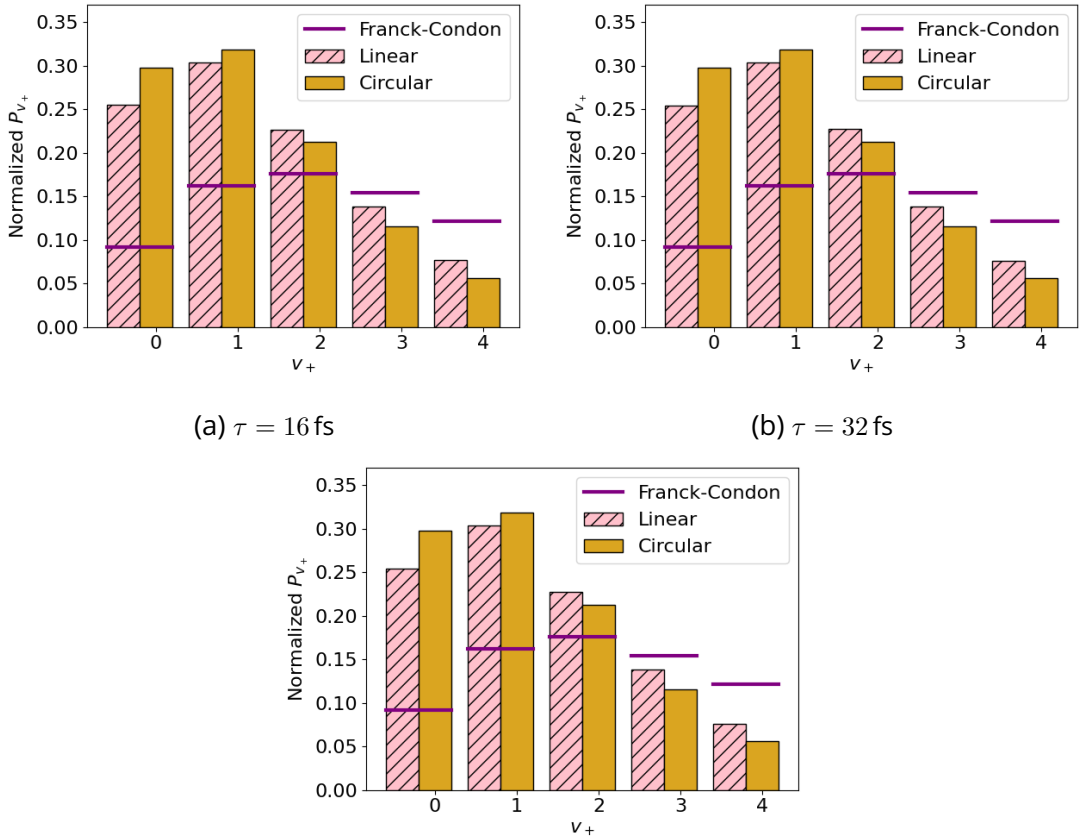

(a) $\tau = 16\,\text{fs}$ (b) $\tau = 32\,\text{fs}$

(c) $\tau = 64\,\text{fs}$

Figure A5.8: Non-FC final H_2^+ populations using linearly (striped pink bars) and circularly (full brown bars) polarized fields, calculated at a peak intensity of $I = 1.6 \times 10^{14}\,\text{W/cm}^2$ by the MO-PPT method. The panels compare pulses with durations of (a) 8 fs FWHM (6 optical cycles), (b) 16 fs FWHM (12 optical cycles) and (c) 32 fs FWHM (24 optical cycles), and a wavelength of 800 nm. FC projections are indicated by horizontal purple lines.

polarization, whether linear or circular, lower eigenstates of H_2^+ are on average more easily populated from the initial and fundamental H_2 population than are higher states. The linear case is not a surprise, as this was shown experimentally by Urbain et al. [1] and later in good agreement with the theoretical work of Kjeldsen and Madsen [2]. Past intensities of a few $10^{13}\,\text{W/cm}^2$, we see that eigenstates $v_+ = 1$, and finally $v_+ = 2$ take the lead in terms of most populated states ahead of the $v_+ = 0$ state, but these changes in population distribution do not affect higher states in a significant way. Also, some transitions are shown to have ionization rate drops at certain intensities. These quenching events occur with a frequency proportional to the number of nodes in the final state involved in the

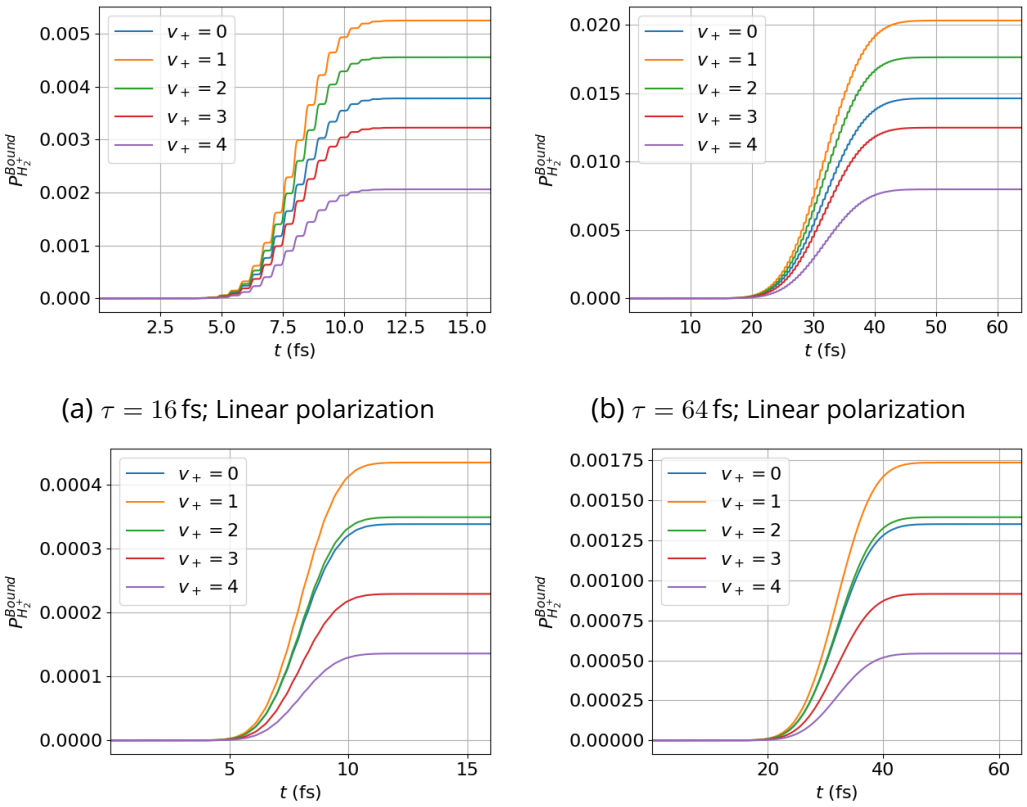

(a) $\tau = 16$ fs; Linear polarization

(b) $\tau = 64$ fs; Linear polarization

(c) $\tau = 16$ fs; Circular polarization

(d) $\tau = 64$ fs; Circular polarization

Figure A5.9: H_2^+ population profiles of eigenstates $v_+ = 0, ..., 4$ during the ionization of H_2 using the semi-classical MO-PPT method, with a field of $\lambda = 266$ nm, of peak intensity $I = 1.6 \times 10^{14}$ W/cm^2. The results are compared for pulses of (a,c) 8 fs FWHM (18 optical cycles) on the left column and (b,d) 32 fs FWHM (72 optical cycles) on the right column, and for (a,b) linearly-polarized fields on the top row and (c,d) circularly-polarized fields on the bottom row.

transition. Since the ionization rate is calculated from the integral of the overlap between the initial state $\chi_0(R)$, a Gaussian-like function, and the final state $\chi_{v_+}(R)$, pondered by the instantaneous molecular ionization rate $W_{H_2}[R,t]$ (see Eq. (5.4)), and because $W_{H_2}[R,t]$ expands toward higher internuclear distances as the intensity is increased (see Fig. A5.13), more nodes of χ_{v_+} are included as the intensity grows, causing variations in the value of the integral, and sometimes reaching zero ionization rates.

On a different note, one might wonder why the ionized population in the population profiles is mainly composed of the $v_+ = 1$ state at large intensities,

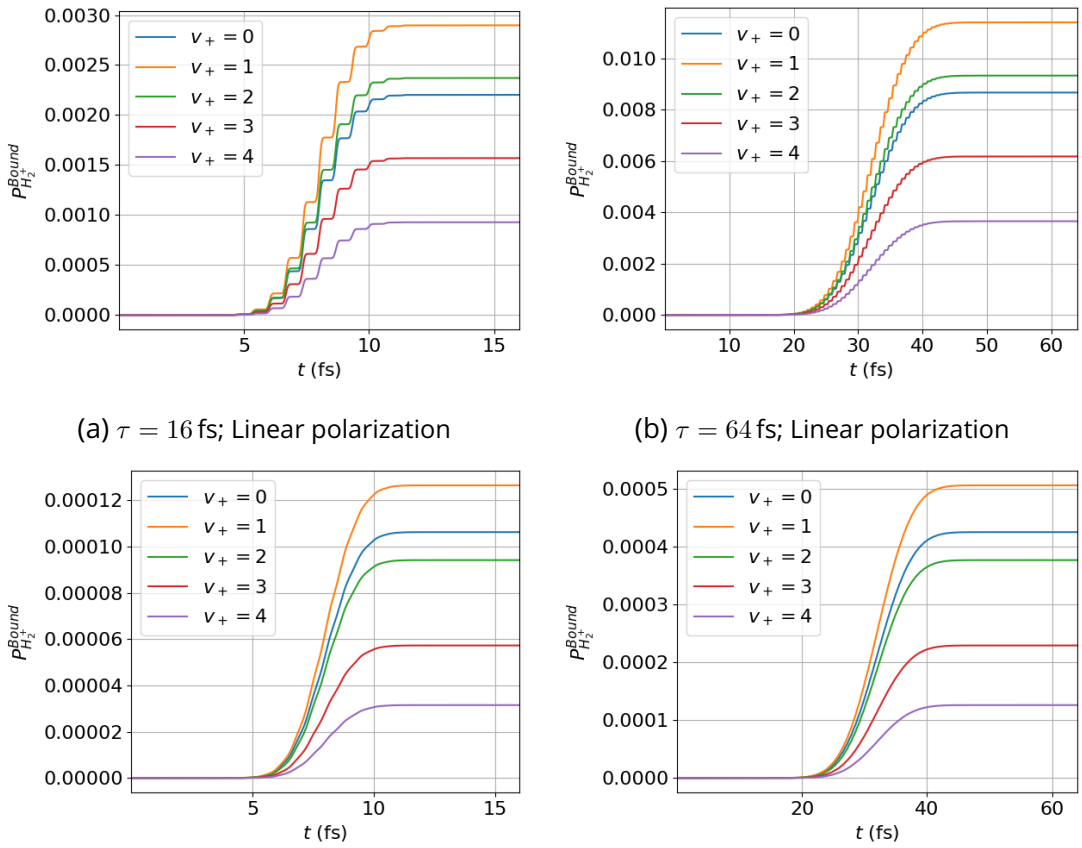

(a) $\tau = 16$ fs; Linear polarization

(b) $\tau = 64$ fs; Linear polarization

(c) $\tau = 16$ fs; Circular polarization

(d) $\tau = 64$ fs; Circular polarization

Figure A5.10: H_2^+ population profiles of eigenstates $v_+ = 0, ..., 4$ during the ionization of H_2 using the semi-classical MO-PPT method, with a field of $\lambda = 400$ nm of peak intensity $I = 1.6 \times 10^{14}$ W/cm^2. The results are compared for pulses of (a,c) 8 fs FWHM (12 optical cycles) on the left column and (b,d) 32 fs FWHM (48 optical cycles) on the right column, and for (a,b) linearly-polarized fields on the top row and (c,d) circularly-polarized fields on the bottom row.

while Fig. A5.12 shows that the $v_+ = 0$ state dominates for intensities below 2×10^{13} W/cm^2. Even though the field mostly passes through much lower intensities than the peak intensity 1.6×10^{14} W/cm^2 during the dynamics, high intensities ionize orders of magnitude more than lower ones, which is why peak intensity values induce the most population transitions during the dynamics, thus allowing a distribution favouring the population of the eigenstate $v_+ = 1$. The argument is actually the same as that previously evoked before concerning the ionization rate differences between a linear and a circular polarization, shown in Figs. A5.3-A5.5.

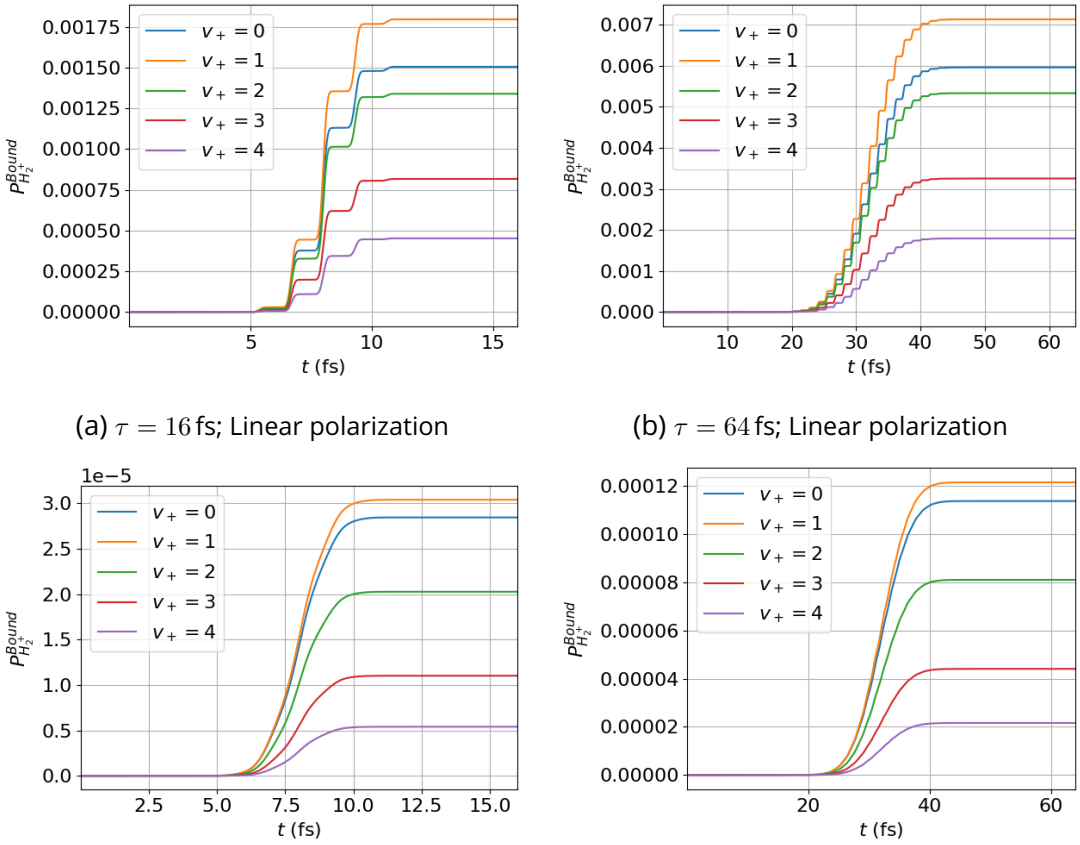

(a) $\tau = 16$ fs; Linear polarization

(b) $\tau = 64$ fs; Linear polarization

(c) $\tau = 16$ fs; Circular polarization

(d) $\tau = 64$ fs; Circular polarization

Figure A5.11: H_2^+ population profiles of eigenstates $v_+ = 0, ..., 4$ during the ionization of H_2 using the semi-classical MO-PPT method, with a field of $\lambda = 800$ nm of peak intensity $I = 1.6 \times 10^{14}$ W/cm^2. The results are compared for pulses of (a,c) 8 fs FWHM (6 optical cycles) on the left column and (b,d) 32 fs FWHM (24 optical cycles) on the right column, and for (a,b) linearly-polarized fields on the top row and (c,d) circularly-polarized fields on the bottom row.

Since the single-ionization rates $\Gamma_0^{v_+}(t)$ (see Eq. (5.4)), shown in Fig. A5.12, are generally quite different from the second-ionization rates $\Gamma_{v_+}^{CE}(t)$ (see Eq. (5.6)), shown in Fig. A5.15, prolonging the ionization dynamics would eventually lead to changes in the population distributions of H_2^+. Indeed, in contrast to the order of priority of the eigenstates to which the fundamental H_2 population is ionized, which favours lower-energy states, Fig. A5.15 reveals that for the transition from the eigenstates of H_2^+ to the continuum of $2H^+$, higher states ionize to the continuum faster than lower states, and even more so at low intensities. This tendency becomes ambiguous for the highest states, as eigenstates

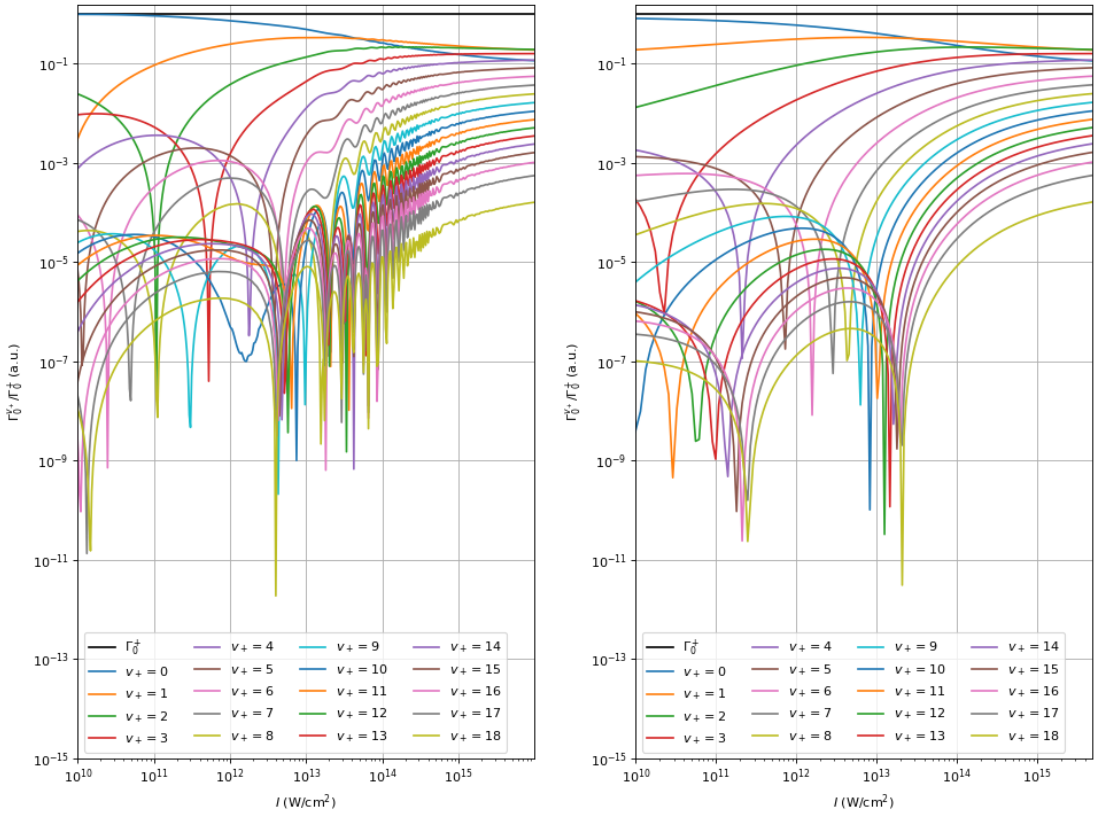

(a) Linear polarization (b) Circular polarization

Figure A5.12: First ionization rate from H_2 towards each bound eigenstate of H_2^+, $\Gamma_0^{v_+}$, normalized with the total ionization rate $\Gamma_0^+ = \sum_{v_+} \Gamma_0^{v_+}$ at different intensities, for (a) a linearly-polarized and (b) a circularly-polarized field, considering the angle $\theta = 0$ at $\lambda = 800$ nm. As colors repeat, it should be noted that lower states are more easily populated, with ionization rates that are generally found higher than for high eigenstates.

distribution from $v_+ = 15$ to $v_+ = 18$ exchange favoured transitions at high intensities, but the phenomenon can generally be regarded as opposite to the first ionization process. Thus, increasing the field intensity beyond the double ionization threshold will effectively modify the apparently static population distribution seen in Figs. A5.6-A5.8.

Finally, as the intensity increases, oscillation patterns are found above an intensity of the order of 10^{13} W/cm^2 in both the first and second eigenstate-resolved ionization rates for a linear polarization of the field, in Figs. A5.12a and A5.15a. These oscillations do not appear in the profiles of the circularly polarized field rates, and this difference can be attributed to differences in the algorithms associated with the molecular PPT formulations in linear and circular polariza-

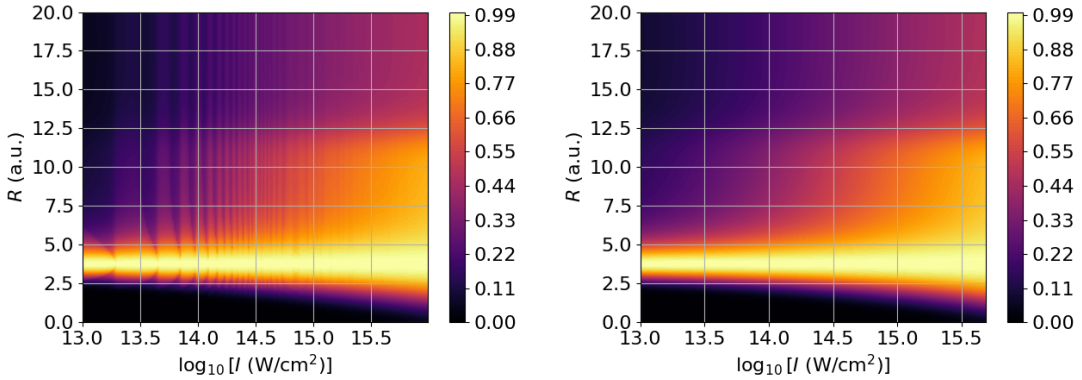

(a) Linear polarization (b) Circular polarization

Figure A5.13: Intensity and R-dependent MO-PPT single ionization rate $W_{\mathrm{H_2}}$ with its maximum value normalized to 1 for each intensity, for (a) a linearly-polarized and (b) a circularly-polarized field of wavelength $\lambda = 800$ nm, parallel to the internuclear axis.

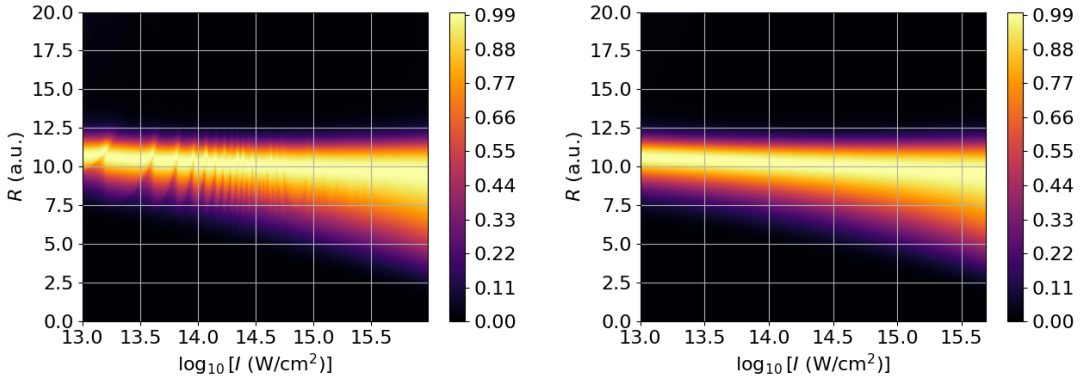

(a) Linear polarization (b) Circular polarization

Figure A5.14: Intensity and R-dependent MO-PPT second ionization rate $W_{\mathrm{H_2^+}}$ with its maximum value normalized to 1 for each intensity, for (a) a linearly-polarized and (b) a circularly-polarized field of wavelength $\lambda = 800$ nm, parallel to the internuclear axis.

tions. Indeed the MO-PPT ionization rates contain terms that are calculated differently depending on the field polarization, with Eqs. (5.16)-(5.17) for a linearly polarized field and Eqs. (5.18)-(5.21) for a circularly polarized field. While both algorithms produce different ionization rate values, the only term that directly induces oscillations in the rate function is $A_0(\omega, \gamma)$. This term is essential to account for the possible multiphoton regime ionization mechanism that is in competition with the quasi-static tunnel ionization mechanism. Lacking in the

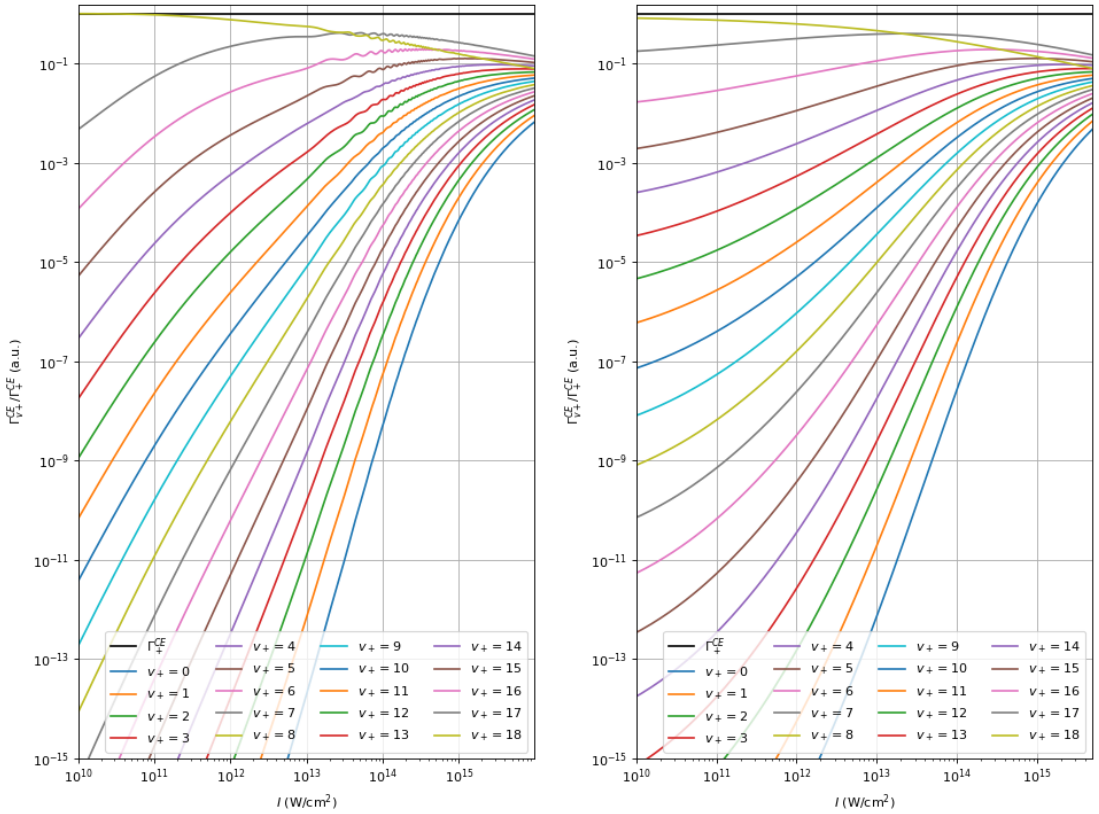

(a) Linear polarization

(b) Circular polarization

Figure A5.15: Second ionization rate from each eigenstate of H_2^+ towards the Coulomb explosion channel, $\Gamma^{\mathrm{CE}}_{v_+}$, normalized with the total ionization rate $\Gamma^{\mathrm{CE}}_{+} = \sum_{v_+} \Gamma^{\mathrm{CE}}_{v_+}$ at different intensities, for (a) a linearly polarized and (b) a circularly polarized field, considering the angle $\theta = 0$ at $\lambda = 800$ nm. As colors repeat, it should be noted that higher states are more easily ionized, with ionization rates that are generally found higher than for low eigenstates.

molecular ADK method, $A_0(\omega, \gamma)$ is calculated in MO-PPT by making a sum over the number of photons $\tilde{n}'$ absorbed above the ionization threshold, as described in Eq. (5.16). The number of photons $\tilde{n}'$ in this sum changes suddenly by one unit as the intensity is increased beyond a value that allows one more photon above the ionization threshold, hence the narrowing "dents" in the ionization rates $W_{H_2}(R,t)$ and $W_{H_2^+}(R,t)$ distributions in Figs. A5.13a and A5.14a. These induced sharp changes in the ionization rate, suddenly admitting wider parts of the $|\langle\chi^*_{v_+}(R)|\sqrt{W_{H_2}[R,t]}|\chi_0(R)\rangle|^2$ and $|\langle\chi^*_{CE}(R)|\sqrt{W_{H_2^+}[R,t]}|\chi_{v_+}(R)\rangle|^2$ overlap functions, enhance the ionization process for each photon absorbed above the ionization threshold, ultimately leading to narrowing oscillations in the integrated

ionization rate profiles, as seen in Figs. A5.12a and A5.15a.

While the results shown in this chapter and its annex are of great scientific interest for the semi-classical simulation of H_2 ionization dynamics in a strong laser field, it is to be noted that the algorithm used for these calculations make use of an earlier version of the electro-nuclear dynamics program. As such, the reader should be warned that using the presented population transfers algorithm would lead to the overestimation of ionization probabilities of the static molecule when compared to the version of the program presented in Chap. 6 and its annex. The lack of σ_u excitation pathways also renders results unreliable when considering long laser pulses.

Bibliography

[1] X. Urbain, B. Fabre, E. M. Staicu-Casagrande, N. de Ruette, V. M. Andrianarijaona, J. Jureta, J. H. Posthumus, A. Saenz, E. Baldit, and C. Cornaggia. Intense-Laser-Field Ionization of Molecular Hydrogen in the Tunneling Regime and Its Effect on the Vibrational Excitation of H_2^+. *Phys. Rev. Lett.*, 92:163004, Apr 2004. URL: https://link.aps.org/doi/10.1103/PhysRevLett.92.163004, doi:10.1103/PhysRevLett.92.163004.

[2] T. K. Kjeldsen and L. B. Madsen. Vibrational excitation of diatomic molecular ions in strong field ionization of diatomic molecules. *Phys. Rev. Lett.*, 95:073004, Aug 2005. URL: https://link.aps.org/doi/10.1103/PhysRevLett.95.073004, doi:10.1103/PhysRevLett.95.073004.

Chapter 6

Electro-nuclear Dynamics of H_2 single and double ionization in ultrafast intense laser pulses

This chapter is an authorized reproduction of an article that has been published in *The Journal of Physical Chemistry A*, 'Attosecond Chemistry' Virtual Special Issue (2024).
DOI: 10.1021/acs.jpca.3c06525

The paper and its original bibliography are enriched by further explanations and analyses of unpublished, related results in an annex at the end of the chapter, after the article itself.

Contents

Electro-nuclear Dynamics of single and double ionization of H_2 in ultrafast intense laser pulses

J.-N. Vigneau,[1,2] **T.-T. Nguyen-Dang**[2)] **and E. Charron**[1*]

[1]Université Paris-Saclay, CNRS, Institut des Sciences Moléculaires d'Orsay, 91405 Orsay cedex, France.
[2]Département de chimie, COPL, Université Laval, 1045 av. de la Médecine, Québec, G1V 0A6, Québec, Canada.

[*]E-mail: eric.charron@universite-paris-saclay.fr

Résumé

Nous présentons une méthode efficace pour modéliser la dynamique d'ionisation simple et double de la molécule H_2 dans un champs laser intense et ultrabref. Cette méthode est basée sur une approche semi-analytique pour calculer les taux d'ionisation moléculaire simple et double en fonction du temps et sur une approche numérique pour décrire le mouvement vibrationnel qui a lieu dans l'ion moléculaire intermédiaire H_2^+. Ce modèle permet de prédire les probabilités d'ionisation simple et double de la molécule H_2 sur une large gamme de fréquences et d'intensités laser avec un temps de calcul limité, tout en fournissant une estimation réaliste de l'énergie des produits d'ionisation dissociative et d'explosion Coulombienne de la molécule H_2. L'effet de la dynamique vibrationnelle sur les rendements d'ionisation et sur les spectres d'énergie cinétique des protons est démontré et, dans le cas de ces derniers, discuté en termes de mécanismes de fragmentation moléculaire en champ intense.

Abstract

We present an efficient method for modeling the single and double ionization dynamics of the H_2 molecule in ultrashort intense laser fields. This method is based on a semi-analytical approach to calculate the time-dependent single and double molecular ionization rates and on a numerical approach to describe the vibrational motion that takes place in the intermediate molecular ion H_2^+. This

model allows for the prediction of the single and double ionization probabilities of the H_2 molecule to be made over a wide range of frequencies and laser intensities with limited computational time, while providing a realistic estimate of the energy of the products of the dissociative ionization and of the Coulomb explosion of the H_2 molecule. The effect of vibrational dynamics on ionization yields and proton kinetic energy release spectra is demonstrated and, in the case of the latter, discussed in terms of basic strong-field molecular fragmentation mechanisms.

6.1 . Introduction

The interaction of gas-phase molecules with intense ultrashort laser fields can often lead to the coupling of electronic and nuclear dynamics, especially in cases where the field is intense enough to induce multiple ionization phenomena. The prototype molecule for exploring these phenomena over the last 30 years has been the H_2 molecule [1–3]. The hydrogen molecule is unique in that its nuclear dynamics unfolds rapidly, on a timescale of just a few femtoseconds, inducing an entanglement of the electronic and nuclear dynamics that is not always easy to decipher. It is also one of the simplest molecules, with a limited number of electronic and nuclear degrees of freedom, for which a variety of realistic and accurate theoretical models have been developed [1, 4]. It is therefore clearly a prototype molecule that has allowed the discovery of various specific and sometimes unexpected molecular mechanisms at work when a molecule is subjected to intense laser fields: Above Threshold Dissociation [5–8], Bond Softening [6–10], Vibrational Trapping also known as Bond Hardening [11–15], Coulomb Explosion [16, 17], and Charge Resonance Enhanced Ionization [18, 19]. All of these fundamental molecular fragmentation mechanisms were discovered and studied in the last decade of the 20th century. At that time, laser pulses with a duration comparable to the vibrational period of H_2 were not yet available to researchers. It is only with the recent development of new light sources that it became possible to use pulses comprising just a few optical cycles, i.e. of slightly less than ten femtoseconds at the carrier wavelength of 800 nm [20]. Thanks to these recent developments, new studies have been carried out with the aim of elucidating in real time the different dynamics at work in the hydrogen molecule fragmentation processes in intense laser fields [21–30].

From a theoretical point of view, although H_2 is one of the simplest molecules we can consider, the accurate modeling of its interaction with an intense laser field, leading to its dissociative ionizations up to its complete Coulomb explosion, remains a real challenge due to the large number of degrees of freedom to be

dealt with, while taking into account the quantum dynamics that unfold on very different time scales for the motion of the electrons (in the attosecond range) and of the nuclei (in the femtosecond range). As a result, many theoretical studies have been performed using simplified models that can only be used in certain limited ranges of laser parameters. Examples include ionization dynamics studies performed with the position of the nuclei fixed [1, 18], photodissociation dynamics studies that do not consider ionization processes [1, 5, 11], or studies performed in reduced dimensionality [30–33]. These types of approaches, which have proven to be very interesting in order to better analyze, understand and sometimes control the processes that take place during or after laser excitation, often impose severe constraints on the conditions under which these models can be applied, for example on the intensity range in which they can realistically be used. While it is true that much more sophisticated models have been developed recently, such as the time-dependent Feshbach close-coupling approach [4], there are applications where it would be extremely useful to have approximate models that could estimate, with reduced computational times, the single and double ionization probabilities of H_2, and at the same time predict the energy of the protons emitted during the fragmentation of the molecule.

This is especially the case in particle-in-cell (PIC) codes, which are widely used in laser-plasma interaction physics. In these systems, the H_2 molecule has recently gained particular interest, as it has been used to demonstrate laser wakefield acceleration of quasi-monoenergetic electron bunches up to very high energies with high repetition rates [34]. For the calculation of single and double ionization processes, the PIC codes currently in use are based on simple Ammosov-Delone-Krainov (ADK) atomic models [35] with ionization potentials adapted to the H_2 molecule [34, 36]. These approaches are very approximate and cannot predict the energy of the emitted protons, which is a variable that can influence plasma dynamics.

In the model proposed here, we have chosen to treat single and double ionization phenomena using the molecular version of the quasi-analytical Perelemov-Popov-Terent'ev (PPT) [37–41] expressions for the ionization rates and to combine it with nuclear wave packet propagation [42]. This combination of an analytical result derived from a semi-classical quasi-static theory of ionization with fully quantum-mechanical time-dependent wave packet calculations is what makes the present approach original. It is aimed at taking into account the nuclear dynamics that is induced by the different excitation and ionization processes. This allows us to consider, in a fairly simple yet realistic way, the ionization of H_2 initially in its ground electronic state, while taking into account the possible stretching of the molecule. Once H_2^+ is formed in its ground electronic state, its

nuclear wave packet is propagated on this state coupled to the first electronic state of the ion. The two wave packets thus formed in H_2^+ can further ionize, giving rise to the Coulomb explosion process. The excitation pathways followed by the molecule are shown schematically in Fig. 6.1. This model allows one to study in detail the influence of vibrational dynamics on single and double ionization processes in the H_2 molecule, while covering a wide range of laser intensities, from relatively low intensities where above threshold dissociation and bond softening processes dominate, to higher intensities where Coulomb explosion becomes the dominant process. It also allows to cover different wavelength ranges and to predict the energy of the emitted protons with a reasonable computational effort.

In the following sections, we first introduce the theoretical model of strong field photoionization and photodissociation dynamics of molecular hydrogen used in this study. Then, we present the influence of vibrational dynamics on ultrashort single-cycle and multi-cycle pulses at different wavelengths and intensities, and finally, we discuss proton kinetic energy release spectra calculated at different intensities. To conclude this introduction, we would like to mention that this work would not have been possible without the invaluable help of our dear late colleague Osman Atabek (April 28, 1946 - June 27, 2022), whose memory we would like to honor with this publication.

6.2 . Methods

In this time-dependent approach, to account for the nuclear dynamics occurring during a single or double ionization event induced by a strong linearly polarized laser pulse, the molecular system is described by the nuclear wave packets $\Psi_{H_2}(R,t)$, $\Psi_g(R,t)$, $\Psi_u(R,t)$ and $\Psi_{\mathrm{C}}(R,t)$, which represent the neutral molecule H_2 in its ground electronic state, the molecular ion H_2^+ in its two lowest electronic states $1s\sigma_g$ and $2p\sigma_u$, and the doubly charged ion H_2^{2+} in the Coulomb explosion channel, respectively. The H_2 molecule is assumed to be initially in its ground vibrational state, with the nuclear wave function

$$\Psi_{H_2}(R,0) = \chi_0(R)\,, \tag{6.1}$$

and with $\Psi_g(R,0) = \Psi_u(R,0) = \Psi_{\mathrm{C}}(R,0) = 0$. The ground vibrational wavefunction $\chi_0(R)$ is obtained by applying Numerov's approach [43, 44] to the potential energy function of the ground electronic state of H_2 [45]. The evolution over a short time interval (of extension δt) of the nuclear wave packet $\Psi_{H_2}(R,t)$ representing the H_2 molecule is then performed numerically in two successive steps. In the first step, the population loss due to the ionization of the neutral molecule

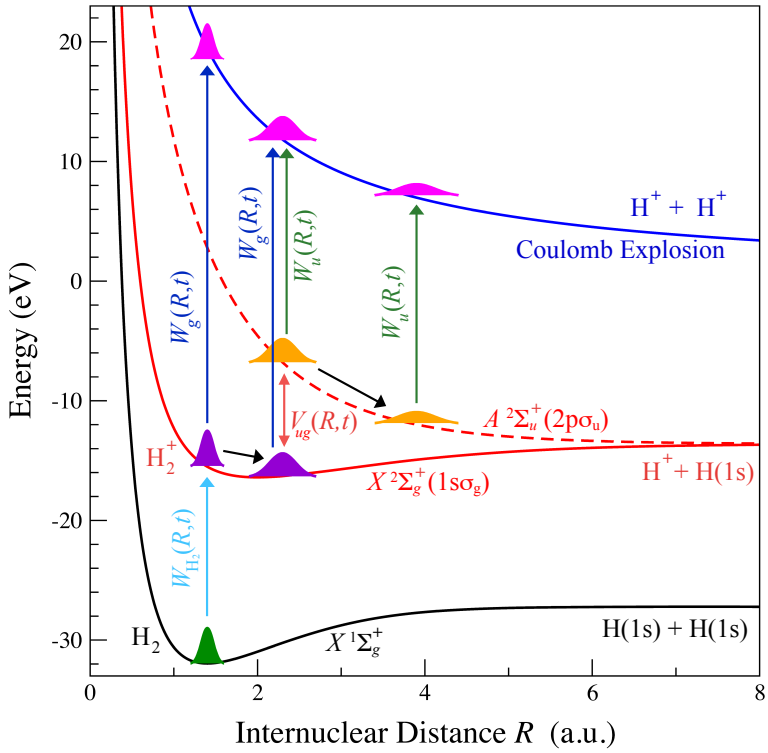

Figure 6.1: Representation of the first and second ionization paths of the H_2 molecule, initially in its electronic and vibrational ground states. The lowest energy potential curve, shown in black, corresponds to the $X^1\Sigma_g^+$ electronic state of H_2. The two red potential curves, solid and dashed, correspond to the two lowest energy electronic states, $X^2\Sigma_g^+$ ($1s\sigma_g$) and $A^2\Sigma_u^+$ ($2p\sigma_u$), of the H_2^+ molecular ion. Finally, the highest energy potential curve, shown in blue, corresponds to the Coulomb repulsion of the doubly ionized $H^+ + H^+$ system. The initial $v = 0$ wave function of H_2 is shown in green. Single ionization generates a vibrational wave packet, shown in purple, on the ground electronic curve of the H_2^+ molecular ion. This wave packet evolves while coupled to the first dissociative excited state of H_2^+, giving rise to a second wave packet, shown in orange. The nuclear dynamics of these two wave packets in the $1s\sigma_g$ and $2p\sigma_u$ electronic states is accompanied by a possible second ionization, which ultimately leads to the Coulomb explosion process, schematically represented here by the three pink wave packets. $W_{H_2}(R,t)$ is the instantaneous single ionization rate of H_2 at internuclear distance R and time t. Similarly, $W_g(R,t)$ and $W_u(R,t)$ are the instantaneous ionizations rates of H_2^+ in the lowest $1s\sigma_g$ and highest $2p\sigma_u$ electronic states. Finally, $V_{ug}(R,t)$ is the radiative coupling between the $1s\sigma_g$ and $2p\sigma_u$ states at distance R and time t.

is taken into account by introducing the instantaneous ionization rate $W_{H_2}(R,t)$,

according to

$$\overline{\Psi}_{H_2}(R,t) = \left[1 - W_{H_2}(R,t)\,\delta t\right]^{\frac{1}{2}}\,\Psi_{H_2}(R,t)\,. \tag{6.2}$$

To evaluate the ionization rate of H_2 in an intense laser field, we use the molecular ionization model [40, 41] derived from the PPT approach [37–39], as described in detail in Vigneau et al. [46] for instance. Finally, in a second step, the resulting wave packet $\overline{\Psi}_{H_2}(R,t)$ is propagated numerically according to

$$\Psi_{H_2}(R,t+\delta t) = \hat{U}_{H_2}(t+\delta t \leftarrow t)\,\overline{\Psi}_{H_2}(R,t)\,, \tag{6.3}$$

with the evolution operator $\hat{U}_{H_2}(t+\delta t \leftarrow t)$ evaluated using the split operator method [47], which optimally splits into three factors associated with the nuclear kinetic energy and potential energy operators [48]. The passage from one to another of these non-commuting factors makes use of Fast Fourier Transforms [47].

From Eq. (6.2) we can deduce that the variation of the population in H_2 between time t and time $t+\delta t$ is equal to

$$\Delta P_{H_2}(t+\delta t \leftarrow t) = -\delta t \int W_{H_2}(R,t)\;|\Psi_{H_2}(R,t)|^2\;dR\,, \tag{6.4}$$

where the minus sign indicates a population loss. It is well known that molecular ionization rates can vary significantly with R, since the ionization potential itself is usually a function of the internuclear distance [46]. We can see in Eq. (6.4) that this important dependence of the ionization rate on R is well accounted for in this model.

This population loss in H_2 essentially populates H_2^+ in its $1s\sigma_g$ electronic ground state [46]. Similar to what is done for H_2, the evolution of the $\Psi_g(R,t)$ and $\Psi_u(R,t)$ wave packets representing H_2^+ is carried out in successive steps. In the first step, the population gain due to the ionization of the neutral molecule in the H_2^+ ground state is calculated using

$$\overline{\Psi}_g(R,t) = \Psi_g(R,t) - i\,\alpha(t)\left[W_{H_2}(R,t)\,\delta t\right]^{\frac{1}{2}}\,\Psi_{H_2}(R,t)\,, \tag{6.5}$$

where $\alpha(t)$ is a normalization factor calculated numerically to impose a population gain in H_2^+ that exactly offsets, during each time step δt, the loss in H_2 given in Eq. (6.4). The nuclear wave packet associated with the first excited electronic state of H_2^+ remains unchanged at this point, with

$$\overline{\Psi}_u(R,t) = \Psi_u(R,t)\,, \tag{6.6}$$

since the ionization of H_2 in an intense laser field produces H_2^+ in its ground electronic state only [46]. In a second step, the two coupled wave packets $\overline{\Psi}_g(R,t)$ and $\overline{\Psi}_u(R,t)$ are propagated numerically according to

$$\begin{bmatrix} \overline{\overline{\Psi}}_g(R,t+\delta t) \\ \overline{\overline{\Psi}}_u(R,t+\delta t) \end{bmatrix} = \hat{U}_{H_2^+}(t+\delta t \leftarrow t) \begin{bmatrix} \overline{\Psi}_g(R,t) \\ \overline{\Psi}_u(R,t) \end{bmatrix}, \tag{6.7}$$

where the evolution operator is evaluated as

$$\begin{aligned} \hat{U}_{H_2^+}(t+\delta t \leftarrow t) \;=\; & \exp\left\{\left[i\,\frac{\hbar\delta t}{4m}\frac{\partial^2}{\partial R^2}\,\mathbf{I}\right]\right\} \times \exp\left\{\left[-i\,\frac{\delta t}{\hbar}\,\mathbf{V}(R,t)\right]\right\} \\ & \times \exp\left\{\left[i\,\frac{\hbar\delta t}{4m}\frac{\partial^2}{\partial R^2}\,\mathbf{I}\right]\right\} \end{aligned} \tag{6.8}$$

to decrease the error to the order $(\delta t)^3$. In this equation, m is the nuclear reduced mass associated with H_2^+, $\mathbf{I}$ is the 2×2 identity matrix, and $\mathbf{V}(R,t)$ is the 2×2 potential matrix composed on its diagonal by the electronic potentials $V_g(R)$ and $V_u(R)$ associated with the 1sσ_g and 2pσ_u states, and by the $V_{ug}(R,t) = -\mu_{ug}(R)E(t)$ non-diagonal radiative coupling term

$$\mathbf{V}(R,t) = \begin{bmatrix} V_g(R) & V_{ug}(R,t) \\ V_{ug}(R,t) & V_u(R) \end{bmatrix}. \tag{6.9}$$

$\mu_{ug}(R)$ is the transition moment between the 1sσ_g and 2pσ_u states, taken from Charron et al. [42]. The kinetic propagation is performed in momentum space and the potential propagation is performed in coordinate space using the diagonal representation of the potential matrix $\mathbf{V}(R,t)$. The evolution operator (6.8) thus allows to describe between the times t and $t+\delta t$ the nuclear dynamics induced in H_2^+ by the kinetic and potential energy of the nuclei, while introducing on an equal footing the laser coupling between the two electronic states $1s\sigma_g$ and $2p\sigma_u$ of H_2^+. It is therefore during this coupled propagation step that the first (2pσ_u) electronic state of H_2^+ is populated. Finally, in a third and last step, the population losses due to the ionization of H_2^+ are taken into account using the molecular-PPT [46] ionization rates $W_g(R,t)$ and $W_u(R,t)$ associated with the $1s\sigma_g$ and $2p\sigma_u$ states

$$\Psi_g(R,t+\delta t) = \left[1 - W_g(R,t+\delta t)\,\delta t\right]^{\frac{1}{2}} \overline{\overline{\Psi}}_g(R,t+\delta t) \tag{6.10a}$$

$$\Psi_u(R,t+\delta t) = \left[1 - W_u(R,t+\delta t)\,\delta t\right]^{\frac{1}{2}} \overline{\overline{\Psi}}_u(R,t+\delta t)\,. \tag{6.10b}$$

These ionization events, which strip the molecule of its last electron, give rise to a Coulomb explosion phenomenon. From Eqs. (6.10) we can derive the vibrational distribution formed in the Coulomb explosion channel $P_{\rm vib}(R, t+\delta t \leftarrow t)$ between times t and $t+\delta t$ as

$$P_{\rm vib}(R, t+\delta t \leftarrow t) = \left[W_g(R,t) \left|\overline{\overline{\Psi}}_g(R,t)\right|^2 + W_u(R,t) \left|\overline{\overline{\Psi}}_u(R,t)\right|^2 \right] \delta t\,. \quad (6.11)$$

Note that this is an incoherent sum of probabilities (corresponding to two orthogonal components of $\Psi_c(R,t)$ not explicitly given here), since the electrons emitted from the 1sσ_g and 2pσ_u orbitals are characterized by different symmetries. Due to the simple $1/R$ law followed by the Coulomb repulsion energy, a simple mapping relates this vibrational probability distribution to the kinetic energy distribution of the emitted protons. This relation is a consequence of the conservation principle [31, 32]

$$P_{\rm c}(E, t+\delta t \leftarrow t)\, dE = P_{\rm vib}(R, t+\delta t \leftarrow t)\, dR \quad (6.12)$$

which leads to

$$P_{\rm c}(E, t+\delta t \leftarrow t) = 2R^2 \left[W_g(R,t) \left|\overline{\overline{\Psi}}_g(R,t)\right|^2 + W_u(R,t) \left|\overline{\overline{\Psi}}_u(R,t)\right|^2 \right] \delta t \quad (6.13)$$

in atomic units [32]. This energy distribution is accumulated over the entire time propagation. The result is the kinetic energy release spectrum $P_{\rm c}(E)$, which is measured in experiments where Coulomb explosion is induced by a strong laser field.

To complete this kinetic energy release spectrum of protons produced by Coulomb explosion, we need of course to add the spectrum resulting from the photodissociation of the molecular ion H_2^+. This additional spectrum is calculated by projecting the nuclear wave packets $\Psi_g(R,t_f)$ and $\Psi_u(R,t_f)$ obtained at the end of the pulse $(t=t_f)$ onto the energy-normalized solutions of the field-free dissociated molecular states, as explained in detail e.g. in Charron et al. [42]. This gives access to the calculation of a complete proton kinetic energy release spectrum $P(E)$, including both the low-energy part associated with the photodissociation of H_2^+ leading to H^+ + H(1s) fragments, and the high-energy part associated with the Coulomb explosion channel leading to H^+ + H^+ fragments.

Finally, the H_2 and H_2^+ populations at each time t are obtained by calculating the norms of the wave packets $\Psi_{H_2}(R,t)$, $\Psi_g(R,t)$ and $\Psi_u(R,t)$, while the population associated with the Coulomb explosion channel can be calculated by accumulating the population losses of the 1sσ_g and 2pσ_u states over the course of the pulse, or by integrating the kinetic energy spectrum $P_{\rm c}(E)$ associated with Coulomb explosion.

6.3 . Results and Discussion

In this section, starting with the case of ultrashort single-cycle pulses, we first evaluate the importance of considering vibrational dynamics in the calculation of proton kinetic energy release (KER) spectra. We then analyze the effect of the vibrational dynamics on the single and double ionization probabilities for pulses of a few optical cycles at 800 nm and at different peak intensities. Finally, we discuss and interpret proton KER spectra calculated at 266 nm for different laser intensities.

From a practical point of view, simulations are performed with a time step δt equal to one thousandth of the optical cycle duration. Thus, at 266 nm this time step is $\delta t \simeq 0.9$ as, while at 800 nm it is about 2.7 as. All results presented here assume a linear polarization of the field and a temporal envelope of the pulse defined by a $\sin^2$ function [1]. The time-dependent electric field is therefore written as

$$E(t) = E_0 \, \sin^2\left(\frac{\pi \, t}{t_f}\right) \cos(\omega t) \tag{6.14}$$

where E_0 is the electric field amplitude and ω the laser carrier frequency.

In theoretical studies dealing with the ionization of H_2 in an intense laser field, it is common to invoke the the small mass of the electrons relative to the mass of the nuclei to get rid of the motion of the nuclei by modeling the electronic dynamics at a fixed inter-nuclear distance [33]. This approximation is chosen mainly for numerical reasons, since a complete quantum calculation including all degrees of freedom of the system, both electronic and nuclear, is computationally extremely expensive. We nevertheless expect that for ultrashort single-cycle pulses, the impact of vibrational dynamics remains limited, even for a molecule as light as H_2. Indeed, in its ground electronic state, H_2 is characterized by a vibrational period of about 7.5 fs, which is clearly longer than the duration of an optical cycle in the range between the near UV and the near IR.

To highlight the influence of vibrational dynamics in the case of ultrashort pulses, we show in panels **a** and **b** (left column) of Fig. 6.2 the Coulomb explosion KER spectra $P_c(E)$ calculated for a single optical cycle pulse at 10^{15} W/cm^2 in the near UV, specifically at 266 nm (panel **a**) and in the near IR, at 800 nm (panel **b**). The results obtained by freezing the vibrational dynamics are shown in dashed lines

[1] This choice is made over that of an experimentally more relevant Gaussian envelope because the two are extremely close in value around the peak of the intense laser pulse, where most excitation processes, in particular tunnel ionization, occur. In addition, the $\sin^2$ envelope has the advantage of having a well-defined beginning and end at finite times, where the system is in a truly field-free condition.

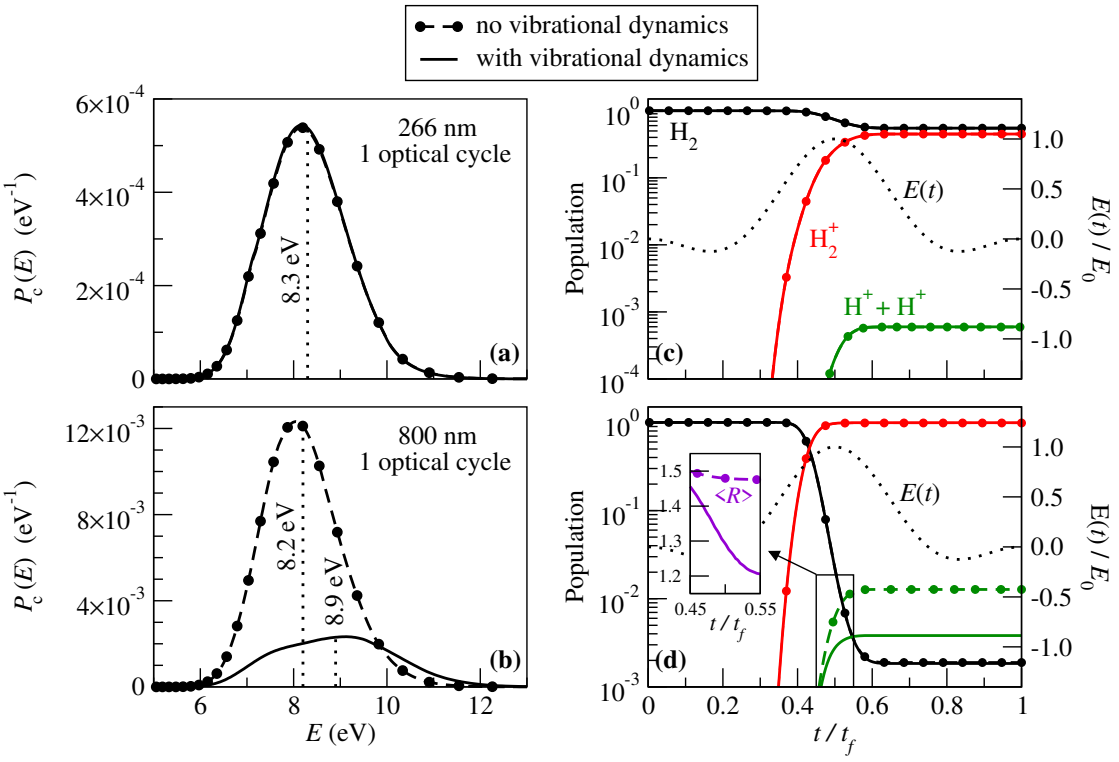

Figure 6.2: Coulomb explosion spectra and ionization dynamics for one-optical-cycle pulses at 266 nm and 800 nm with a peak intensity of $I = 10^{15}$ W/cm^2. The first row (panels **a** and **c**) corresponds to 266 nm, while the second is for 800 nm. The dashed curves with circles are obtained by freezing the nuclear dynamics, while the solid curves take the nuclear dynamics into account. The left side of the figure (panels **a** and **b**) shows the Coulomb explosion spectra $P_c(E)$. The right side of the figure (panels **c** and **d**) shows the time evolution of the H_2 populations in black, H_2^+ in red and $H^+ + H^+$ in green on a logarithmic scale (left axis). The inset in panel **d** shows the time evolution of the average internuclear distance $\langle R \rangle$ (in atomic units) of the H_2^+ $1s\sigma_g$ wave packet in the case where the nuclear dynamics is frozen (purple dashed line with circles) and in the case where it is not (purple solid line). The dotted black lines in panels **c** and **d** show the time dependence of the normalized electric field $E(t)/E_0$ on a linear scale (right axis).

with circles, while the solid curves are associated with the complete calculation taking into account the motion of the nuclei.

At 266 nm there is almost no difference between the two curves, which are superimposed on top of each other, indicating that taking the vibrational dynamics into account is not necessary in the case of a pulse with a total duration of only 0.9 fs. Note that the calculated Coulomb explosion peak, slightly asymmetric, is centered on an average kinetic energy of about 8.3 eV per proton. This

average energy cannot be derived from a simple projection of the initial wave function of H_2 onto the Coulomb energy curve $E = 1/R$, since this simplistic approach would give, for an average internuclear distance in H_2 of $R_{eq} \simeq 1.4$ a.u., an average energy of 9.7 eV. The observed shift to a lower energy (8.3 eV) is due to the fact that the rates of first ionization, $W_{H_2}(R,t)$, and of second ionization, $W_g(R,t)$, increase significantly with the internuclear distance [46] due to a gradual decrease of the respective molecular ionization potentials with the internuclear distance. This property of the ionization rates therefore tends to favor the ionization of the part of the initial wavefunction located at $R > R_{eq}$ to the detriment of the part at $R < R_{eq}$, thus inducing a Coulomb explosion peak at a lower energy than what would have been estimated in a purely vertical excitation scheme.

Continuing with the case of a 266 nm pulse, the panel **c** in Fig. 6.2 shows the population dynamics during that pulse in a logarithmic scale. The populations in H_2, H_2^+ and in the Coulomb explosion channel are shown in black, red and green respectively. Here also, the results of the calculations with and without vibrational dynamics are superimposed. The time evolution of the electric field is also shown schematically on this graph as a black dotted line. We can see a single burst of single and double ionization, around $t = t_f/2$, i.e. at the time when the electric field is at its maximum, delivering a peak intensity of 10^{15} W/cm^2.

If we now look in panel **b** of Fig. 6.2 at the influence of the vibrational dynamics on the Coulomb explosion spectrum at 800 nm in the case of a single optical cycle, the contrast with what we have just discussed at 266 nm is clearly visible. Indeed, the KER spectra calculated with and without vibrational dynamics are quite different. This is due to the fact that at 800 nm the total duration of the single-cycle pulse is 2.7 fs. This duration is not negligible compared to the characteristic time associated with the motion of the nuclei (7.5 fs). An onset of vibrational dynamics can therefore occur during the pulse itself. At the level of the KER spectrum, this effect is amplified by the fact that a small displacement of the nuclei can cause a rather large shift of the Coulomb explosion peak, due to the law of repulsion in $E = 1/R$. For example, a Coulomb explosion occurring at $R = 1.4$ a.u. would produce a peak at 9.7 eV, whereas at $R = 1.7$ a.u. the associated energy would be only 8.0 eV. We can also see in panel **b** of Fig. 6.2 that the inclusion of vibrational dynamics results in a less intense Coulomb explosion peak at a slightly higher energy (8.9 eV) than without vibrational dynamics (8.2 eV). As we will see, this effect can be explained by the vibrational dynamics induced at short times.

In panel **d** of Fig. 6.2 we can observe that during the 800 nm pulse the population loss in H_2 (black line) and the population gain in H_2^+ (red line) are strictly

identical with and without vibrational dynamics. In contrast, the Coulomb explosion probability (green lines) decreases significantly with the inclusion of vibrational dynamics. This variation in the Coulomb explosion probabilities for identical H_2^+ populations is due to the fact that once H_2^+ is produced, a slight motion of the nuclei occurs. This can be seen in the inset within panel **d**. It shows the time evolution of the average internuclear distance $\langle R \rangle$ associated with the wave packet $\Psi_g(R,t)$ of H_2^+ between times $t = 0.45\,t_f$ and $t = 0.55\,t_f$, i.e. when Coulomb explosion occurs near the peak of the pulse. Single ionization of H_2 initially produces a wave packet in H_2^+ around $\langle R \rangle \simeq 1.5$ a.u. This ionization at an internuclear distance larger than the equilibrium distance of H_2 (1.4 a.u.) is due to the fact that the ionization potential decreases with the internuclear distance, and therefore the laser field ionizes more efficiently, and therefore more rapidly, the part of the H_2 vibrational wave function located at $R > R_{eq} = 1.4$ a.u. than the part located at a shorter internuclear distance, which ionizes more slowly. Thus, H_2^+ formation proceeds progressively, starting with higher internuclear distances and then with shorter distances. This time and R-dependent phenomenon induces some vibrational dynamics towards small inter-nuclear distances, which in turn leads to a temporal variation of the average internuclear distance in H_2^+. In a separate calculation, we could verify that removing this R-dependence of the ionization rate suppresses the small initial compression of the chemical bond in H_2^+. This motion toward shorter distances when vibrational dynamics is taken into account explains the shift of the Coulomb explosion peak toward higher energies. It also explains the lower probability of Coulomb explosion as the second ionization potential increases at shorter distances.

We now turn our attention to the double ionization process with pulses of several optical cycles. Fig. 6.3 shows the final populations (at $t = t_f$) in H_2 (black lines), in H_2^+ (red lines) and in the Coulomb explosion channel $H^+ + H^+$ (green lines) as a function of the peak laser intensity in the case of a pulse of 12 optical cycles at 800 nm (corresponding to a $\sin^2$ envelope of total duration 32 fs and full width at half maximum FWHM 16 fs). The dashed lines with circles lines show the results obtained by freezing the vibrational dynamics, while the solid lines take it into account. The laser intensities considered range from 5×10^{13} W/cm^2 to 5×10^{15} W/cm^2, corresponding to maximum electric field amplitudes between 0.038 and 0.38 a.u., thus approaching the electric field felt by an electron in a 1s orbital of the hydrogen atom, while remaining below this threshold where the laser field would completely dominate the attractive Coulomb field of the nuclei.

We can immediately see that the inclusion of vibrational dynamics has a very small, almost negligible effect on the final non-ionized population of H_2, what-

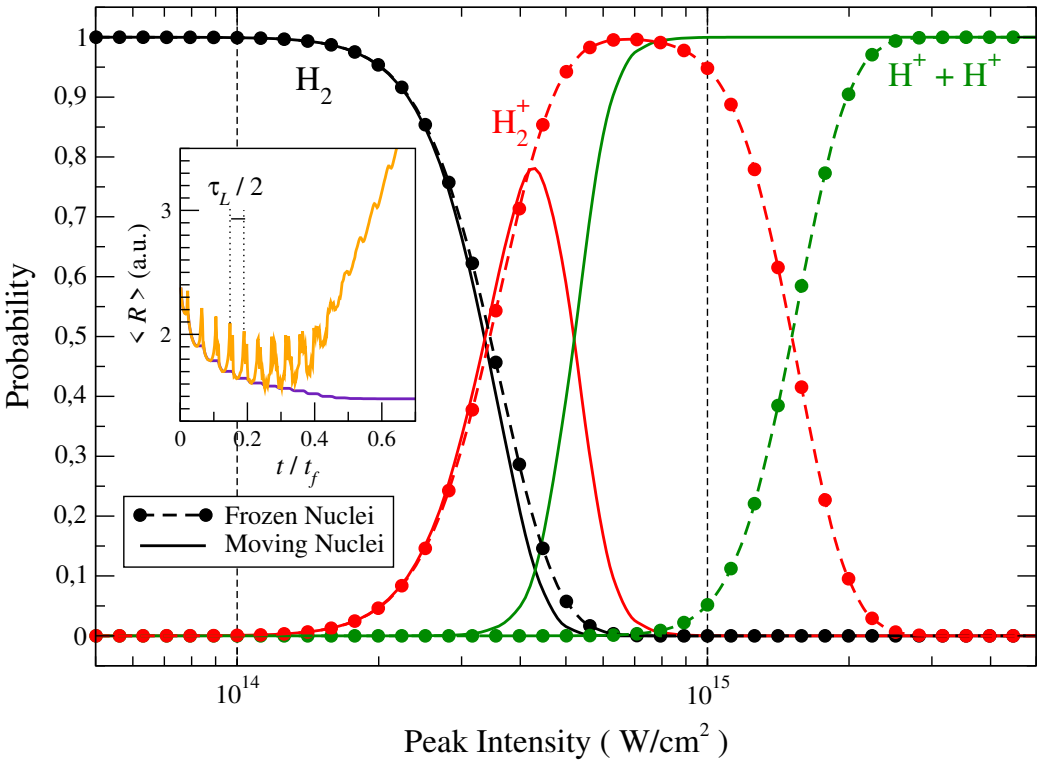

Figure 6.3: Final populations in H_2 (black lines), in H_2^+ (red lines), and in the Coulomb explosion channel $H^+ + H^+$ (green lines) as a function of the peak intensity (log scale between 5×10^{13} W/cm^2 and 5×10^{15} W/cm^2) using a 800 nm linearly polarized field with a $\sin^2$ pulse envelope of total duration of 32 fs, corresponding to 12 optical cycles. The dashed lines with circles show the results obtained by freezing the vibrational dynamics, while the solid lines take it into account. The inset shows the time evolution of the average internuclear distance $\langle R\rangle$ (in atomic units) of H_2^+ between $t=0$ and $t=0.7\,t_f$ for the peak intensity 6.3×10^{14} W/cm^2 in the case where the nuclear dynamics is frozen (lower decreasing purple line) and in the case where it is not (upper oscillating orange line).

ever the laser intensity considered. In practice, H_2 remains almost entirely in the ground vibrational state $v=0$ for the entire duration of the pulse, and the vibrational wave packet describing the H_2 molecule (not shown here) evolves only by a gradual decrease of its norm. From all the simulations we have performed we can conclude that the neutral molecule H_2 is not affected by any nuclear motion during the pulse, whatever the pulse intensity. By comparing the solid and dashed red lines in Fig. 6.3, we can also note that when the laser intensity is too low to induce the removal of the second electron, i.e. for intensities below 4×10^{14} W/cm^2, the final H_2^+ molecular ion population is virtually unaffected

by the inclusion of vibrational dynamics. At such intensities, ionization calculations performed at fixed inter-nuclear distances are therefore very realistic. In contrast, for laser intensities high enough to induce double ionization of the molecule, the final populations in H_2^+ and in the Coulomb explosion channel differ significantly with and without vibrational dynamics. This is because, once formed, the wave packet describing the H_2^+ molecular ion undergoes significant vibrational dynamics, leading it to explore internuclear distances greater than the distance at which it was formed. This is confirmed by the inset in Fig. 6.3, which shows the time evolution of the average internuclear distance associated with H_2^+, with and without vibrational dynamics. When the vibrational dynamics is frozen, the average internuclear distance at which H_2^+ is formed decreases progressively between the beginning of the pulse at $t = 0$ and the pulse peak at $t = t_f/2$. This is because higher laser intensities allow the ionization of the molecule to occur at shorter internuclear distances, where the ionization potential is higher. We thus observe that initially H_2^+ is formed around $R = 2.4$ a.u., but that from $t = t_f/2$ the average internuclear distance in H_2^+ stabilizes around $R = 1.5$ a.u. The range of internuclear distances seen by H_2^+ is therefore, in this case, rather limited to short internuclear distances where double ionization is at a disadvantage due to a high second ionization potential. However, when the vibrational dynamics is taken into account, a completely different result is observed. In this case, at each half-optical-cycle, a burst of ionization occurs at short internuclear distances, followed by an evolution of H_2^+ towards larger internuclear distances. Then, half an optical cycle later, a new wave packet is again formed in H_2^+ at short internuclear distance, thus decreasing the average inter-nuclear distance in H_2^+. This phenomenon then repeats itself at every half optical cycle, producing the oscillations shown in the inset. This is reflected in the evolution of the average internuclear distance $\langle R \rangle$ of H_2^+ by the appearance of a series of peaks separated by half an optical period ($\tau_L/2$, see the inset in Fig. 6.3). Moreover, once the peak of the pulse is reached, single ionization begins to saturate and the mean internuclear distance in H_2^+ starts to increase almost linearly with time up to relatively high values, e.g. $R = 3.1$ a.u. at $t = 0.6\,t_f$. By traveling toward large internuclear distances, the molecular ion H_2^+ explores regions where the ionization potential is lower than at short distances, allowing double ionization at relatively moderate laser intensities. This double ionization mechanism is obviously absent in a calculation that freezes the motion of the nuclei. This explains why the intensity threshold at which double ionization begins is higher when the vibrational dynamics are frozen.

To highlight these differences on a larger intensity scale, Fig. 6.4 shows the single and double ionization probabilities as a function of intensity on a logarithmic scale for the same laser parameters as in Fig. 6.3. The black dashed lines with

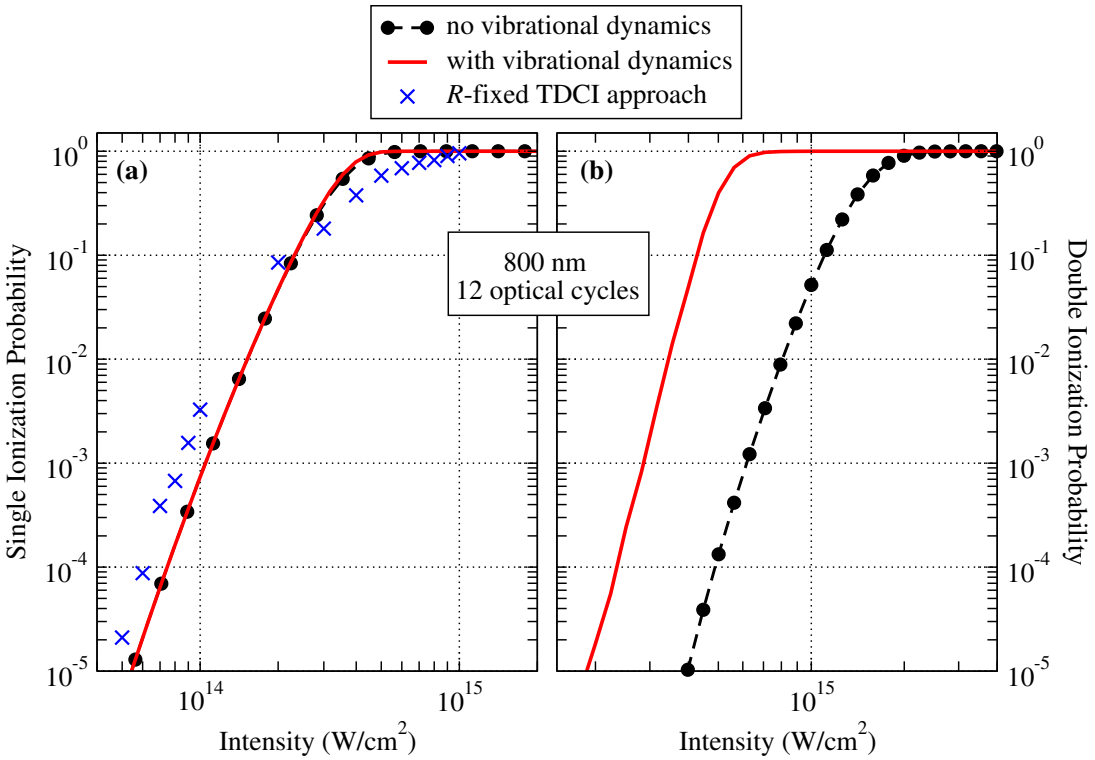

Figure 6.4: Single (panel **a**) and double (panel **b**) ionization probabilities in a log-log scale as a function of the peak intensity between 4×10^{13} W/cm^2 and 2×10^{15} W/cm^2 (panel **a**) and between 1.5×10^{14} W/cm^2 and 4×10^{15} W/cm^2 (panel **b**) using a 800 nm linearly polarized field with a $\sin^2$ pulse envelope of total duration of 32 fs, corresponding to 12 optical cycles. The black dashed lines with circles show the results obtained by freezing the vibrational dynamics, while the solid red lines take it into account. The blue crosses were extracted from Awasthi et al. [49] who used an $R-$fixed TDCI approach with the same laser parameters.

circles show the results obtained by freezing the vibrational dynamics, while the red solid lines take it into account. Panel **a** is devoted to the probability of single ionization, and panel **b** shows the probability of double ionization. The blue crosses show the single ionization probability obtained by a full Time-Dependent Configuration Interaction (TDCI) calculation [49–51], in which the two-electron time-dependent Schrödinger equation was solved assuming that the vibrational motion is frozen and using CI wavefunctions consisting of thousands of configurations using Kohn-Sham (DFT) molecular orbitals expressed in an extended B-spline basis. The TDCI data used here were taken from Awasthi et al. [49]. We see that our model including vibrational motion is in fairly good agreement with the full TDCI results obtained with fixed nuclei, confirming our earlier conclusion

that the single ionization process can be safely described without considering vibrational dynamics. Finally, for the second ionization (panel **b** of Fig. 6.4), we can see that regardless of the laser intensity, taking into account the vibrational dynamics increases the probability of double ionization significantly, since in most cases the probability of double ionization is underestimated by several orders of magnitude when the nuclei are fixed.

In this final section, we present characteristic proton Kinetic Energy Release (KER) spectra $P(E)$ predicted by our theoretical model at 266 nm for different laser intensities. These spectra, given in Fig. 6.5, are calculated for a total pulse duration of 32 fs corresponding to 36 optical cycles. The total KER spectrum $P(E)$, i.e. including both the H^+ + H(1s) dissociation channel of the H_2^+ molecular ion and the H^+ + H^+ Coulomb explosion channel, is shown as a solid blue line, while the spectrum $P_c(E)$ associated only with the Coulomb explosion channel is shown as a dashed red line.

The KER spectra calculated for the peak intensity 2×10^{14} W/cm^2 is shown in the upper left panel **(a)**. At this relatively modest intensity we can see that there is no Coulomb explosion and that the entire spectrum corresponds to the photodissociation of the H_2^+ molecular ion. We can also see that this spectrum essentially consists of a series of two consecutive peaks, with the higher energy peak largely dominating the lower energy peak. This is characteristic of an above threshold dissociation (ATD) process [5–9]. This effect is illustrated in Fig. 6.6, which shows the field-dressed potential energy curves [52] of the H_2^+ molecule. At 266 nm the potential curve of the electronic ground state 1sσ_g (black dashed line $|\mathrm{g}, 0\hbar\omega\rangle$) crosses the potential curve of the 3-photon dressed excited state 2pσ_u (red dashed line $|\mathrm{u}, 3\hbar\omega\rangle$) at an internuclear distance close to the equilibrium distance of 2 a.u. of H_2^+. The molecular ion H_2^+, once formed by the ionization of H_2, readily absorbs 3 photons and begins to dissociate in the $|\mathrm{u}, 3\hbar\omega\rangle$ channel. The separating atomic fragments then pass through the avoided crossing between the $|\mathrm{g}, 2\hbar\omega\rangle$ and $|\mathrm{u}, 3\hbar\omega\rangle$ channels, around $R \simeq 3.3$ a.u., where the molecule re-emits a quanta of photon energy to the radiation field by stimulated emission. The photodissociation of the molecular ion H_2^+ then proceeds adiabatically along the $|\mathrm{g}, 2\hbar\omega\rangle$ pathway, giving rise to the main peak of the KER spectrum at energy $E \simeq 2.7$ eV. The peak observed at lower energies ($E \simeq 0.1$ eV) is due to a bond softening [5–9] (BS) mechanism, which occurs when the potential barrier holding the bond is lowered sufficiently by the radiative interaction in the dressed potential curve picture that the molecule becomes unbound. The energy difference between these two peaks is half the photon energy (2.65 eV), since each fragment (H or H^+) carries half the total energy released in the dissociation. The **(a')** panel within the **(a)** panel of Fig. 6.5 shows a zoom of the

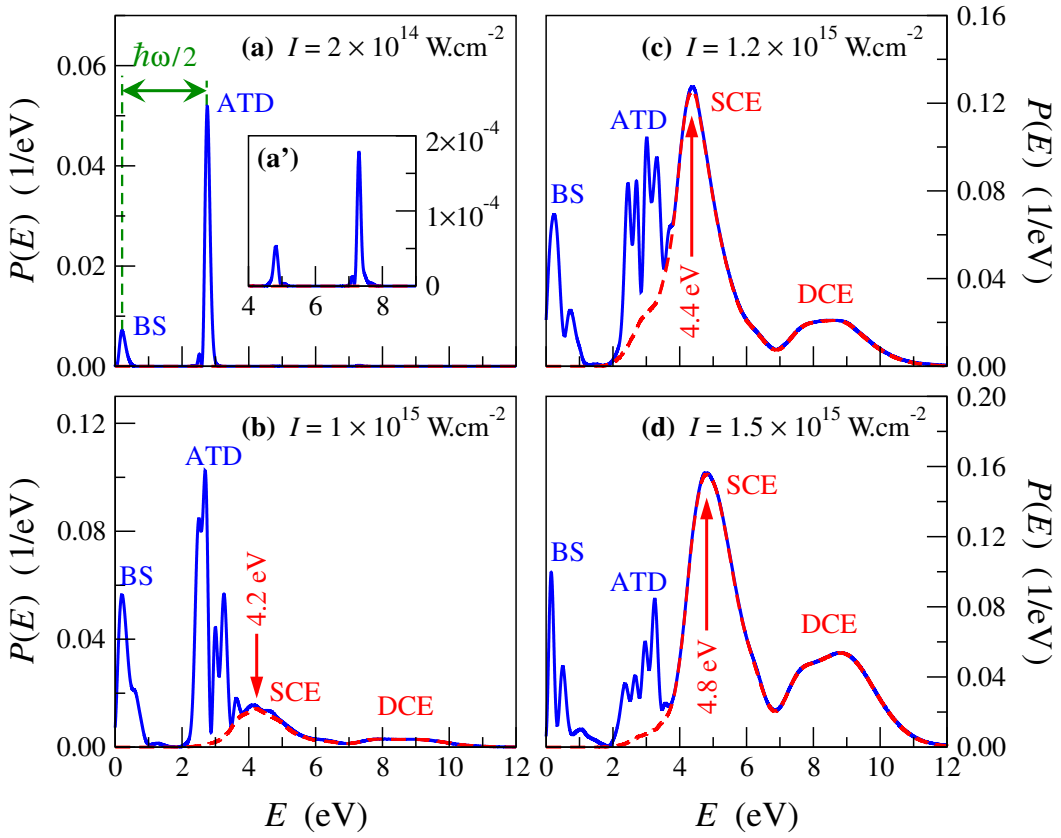

Figure 6.5: Proton Kinetic Energy Release (KER) spectra calculated at 266 nm for a peak intensity of 2×10^{14} W/cm^2 (panels **a** and **a'**), 10^{15} W/cm^2 (panel **b**), 1.2×10^{15} W/cm^2 (panel **c**) and 1.5×10^{15} W/cm^2 (panel **d**). Panel **a'** is a simple zoom of panel **a** between 4 and 9 eV. The electric field envelope is characterized by a sin^2 shape, and the total pulse duration is 32 fs, corresponding to 36 optical cycles. The total KER spectra $P(E)$ are shown with blue solid lines, and the red dashed lines correspond to the KER spectra $P_c(E)$ associated only with the Coulomb explosion channel. The total probabilities of photodissociation and Coulomb explosion are 1.2 % and 0 % in panel (**a**), 8.4 % and 3.6 % in panel (**b**), 10.4 % and 27.6 % in panel (**c**), and 8.8 % and 43.8 % in panel (**d**), respectively. The acronyms BS, ATD, SCE and DCE stand for Bond Softening, Above Threshold Dissociation, Sequential Coulomb Explosion and Direct Coulomb Explosion respectively.

same spectrum over a higher energy range, between 4 and 9 eV. Two additional peaks can be seen in this energy range, much less intense than the two main peaks already described. They correspond to the asymptotic dissociation channels $|\mathrm{u}, 3\hbar\omega\rangle$ and $|\mathrm{g}, 4\hbar\omega\rangle$. These two higher order peaks consist of a replica of the two peaks already described, which is consistent with the periodicity of the dressed potential curves.

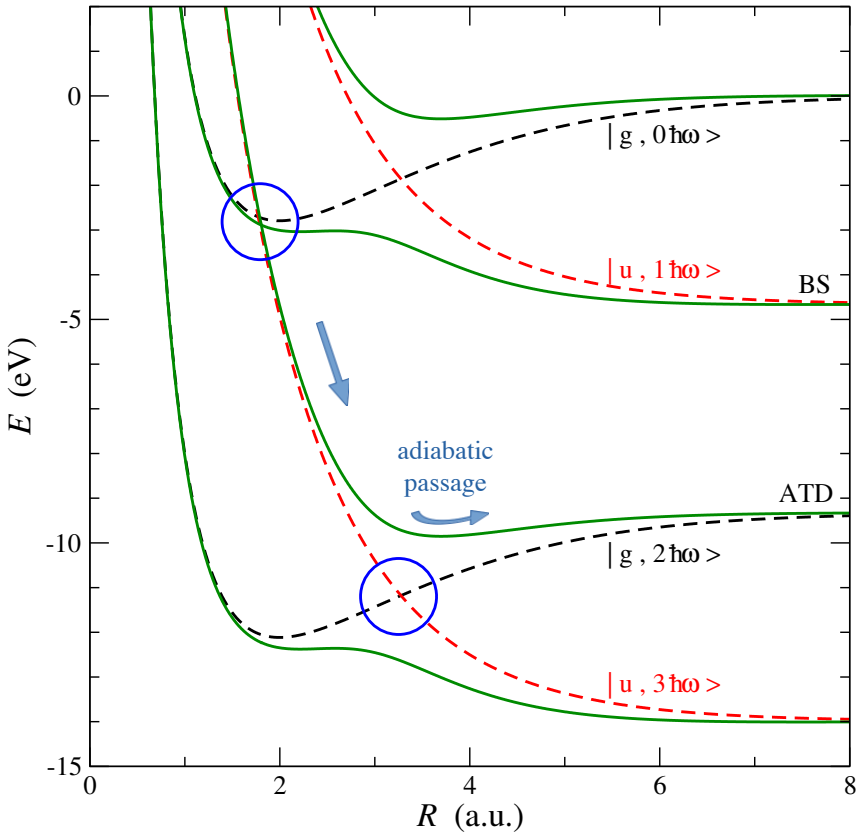

Figure 6.6: H_2^+ $1s\sigma_g$ (dashed black line) and $2p\sigma_u$ (dashed red line) diabatic dressed potential curves for a radiation at 266 nm. The adiabatic dressed potential curves are shown as solid green lines for the laser intensity $I = 2 \times 10^{14}$ W/cm^2. The two most important potential curve crossings, which determine the photodissociation dynamics, are highlighted by the two blue circles. The asymptotic channels corresponding to Bond Softening and Above Threshold Dissociation are labeled by the acronyms BS and ATD.

As the laser intensity increases, double ionization occurs, changing the kinetic energy spectrum of the protons. This can be seen in the panel **(b)** of Fig. 6.5, for the peak intensity 10^{15} W/cm^2. In addition to the BS and ATD peaks, higher energy protons, mainly between 3 and 6 eV, emerge from the ionization of H_2^+ at internuclear distances between 2.2 and 4.5 u.a. This is therefore a sequential mechanism of Coulomb explosion of H_2 via the intermediate step of formation and stretching of H_2^+. The peak associated with this process is therefore labeled SCE for Sequential Coulomb Explosion in Fig. 6.5. As observed experimentally [31, 32], this peak grows and shifts to higher energies with increasing laser intensity, because the second ionization takes place at shorter internuclear distances for higher intensities. This effect is also observed in our calculations,

with the SCE peak shifting from about 4.2 eV at 10^{15} W/cm^2 (panel **b**) to 4.4 eV at 1.2×10^{15} W/cm^2 (panel **c**) and to 4.8 eV at 1.5×10^{15} W/cm^2 (panel **d**). Finally, as the laser intensity increases, a second, higher energy Coulomb explosion peak is gradually formed, in the range of 7 to 10 eV, corresponding to double ionization at very short internuclear distances of the order of 1 to 2 a.u. This mechanism therefore corresponds to direct double ionization without the intermediate step of stretching of the molecular ion H_2^+. This peak is therefore labeled DCE for Direct Coulomb Explosion in Fig. 6.5.

6.4 . Conclusions

In a previous work [46] we have shown how well the PPT theory describes the single and double ionization rates of the H_2 molecule for fixed nuclear geometries, considered as a parameter of the molecule, in a wide range of field frequency and intensity conditions covering both the tunnel and multiphoton ionization regimes. Capitalizing on this, we have developed an algorithm that combines the PPT description of the ionization steps with a quantum mechanical wave packet propagation procedure that takes into account the field-induced nuclear dynamics on all relevant channels during the ionization processes. Our calculations have highlighted the very important role played by nuclear dynamics in the H_2^+ molecular ion, with a strong influence on the double ionization of the molecule. Indeed, if the vibrational dynamics are not taken into account, the double ionization probabilities are generally underestimated by several orders of magnitude. We have also shown that this model gives realistic estimates of the ionization probabilities and allows one to easily calculate the kinetic energy of the protons emitted by photodissociation of H_2^+ through Above Threshold Dissociation and Bond Softening pathways and by Coulomb Explosion, thus unraveling the intensity dependent superposition of signals arising from these channels. This model can be used to obtain an approximate estimate of quantities of interest in the physics of laser-plasma interactions, where it could find some applications over a wide range of laser intensities, pulse durations, and wavelengths.

Bibliography

[1] A. Giusti-Suzor, F. H. Mies, L. F. DiMauro, E. Charron, and B. Yang. Dynamics of H_2^+ in intense laser fields. *J. Phys. B*, 28(3):309, 1995. URL: https://iopscience.iop.org/article/10.1088/0953-4075/28/3/006, doi:10.

1088/0953-4075/28/3/006.

[2] B. Sheehy and L. F. DiMauro. Atomic and molecular dynamics in intense optical filds. *Annual Review of Physical Chemistry*, 47(1):463–494, 1996. arXiv:https://doi.org/10.1146/annurev.physchem.47.1.463, doi:10.1146/annurev.physchem.47.1.463.

[3] J. H. Posthumus. The dynamics of small molecules in intense laser fields. *Reports on Progress in Physics*, 67(5):623, 2004. URL: https://iopscience.iop.org/article/10.1088/0034-4885/67/5/R01, doi:10.1088/0034-4885/67/5/R01.

[4] A. Palacios, J. L. Sanz-Vicario, and F. Martín. Theoretical methods for attosecond electron and nuclear dynamics: applications to the H_2 molecule. *J. Phys. B: At., Mol. Opt. Phys.*, 48(24):242001, 2015. URL: https://iopscience.iop.org/article/10.1088/0953-4075/48/24/242001, doi:10.1088/0953-4075/48/24/242001.

[5] A. Giusti-Suzor, X. He, O. Atabek, and F. H. Mies. Above-threshold dissociation of H_2^+ in intense laser fields. *Phys. Rev. Lett.*, 64:515–518, Jan 1990. URL: https://link.aps.org/doi/10.1103/PhysRevLett.64.515, doi:10.1103/PhysRevLett.64.515.

[6] P. H. Bucksbaum, A. Zavriyev, H. G. Muller, and D. W. Schumacher. Softening of the H_2^+ molecular bond in intense laser fields. *Phys. Rev. Lett.*, 64:1883–1886, 1990. URL: https://link.aps.org/doi/10.1103/PhysRevLett.64.1883, doi:10.1103/PhysRevLett.64.1883.

[7] A. Zavriyev, P. H. Bucksbaum, H. G. Muller, and D. W. Schumacher. Ionization and dissociation of H_2 in intense laser fields at 1.064 μm, 532 nm, and 355 nm. *Phys. Rev. A*, 42:5500–5513, 1990. URL: https://link.aps.org/doi/10.1103/PhysRevA.42.5500, doi:10.1103/PhysRevA.42.5500.

[8] B. Yang, M. Saeed, L. F. DiMauro, A. Zavriyev, and P. H. Bucksbaum. High-resolution multiphoton ionization and dissociation of H_2 and D_2 molecules in intense laser fields. *Phys. Rev. A*, 44:R1458–R1461, Aug 1991. URL: https://link.aps.org/doi/10.1103/PhysRevA.44.R1458, doi:10.1103/PhysRevA.44.R1458.

[9] G. Jolicard and O. Atabek. Above-threshold-dissociation dynamics of H_2^+ with short intense laser pulses. *Phys. Rev. A*, 46:5845–5855, Nov 1992. URL: https://link.aps.org/doi/10.1103/PhysRevA.46.5845, doi:10.1103/PhysRevA.46.5845.

[10] O. Atabek and G. Jolicard. Spectral widths of H_2^+ multiphoton dissociation with short intense laser pulses. *Phys. Rev. A*, 49:1186–1195, Feb 1994. URL: https://link.aps.org/doi/10.1103/PhysRevA.49.1186, doi:10.1103/PhysRevA.49.1186.

[11] A. Giusti-Suzor and F. H. Mies. Vibrational trapping and suppression of dissociation in intense laser fields. *Phys. Rev. Lett.*, 68:3869–3872, Jun 1992. URL: https://link.aps.org/doi/10.1103/PhysRevLett.68.3869, doi:10.1103/PhysRevLett.68.3869.

[12] G. Yao and S.-I. Chu. Molecular-bond hardening and dynamics of molecular stabilization and trapping in intense laser pulses. *Phys. Rev. A*, 48:485–494, Jul 1993. URL: https://link.aps.org/doi/10.1103/PhysRevA.48.485, doi:10.1103/PhysRevA.48.485.

[13] A. Zavriyev, P. H. Bucksbaum, J. Squier, and F. Saline. Light-induced vibrational structure in H_2^+ and D_2^+ in intense laser fields. *Phys. Rev. Lett.*, 70:1077–1080, Feb 1993. URL: https://link.aps.org/doi/10.1103/PhysRevLett.70.1077, doi:10.1103/PhysRevLett.70.1077.

[14] E. E. Aubanel, J.-M. Gauthier, and A. D. Bandrauk. Molecular stabilization and angular distribution in photodissociation of H_2^+ in intense laser fields. *Phys. Rev. A*, 48:2145–2152, Sep 1993. URL: https://link.aps.org/doi/10.1103/PhysRevA.48.2145, doi:10.1103/PhysRevA.48.2145.

[15] E. E. Aubanel, A. Conjusteau, and A. D. Bandrauk. Effect of rotations on stabilization in high-intensity photodissociation of H_2^+. *Phys. Rev. A*, 48:R4011–R4014, Dec 1993. URL: https://link.aps.org/doi/10.1103/PhysRevA.48.R4011, doi:10.1103/PhysRevA.48.R4011.

[16] K. Codling, L. J. Frasinski, and P. A. Hatherly. Multiphoton ionisation of H_2 and D_2 using an intense sub-picosecond laser. *J. Phys. B*, 21(15):L433, 1988. URL: https://iopscience.iop.org/article/10.1088/0953-4075/21/15/003, doi:10.1088/0953-4075/21/15/003.

[17] K. Codling and L. J. Frasinski. Dissociative ionization of small molecules in intense laser fields. *J. Phys. B*, 26(5):783, 1993. URL: https://iopscience.iop.org/article/10.1088/0953-4075/26/5/005, doi:10.1088/0953-4075/26/5/005.

[18] T. Zuo and A. D. Bandrauk. Charge-resonance-enhanced ionization of diatomic molecular ions by intense lasers. *Phys. Rev. A*, 52:R2511–R2514, Oct 1995. URL: https://link.aps.org/doi/10.1103/PhysRevA.52.R2511, doi:10.1103/PhysRevA.52.R2511.

[19] E. Constant, H. Stapelfeldt, and P. B. Corkum. Observation of enhanced ionization of molecular ions in intense laser fields. *Phys. Rev. Lett.*, 76:4140–4143, May 1996. URL: https://link.aps.org/doi/10.1103/PhysRevLett.76.4140, doi:10.1103/PhysRevLett.76.4140.

[20] P. B. Corkum and F. Krausz. Attosecond science. *Nat. Phys.*, 3(6):381–387, 2007. URL: https://www.nature.com/articles/nphys620, doi:10.1038/nphys620.

[21] Th. Ergler, A. Rudenko, B. Feuerstein, K. Zrost, C. D. Schröter, R. Moshammer, and J. Ullrich. Time-Resolved Imaging and Manipulation of H_2 Fragmentation in Intense Laser Fields. *Phys. Rev. Lett.*, 95:093001, Aug 2005. URL: https://link.aps.org/doi/10.1103/PhysRevLett.95.093001, doi:10.1103/PhysRevLett.95.093001.

[22] F. Légaré, Kevin F. Lee, I. V. Litvinyuk, P. W. Dooley, A. D. Bandrauk, D. M. Villeneuve, and P. B. Corkum. Imaging the time-dependent structure of a molecule as it undergoes dynamics. *Phys. Rev. A*, 72:052717, Nov 2005. URL: https://link.aps.org/doi/10.1103/PhysRevA.72.052717, doi:10.1103/PhysRevA.72.052717.

[23] Th. Ergler, A. Rudenko, B. Feuerstein, K. Zrost, C. D. Schröter, R. Moshammer, and J. Ullrich. Spatiotemporal Imaging of Ultrafast Molecular Motion: Collapse and Revival of the D_2^+ Nuclear Wave Packet. *Phys. Rev. Lett.*, 97:193001, Nov 2006. URL: https://link.aps.org/doi/10.1103/PhysRevLett.97.193001, doi:10.1103/PhysRevLett.97.193001.

[24] Th. Ergler, B. Feuerstein, A. Rudenko, K. Zrost, C. D. Schröter, R. Moshammer, and J. Ullrich. Quantum-Phase Resolved Mapping of Ground-State Vibrational D_2 Wave Packets via Selective Depletion in Intense Laser Pulses. *Phys. Rev. Lett.*, 97:103004, Sep 2006. URL: https://link.aps.org/doi/10.1103/PhysRevLett.97.103004, doi:10.1103/PhysRevLett.97.103004.

[25] H. Niikura, D. M. Villeneuve, and P. B. Corkum. Controlling vibrational wave packets with intense, few-cycle laser pulses. *Phys. Rev. A*, 73:021402, Feb 2006. URL: https://link.aps.org/doi/10.1103/PhysRevA.73.021402, doi:10.1103/PhysRevA.73.021402.

[26] A. Rudenko, Th. Ergler, B. Feuerstein, K. Zrost, C. D. Schröter, R. Moshammer, and J. Ullrich. Time-resolved measurements with intense ultrashort laser pulses: a 'molecular movie' in real time. *Journal of Physics: Conference Series*, 88(1):012050, nov 2007. URL: https://iopscience.iop.org/

article/10.1088/1742-6596/88/1/012050, doi:10.1088/1742-6596/88/1/012050.

[27] I. A. Bocharova, H. Mashiko, M. Magrakvelidze, D. Ray, P. Ranitovic, C. L. Cocke, and I. V. Litvinyuk. Direct coulomb-explosion imaging of coherent nuclear dynamics induced by few-cycle laser pulses in light and heavy hydrogen. *Phys. Rev. A*, 77:053407, May 2008. URL: https://link.aps.org/doi/10.1103/PhysRevA.77.053407, doi:10.1103/PhysRevA.77.053407.

[28] C. R. Calvert, W. A. Bryan, W. R. Newell, and I. D. Williams. Time-resolved studies of ultrafast wavepacket dynamics in hydrogen molecules. *Physics Reports*, 491(1):1–28, 2010. URL: https://www.sciencedirect.com/science/article/pii/S0370157309002889, doi:https://doi.org/10.1016/j.physrep.2009.12.004.

[29] A. Palacios, P. Rivière, A. Gonzalez-Castrillo, and F. Martin. *XUV Lasers for Ultrafast Electronic Control in H2*, pages 25–48. Springer International Publishing, Cham, 2014. URL: https://link.springer.com/chapter/10.1007/978-3-319-02051-8_2, doi:10.1007/978-3-319-02051-8_2.

[30] P. Lu, J. Wang, H. Li, K. Lin, X. Gong, Q. Song, Q. Ji, W. Zhang, J. Ma, H. Li, H. Zeng, F. He, and J. Wu. High-order above-threshold dissociation of molecules. *Proceedings of the National Academy of Sciences*, 115(9):2049–2053, 2018. URL: https://www.pnas.org/doi/abs/10.1073/pnas.1719481115, doi:10.1073/pnas.1719481115.

[31] S. Saugout, C. Cornaggia, A. Suzor-Weiner, and E. Charron. Ultrafast electronuclear dynamics of $\mathrm{h_2}$ double ionization. *Phys. Rev. Lett.*, 98:253003, Jun 2007. URL: https://link.aps.org/doi/10.1103/PhysRevLett.98.253003, doi:10.1103/PhysRevLett.98.253003.

[32] S. Saugout, E. Charron, and C. Cornaggia. $\mathrm{H_2}$ double ionization with few-cycle laser pulses. *Phys. Rev. A*, 77:023404, Feb 2008. URL: https://link.aps.org/doi/10.1103/PhysRevA.77.023404, doi:10.1103/PhysRevA.77.023404.

[33] J.-N. Vigneau, T.-T. Nguyen-Dang, E. Charron, and O. Atabek. Strong-field molecular ionization beyond the single active electron approximation. *The Journal of Chemical Physics*, 157(13):134304, 10 2022. URL: https://pubs.aip.org/aip/jcp/article-abstract/157/13/134304/2841883/Strong-field-molecular-ionization-beyond-the?redirectedFrom=fulltext, arXiv:https://pubs.aip.org/aip/jcp/

article-pdf/doi/10.1063/5.0111636/16550642/134304_1_online.pdf, doi:10.1063/5.0111636.

[34] F. Salehi, M. Le, L. Railing, M. Kolesik, and H. M. Milchberg. Laser-accelerated, low-divergence 15-mev quasimonoenergetic electron bunches at 1 khz. *Phys. Rev. X*, 11:021055, Jun 2021. URL: https://link.aps.org/doi/10.1103/PhysRevX.11.021055, doi:10.1103/PhysRevX.11.021055.

[35] M. V Ammosov, N. B. Delone, and V. P. Krainov. Tunnel ionization of complex atoms and of atomic ions in an alternating electromagnetic field. *Sov. Phys. JETP*, 64(6):1191, 1986.

[36] E. P. Maldonado, R. Elgul Samad, A. V. Felicio Zuffi, F. Bittencourt Dutra Tabacow, and N. Dias Vieira. Self-modulated laser-plasma acceleration in a H_2 gas target, simulated in a spectral particle-in-cell algorithm: wakefield and electron bunch properties. In *2019 SBFoton International Optics and Photonics Conference (SBFoton IOPC)*, pages 1–5, 2019. doi:10.1109/SBFoton-IOPC.2019.8910252.

[37] A. M. Perelomov, V. S. Popov, and M. V. Terent'ev. Ionization of atoms in an alternating electric field. *J. Exp. Theor. Phys.*, 23:924–934, 1966. URL: http://jetp.ras.ru/cgi-bin/dn/e_023_05_0924.pdf.

[38] A. M. Perelomov, V. S. Popov, and M. V. Terent'ev. Ionization of atoms in an alternating electric field II. *J. Exp. Theor. Phys.*, 24:207–217, 1966. URL: http://jetp.ras.ru/cgi-bin/dn/e_024_01_0207.pdf.

[39] A. M. Perelomov and V. S. Popov. Ionization of atoms in an alternating electric field III. *J. Exp. Theor. Phys.*, 25:336–343, 1967. URL: http://jetp.ras.ru/cgi-bin/dn/e_025_02_0336.pdf.

[40] X. M. Tong, Z. X. Zhao, and C. D. Lin. Theory of molecular tunneling ionization. *Phys. Rev. A*, 66:033402, Sep 2002. URL: https://link.aps.org/doi/10.1103/PhysRevA.66.033402, doi:10.1103/PhysRevA.66.033402.

[41] E. P. Benis, J. F. Xia, X. M. Tong, M. Faheem, M. Zamkov, B. Shan, P. Richard, and Z. Chang. Ionization suppression of Cl_2 molecules in intense laser fields. *Phys. Rev. A*, 70:025401, Aug 2004. URL: https://link.aps.org/doi/10.1103/PhysRevA.70.025401, doi:10.1103/PhysRevA.70.025401.

[42] E. Charron, A. Giusti-Suzor, and F. H. Meis. Coherent control of photodissociation in intense laser fields. *J. Chem. Phys.*, 103(17):7359–7373, 11 1995. URL: https://pubs.aip.org/aip/jcp/article-abstract/103/17/

7359/180043/Coherent-control-of-photodissociation-in-intense?redirectedFrom=fulltext, doi:10.1063/1.470308.

[43] B. Numerov. A Method of Extrapolation of Perturbations. *Monthly Notices of the Royal Astronomical Society*, 84(8):592–602, 06 1924. doi:10.1093/mnras/84.8.592.

[44] B. Numerov. Note on the numerical integration of $d^2x/dt^2 = f(x,t)$. *Astronomische Nachrichten*, 230(19):359–364, 1927. URL: https://onlinelibrary.wiley.com/doi/abs/10.1002/asna.19272301903, doi:https://doi.org/10.1002/asna.19272301903.

[45] W. Kolos and L. Wolniewicz. Potential-Energy Curves for the $X^1\Sigma_g^+$, $b^3\Sigma_u^+$, and $C^1\Pi_u$ States of the Hydrogen Molecule. *The Journal of Chemical Physics*, 43(7):2429–2441, 05 2004. doi:10.1063/1.1697142.

[46] J.-N. Vigneau, O. Atabek, T.-T. Nguyen-Dang, and E. Charron. Strong field non-Franck–Condon ionization of H_2: a semi-classical analysis. *The European Physical Journal Special Topics*, 232(13):2081–2093, 2023. URL: https://link.springer.com/article/10.1140/epjs/s11734-022-00750-z, doi:10.1140/epjs/s11734-022-00750-z.

[47] M. D. Feit, J. A. Fleck, and A. Steiger. Solution of the Schrödinger equation by a spectral method. *Journal of Computational Physics*, 47(3):412–433, 1982. URL: https://www.sciencedirect.com/science/article/pii/0021999182900912, doi:https://doi.org/10.1016/0021-9991(82)90091-2.

[48] A. D. Bandrauk and H. Shen. Exponential split operator methods for solving coupled time-dependent Schrödinger equations. *The Journal of Chemical Physics*, 99(2):1185–1193, 07 1993. URL: https://pubs.aip.org/aip/jcp/article-abstract/99/2/1185/688669/Exponential-split-operator-methods-for-solving?redirectedFrom=fulltext, doi:10.1063/1.465362.

[49] M. Awasthi, Y. V. Vanne, A. Saenz, A. Castro, and P. Decleva. Single-active-electron approximation for describing molecules in ultrashort laser pulses and its application to molecular hydrogen. *Phys. Rev. A*, 77:063403, Jun 2008. URL: https://link.aps.org/doi/10.1103/PhysRevA.77.063403, doi:10.1103/PhysRevA.77.063403.

[50] Y. V. Vanne and A. Saenz. Numerical treatment of diatomic two-electron molecules using a B-spline based CI method. *J. Phys. B*, 37(20):4101, oct

2004. URL: https://iopscience.iop.org/article/10.1088/0953-4075/37/20/005, doi:10.1088/0953-4075/37/20/005.

[51] M. Awasthi, Y. V. Vanne, and A. Saenz. Non-perturbative solution of the time-dependent Schrödinger equation describing H_2 in intense short laser pulses. *J. Phys. B*, 38(22):3973, oct 2005. URL: https://iopscience.iop.org/article/10.1088/0953-4075/38/22/005, doi:10.1088/0953-4075/38/22/005.

[52] A. D. Bandrauk and M. L. Sink. Photodissociation in intense laser fields: Predissociation analogy. *J. Chem. Phys*, 74(2):1110–1117, 01 1981. URL: https://pubs.aip.org/aip/jcp/article-abstract/74/2/1110/839239/Photodissociation-in-intense-laser-fields?redirectedFrom=fulltext, doi:10.1063/1.441217.

Annex to: Electro-nuclear Dynamics of H_2 single and double ionization in ultrafast intense laser pulses

The article presented above puts into light the importance of including vibrational motion in the molecular dynamics in order to not underestimate the probability of double ionization, comparing dissociative ionization simulations of H_2 up to its Coulomb Explosion or dissociation as H_2^+ with similar semi-classical ionization rate calculation methods that do not include the vibrational dynamics. One will deduce from the explanations of the method, through Eqs. (6.1)-(6.13), that the algorithm has drastically evolved from our previous article, inserted in this thesis in Chapter 5.

This article, entitled "Strong Field Non-Franck-Condon Ionization of H_2: A Semi-Classical Analysis", made explicit use of the eigenstates of H_2^+ and of the continuum states of the Coulomb explosion channel to project populations from one state to the other, taking into consideration the ionization rate to ponder the overlapping functions before integration, giving ultimately our transferred populations (see Eqs. (5.4) and (5.7)).

This method is quite different from the ionization and wave packet propagation method described in the article "Electro-nuclear Dynamics of H_2 single and double ionization in ultrafast intense laser pulses" of Chapter 6.

To provide an intermediate approach between these two proposals, in this appendix we present additional simulations using the algorithm from Chapter 6, but freezing the vibrational wave packet propagation dynamics. It remains to be seen how this intermediate method compares with the "static" algorithm based on the population exchanges of Chapter 5 and with the full "dynamic" wave packet algorithm of Chapter 6. In the remainder of this appendix, the intermediate method of freezing the vibrational degrees of freedom in the approach described in Chapter 6 will be referred to as the "static" wave packet approach.

Single and double ionization dynamics

First, let's look at the population profiles from the three possible configurations of our molecule of interest in Fig. A6.1: H_2 (blue line), H_2^+ (orange line) and $2H^+$ (green line). Each profile contains plateaux throughout the simulation, as expected for linearly polarized field interactions. Indeed, the field intensity oscillates from zero to local maxima, equidistant by half an optical cycle. These equidistant maxima transpose on the population profiles as sharp transitions from one configuration to the other, explaining the increased number of plateaux for the shortest wavelength 266 nm (Figs. A6.1a, A6.1c and A6.1e), compared to the wavelength 800 nm, and the consistency in the number of plateaux from one method to the other, since the same field parameters were used.

In all simulations, a pulse of peak intensity $I = 10^{15}$ W/cm^2 and duration $\tau \approx 32$ fs is sufficient to fully ionize H_2, since all H_2 populations were completely ionized by the time the peak intensity was reached.

The dynamics of double ionization, on the other hand, is very different from one method to another, and from one wavelength to another. The eigenstate population model, Figs. A6.1a-A6.1b, overestimates the double ionization probability compared to the static wave packet model, Figs. A6.1c-A6.1d. The former ionizes up to 82% of H_2^+ at $\lambda = 266$ nm, and 98% at $\lambda = 800$ nm, while the latter barely ionizes up to 3% and 7% at 266 and 800 nm, respectively. As shown in the article, including the nuclear propagation via the split-operator algorithm with the wave packet model induces more double ionization than the static wave packet model, up to 32% at $\lambda = 266$ nm and complete Coulomb explosion of the molecule at $\lambda = 800$ nm, Figs. A6.1e-A6.1f. These final values are below the eigenstates method estimation at 266 nm, and slightly above the same estimation at 800 nm.

Although null for non-vibrational dynamics in Figs. A6.1a-A6.1d and negligible for propagating wave packets in Figs. A6.1e-A6.1f, all subfigures contain an 'absorbed' population, P_{abs} (red line), that constitutes dissociative populations that have propagated asymptotically into the absorbing boundary.

One might wonder, from the observations made between the static methods of Fig. A6.1, how it is possible to get double ionization probabilities so far apart from models that are supposed to make quite similar approximations on paper. The answer lies in the use (or lack thereof) of phase and propagation in the two simplest models.

Indeed, projection of populations from one eigenstate to another as a means of calculating ionization rates completely neglects the fact that wave packets are

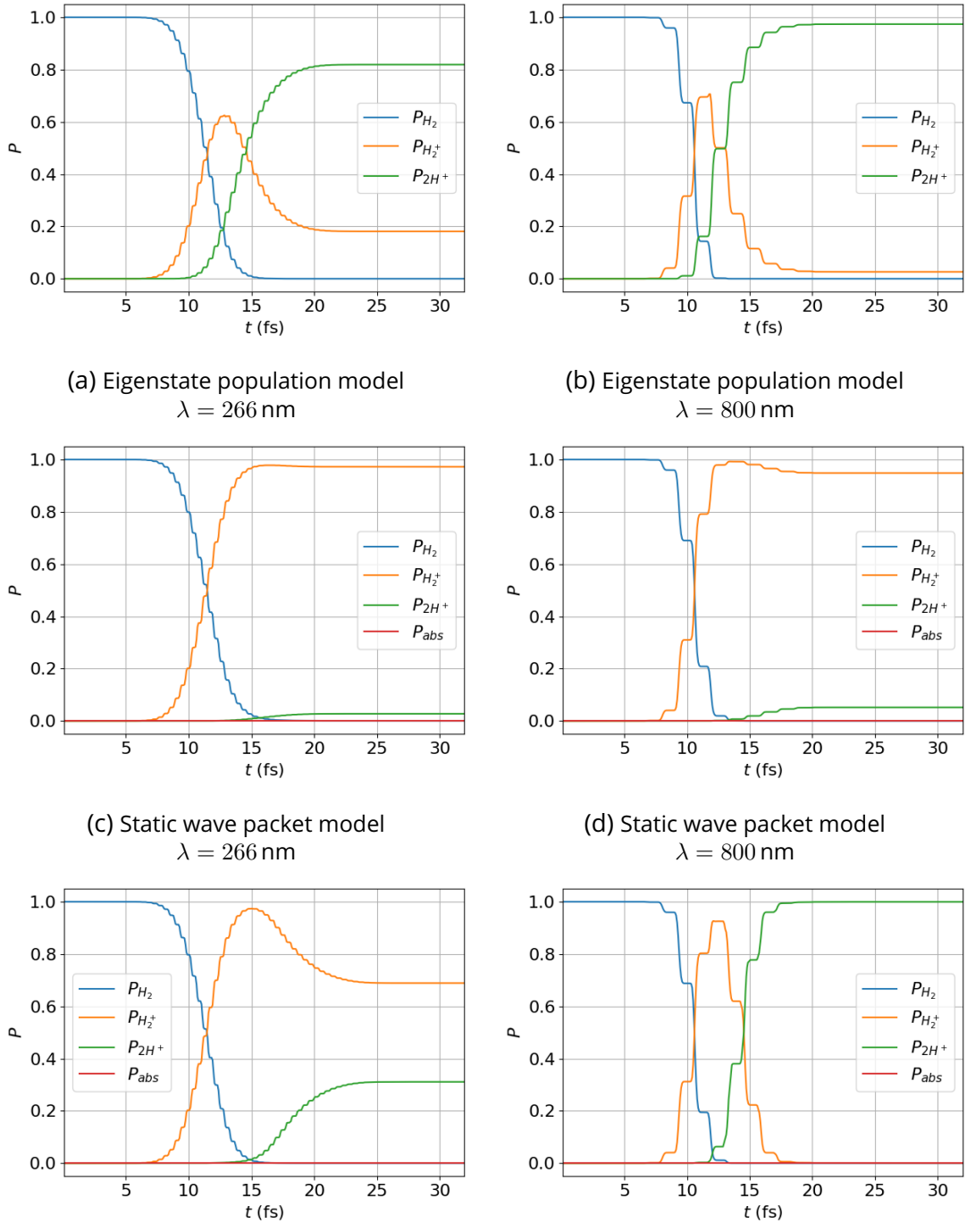

(a) Eigenstate population model $\lambda = 266\,\text{nm}$

(b) Eigenstate population model $\lambda = 800\,\text{nm}$

(c) Static wave packet model $\lambda = 266\,\text{nm}$

(d) Static wave packet model $\lambda = 800\,\text{nm}$

(e) Propagating wave packet model $\lambda = 266\,\text{nm}$

(f) Propagating wave packet model $\lambda = 800\,\text{nm}$

Figure A6.1: Population profiles of H_2 (blue line), H_2^+ (orange line), $2H^+$ (green line) and lost population from dissociation past the discretized grid (red line) for an intensity 10^{15} W/cm^2 at 266 nm with 36 optical cycles for the left column (a,c,e) and at 800 nm with 12 optical cycles for the right column (b,d,f). A comparison is made between the different molecular dynamics algorithms: eigenstate population transfer method in the top row (a,b), static wave packet transfer in the middle row (c,d) or propagating wave packet transfer in the bottom row (e,f).

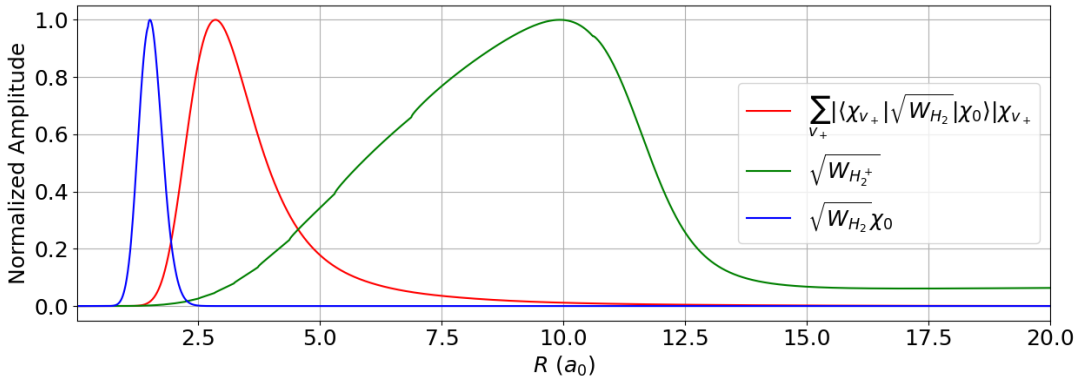

Figure A6.2: Normalized plot of the wave packets generated in H_2^+ by the single, instantaneous ionization of H_2 in its ground vibrational state χ_0 at an intensity of 10^{15} W/cm^2 with phase or sign factors taken into account (blue line - wave packet based methods) and without phase or sign factors taken into account (red line - population transfer based method). The R dependence of the $[W_{H_2^+}(R)]^{\frac{1}{2}}$ amplitude associated with the H_2^+ ionization probability is also shown in this plot (green line).

combinations of these eigenstates each with its respective phase factor. Indeed, to understand why the model based on simple population transfers greatly overestimates the probability of double ionization at low intensity, we need only to look at the wave packet that would be projected onto H_2^+ from H_2 if we neglect the phases or signs associated with the different v_+ vibrational levels components of that molecular ion wave packet. The resulting wave packet

$$\psi_{\text{no phase}}(R) \sim \sum_{v_+} |\langle\, \chi_{v_+} \,|\, [W_{H_2}]^{\frac{1}{2}} \,|\, \chi_0 \,\rangle|\ \chi_{v_+}(R), \tag{A6.1}$$

is shown in red on Fig A6.2. This wave packet is unphysically shifted to large internuclear distances compared to the

$$\psi_{\text{proj}}(R) \sim [W_{H_2}]^{\frac{1}{2}}\ \chi_0(R), \tag{A6.2}$$

wave packet (shown in blue) that should normally be formed if the phases associated with the different v_+ vibrational levels of the ion were properly accounted for. Since the H_2^+ ionization rate increases significantly with the inter-nuclear distance (see the $[W_{H_2^+}]^{\frac{1}{2}}$ function shown in green in Fig. A6.2), this non-physical shift in the wave packet formed significantly and unreasonably increases the probability of double ionization predicted by the simple model based on population transfers, leading to a significant overestimation of the double ionization probability for intensities below the double ionization saturation limit.

Furthermore, if the model based on static vibrational wave packets underestimates the probability of double ionization compared to the dynamic model, it's because in the dynamic model the wave packets generated in H_2^+ are free to move during the pulse to inter-nuclear distances greater than the equilibrium distance, where the ionization rate is much higher than at short distances (see the green line in Fig. A6.2.

H_2 Dynamics

As noted above, the population profiles of H_2 are quite similar from one method to the other. This is mainly due to the fact that the ground state of H_2 is practically the only one that really contributes to the vibrational dynamics of the neutral molecule, and since this state is localized at the bottom of the H_2 potential, its vibrational range is significantly reduced. However, since the vibrational wave packet representing the neutral molecule may, in principle, differ from its ground eigenstate form, the evolution of the total population in H_2 and of the population of the vibrational ground state are shown in Fig. A6.3 by a light and dark blue line, respectively. Whatever the wavelength chosen, 266 nm or 800 nm, and whatever the method used, the results obtained are extremely close, demonstrating that a simple method based on kinetic equations for the populations which does not take vibrational dynamics into account is sufficient to describe population loss in the neutral.

The average internuclear distances associated with these wave packets are plotted in Fig. A6.4, showing considerable differences from one wavelength to another, and from one method to another. As expected, the value of $\langle R \rangle_{H_2}$ associated to the eigenstates method is constant, Figs. A6.4a-A6.4b.

In the case of static wave packets, Figs. A6.4c-A6.4d, $\langle R \rangle_{H_2}$ decreases continuously, a result that can be explained by the results of Fig. A5.13 generated for the annex of Chap. 5. $W_{H_2}(R,t)$ is calculated in the same way for all methods, in this case using the semi-classical theory of Perelomov, Popov and Terent'ev for a molecule (MO-PPT), and it is found to widen as a Gaussian-like function from its center around 4 a.u. towards lower and higher R values when the intensity of the field is increased. Since $\psi_{H_2}(R,0) = \chi_0(R)$ is also a Gaussian-like function, centered at $R_{eq} \approx 1.44$ a.u., the parts of the wave function located at higher internuclear distances will ionize faster than the parts located at short distances, and a larger part of the wave function will be ionized when local field maxima are reached. During the dynamics, when the field is at near-zero intensities, plateaux are observed because there is no ionization and the wave packet

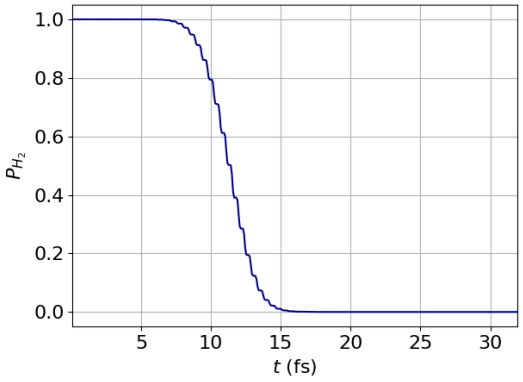

(a) Eigenstate population model
$\lambda = 266\,\text{nm}$

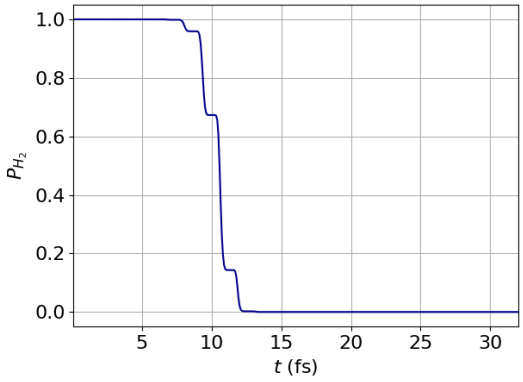

(b) Eigenstate population model
$\lambda = 800\,\text{nm}$

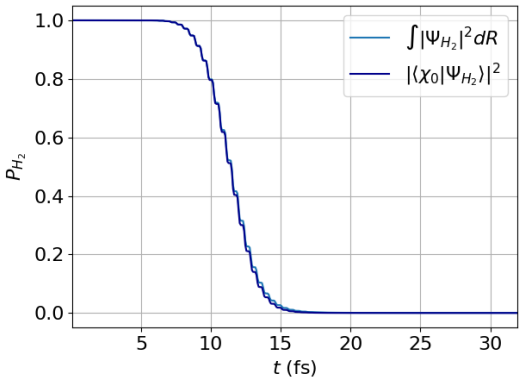

(c) Static wave packet model
$\lambda = 266\,\text{nm}$

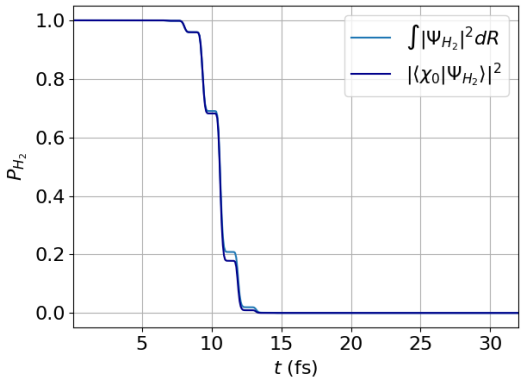

(d) Static wave packet model
$\lambda = 800\,\text{nm}$

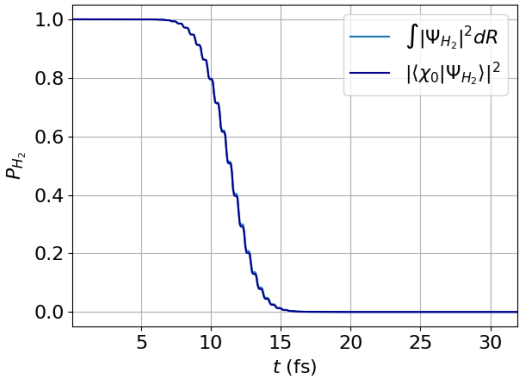

(e) Propagating wave packet model
$\lambda = 266\,\text{nm}$

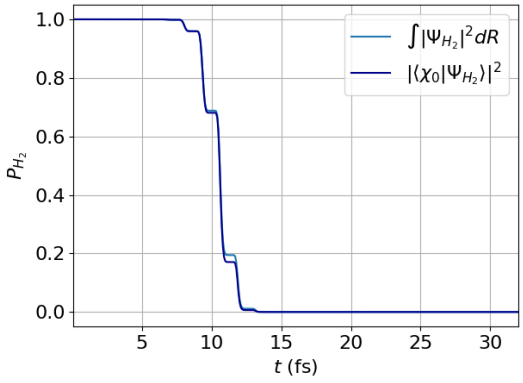

(f) Propagating wave packet model
$\lambda = 800\,\text{nm}$

Figure A6.3: Population profiles of H_2 (light blue line) and its projection onto the ground state $\chi_0(R)$ (dark blue line) over a 10^{15} W/cm^2 field of wavelength 266 nm, 36 optical cycles for the left column (a,c,e) and 800 nm, 12 optical cycles for the right column (b,d,f). A comparison is made between the different molecular dynamics algorithms: eigenstate population transfer in the top row (a,b), static wave packet transfer in the middle row (c,d) or propagating wave packet transfer in the bottom row (e,f).

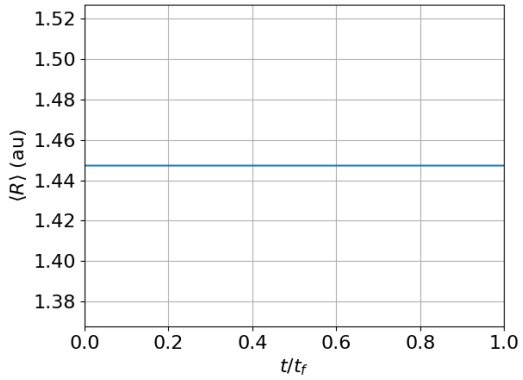

(a) Eigenstate population model $\lambda = 266\,\text{nm}$

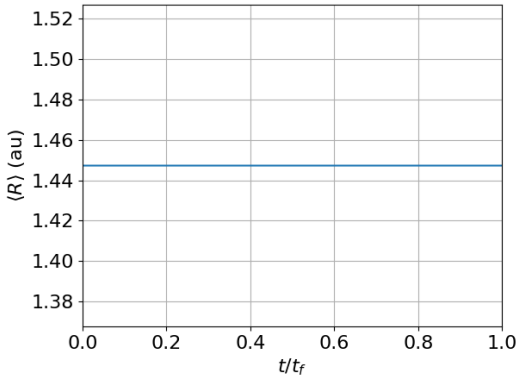

(b) Eigenstate population model $\lambda = 800\,\text{nm}$

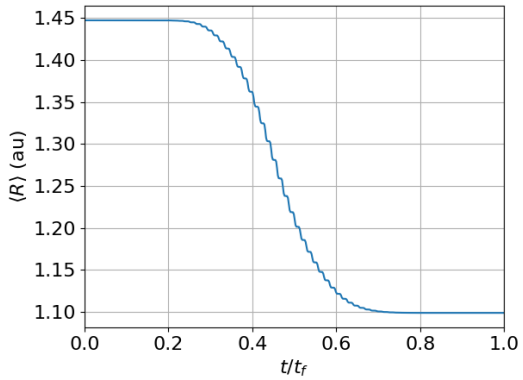

(c) Static wave packet model $\lambda = 266\,\text{nm}$

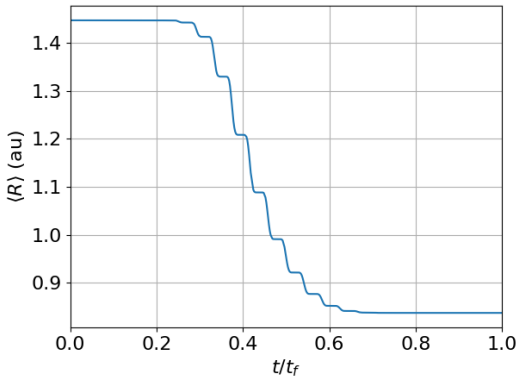

(d) Static wave packet model $\lambda = 800\,\text{nm}$

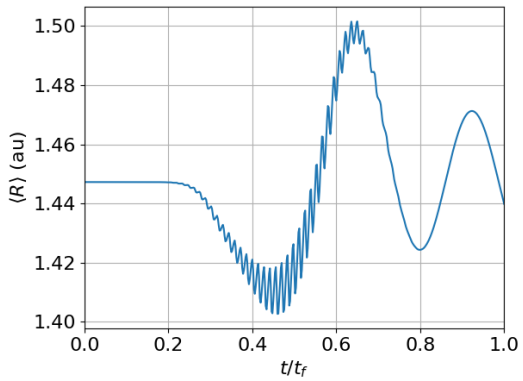

(e) Propagating wave packet model $\lambda = 266\,\text{nm}$

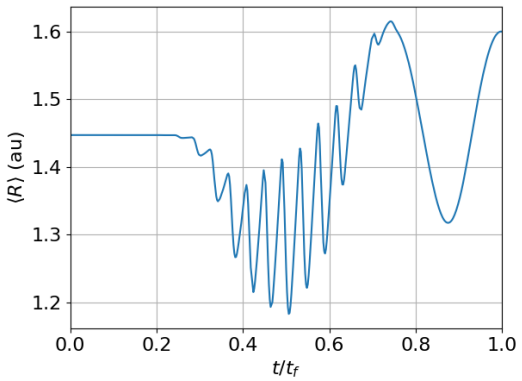

(f) Propagating wave packet model $\lambda = 800\,\text{nm}$

Figure A6.4: Average internuclear distance $\langle R \rangle$ in H_2 for a $10^{15}\,\text{W/cm}^2$ field of wavelength 266 nm, 36 optical cycles for the left column (a,c,e) and 800 nm, 12 optical cycles for the right column (b,d,f). A comparison is made between the different molecular dynamics algorithms: eigenstate population transfer in the top row (a,b), static wave packet transfer in the middle row (c,d) or propagating wave packet transfer in the bottom row (e,f).

does not propagate.

Furthermore, the average internuclear distance at the end of the dynamics is lower for $\lambda = 800$ nm (0.83 a.u.) while it is higher for $\lambda = 266$ nm (1.10 a.u.). This difference is caused by the delay in the single ionization of H_2 within the lower wavelength dynamics: Since the ionization rate of the neutral molecule is globally higher at 800 nm, most of the population subjected to such a field is already ionized before the peak intensity is reached. As such, the ionization process has occurred under a W_{H_2} distribution that is narrower than it would have been at maximum intensity and it is contained within high internuclear distance values. As a consequence, the remaining post-dynamic wave packet, although close to totally ionized, has been pushed towards lower R values than the wave packet that remains by the end of a $\lambda = 266$ nm dynamics.

The last figures, A6.4e and A6.4f, show the motion of the propagating wave packets within the potential of H_2, a potential that requires a lot of energy to induce dissociation. For this reason, $\langle R \rangle_{H_2}$ is seen to oscillate around the equilibrium internuclear distance value, $R_{eq} \approx 1.44$ a.u., in both dynamics. Two characteristics of the oscillation patterns differ from one wavelength to the other: the frequency of the faster oscillations that occur in the middle of the dynamics (t/t_f between 0.25 and 0.75), and the amplitude of both the fast and and slow oscillations. High-frequency oscillations are a direct result of the interaction of the field with the molecule. Their amplitude is highest in the middle of the dynamics, when the field amplitude is close to its maximum, and during these local maxima of the field, parts of the H_2 wave packet are ionized, temporarily reducing the average internuclear distance to lower values. Since a higher frequency field contains more optical cycles than lower frequencies for the same pulse duration, the ionization —and $\langle R \rangle_{H_2}$ decrease— events occur more frequently. On the other hand, lower frequencies subject the molecule to longer local maxima, thus reducing $\langle R \rangle_{H_2}$ considerably more than higher frequencies. In both cases, shifting the average value of the internuclear distance causes the wave packet to oscillate in proportion to the displacement, thus inducing higher amplitudes from the $\lambda = 800$ nm field.

H_2^+ Dynamics

H_2^+ eigenstate formation can be compared from one method to the other by projecting the static/dynamic wave packet $\psi_g(R,t)$ onto the said eigenstates of the molecular ion

$$P_{v_+}(t) = \Big| \int \chi_{v_+}(R)\, \psi_g(R,t)\, dR \Big|^2, \tag{A6.3}$$

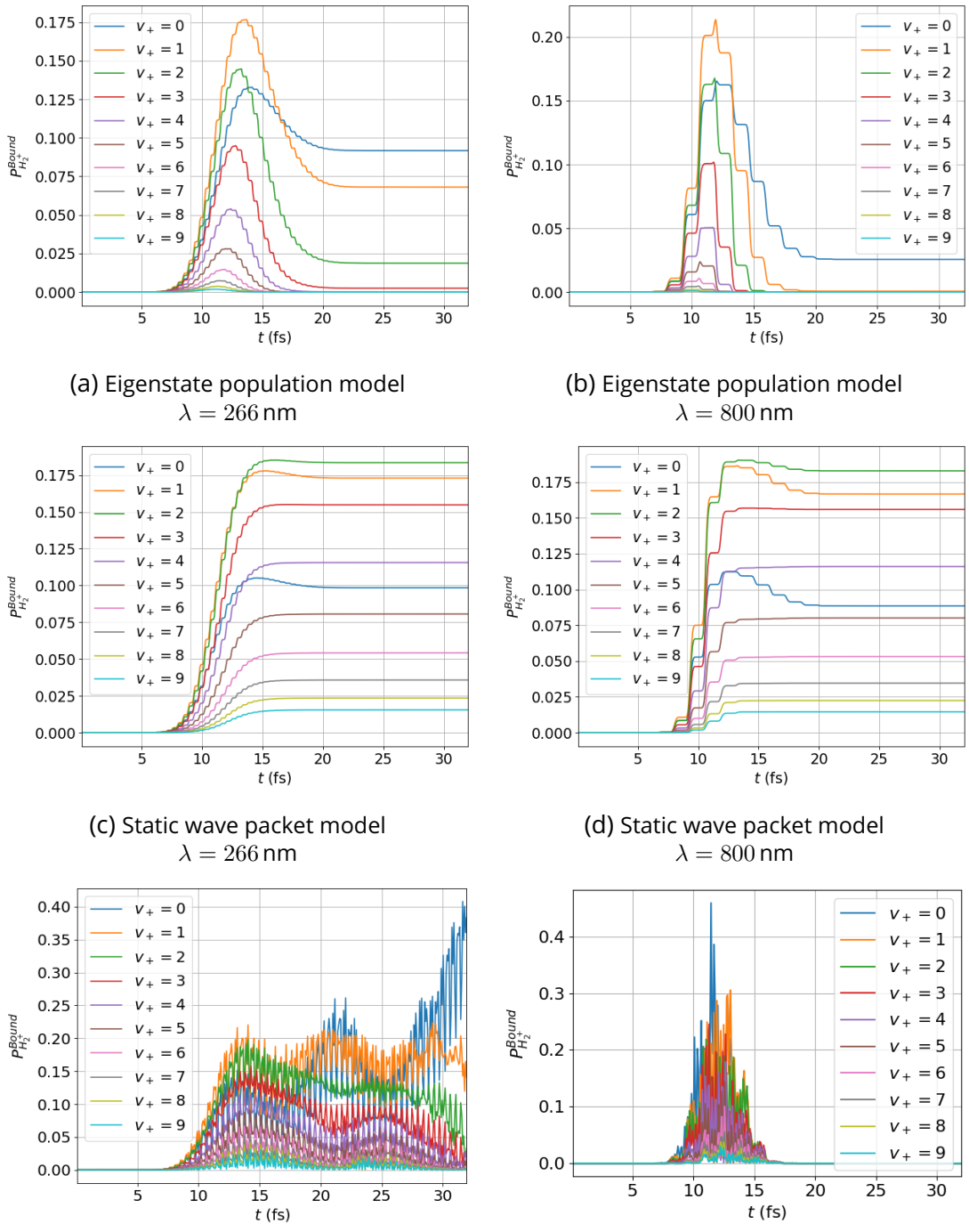

(a) Eigenstate population model $\lambda = 266\,\text{nm}$

(b) Eigenstate population model $\lambda = 800\,\text{nm}$

(c) Static wave packet model $\lambda = 266\,\text{nm}$

(d) Static wave packet model $\lambda = 800\,\text{nm}$

(e) Propagating wave packet model $\lambda = 266\,\text{nm}$

(f) Propagating wave packet model $\lambda = 800\,\text{nm}$

Figure A6.5: Population profiles of all vibrational eigenstates v_+ of H_2^+ for a $10^{15}\,\text{W/cm}^2$ field of wavelength 266 nm, 36 optical cycles for the left column (a,c,e) and 800 nm, 12 optical cycles for the right column (b,d,f). A comparison is made between the different molecular dynamics algorithms: eigenstate population transfer in the top row (a,b), static wave packet transfer in the middle row (c,d) or propagating wave packet transfer in the bottom row (e,f).

resulting in parts of the wave packet being bound to specific vibrational eigenstates.

In the case of the eigenstates population method, as discussed in the annex of the previous article, single ionization rates favour the population of lower states, with state $v_+ = 1$ taking the lead at the peak intensity $I = 10^{15}$ W/cm^2, followed by $v_+ = 2, 0$ and 3, increasing in order (Fig. A5.12a), while double ionization rates deplete higher states faster towards Coulomb explosion (Fig. A5.15a). This peculiarity of the double ionization rate at such intensities brings the population profiles for both wavelengths to an order corresponding to end-of-dynamic populations often found to be in decreasing order from the lowest state $v_+ = 0$ to the highest.

Static wave packets are initially ionized towards H_2^+ bound states exactly the same way than they are with eigenstates population transfers, as

$$\psi_g(R, \delta t) \propto \left[W_{\mathrm{H}_2}\delta t\right]^{\frac{1}{2}} \chi_0(R) \tag{A6.4}$$

and

$$P_{v_+}(\delta t) \propto \left|\left\langle \chi_{v_+} \middle| \left[W_{\mathrm{H}_2}\delta t\right]^{\frac{1}{2}} \middle| \chi_0 \right\rangle\right|^2 . \tag{A6.5}$$

As the dynamics evolves over time, ψ_{H_2} differs furthermore from χ_0, and the generated wave packet ψ_g may strongly differ from the linear combination of eigenstates predicted by Eq. (A6.5). In this method, the rightmost part of the wave packet is ionized faster, which changes the distribution of the bound populations over time, bringing the end-of-dynamics populations $P_{v_+=2}(t_f) > P_1(t_f) > P_3(t_f) > P_4(t_f) > P_0(t_f) > P_5(t_f) > ...$, as depicted in Figs. A6.5c and A6.5d. Of course, this change can also be attributed to the double ionization depletion process.

Adding the vibrational propagation to the molecular dynamics brings a night-and-day comparison between different wavelengths, as H_2^+ is only partially ionized at $\lambda = 266$ nm (Fig. A6.1e) and fully ionized in the case of a 800 nm field (Fig. A6.1f). From this last sentence, one might wonder why double ionization of H_2 is more efficient with lower energy photons with the same pulse duration. This phenomenon will be better explained by the following analysis of the average internuclear distance of the wave packet, but states populations can still be addressed by keeping in mind that the propagation of the wave packet allows its evolution towards higher internuclear distances, where it is more easily ionized due to its overlap with the calculated ionization rate $W_{\mathrm{H}_2^+}$. As with the static wave packet method, the initial population distribution of this method matches

the predictions of the eigenstate population transfer method, but this similarity quickly disappears. After that, the vibrational motion within the fs time scale dynamics brings ψ_g to domains of larger R and higher ionization probability.

In our latest molecular dynamics simulation algorithm, since we have added vibrational propagation of the wave packet, it has become important to include dissociative pathways of H_2^+ to the already implemented Coulomb Explosion in $2H^+$. A photodissociation process induced by the coupling with the first excited state of H_2^+ is indeed not negligible under certain parameters of the field. We have thus decided to introduce the coupling to the $^1\Sigma_u^+$ molecular ion channel from the $^1\Sigma_g^+$ channel. While it is possible to ionize the wave packet from ψ_u, its potential is strongly dissociative and would lead to total dissociation if no external forces were applied.

Since the eigenstate method allows population transfers only to bound states of $^1\Sigma_g^+$, and since they are orthogonal to the dissociative continuum states describing Above-Threshold Dissociation (ATD) [1–5], the total population of H_2^+ (see Eq.(A6.5)) is not plotted in Fig. A6.6, which shows populations of $^1\Sigma_g^+$ and $^1\Sigma_u^+$, nor has it been plotted in Fig. A6.7, which shows bound and dissociated populations within $^1\Sigma_g^+$.

Similarly to the population transfers method, since the static wave packets method (SW) does not involve split-operator propagation, the population within H_2^+ is exclusively found in the $^1\Sigma_g^+$ configuration, with

$$P_{H_2^+}(t) = \langle \psi_g | \psi_g \rangle = \int |\psi_g(R,t)|^2 \, dR \tag{A6.6}$$

as shown in Figs. A6.6a and A6.6b for $\lambda = 266$ and 800 nm, respectively. This is not to say that some of the ionized wave packet cannot dissociate in its H_2^+ configuration, but rather that when it does, as shown by the slight dissociative population P_{diss} in Figs. A6.7a and A6.7b, it is via an ATD mechanism within the $^1\Sigma_g^+$ potential. The non-zero dissociative population, P_{diss}, although almost negligible, can be seen on both profiles of $\lambda = 266$ and 800 nm in Figs. A6.7a, A6.7b.

The propagating wave packet method uses the split-operator algorithm throughout the dynamics to account for the vibrational motion of neutral H_2 and ionic H_2^+ in the complete dissociative ionization simulation. Once part of the ground state wave packet ψ_{H_2} has been ionized to ψ_g, it propagates on a longer timescale within the $^1\Sigma_g^+$ potential, while simultaneously being transferred in the $^1\Sigma_u^+$ potential through a field-induced $g - u$ coupling. The population of both states of the molecular ion,

$$P_{H_2^+}(t) = \langle \psi_g | \psi_g \rangle + \langle \psi_u | \psi_u \rangle = P_g(t) + P_u(t) \,, \tag{A6.7}$$

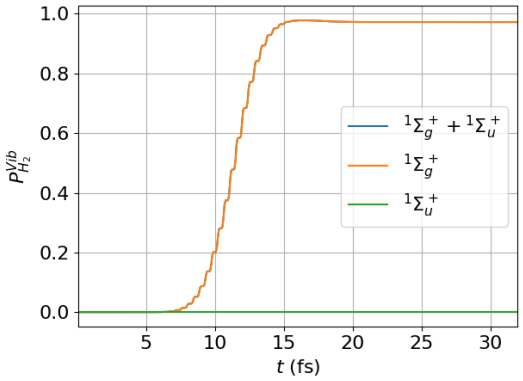

(a) Static wave packet model $\lambda = 266\,\text{nm}$

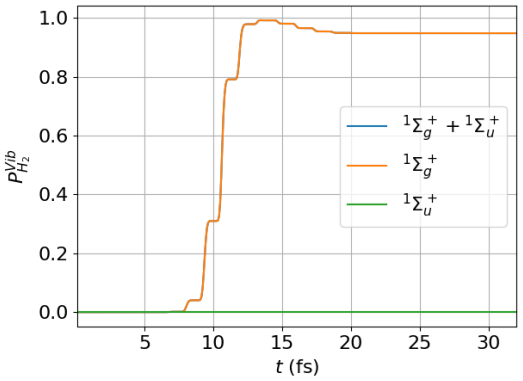

(b) Static wave packet model $\lambda = 800\,\text{nm}$

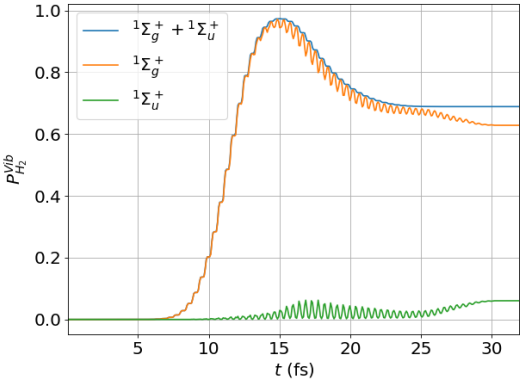

(c) Propagating wave packet model $\lambda = 266\,\text{nm}$

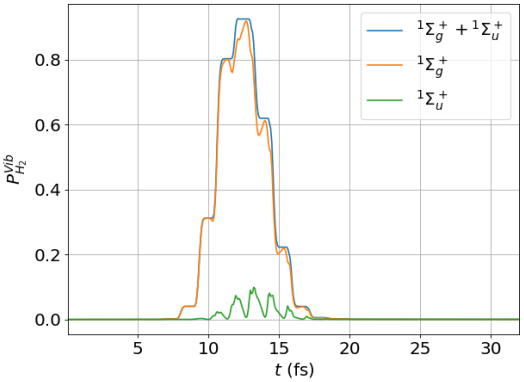

(d) Propagating wave packet model $\lambda = 800\,\text{nm}$

Figure A6.6: Population profiles of H_2^+ (blue line) split between the $^1\Sigma_g^+$ (orange line) and $^1\Sigma_u^+$ (green line) electronic states for a 10^{15} W/cm^2 field of wavelength 266 nm, 36 optical cycles for the left column (a,c) and 800 nm, 12 optical cycles for the right column (b,d). A comparison is made between the different molecular dynamics algorithms: static wave packet transfer in the top row (a,b) or propagating wave packet transfer in the bottom row (c,d).

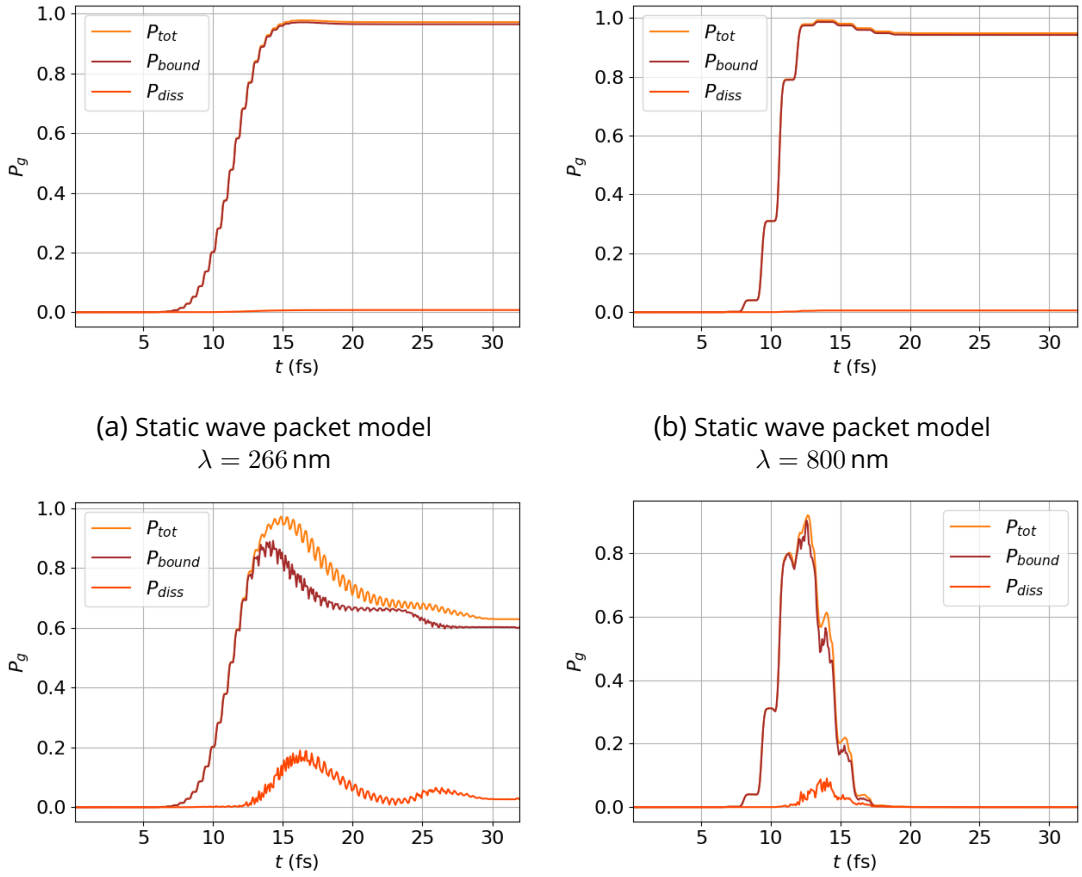

(a) Static wave packet model $\lambda = 266\,\text{nm}$

(b) Static wave packet model $\lambda = 800\,\text{nm}$

(c) Propagating wave packet model $\lambda = 266\,\text{nm}$

(d) Propagating wave packet model $\lambda = 800\,\text{nm}$

Figure A6.7: Bound (brown line), dissociative (orange-red line) and total (orange-yellow) population profiles within the ${}^1\Sigma_g^+$ electronic state of H_2^+ for a 10^{15} W/cm^2 field of wavelength 266 nm, 36 optical cycles for the left column (a,c) and 800 nm, 12 optical cycles for the right column (b,d). A comparison is made between the different molecular dynamics algorithms: static wave packet transfer in the top row (a,b) or propagating wave packet transfer in the bottom row (c,d).

can be seen oscillating in Figs. A6.6c and A6.6d. This oscillation pattern comes to an end in the last few fs of the dynamics, when the field is at a lower intensity. Since $P_g(t)$ can be divided into bound and dissociative states, we can also write this population as

$$P_g(t) = \sum_{v_+} |\langle \chi_{v_+} | \psi_g \rangle|^2 + \int |\langle \chi_\varepsilon | \psi_g \rangle|^2 \, d\varepsilon = P_g^{bound}(t) + P_g^{diss}(t) \,, \tag{A6.8}$$

where $\chi_{v_+}(R)$ is the bound eigenstate of H_2^+ associated to the ionic vibrational channel v_+ and where $\chi_\varepsilon(R)$ denotes the dissociative continuum states of the $^1\Sigma_g^+$ potential.

At 266 nm, since the population is not fully ionized to the Coulomb explosion channel by the end of the dynamics, we can see that over a final population $P_{H_2^+}(t_f) \approx 70\%$, the population within the $^1\Sigma_u^+$ potential is about 7% (Fig. A6.6c), the bound population of $^1\Sigma_g^+$ is about 60%, and its dissociative population is about 3%. While most of the ionized population remains bound, a non-negligible fraction dissociates before reaching a double-ionization-induced Coulomb explosion. Of the dissociated H_2^+, most (2:1) will come from the $^1\Sigma_u^+$ channel.

Fig. A6.8e shows the evolution of the average internuclear distance $\langle R \rangle$ at 266 nm. $\langle R \rangle$ oscillates very rapidly and at a frequency that follows the local minima and maxima of the field. Initially, $\langle R \rangle$ is about 1.85 a.u., a value higher than $R_{eq}(H_2) \approx 1.44$ a.u. because the ionization rate $W_{H_2}(R)$ overlaps strongly with the ground state wave function of H_2, $\chi_0(R)$, at such a distance. During the first half of the dynamics, each local field maximum encountered is higher than the previous one. As the intensity grows, the associated ionization rate becomes wider, ionizing more of the wave packet at smaller internuclear distances, and each of the ionization events thus lowers the average internuclear distance—that is, up until most of the wave packet is already ionized. Since vibrational motion is included in the method, at the end of the pulse and therefore at low field intensities the wave packet propagates toward an oscillation around the equilibrium distance of the H_2^+ potential, $R_{eq}(H_2^+) \approx 2.0$ a.u. Most of the population is distributed within bound states, and the average internuclear distance does not exceed a value of ≈ 2.18 a.u., maximum average distance reached at the end of the pulse.

At a wavelength of 800 nm, Fig. A6.8f, the duration of an optical cycle of the field is three times longer, so for the same total duration of about 32 fs, fewer local maxima are observed but their duration is longer. Initially, the field takes longer to reach the first local intensity maximum. Because ionization events occur on a longer timescale, the average internuclear distance is reduced during ionization to values near 1.0 a.u., quite shorter than the minimum value of 1.4 a.u.

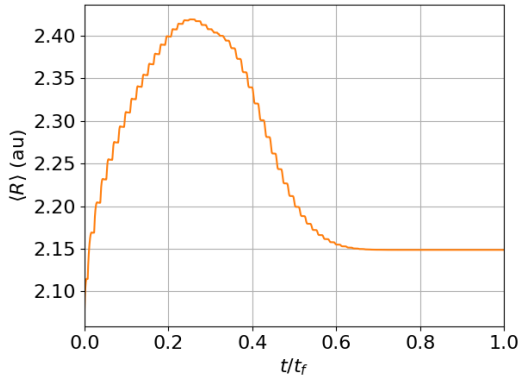

(a) Eigenstate population model
$\lambda = 266\,\text{nm}$

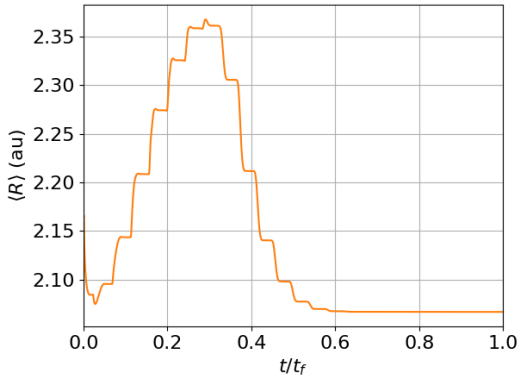

(b) Eigenstate population model
$\lambda = 800\,\text{nm}$

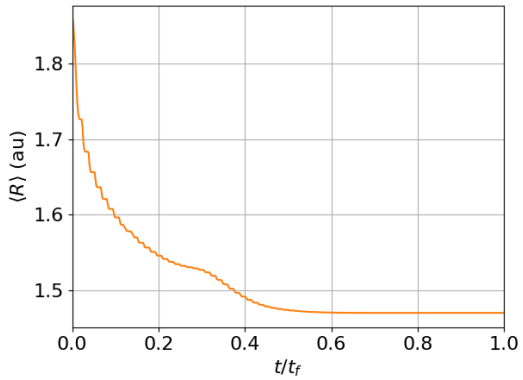

(c) Static wave packet model
$\lambda = 266\,\text{nm}$

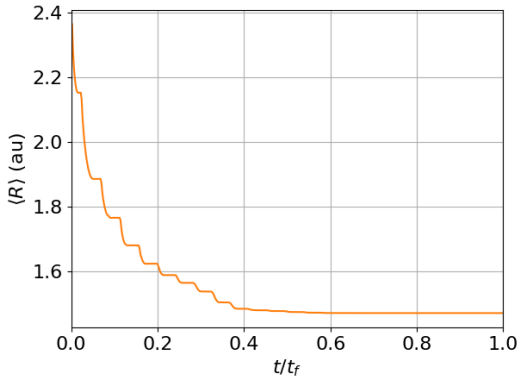

(d) Static wave packet model
$\lambda = 800\,\text{nm}$

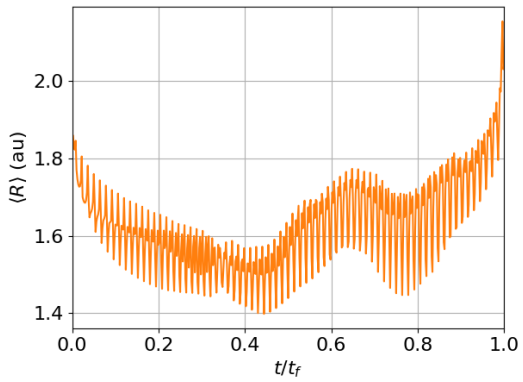

(e) Propagating wave packet model
$\lambda = 266\,\text{nm}$

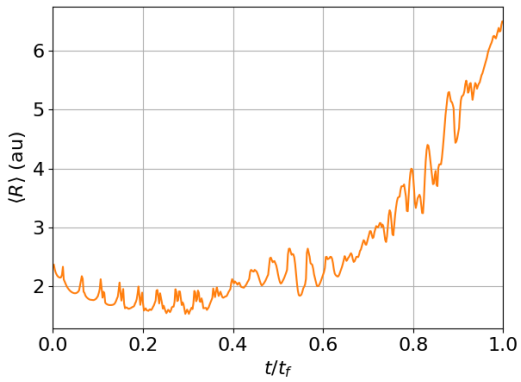

(f) Propagating wave packet model
$\lambda = 800\,\text{nm}$

Figure A6.8: Average internuclear distance $\langle R \rangle$ in H_2^+ for a $10^{15}\,\text{W/cm}^2$ field of wavelength 266 nm, 36 optical cycles for the left column (a,c,e) and 800 nm, 12 optical cycles for the right column (b,d,f). A comparison is made between the different molecular dynamics algorithms: eigenstate population transfer in the top row (a,b), static wave packet transfer in the middle row (c,d) or propagating wave packet transfer in the bottom row (e,f).

observed at 266 nm. Since the H_2^+ wave packet has time to propagate to higher R, when the field reaches another local maximum, more of that wave packet is ionized due to better overlap between that wave packet and the ionization rate $W_{H_2^+}(R)$. This mechanism of vibrational dynamics at the Ti:Sapphire fundamental harmonic is effective enough to completely ionize H_2^+ just after the peak of the pulse. The remaining H_2^+ wave packet then propagates to higher internuclear distances.

The average internuclear distance $\langle R \rangle$ in H_2^+, shown in Figs. A6.8c at 266 nm and A6.8d at 800 nm, decreases continuously during the dynamics simulated with the static wave packet model for the same reason as in Figs. A6.4c and A6.4d for H_2. At 266 nm, an inflection point is seen in Fig. A6.8c in the step-like $\langle R \rangle$ function around $t/t_f = 0.33$, which can be explained by the evolution of $\langle R \rangle$ in H_2 with the same laser parameters (see Fig. A6.4c). This timing corresponds exactly to the time at which a visible change is observed in the average internuclear distance in H_2, so that when the wave packet generated in H_2^+ and the source wave packet in H_2 move both to lower R values, the decrease of the average internuclear distance in H_2^+ is suddenly accelerated. Since ionization events take more time at 800 nm, the same phenomenon occurs, but is overshadowed by the amplified staircase profile of the population.

As shown in Figs. A6.8a and A6.8b, the average internuclear distance profiles are also staircase-shaped for dynamics using projection onto eigenstates, a characteristic of such dynamics under a linearly polarized field. In contrast to static wave packets, $\langle R \rangle$ can and does increase over the course of the simulation, as it depends on the time-dependent state population distribution. As seen in Fig. 4.1, higher states reach lower internuclear distances, but since the repulsion wall of the potential is steeper than the long-range attraction slope, $\langle R \rangle$ increases with the energy of the state.

At a wavelength of 266 nm, Fig. A6.8a, the initial average internuclear distance is about 2.10 a.u., slightly higher than $R_{eq}(H_2^+)$, and it increases during the dynamics to a maximum of about 2.42 a.u. before converging to a static 2.15 a.u. The profile trend follows the rationale of the single and double ionization rates in such a field, shown in Figs. A5.12a and A5.15a respectively. As $\langle R \rangle$ increases, the dynamics is driven by a single ionization process, and as the intensity increases, the distribution of states favoured for population transfer shifts to states slightly higher than the ground state. This increase toward other low-energy states induces an increase in the average internuclear distance, a trend that is reversed once the double ionization process becomes non-negligible. Above a certain intensity, double ionization induces the depletion of high-energy states, so that the ground state takes the lead in the distribution at the end of the pulse. As a

mixture of vibrational states remains at the end of the pulse, and not just the ground state, $\langle R \rangle$ is not quite reduced to $R_{eq}(H_2^+)$, but it comes close.

A rather similar dynamics is also observed at a wavelength of 800 nm, Fig. A6.8b, except that the average internuclear distance is initially around 2.17 a.u. and that it decreases slightly before the above-mentioned increase. From Fig. A5.12a, we can see that at very low intensities $I \approx 10^{10}$ W/cm^2, although $v_+ = 0$ is more populated than other states, $v_+ = 2, 3$ are more populated than $v_+ = 1$. From then on, increasing the intensity up to $I \approx 10^{11}$ W/cm^2 decreases the transfer rates toward $v_+ = 2, 3$ in favour of $v_+ = 1$, a change that induces the decrease of the average internuclear distance.

Coulomb Explosion Kinetic Energy Distributions

Once H_2^+ is ionized, only protons remain in the observed system, so a Coulomb explosion dynamics starts, and the potential energy of the protons is simply inversely proportional to the internuclear distance. Asymptotically, this potential energy is transformed into kinetic energy.

Since the discretized continuum containing the vibrational dissociative states associated with Coulomb explosion is prepared as completely as possible, it is possible to observe a large number of channels at different energies, and such population profiles become easier to observe as contour plots during the evolution of the dynamics. The time- and energy-resolved probabilities of Coulomb explosion are shown in Figs. A6.9a and A6.9b using the eigenstate population transfer method. Once the double ionization process starts, at about 12 fs, lower energies are populated before spreading to slightly higher energies, ending up as a Gaussian-like distribution between 3 eV to 6 eV. This "tail" seen at the beginning of the dynamics is caused by the ionization of low-energy states, which are the most populated. As the field evolves toward its peak intensity at $t \approx 16$ fs, higher states become more populated, as explained by the single ionization rate, which also favours ionization into higher energy states during the double ionization. At the end of the dynamics, the kinetic energy distribution (KED) is broad, due to the similarly broad distribution of internuclear distances generated by the single ionization.

The time-resolved KED contour plots obtained using the static wave packet method and shown in Figs. A6.9c and A6.9d reveal that with this model double ionization occurs from the moment the laser intensity is at its maximum, and thereafter these Gaussian-like kinetic energy distributions centered at a specific energy vary very little with time. As shown previously in Figs. A6.1c and A6.1d,

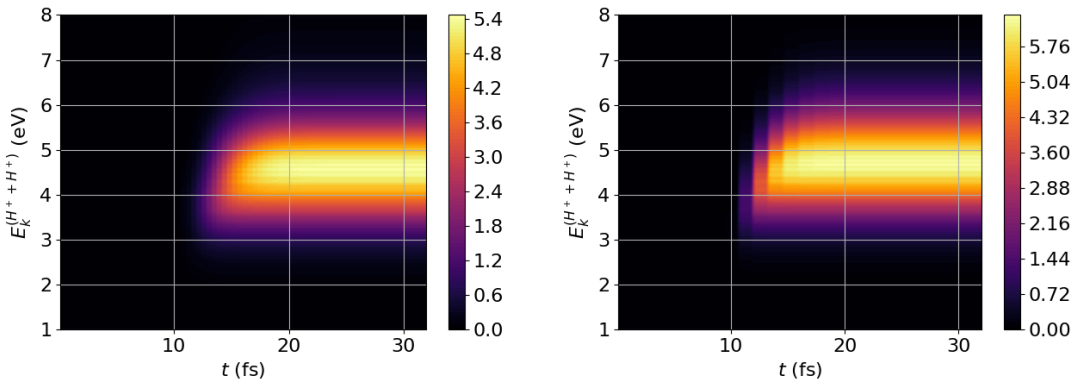

(a) Eigenstate population model $\lambda = 266\,\text{nm}$

(b) Eigenstate population model $\lambda = 800\,\text{nm}$

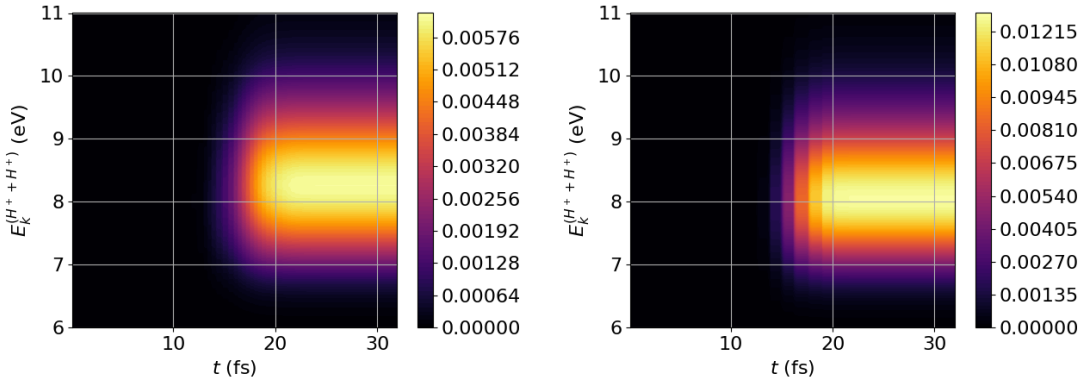

(c) Static wave packet model $\lambda = 266\,\text{nm}$

(d) Static wave packet model $\lambda = 800\,\text{nm}$

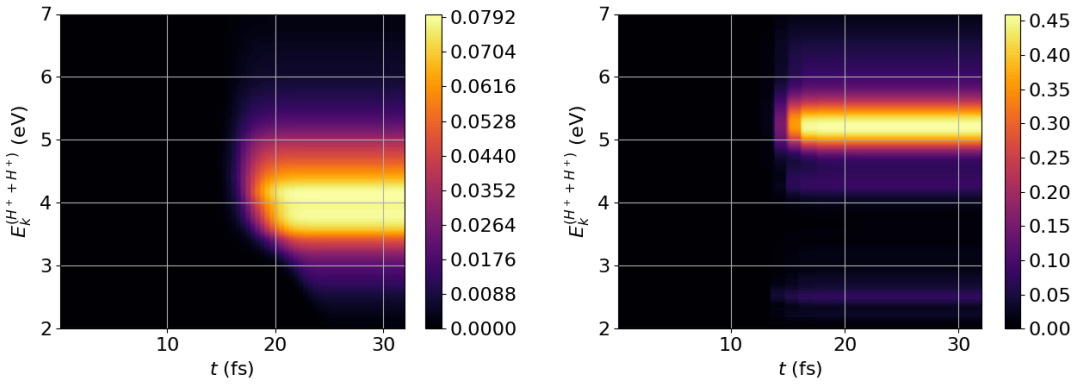

(e) Propagating wave packet model $\lambda = 266\,\text{nm}$

(f) Propagating wave packet model $\lambda = 800\,\text{nm}$

Figure A6.9: Contour plot of the time- and energy-resolved proton kinetic energy distributions arising from Coulomb explosion of H_2 for a $10^{15}\,\text{W/cm}^2$ field of wavelength 266 nm, 36 optical cycles for the left column (a,c,e) and 800 nm, 12 optical cycles for the right column (b,d,f). A comparison is made between the different molecular dynamics algorithms: eigenstate population transfer in the top row (a,b), static wave packet transfer in the middle row (c,d) or propagating wave packet transfer in the bottom row (e,f).

most of the population is ionized up to H_2^+, but remains within this state of the molecule, with a brief double ionization event around the peak intensity of the field. This is the reason why the distribution is shaped like a Gaussian: because the ionization occurs over a short variation in intensity, which brings the ionized wave packet as is it shaped by its overlap with the ionization rate. The energy distribution is located in the interval between 7 and 10 eV, which is quite higher than the distribution with other methods, because since the wave packet is static, the fundamental, low-R source wave packet $\psi_{H_2}(R,0) = \chi_0(R)$ sets the final kinetic energy to values associated with internuclear distances close to the equilibrium distance $R_{eq}(H_2)$.

For both methods, the main differences between the 266 and 800 nm contours are the widths of the plateau durations, that are slightly longer for the highest wavelength. Since the population dynamics are λ-dependent for the propagating wave packet method (see Figs. A6.1e and A6.1f), the KED evolution during the dynamics is also λ-dependent.

At 266 nm, Fig. A6.9e, the wave packet is initially ionized at relatively short, near-equilibrium internuclear distances, which, because of their inversely proportional relationship, bring the distribution to energies close to 6 eV. The implemented vibrational motion allows the wave packet to propagate toward dissociative R values, and part of the propagating wave packet is subsequently ionized to its Coulomb explosion ionic state at relatively larger R values. Over time, the tail of the distribution, initially set around relatively higher energies, is thus brought down to lower energy values. At the end of the dynamics, the KED range is set around 3 to 6 eV. A slightly different scenario is observed when the wavelength is increased to 800 nm, as shown in Fig. A6.9f. At the peak of the pulse, H_2 is then already fully ionized up to its Coulomb explosion. Thus, the wave packet does not have much time to expand to higher R values (as seen at 266 nm), leading to Coulomb explosion at energies around 4 to 6 eV.

At the end of the dynamics, the dissociation probabilities and their associated kinetic energy distributions can originate either from the dissociation of the molecule in the H_2^+ potentials or during the Coulomb explosion. The former KED spectra have been plotted for all methods, comparing simulations at 266 and 800 nm, but only the propagating wave packet method can be fully considered for a realistic simulation of these spectra.

Figures A6.10a and A6.10b show the KED using the eigenstate projection method at 266 and 800 nm. They have a quasi-Gaussian shape and are distributed in an energy range between 2 and 8 eV. The peculiarity of the spectra obtained by this method is that they contain small oscillations of different frequencies over

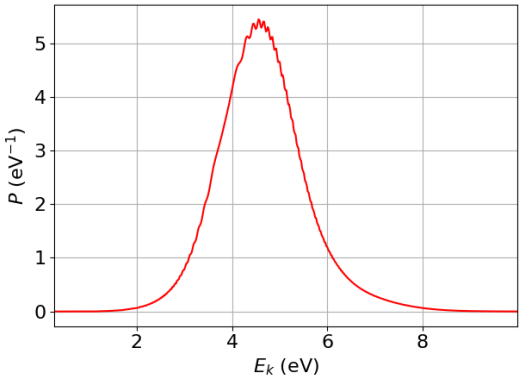

(a) Eigenstate population model
$\lambda = 266\,\text{nm}$

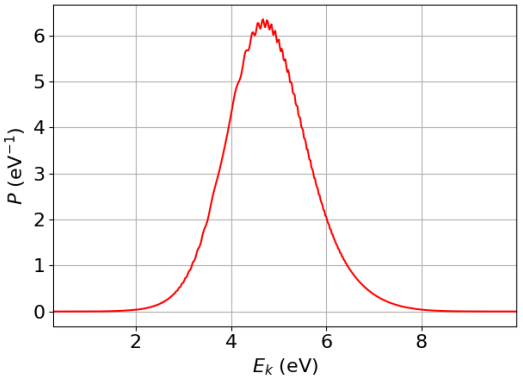

(b) Eigenstate population model
$\lambda = 800\,\text{nm}$

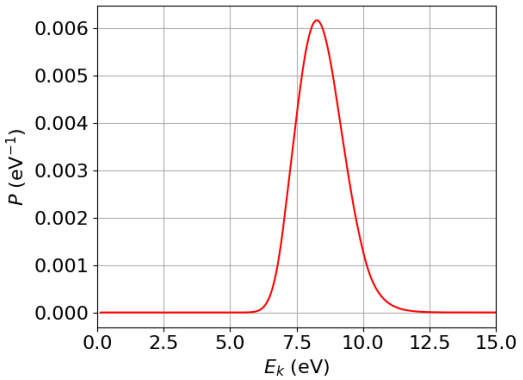

(c) Static wave packet model
$\lambda = 266\,\text{nm}$

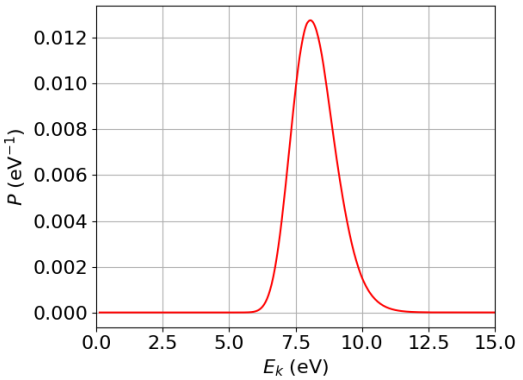

(d) Static wave packet model
$\lambda = 800\,\text{nm}$

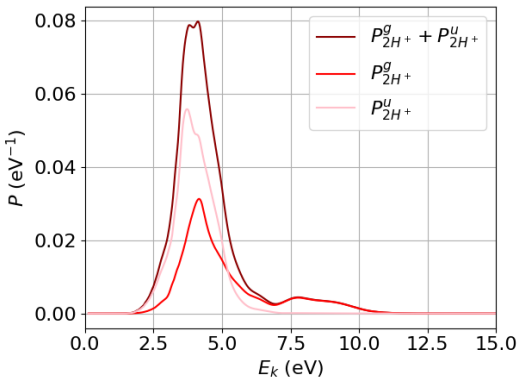

(e) Propagating wave packet model
$\lambda = 266\,\text{nm}$

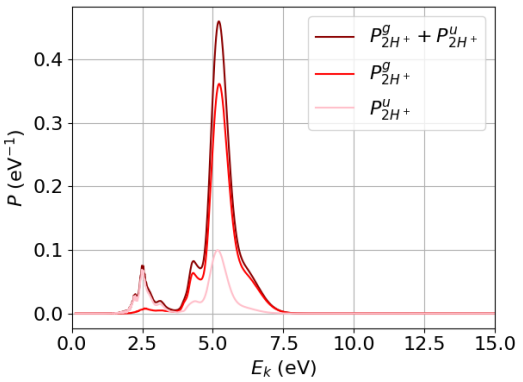

(f) Propagating wave packet model
$\lambda = 800\,\text{nm}$

Figure A6.10: Final proton kinetic energy distributions resulting from the Coulomb explosion of H_2 (dark red line) split in the contributions from the $^1\Sigma_g^+$ (red line) and $^1\Sigma_u^+$ (pink line) electronic states of H_2^+ with a 10^{15} W/cm^2 field of wavelength 266 nm, 36 optical cycles for the left column (a,c,e) and 800 nm, 12 optical cycles for the right column (b,d,f). A comparison is made between the different molecular dynamics algorithms: eigenstate population transfer in the top row (a,b), static wave packet transfer in the middle row (c,d) or propagating wave packet transfer in the bottom row (e,f).

their range of interest. The quenching events associated with these oscillations are directly related to the zero values of the ionization rate found in the first ionization process, as shown in Fig. A5.12a. Since the applied ionization rate is the result of the integral of the overlap between the initial state $\chi_0(R)$, the final state $\chi_{v_+}(R)$ and the R-dependent ionization rate W_{H_2}(R), and since the latter allows ionization in a wider range of internuclear distances as the intensity increases, some intensities give a null integral for certain transitions, hence the varying quenching events at certain intensities. Since the populations evolve over time and the quenched transitions vary from one intensity to the other, the small oscillations found in these spectra are relatively irregular.

The KED obtained by the static wave packet method also generate Gaussian-like spectra as shown in Figs. A6.10c at 266 nm and A6.10d) at 800 nm, but as discussed above, the energy range is quite higher than for the other two methods because the wave packet is never displaced. Centered at low R, the resulting proton energy is around 6 to 11 eV, and, being averaged, the small oscillations observed with the eigenstate population transfer method disappear. For this algorithm, no H_2^+ dissociation KED would make physical sense, since the wave packet does not propagate over time.

From the propagating wave packet method, since the population can evolve in the $^1\Sigma_g^+$ and $^1\Sigma_u^+$ potentials, H_2^+ can be ionized from both electronic states, as shown in Figs. A6.10e and A6.10f. At 266 nm, the main energy peak, centered at around 4 eV, comes from a mixture of both configurations, since H_2^+ was ionized only gradually, thus allowing coupling and exchange between the two considered potentials of the molecule. At the higher wavelength of 800 nm, the two peaks come mainly from two different sources: the one centered at 5.2 eV from $^1\Sigma_g^+$ and the smaller one at 2.5 eV from $^1\Sigma_u^+$. This difference between the source wave packets can be explained by the time lapse between a first burst of ionization at lower intensity, which populates H_2^+ in its ground electronic state, and then, as time passes, this wave packet propagates into a bifurcation of the gerade part of the wave packet, which is mainly bound to lower R values, and an ungerade fraction, which propagates freely towards dissociation. Once both fractions are well separated, a second burst of ionization occurs near the peak intensity and transfers all the remaining population from H_2 to H_2^+ in a single step, but it also ionizes both gerade and ungerade fractions of the H_2^+ wave packet toward the Coulomb explosion. This explains the presence of two separate peaks of different amplitudes and kinetic energies in the KED. Such sequential dissociative double ionization events have also been investigated by Yuen and Lin with the larger molecule N_2 [6], which brought the researchers to similar results where KED of the dissociated atoms were divided between two

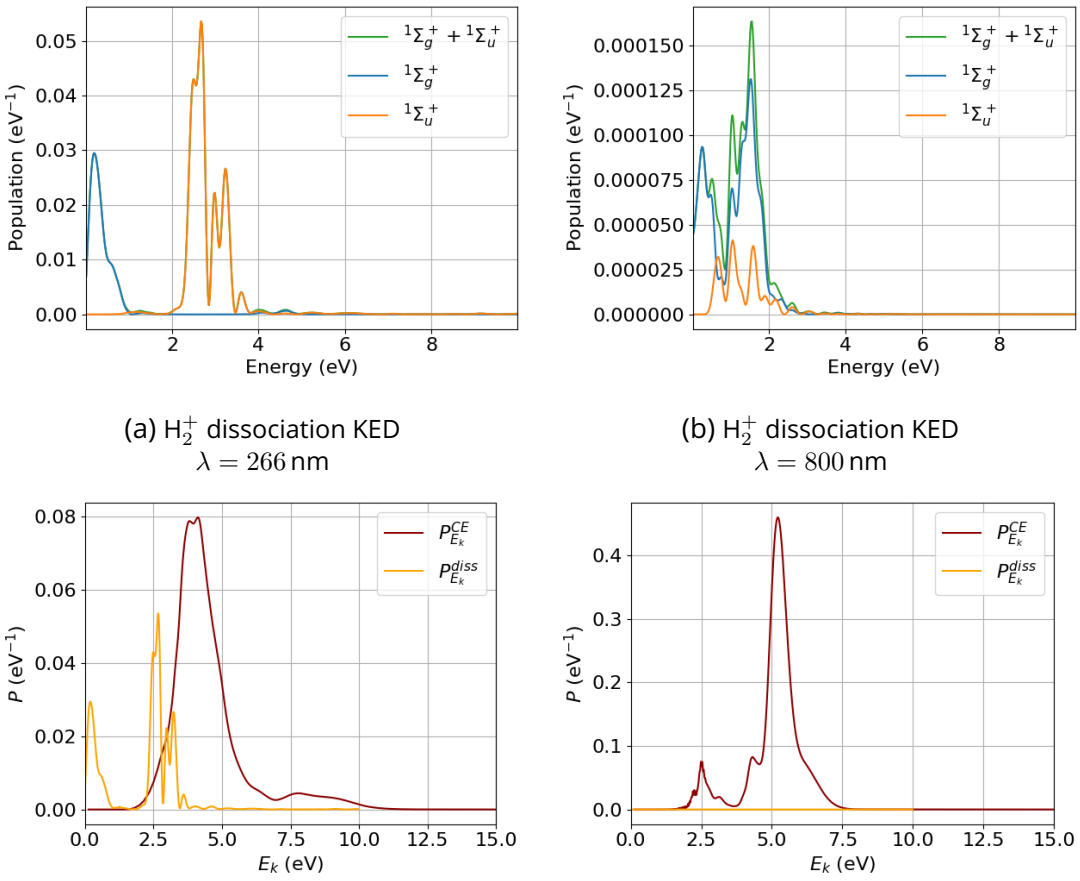

(a) H_2^+ dissociation KED
$\lambda = 266$ nm

(b) H_2^+ dissociation KED
$\lambda = 800$ nm

(c) Total KED
$\lambda = 266$ nm

(d) Total KED
$\lambda = 800$ nm

Figure A6.11: Final proton kinetic energy distributions (KED) from the dissociation of H_2^+ within the gerade $^1\Sigma_g^+$ and ungerade $^1\Sigma_u^+$ electronic states, for a 10^{15} W/cm^2 field of wavelength 266 nm, 36 optical cycles for the left column (a,c) and 800 nm, 12 optical cycles for the right column (b,d). The top row displays the dissociative KEDs alone (a,b) while the bottom row displays dissociative KEDs (yellow line) as well as the Coulomb Explosion KED (brown line) (c,d).

peaks of different energies; lower energies coming from sequential ionization.

The KEDs resulting from the dissociation of H_2^+ are generally found at lower energies than those resulting from Coulomb explosion, because the Coulomb repulsion energy between protons is generally larger than the dissociation energy between a neutral H(1s) and a proton. This is the case for the dynamics observed in Figs. A6.11a and A6.11b, at 266 and 800 nm, respectively. At 800 nm the dissociation of the stable ionized molecule is negligible compared to the Coulomb explosion. The comparison between Fig. A6.11b and Fig. A6.11d shows that the Coulomb explosion probability is 3 orders of magnitude higher than the dissociation of the intermediate molecular ion. At 266 nm, Fig. A6.11c, while the Coulomb explosion probability is dominant, a large part of H_2^+ dissociates at energies below 1 eV for the $^1\Sigma_g^+$ channel and at energies between 2 and 4 eV for the $^1\Sigma_u^+$ channel. These peaks were discussed in the main article as physically resulting from Bond Softening (BS) and Above-Threshold Dissociation (ATD), respectively, while the two other higher energy peaks result from direct double ionization and sequential double ionization.

Bibliography

[1] A. Giusti-Suzor, X. He, O. Atabek, and F. H. Mies. Above-threshold dissociation of H_2^+ in intense laser fields. *Phys. Rev. Lett.*, 64:515–518, Jan 1990. URL: https://link.aps.org/doi/10.1103/PhysRevLett.64.515, doi:10.1103/PhysRevLett.64.515.

[2] P. H. Bucksbaum, A. Zavriyev, H. G. Muller, and D. W. Schumacher. Softening of the H_2^+ molecular bond in intense laser fields. *Phys. Rev. Lett.*, 64:1883–1886, 1990. URL: https://link.aps.org/doi/10.1103/PhysRevLett.64.1883, doi:10.1103/PhysRevLett.64.1883.

[3] A. Zavriyev, P. H. Bucksbaum, H. G. Muller, and D. W. Schumacher. Ionization and dissociation of H_2 in intense laser fields at 1.064 μm, 532 nm, and 355 nm. *Phys. Rev. A*, 42:5500–5513, 1990. URL: https://link.aps.org/doi/10.1103/PhysRevA.42.5500, doi:10.1103/PhysRevA.42.5500.

[4] B. Yang, M. Saeed, L. F. DiMauro, A. Zavriyev, and P. H. Bucksbaum. High-resolution multiphoton ionization and dissociation of H_2 and D_2 molecules in intense laser fields. *Phys. Rev. A*, 44:R1458–R1461, Aug 1991. URL: https://link.aps.org/doi/10.1103/PhysRevA.44.R1458, doi:10.1103/PhysRevA.44.R1458.

[5] G. Jolicard and O. Atabek. Above-threshold-dissociation dynamics of H_2^+ with short intense laser pulses. *Phys. Rev. A*, 46:5845–5855, Nov 1992. URL: https://link.aps.org/doi/10.1103/PhysRevA.46.5845, doi:10.1103/PhysRevA.46.5845.

[6] C. H. Yuen and C. D. Lin. Density-matrix approach for sequential dissociative double ionization of molecules. *Phys. Rev. A*, 106:023120, Aug 2022. URL: https://link.aps.org/doi/10.1103/PhysRevA.106.023120, doi:10.1103/PhysRevA.106.023120.

Chapter 7 Conclusion

7.1 . Summary

The thesis is structured in two parts:

- The **First Part** is about the TD-MCSCF program MEDYS and its application to the study of the limits of the SAE approximation, developed in **Chapters 2** and **3**.
- The **Second Part** is about the implementation of dissociation dynamics in a newly-coded program that makes use of the semi-classical methods MO-ADK and MO-PPT to simulate the ionization dynamics, in a complete molecular simulation approach, developed in **Chapters 4** to **6**.

Starting with the **First Part**, in **Chapter 2**, the Many-Electrons Dynamics System (MEDYS) program was reviewed to introduce the research work that has been done beyond the Single Active Electron (SAE) approximation.

In the article inserted in **Chapter 3**, the adiabatic switch-off parameter implemented in MEDYS was used to investigate the effect of the electronic correlation on the end-of-the-pulse single ionization probabilities at fixed internuclear distances R, ranging from equilibrium ($R_{\mathrm{eq}} = 1.4\,$a.u.) to elongated ($R_{\mathrm{elong}} = 5.0\,$a.u.) and quasi-dissociative ($R_{\mathrm{diss}} = 10.2\,$a.u.). It was found that while there are no significant differences in the R_{eq} and R_{diss} ionization probabilities from fully-correlated dynamics and switched-off correlation, the elongated conformations give rise to events of ionization quenching and exaltation. These phenomena were attributed to Resonance Enhanced Multiphoton Ionization (REMPI) mechanisms occurring at internuclear distances high enough for the correlation to be non-negligible, and not so high that the compositions in σ_g and σ_u are not similar (and thus not inducing destructive interferences).

The following **Annex** reinforced this explanation by analyzing results from elongated $R = 4.0$ a.u. and $R = 6.0$ a.u., and comparing population profiles at intensities that induce quenching and exaltation events for all elongated internuclear distances.

The **Second Part** of the thesis begins in **Chapter 4** with a presentation of the equations used in the different versions of our semi-classical ionization dynamics algorithm. An iterative population transfer method derived from the TDSE was presented, as well as kinetic equations including the vibrational motion of the nuclei. The split-operator method used to propagate the nuclear wave packets was also introduced.

The semi-classical methods MO-ADK and MO-PPT were presented in **Chapter 5** in an article that compared the effects of 1) the chosen method for the description of ionization, and 2) the polarization, the intensity and the frequency of the field on the single ionization probability and on the non-FC distribution of the eigenstates populations. The MO-PPT method, which takes into account the influence of the applied wavelength, was confirmed to be more suitable than the MO-ADK approach for representing the ionization probability at values of the Keldysh parameter close to or above 1, *i.e.* at relatively low intensity and/or relatively high frequency, a domain favorable for ionization in the multiphoton regime. At the same fluence, circular polarization of the field requires higher peak intensities than linear polarization to reach the saturation of the single and double ionization probabilities. In addition, when taking into consideration the R-dependent semi-classical ionization rate, the induced non-FC distribution was found to favour ionization toward lower vibrational eigenstates of H_2^+ than what was predicted by the Franck-Condon approximation.

As a supplement to the research reported in the inserted article, an **Annex** explained that the ionization probability saturation is reached faster with a linearly polarized field, because its ionization rate becomes much higher than with a circularly polarized field, and because even if it is only for a very short duration, the integrated rate is higher. It was also shown that the non-FC distribution depends on the field frequency, but not on the pulse duration, as long as the saturation of the ionization is not reached. This effect was shown to be due to the relative similarity of the ionization rate distribution over time. The ionized population, on the other hand, grows with the duration of the pulse.

The population transfer via the eigenstate projection method was then remodeled in **Chapter 6** to allow for amplitude transfer of the wave packets and finally to include the nuclear vibrational dynamics. The implementation of the R-propagation brought significant differences in the double ionization proba-

bilities, sometimes changing them by orders of magnitude, as the molecule in this case explores regions of large internuclear distance where ionization is generally easier. From the generated kinetic energy spectra of the released ions, peaks could be attributed to Above Threshold Dissociation, Bond Softening and Coulomb Explosion.

The following **Annex** highlighted discrepancies in the models and their resulting observables in terms of population profiles, average internuclear distance and KED spectra. The eigenstates projection method was shown to overestimate the double ionization process due to the unrealistic generation of populations at large internuclear distances, a result of neglecting the phase during the transfer of the populations from H_2 to H_2^+. Conversely, an underestimation of the double ionization probability was found with the static wave packet method as they could not propagate to higher internuclear distances over time, thus reducing the overlap with the ionization rate function of H_2^+. Both of the above models that do not consider vibrational dynamics failed to reproduce the KED spectra, and the static wave packet method unsurprisingly overestimated the energy of the protons emitted during the Coulomb explosion of the molecule. Finally, neither could account for the non-negligible H(1s)$+$H$^+$ dissociation energy released at various wavelengths.

7.2 . Research Directions and Future Plans

As research avenues emerge from the projects I worked on during my PhD, plans are already being made for possible improvements in the coming years.

Since the MEDYS ionization continuum requires an exhaustive discretized basis of Volkov states or plane waves, Nguyen-Dang's laboratory has started to implement a propagated Gaussian basis to accurately compute the momentum distribution of the photoelectron once it is ionized by storing the parameters of the fitting Gaussians and propagating them over all time steps. The process thus gains in precision thanks to the completeness of the basis for an overall low computational cost for short dynamics.

A lot of computational resources are preserved with a semi-classical approach to the ionization dynamics, despite the lack of consideration of multi-electronic processes arising from electronic correlation. In the future, we aim to extract ionization rate datasets from the ab initio program MEDYS to fit fully-correlated results to analytical approaches, thus preserving the efficiency of ionization dynamics through complete molecular simulations, while adding the robustness of MEDYS' TD-MCSCF/TDCI method.

Both MEDYS and the semi-classical dissociative ionization codes have been programmed to adapt to systems more complex than H_2. A theoretical study of diatomics, including N_2 and O_2, would be interesting to compare the importance of electron correlation and vibrational dynamics on the ionization probabilities and on the kinetic energy distribution of the photo-fragments.

Synthèse en français

La thèse est structurée en **deux parties** qui explorent les principaux projets investigués au cours du doctorat.

Partie I – La première partie est une étude préliminaire sur les limites quantitatives de l'approximation du seul électron actif (*Single Active Electron*; SAE) à l'aide du programme MEDYS de type champ autocohérent multi-configuration dépendant du temps (*Time-Dependent Multi-Configurations Self-Consistent Field*; TD-MCSCF) du laboratoire Nguyen-Dang de l'Université Laval, sur lequel de plus amples explications sont données dans les **chapitres** 2 et 3.

Le **chapitre** 2 présente la théorie derrière la méthode post-Hartree-Fock (post-HF) utilisée pour résoudre l'équation de Schrödinger dépendante du temps (*Time-Dependent Schrödinger Equation*; TDSE), suivie d'une description de l'algorithme MEDYS utilisé dans le présent travail pour simuler entièrement la dynamique d'ionisation simple comprenant la corrélation électronique complète de la molécule neutre H_2 à des distances internucléaires fixes et en utilisant des considérations d'approximation en champ laser intense (*Strong-Field Approximation*; SFA). Les bases nécessaires à une représentation raisonnable des chemins d'ionisation sont ensuite expliquées dans le même chapitre, se terminant par une présentation des paramètres associés au champ laser fort pulsé, et des observables résultant de la dynamique.

Le **chapitre** 3 est une insertion de l'article publié intitulé « Strong-Field Molecular Ionization Beyond the Single Active Electron Approximation, » une publication qui démontre le fruit de notre exploration des limites quantitatives de l'approximation SAE en comparant la dynamique d'ionisation en situation d'électrons entièrement corrélés avec une dynamique à corrélation adiabatiquement désactivée. Les profils de probabilité totale d'ionisation en fonction de l'intensité maximale du champ ont été tracés pour les deux types de dynamique, et deux observations principales ont été faites à partir de ces figures. Le premier (1) est qu'à la géométrie d'équilibre de la molécule, nous avons perçu un saut soudain vers une ionisation totale au-delà des intensités maximales supérieures à 10^{16} W/cm^2, ce qui indique un événement d'ionisation tunnel au-dessus de la barrière (*Over-the-Barrier Tunnel Ionization*; OBTI). L'autre observation (2) est que même si une augmentation relativement douce de la probabilité a été observée aux géométries d'équilibre et dissociatives, la dynamique d'ionisation des molécules allongées dénotait une extinction et une exaltation partielles en fonction de l'intensité maximale lorsque les électrons étaient entièrement corrélés, un phénomène qui ne se produisait pas dans le cadre de l'approximation SAE. De tels phénomènes dépendants des paramètres ont été attribués à un mécanisme d'ionisation multiphotonique renforcé par résonance (*Resonance-Enhanced Multiphoton Ionization*; REMPI) provoquant une interférence entre les voies d'excitation et d'ionisation. Cet article est suivi d'une annexe qui présente une analyse allant au-delà de ce qui a été publié, et fournit des résultats sur la dynamique à des distances internucléaires allongées qui soutiennent le fait que des événements d'ionisation d'extinction et d'exaltation peuvent également se produire à des valeurs R entourant le $R = 5,0$ au. présenté dans l'article. À cette fin, des profils de population des états propres et des fonctions d'état de configuration sont présentés pour les événements d'extinction et d'exaltation de la population, pour les trois configurations allongées de H_2, y compris celle publiée dans l'article original.

Partie II – La deuxième partie se concentre sur l'étude de la dynamique complète d'ionisation dissociative de la molécule en utilisant des méthodes semi-classiques pour décrire les événements d'ionisation et faciliter la mise en œuvre du mouvement vibratoire des noyaux ; un projet qui a nécessité l'écriture d'un tout nouveau code au sein du groupe de recherche Atabek & Charron de l'Université Paris-Saclay, abordé dans les **chapitres** 4 à 6.

Le **chapitre** 4 couvre le développement des différents algorithmes utilisés dans l'implémentation semi-classique de la dynamique d'ionisation. À partir de l'équation de Schrödinger dépendant du temps, les processus d'ionisation séquentiels sont représentés d'une manière qui implique des échanges complexes d'amplitudes de paquets d'ondes, tandis que des transferts de population successifs sont obtenus à partir de projections sur les états propres, décrit dans l'article du Eur. Phys. J. Spec. Top. « Strong Field Non-Franck-Condon Ionization of H_2: A Semiclassical Analysis. » Ce chapitre présente également les équations cinétiques incluant la propagation des paquets d'ondes vibrationels pour introduire le modèle utilisé dans l'article du J. Phys. Chem. A « Electro-nuclear Dynamics of H_2 single and double ionization in ultrafast intense laser pulses. » La méthode de l'opérateur fractionné (*Split-Operator*) utilisée pour la propagation des paquets d'ondes nucléaires est ensuite discutée, avant d'expliquer les observables générés qui sont analysés au cours de la dynamique.

Le **chapitre 5** constitue une première étape du projet, qui est discutée dans l'article du Eur. Phys. J. Spec. Top., « Strong Field Non-Franck-Condon Ionization of H_2: A Semiclassical Analysis. » Cet article couvre en détail les équations utilisées pour l'ionisation avec la méthode moléculaire des scientifiques Ammosov Delone et Kraïnov (MO-ADK) ou la méthode moléculaire de Popov Perelomov et Terent'ev (MO-PPT). Des simulations de la dynamique d'ionisation de H_2 en champ fort ont été comparées entre les deux méthodes, pour des polarisations linéaires ou circulaires du champ. À une fluence similaire, il a été démontré que la polarisation linéaire saturait la probabilité d'ionisation à des intensités de crête inférieures à celles de la polarisation circulaire. Les distributions de population non-Franck-Condon sur les états propres de H_2^+ ont été comparées à la distribution de Franck-Condon, et son déplacement des populations vers des niveaux d'énergie inférieurs a été attribué à la dépendance en R du taux d'ionisation calculé à partir de MO-ADK ou MO-PPT. L'article est suivi d'une annexe qui présente des représentations visuelles de l'anisotropie de l'ionisation selon l'angle d'incidence du champ, ainsi que la fonction de Padé ajustée à la valeur t_0 nécessaire dans la méthode moléculaire PPT. Les polarisations linéaire et circulaire sont en outre analysées en termes de taux d'ionisation pour expliquer comment les deux polarisations n'induisent pas de probabilités d'ionisation similaires à une même fluence.

Le **chapitre 6** inclut l'article issu du J. Phys. Chem. A « Electro-nuclear Dynamics of H_2 single and double ionization in ultrafast intense laser pulses » et une annexe subséquente qui s'intéresse aux différences entre les observables produites par les méthodes impliquant des paquets d'ondes nucléaires, statiques ou propagées, et les transferts de population de projections d'états propres, sujet du chap. 5. Les dynamiques vibrationnelles sont mises de l'avant dans cet article qui met en évidence leur rôle crucial dans la simulation de l'ionisation dissociative de H_2. L'importance du mouvement des noyaux est particulièrement démontrée dans les processus de seconde ionisation, où les paquets d'ondes vibrationnels statiques sous-estiment largement les probabilités d'ionisation. Le modèle suggéré de dynamique moléculaire complète est utilisé pour générer des résultats réalistes grâce aux spectres de distribution en énergie cinétique (*Kinetic Energy Distribution*; KED) des protons émis via la photodissociation de H_2^+, englobant les événements de dissociation au-dessus du seuil (*Above-Threshold Dissociation*; ATD), de relaxation des liaisons (*Bond Softening*; BS), et à partir de l'explosion coulombienne des protons restant. L'annexe étudie les différences entre les profils de population, les distances internucléaires moyennes et les spectres KED résultants tout en revenant aux principes des taux d'ionisation semi-classiques calculés en annexe du chap. 5.

La thèse est conclue dans le **chapitre 7** avec un bref résumé de tous les chapitres et quelques plans futurs de recherche, tels que le développement de taux d'ionisation analytiques à partir des méthodes post-HF, la poursuite approfondie de l'étude de la limite quantitative de l'approximation SAE et l'implémentation d'un continuum ionique alternative qui impliquerait la propagation de gaussiennes.